



**DGK** Deutsche Geodätische Kommission  
bei der Bayerischen Akademie der Wissenschaften

---

Reihe C

Dissertationen

Heft Nr. 660

**Stefan Josef Auer**

**3D Synthetic Aperture Radar Simulation  
for Interpreting Complex Urban Reflection Scenarios**

**München 2011**

---

Verlag der Bayerischen Akademie der Wissenschaften  
in Kommission beim Verlag C. H. Beck

ISSN 0065-5325

ISBN 978-3-7696-5072-3





## 3D Synthetic Aperture Radar Simulation for Interpreting Complex Urban Reflection Scenarios

Vollständiger Abdruck  
der von der Fakultät für Bauingenieur- und Vermessungswesen  
der Technischen Universität München  
zur Erlangung des akademischen Grades eines  
Doktor-Ingenieurs (Dr.-Ing.)  
genehmigten Dissertation

von

Dipl.-Ing. Stefan Josef Auer

München 2011

---

Verlag der Bayerischen Akademie der Wissenschaften  
in Kommission beim Verlag C. H. Beck

Adresse der Deutschen Geodätischen Kommission:



Deutsche Geodätische Kommission

Alfons-Goppel-Straße 11 • D – 80 539 München

Telefon +49 – 89 – 23 031 1113 • Telefax +49 – 89 – 23 031 -1283 / - 1100

e-mail hornik@dgfi.badw.de • <http://www.dgk.badw.de>

Prüfungskommission

Vorsitzender: Univ.-Prof. Dr.-Ing. Dr. h.c. mult. Reiner Rummel

Prüfer der Dissertation: 1. Univ.-Prof. Dr.-Ing. habil. Richard Bamler

2. Univ.-Prof. Dr.-Ing. habil. Stefan Hinz, Universität Karlsruhe

3. Prof. Antonio Iodice, Ph.D, Università degli Studi di Napoli Federico II, Italien

Die Dissertation wurde am 09.12.2010 bei der Technischen Universität München eingereicht  
und durch die Fakultät für Bauingenieur- und Vermessungswesen am 11.03.2011 angenommen.

---

© 2011 Deutsche Geodätische Kommission, München

Alle Rechte vorbehalten. Ohne Genehmigung der Herausgeber ist es auch nicht gestattet,  
die Veröffentlichung oder Teile daraus auf photomechanischem Wege (Photokopie, Mikrokopie) zu vervielfältigen.

ISSN 0065-5325

ISBN 978-3-7696-5072-3

# Abstract

Due to the high spatial resolution of up to 1 m, very high resolution spaceborne SAR sensors such as TerraSAR-X/TanDEM-X or COSMO-SkyMed enable the monitoring of single objects on the earth surface. However, the interpretation of the appearance of objects on SAR images is difficult due to distortion effects like foreshortening or layover. So far, the nature of scatterers evoking prominent SAR image features is still not known in detail. Simulation methods based on rendering algorithms enable to support the visual interpretation of SAR images, as the focus can be set on the object geometry. Mainly developed for providing test data sets, simulators reported in the literature are limited to the azimuth-range plane. Additional methods for exploiting the geometry of simulated data still have to be developed. In order to overcome these limitations, the work presented in this thesis addresses three new aspects. First, *SAR simulation is conducted in three dimensions*, including the elevation domain. Second, methods for the *directed analysis of image signatures* are introduced. Finally, the *inversion of SAR imaging systems* is simulated for analyzing the physical origin of SAR image signatures.

In order to meet these objectives, a SAR simulator named RaySAR has been developed based on ray tracing methods which provides simulation products in three steps: modeling, sampling, and 3D analysis of scatterers. In the modeling step, the geometry and surface parameters of objects are defined within a virtual scene. Geometrical and radiometrical information about signal contributions is captured by sampling the scene. To this end, POV-Ray, an open-source ray tracer, is adapted in order to provide output data in SAR geometry. In this regard, an ideal SAR system is simulated which is characterized by infinite resolution in azimuth, range, and elevation. Specular reflections are detected based on a geometrical analysis of the signal path. In the last step, scatterers are analyzed in three dimensions based on images simulated in the azimuth-range plane. Layover situations can be resolved due to the availability of 3D information. Moreover, SAR image signatures can be linked with the geometry of simulated objects.

The results of different case studies show potentials and limitations of the simulation concept. With regard to the sampling step, limitations occur due to simplified reflection models and a partial loss of diffuse multiple reflections. However, RaySAR fully covers specular reflections and enables to simulate object models characterized by a high level of detail. Concerning the required level of detail of building models, at least basic facade details have to be geometrically described. Triple reflections at building corners are confirmed as prominent building hints on SAR images. In addition, signal reflections of bounce levels larger than 3 are likely to appear for isolated buildings. When using detailed building models, simulated signatures can be automatically linked to real SAR data. Thereafter, the inversion of the SAR imaging process is enabled by identifying the corresponding scatterers on the 3D model of the simulated scene. The case studies reveal, that a high number of SAR image signatures do not directly represent the geometry of objects. For instance, multiple reflections may be localized in 3D space next to buildings, on ground or even beneath the ground level.

# Zusammenfassung

Aktuelle satellitengetragene SAR-Systeme wie TerraSAR-X/TanDEM-X oder COSMO-SkyMed ermöglichen die Überwachung von Einzelobjekten an der Erdoberfläche aufgrund ihrer hohen räumliche Auflösung. Die Interpretation des Erscheinungsbilds von Objekten in SAR-Bildern ist dennoch schwierig aufgrund von Verzerrungseffekten wie der Verkürzung oder Überlagerung von Objektinformation. Die Natur von Streuern, die deutlich sichtbare SAR-Bildsignaturen hervorrufen, ist bislang noch nicht im Detail bekannt. Auf Render-Algorithmen basierende Simulationsmethoden ermöglichen die Unterstützung der visuellen Interpretation von SAR-Bildern, indem das Augenmerk auf die Geometrie von Objekten gelegt werden kann. Bisher veröffentlichte Simulationsverfahren wurden hauptsächlich für die Erzeugung von Testdatensätzen entwickelt und sind auf die Azimut-Entfernung-Ebene begrenzt. Weitergehende Methoden für die Auswertung der geometrischen Information simulierter Daten müssen noch entwickelt werden. Der in dieser Doktorarbeit präsentierte Ansatz spricht drei neue Aspekte an, um diese Limitierungen zu überwinden. Zum einen wird die Simulation von SAR-Daten in drei Dimensionen durchgeführt, einschließlich der Elevationsrichtung. Zudem werden Methoden aufgezeigt für eine gesteuerte Analyse von Bildsignaturen. Schließlich wird die Inversion eines SAR-Abbildungssystems simuliert, um den physikalischen Ursprung von SAR-Bildsignaturen feststellen zu können.

Für die Realisierung dieser Ziele wurde ein SAR-Simulator namens RaySAR entwickelt, der auf Raytracing-Methoden basiert und Simulationsprodukte anhand von drei Arbeitsschritten bereitstellt: Modellierung, Abtastung und 3D Analyse von Streuern. Der Modellierungsschritt beinhaltet die Definition der Geometrie und Oberfläche von Objekten innerhalb einer virtuellen Szene. Geometrische und radiometrische Informationen über Signalbeiträge werden durch die Abtastung der Szene erfasst. In diesem Zusammenhang wird ein ideales SAR-System simuliert, welches eine unendliche Auflösung in Azimut-, Entfernungs- und Elevationsrichtung besitzt. Spiegelnde Reflexionen werden erkannt anhand einer geometrischen Analyse des Signalpfads. Im letzten Arbeitsschritt werden auf der Grundlage von simulierten Bilddaten in der Azimut-Entfernung-Ebene Streuer im dreidimensionalen Raum analysiert. Überlagerungseffekte in SAR-Bildern lassen sich dabei durch die Verfügbarkeit von 3D Information auflösen. Darüber hinaus können SAR-Bildsignaturen mit der Geometrie von simulierten Objekten in Verbindung gebracht werden.

Die Ergebnisse von verschiedenen Fallstudien zeigen das Leistungsvermögen und Grenzen des Simulationskonzepts. Limitierende Faktoren bei der Abtastung sind vereinfachte Reflexionsmodelle und ein Teilverlust von diffusen Mehrfachreflexionen. Jedoch erlaubt RaySAR die vollständige Erfassung von spiegelnden Reflexionen und ermöglicht die Simulation von hochdetaillierten Objektmodellen. In Bezug auf den notwendigen Detailierungsgrad von Gebäudemodellen müssen zumindest grundlegende Fassadendetails geometrisch beschrieben sein. Dreifachreflexionen an Gebäudeecken werden als hervortretendes Bildmerkmal für Gebäude bestätigt. Zudem ist das Auftreten von Reflexionsgraden größer als 3 wahrscheinlich für freistehende Gebäude. Die Verwendung detaillierter Gebäudemodelle ermöglicht eine automatische Verknüpfung von simulierten Bildsignaturen und realen SAR-Daten. Daraus ergibt sich die Möglichkeit, den SAR-Abbildungsprozess umzukehren und die zugehörigen Streuer im 3D Modell der simulierten Szene zu identifizieren. Die Fallstudien zeigen, dass eine große Anzahl von SAR-Bildsignaturen die Geometrie von Objekten nicht direkt repräsentieren. Mehrfachreflexionen können im dreidimensionalen Raum beispielsweise neben Gebäuden, auf Bodenhöhe oder sogar unterhalb der Erdoberfläche lokalisiert werden.

# Contents

<b>1</b>	<b>Introduction</b>	<b>7</b>
1.1	Scientific relevance of the topic	7
1.2	Objectives and focus	8
1.3	Reader's guide	9
<b>2</b>	<b>Basics and state of the art</b>	<b>10</b>
2.1	Basics on Synthetic Aperture Radar	10
2.1.1	<i>SAR imaging and radar signal</i>	10
2.1.2	<i>VHR SAR for urban areas</i>	12
2.1.3	<i>Geometrical distortions in SAR images</i>	13
2.1.4	<i>SAR image signatures representing buildings</i>	15
2.1.5	<i>Methods for the localization of scatterers using SAR data</i>	19
2.2	Introduction to render techniques	24
2.2.1	<i>The render equation</i>	25
2.2.2	<i>Rendering algorithms</i>	26
2.2.3	<i>Relevance of render techniques for SAR simulation</i>	28
2.3	SAR simulation - state of the art	29
2.3.1	<i>Concepts for SAR simulation</i>	29
2.3.2	<i>VHR SAR simulation for urban areas</i>	31
2.3.3	<i>Discussion of most related work</i>	31
<b>3</b>	<b>Introduction to RaySAR</b>	<b>34</b>
3.1	3D SAR simulation approach - new aspects	34
3.2	Motivation for using POV-Ray	35
3.3	SAR simulation concept - modeling, sampling, 3D analysis	35
<b>4</b>	<b>Modeling - definition of 3D scenes</b>	<b>37</b>
4.1	Data sources for 3D building models	37
4.2	Design of the virtual SAR system	39
4.3	SAR simulation radiometry	39
4.3.1	<i>Reflection models for SAR simulation</i>	39
4.3.2	<i>Comparison to radar reflection models</i>	41
4.3.3	<i>Evaluation of POV Ray reflection models</i>	44
4.4	Modeling step - summary	45
<b>5</b>	<b>Sampling - extraction of data in SAR geometry</b>	<b>47</b>
5.1	Extraction of geometrical information	47
5.1.1	<i>Detection of reflection contributions</i>	47
5.1.2	<i>Focusing in azimuth</i>	49
5.1.3	<i>Focusing in elevation</i>	53
5.1.4	<i>Detection of specular reflections</i>	55
5.2	Evaluation of the simulation of multiple reflections	55
5.2.1	<i>Strength of multiple reflected signals</i>	56
5.2.2	<i>Proportion between multiple reflections and direct backscattering</i>	57
5.2.3	<i>Geometrical and radiometrical completeness</i>	58
5.3	Sampling step - summary	60
<b>6</b>	<b>Methods for SAR simulation in 3D</b>	<b>62</b>
6.1	3D models for simulation examples	62
6.2	Simulation in azimuth and range	62

6.3	Analysis in elevation	64
6.3.1	<i>Height profiles</i>	64
6.3.2	<i>Amplitude distribution in elevation</i>	66
6.3.3	<i>Scatterer histograms</i>	68
6.4	3D analysis of multiple reflections	70
6.4.1	<i>3D localization of signatures</i>	70
6.4.2	<i>Identification of reflecting surfaces</i>	72
6.5	Discussion	74
<b>7</b>	<b>Case studies</b>	<b>76</b>
7.1	Differences in the level of detail	76
7.1.1	<i>University of Stuttgart</i>	76
7.1.2	<i>Eiffel Tower, Paris</i>	79
7.2	Multi-body scenes: Wynn Hotel, Las Vegas	83
7.2.1	<i>Simulation of 2D maps</i>	83
7.2.2	<i>Scatterer histograms</i>	85
7.2.3	<i>Height profiles for visualizing elevation information</i>	86
7.3	Analysis of scatterers: main railway station, Berlin	88
7.3.1	<i>Characteristics of urban scene</i>	88
7.3.2	<i>Simulation of maps in azimuth and range</i>	92
7.3.3	<i>Correspondence of simulated signatures to persistent scatterers</i>	93
7.3.4	<i>Comparison of simulated height profiles to results from SAR tomography</i>	97
7.3.5	<i>Identification of scatterers</i>	100
7.3.6	<i>3D positions of simulated signal responses</i>	105
<b>8</b>	<b>Discussion and outlook</b>	<b>107</b>
<b>A</b>	<b>Radar reflection models</b>	<b>110</b>
<b>B</b>	<b>POV-Ray: Introduction and Modeling</b>	<b>112</b>
B.1	Introduction to POV-Ray	112
B.2	Modeling in the POV-Ray editor	112
<b>C</b>	<b>List of abbreviations</b>	<b>115</b>



# 1 Introduction

Remote Sensing from space enables to image regions of large scale on the earth surface. As the data are captured by a sensor mounted on a satellite, object information is provided without the requirement of measurements in the field. Exploiting datasets over time enables to detect object changes, e.g. using optical data or radar data. For instance, different approaches for monitoring changes within city areas have been developed which are based on the exploitation of synthetic aperture radar (SAR) data. In this context, salient SAR image signatures as source of information are commonly referred to as *scatterers*. So far, the nature of scatterers occurring due to multiple reflections of radar signals at urban objects is not known in detail. Understanding the correspondence of salient reflection effects to building features is mandatory in order to evaluate results of deformation analysis, object extraction or change detection in urban areas.

The topic of this thesis is *3D simulation and geometrical analysis of deterministic scattering effects occurring on very high resolution SAR images*. To this end, a new simulation approach is developed which is focused on radar signal reflection at man-made objects, especially buildings. In the following, the scientific relevance of the topic is introduced.

## 1.1 Scientific relevance of the topic

SAR sensors, operated on airplanes or on satellites, enable imaging and monitoring of the earth surface. Compared to sensors covering the spectrum of visible light, SAR sensors offer two major advantages. First, imaging is almost independent from weather conditions and can be conducted at day and night due to the active emission of radar signals. Second, besides radiometric information, distance information is provided directly due to measurement of the runtime of signals. Hence, the change of scene radiometry and the deformation of objects can be analyzed over time, that is of major interest in urban areas.

While airborne SAR data are captured by flight campaigns, SAR satellites follow orbits in space and provide almost global coverage. After the initial launch of the sensor, areas of interest can be imaged periodically at low cost according to the revisit time of the satellite. Very high resolution (VHR) SAR sensors such as TerraSAR-X/TanDEM-X (Krieger et al., 2007; Eineder et al., 2009; Pitz and Miller, 2010; Werninghaus and Buckreuss, 2010; Breit et al., 2010) or COSMO-SkyMed (Lombardo, 2004) provide data having a spatial resolution of up to 1 m. Geometrical information about the shape of man-made objects in the SAR imaging plane can be extracted. For instance, buildings are represented by linear features or salient point scatterers in the imaging plane. Focusing on dominant scatterers representing single buildings enables to monitor deformations with respect to the surrounding ground or even relative movements between different building parts (Gernhardt et al., 2010). In the context of building monitoring, radar signals interacting with facades and the surrounding ground as well as signals multiple reflected at windows, balconies or roof structures are of special interest.

However, geometrical distortions in SAR data hamper the interpretation of VHR SAR images and have to be dealt with when extracting object features in urban areas (Soergel et al., 2006). Simulation methods support the understanding of reflection phenomena occurring at man-made objects. Different simulation approaches have been developed, aiming at a realistic representation of real SAR data. A copy of SAR data is considered as the theoretically best result. Random scattering effects are commonly accounted for or added artificially after the simulation of deterministic data components. At present, SAR simulators aim at supporting the visual interpretation of SAR data or at testing SAR systems or algorithms developed for processing real SAR data.

The analysis of deterministic scatterers on a geometrical basis or the separation of scatterers in 2D or 3D has not been realized so far. Hence, the nature of dominant SAR image signatures, which form the basis for the generation of SAR products, is still not known in detail. The SAR simulation approach introduced in this thesis concentrates on this open field of research. Deterministic reflection effects are simulated in three dimensions and methods for supporting the interpretation and analysis of simulation results are provided. The main goal is to geometrically link SAR image signatures to the geometry of the corresponding urban objects. In this context, multiple reflected radar signals are expected to cause strong signal responses and, hence, are of major importance.

## 1.2 Objectives and focus

The development and applications of SAR simulation methods presented in this work are focused on *man-made objects* imaged by *VHR spaceborne SAR sensors*. Urban areas or inhabited areas are of special interest since most methods for exploiting SAR data aim at the detection of changes affecting human life. Moreover, the number of deterministic SAR image signatures is expected to be bigger for man-made objects than for areas dominated by vegetation or open fields. The reason is that buildings, bridges, etc. are composed by regular structures such as flat surfaces, curved surfaces or corners formed by two or three intersecting planes. Thus, the probability of the occurrence of direct backscattering or of multiple reflections at the earth surface is assumed to be linked to the regularity of imaged objects. Feature extraction tools designed for dominant SAR image features are able to separate geometrical or radiometrical information about objects from noise. Moreover, the distance information shows higher stability for salient scatterers, offering the possibility to detect deformation in the range of millimeters per year from space. The development of a SAR simulator for analyzing VHR SAR data is mandatory to understand reflection effects occurring at single objects, now visible in the new generation of SAR data. Basically, there are two major objectives and one minor objective to be fulfilled by the simulation approach:

**Objective 1:** 3D SAR simulation using object models of high detail

The SAR simulation concept has to be focused on deterministic reflection effects, especially multiple reflections. SAR data have to be simulated in three dimensions (azimuth, range, and elevation) using 3D object models characterized by a high level of detail. SAR processing effects affecting the geometrical position of multiple reflections have to be accounted for. Signal contributions have to be detected within the simulated scene. Information about the type of scattering process has to be provided. Eventually, different kinds of reflection effects have to be separated to enable a directed analysis of scatterers of interest.

**Objective 2:** Enhancement of knowledge about the nature of scatterers

Besides support for the visual interpretation of SAR data, additional tools for a detailed geometrical and quantitative analysis have to be developed in order to enhance knowledge about the nature of scatterers. First, simulation methods have to be developed for compensating geometrical effects occurring due to the SAR imaging principle. Second, the correspondence of image signatures to building features has to be analyzed. To this end, the 3D position of scatterers has to be found within simulated scenes. Finally, the inversion of the SAR imaging process has to be realized. For that purpose, reflecting surfaces contributing to salient image pixels have to be identified at simulated object models.

**Minor objective 3:** Use of existing software packages

Existing software components shall be used for SAR simulation since they are expected to offer reliable, optimized and fast source code libraries as well as progressive simulation algorithms.

Furthermore, prominent software packages are anticipated to be maintained for future computer platforms. Thus, given simulation tools will be adapted to the problem of SAR simulation. In addition, essential own developments need to be added in order to provide necessary information in SAR geometry. Integration of existing methods is expected to save time which can be used for realizing the geometrical analysis of scatterers after the simulation of SAR data.

While pursuing the objectives, several preconditions and requirements have to be met:

- ◇ The geometrical correctness of simulation results is more important than the radiometrical correctness.
- ◇ Simplified SAR reflection models are anticipated to be sufficient for approximating and analyzing dominant SAR image features. Due to this compromise, integration and simulation of 3D object models of high detail is expected to be feasible.
- ◇ Specular and diffuse reflection of radar signals have to be modeled simultaneously.
- ◇ Random scattering effects are not of major interest and are considered as negligible.
- ◇ Generally, the basic aim is not to provide copies of SAR data but to describe the spatial distribution of salient image signatures for a given SAR imaging geometry. Deterministic scattering effects of interest may be emphasized when reasonable.

## 1.3 Reader's guide

The thesis is structured as follows. Basics on SAR, methods for SAR simulation and rendering techniques are given in chapter 2. Thereafter, new aspects of the thesis with regard to related work and the concept for SAR simulation are introduced in chapter 3. Requirements for the modeling of scenes are discussed in chapter 4. In this regard, the main focus is on the definition of object geometries and on reflection properties of surfaces. In chapter 5, the extraction of geometrical information in the SAR imaging geometry is explained. Besides, limitations of the simulator with respect to the detection of signal reflections are discussed. New methods for SAR simulation in three dimensions are introduced in chapter 6. To this end, simulation results are presented and discussed for two basic shapes. In chapter 7, simulation results are shown for different 3D building models and are compared to VHR SAR data. For single buildings and multi-body scenes, the influence of the level of detail of object models on simulation products is evaluated. Moreover, simulated data are linked to real data in order to analyze the nature of SAR image signatures. Finally, the results of the thesis and an outlook to future work are given in chapter 8.

## 2 Basics and state of the art

This chapter covers the relevant theory for the introduction and discussion of the SAR simulation approach proposed in this thesis. Basically, two different fields of research are connected: *render techniques* which are applied for supporting the interpretation of data captured by *SAR sensors*. Fundamental theory corresponding to these fields are introduced in chapters 2.1 and 2.2, respectively. Afterward, a literature survey on SAR simulation approaches is given followed by a discussion of related work.

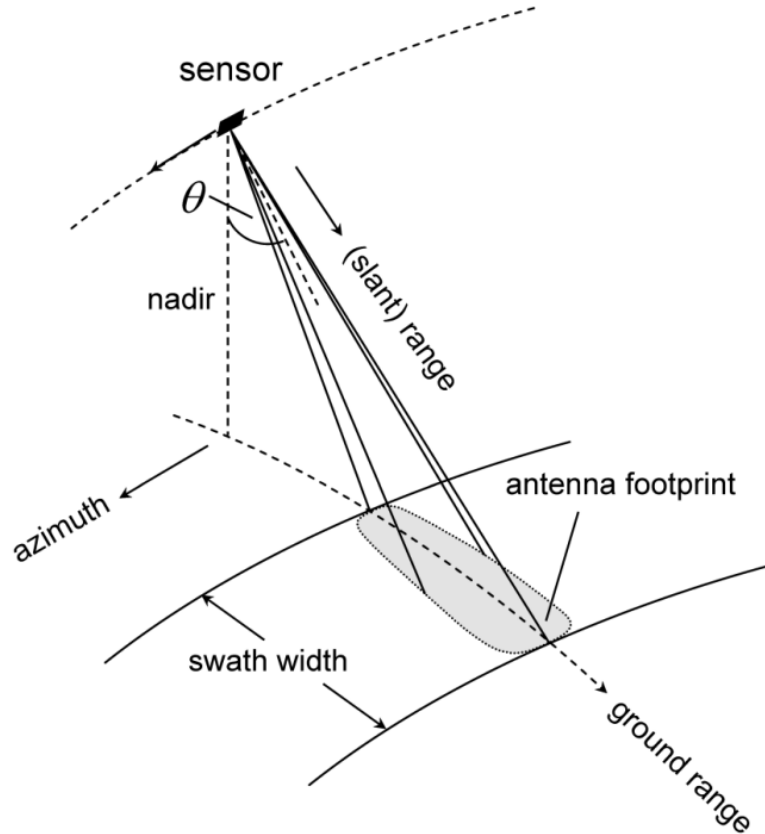


Fig. 1. Imaging geometry of a SAR sensor following its orbit in azimuth direction. The direction of the signal emission (range direction) is defined by look angle  $\theta$  with respect to the nadir pointing orthogonally to the earth surface. Objects are imaged within the antenna footprint.

### 2.1 Basics on Synthetic Aperture Radar

#### 2.1.1 SAR imaging and radar signal

The expression *synthetic aperture radar (SAR)* characterizes radar systems forming an artificially extended antenna in flight-direction, which are operated airborne or spaceborne. Capturing SAR data is independent from day time due to the active emission of signals. Moreover, imaging the earth surface by means of radar signals is almost independent of weather conditions, what is a major advantage compared to sensors in the optical or infrared spectrum. In the following, only a brief introduction is given to synthetic aperture radar. Detailed information about the functionality of SAR systems can be found in Skolnik (1990), Henderson and Lewis (1998), and Cumming and Wong (2005).

In figure 1, the imaging geometry is shown for a SAR sensor following its orbit. The SAR

Launch date	June 15th, 2007
Antenna size	4.8 m x 0.8 m
Altitude	514km
Inclination	97.44°, sun-synchronous
Velocity	7.6km per second
Revisit time	11 days
Range of incidence angle	22° - 55°
Scene size	5km in azimuth, 10km in range
Pulse repetition frequency	3000Hz - 6000Hz
Radar center frequency	9.65GHz
Signal wavelength	3.1 cm (X-Band)
Spatial resolution	1.1 m in azimuth, 0.6 m in range
Polarization	HH, VV, HV, VH; experimental: full polarization

Table 1. Parameters of the TerraSAR-X satellite.

sensor's line-of-sight coordinate is called *slant range* or *range*. It is commonly located in a plane orthogonal to the flight direction but may also be squinted, i.e. not orthogonal to the line-of-flight. The *look angle*  $\theta$  of the SAR sensor with respect to the *nadir* defines the direction of the line-of sight. In standard SAR imaging mode, called *stripmap mode*, both the look angle and the squint angle of the SAR sensor's line of sight are kept more or less stable. Hence, continuous imaging along the synthetic aperture is enabled what is reasonable for imaging areas of large scale. The local *angle of incidence*  $\theta_i$  at the earth surface corresponds to the angle between the SAR sensor's line-of-sight to the surface and the normal to the tangent plane at that surface. Electromagnetic signals are emitted in pulsed form expanding in a beam in slant range direction which covers the antenna footprint at the earth surface. Signal responses backscattered from objects within the antenna footprint are detected at the sensor. In Table 1, the basic system parameters of the TerraSAR-X satellite are summarized (Eineder et al., 2009; Pitz and Miller, 2010; Werninghaus and Buckreuss, 2010; Breit et al., 2010).

The position of a SAR image signature is defined by

- ◇ the *azimuth* coordinate  $x$  along the orbit
- ◇ the slant range coordinate  $r$  captured along the line-of-sight of the SAR sensor

Besides amplitude information giving information about the strength of the backscattered signal, distance information is provided based on measurement of the runtime of the electromagnetic signal. The radar signal can be characterized by

$$u(\tau) = A \cdot \exp(j(2\pi f_0 \tau + \Phi)) \quad (1)$$

where  $\tau$  is the fast time variable,  $A$  is the signal amplitude,  $j$  is the imaginary unit, and  $f_0$  is the radar center frequency. The phase  $\Phi$  for a point scatterer is defined as

$$\Phi = -\frac{4\pi}{\lambda}R - n \cdot 2\pi \quad (2)$$

where  $R$  is the spatial distance between the SAR sensor and the imaged object,  $\lambda$  is the signal

wavelength, and  $n$  is an integer keeping  $\Phi$  within the interval between 0 and  $2\pi$ . For the sake of simplicity, the phase delay caused by the atmosphere as well as phase contributions occurring due to the scattering of signals on the earth surface are neglected. The signal intensity  $I$  is derived by squaring the amplitude  $A$ , i.e.  $I = A^2$ . Being related to the frequency of the carrier signal, the signal wavelength is

$$\lambda = \frac{c}{f_0} \quad (3)$$

where  $c$  is the velocity of light. SAR wave signals are emitted either in horizontal or in vertical polarization and are detected in horizontal and/or vertical polarization (see e.g. Tsang and Kong (2001) for further information about the polarization of radar signals). For example, TerraSAR-X covers the combinations HH, i.e. emission and detection of horizontal polarized radar signals, VV, HV and VH in standard mode (see Table 1).

The measurement of the signal runtime in slant range direction is enabled by emitting a chirp, whose signal power is temporally distributed. During post-processing of the SAR raw data (Bamler, 1992; Franceschetti and Lanari, 1999), the signal power is regained by correlating the received signal with a reference chirp in range. For instance, the processed signal response of a corner reflector is a *sinc*-function. In theory, the width of the *sinc*-function's main lobe determines the resolution in range and is

$$\delta_r = \frac{c}{2f_r} \quad (4)$$

where  $f_r$  is the bandwidth of the chirp emitted by the radar antenna.

In azimuth direction, objects at the earth surface are imaged coherently by a synthetic antenna. To this end, the motion of the platform is utilized for collecting SAR raw data of a target over a short time period. The signal power in azimuth is regained by correlation of the SAR raw data with a reference chirp in azimuth. Comparable to the range domain, the signal response of a corner reflector yields a sinc function whose mainlobe width defines the spatial resolution of the SAR system in azimuth:

$$\delta_x = \frac{L}{2} \quad (5)$$

where  $L$  is the physical length of the radar antenna.

SAR systems operated in *spotlight mode* reach a spatial resolution in azimuth which is higher than the theoretical limit given by equation 5. The length of the synthetic aperture is increased by squinting the radar beam in direction to the area to be imaged. Thereby, the target bandwidth in azimuth becomes larger than in standard stripmap mode. In case of TerraSAR-X, the spatial resolution in azimuth is improved from 3.3 m in stripmap mode to 1.1 m in high resolution spotlight mode (see Table 1). As major drawback of spotlight mode, continuous imaging of the earth surface is not possible. Hence, the area of interest has to be defined a-priori.

### 2.1.2 VHR SAR for urban areas

When imaged by SAR sensors of lower resolution, e.g. ERS-1/2 (Attema et al., 1998) or Envisat (Louet and Bruzzi, 1999), man-made objects are included in a low number of resolution cells. Hence, monitoring of objects of interest such as residential buildings, industrial buildings, bridges, etc. is limited or even impossible. For instance, in Perski et al. (2007) the collapse of large buildings is analyzed based on distance information corresponding to salient point signatures. To this end, data stacks of the ERS-1/2 and Envisat satellite missions are processed using

Persistent Scatterer Interferometry (see chapter 2.1.5). However, the detection of deformation signals at buildings is limited by the low number of point signatures representing the objects of interest.

VHR SAR sensors such as TerraSAR-X (Pitz and Miller, 2010) or COSMO-SkyMed (Lombardo, 2004) provide SAR data having a spatial resolution of up to 1 m. In that kind of data, radar signals representing single objects are distributed over a high number of resolution cells. Hence, SAR image signatures corresponding to man-made objects become visible. For instance, in Bamler and Eineder (2008) salient SAR image features representing the Cheops pyramid in VHR spotlight TerraSAR-X data are introduced and interpreted. Figure 2 contains two SAR images of an urban area in Las Vegas, USA, comprising urban settlements, vegetated areas and the Las Vegas Convention Center. The images have been provided by the ERS satellite and TerraSAR-X in VHR spotlight mode. Captured in C-Band, the spatial resolution of the ERS data is 5 m x 25 m in azimuth and range, respectively. The signal to clutter ratio is much higher in the TerraSAR-X image ending up at a higher contrast in the high resolution data. Moreover, the number of signatures representing buildings in the TerraSAR-X data is much higher due to the increased resolution in azimuth and range. While distinguishing single objects in the ERS data is almost impossible, buildings and urban structures are clearly visible on the TerraSAR-X image. Hence, data from spaceborne VHR SAR sensors become interesting for building extraction or change detection methods using SAR amplitude data. In (Adam et al., 2008), the increase of the number of salient signatures in TerraSAR-X data of urban areas is reported, also showing that the increase of the signal to clutter ratio provides better phase stability for dominant scatterers. Thus, monitoring of deformations of single objects based on phase information is enabled (Gernhardt et al., 2010; Zhu and Bamler, 2009).

Nonetheless, distinguishing between random scattering effects and deterministic scattering effects is challenging. The nature of SAR image signatures occurring due to multiple reflections of radar signals at man-made objects is not understood to all ends. In figure 3, an optical image and a TerraSAR-X temporal average image of the Maison de la Radio in Paris, France, is shown. The temporal average image has been created by incoherent averaging 6 TerraSAR-X VHR spotlight images. Visual orientation within the optical image, captured from a bird's eye view, is less complicated due to the distinguishable building shape. In contrast, visual interpretation of building properties on the SAR image is not straightforward. Objects are mapped into the SAR data depending on the spatial distance with respect to the SAR sensor. Dominant image signatures occur due to multiple reflections at intersecting walls or building corners illuminated by the SAR sensor. Geometrical distortions affecting the imaging of objects in SAR data are introduced in the following subsection.

### 2.1.3 Geometrical distortions in SAR images

Figure 4 shows the imaging geometry of a SAR sensor in a plane defined orthogonally to the azimuth direction. The axis perpendicular to azimuth and range is referred to as *cross-range direction* or *elevation*. The SAR sensor emits a signal with look angle  $\theta$  whose pulse width determines the resolution in range  $\delta_r$ . As can be seen in the figure, several objects such as ground surfaces or building features may have the same spatial distance with respect to the SAR sensor. For instance, signals may be backscattered

- ◇ diffuse from distributed scatterers, e.g. trees or bushes,
- ◇ diffuse from building or ground surfaces whose surface roughness is not negligible with respect to the signal wavelength,
- ◇ specular at building corners due to double of multiple reflections, or
- ◇ specular at building surfaces hit perpendicularly by the radar signal.

As the SAR system does not provide angular information in the range-elevation plane, all signal contributions shown in figure 4 are integrated into the same resolution cell, i.e. the separation



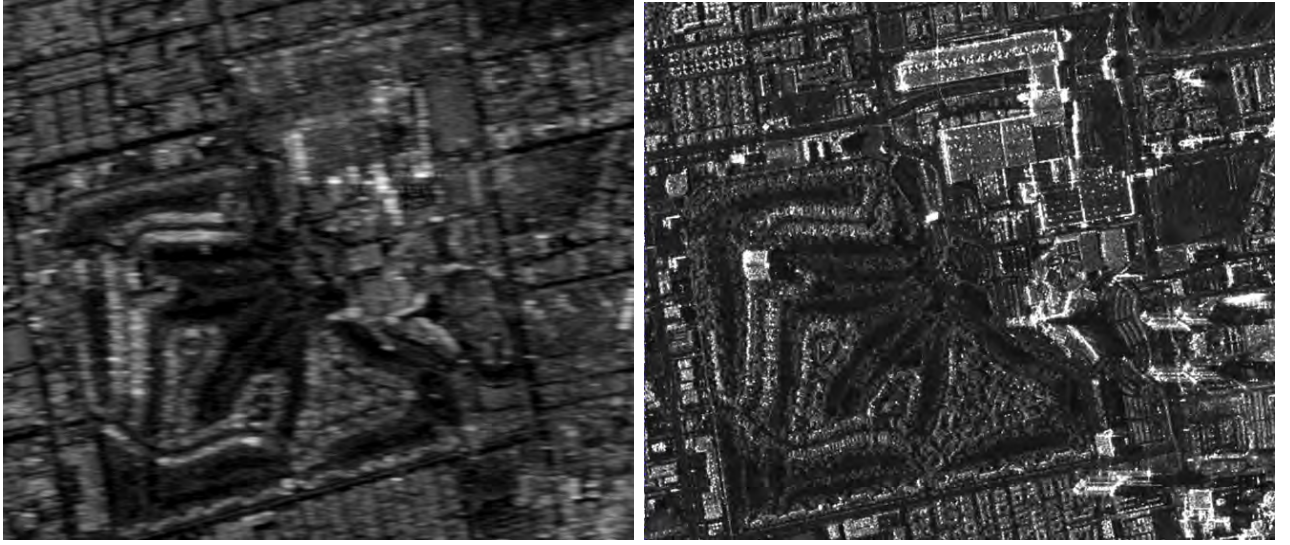


Fig. 2. Different resolution levels of SAR data for an urban area in Las Vegas, USA. Left: SAR image provided by ERS satellite operated by the European Space Agency (ESA). Spatial resolution: 5 m x 25 m in azimuth and range. Right: VHR spotlight image provided by TerraSAR-X. Spatial resolution: 1.1 m x 0.6 m in azimuth and range. The visibility of signatures representing single objects is much improved.

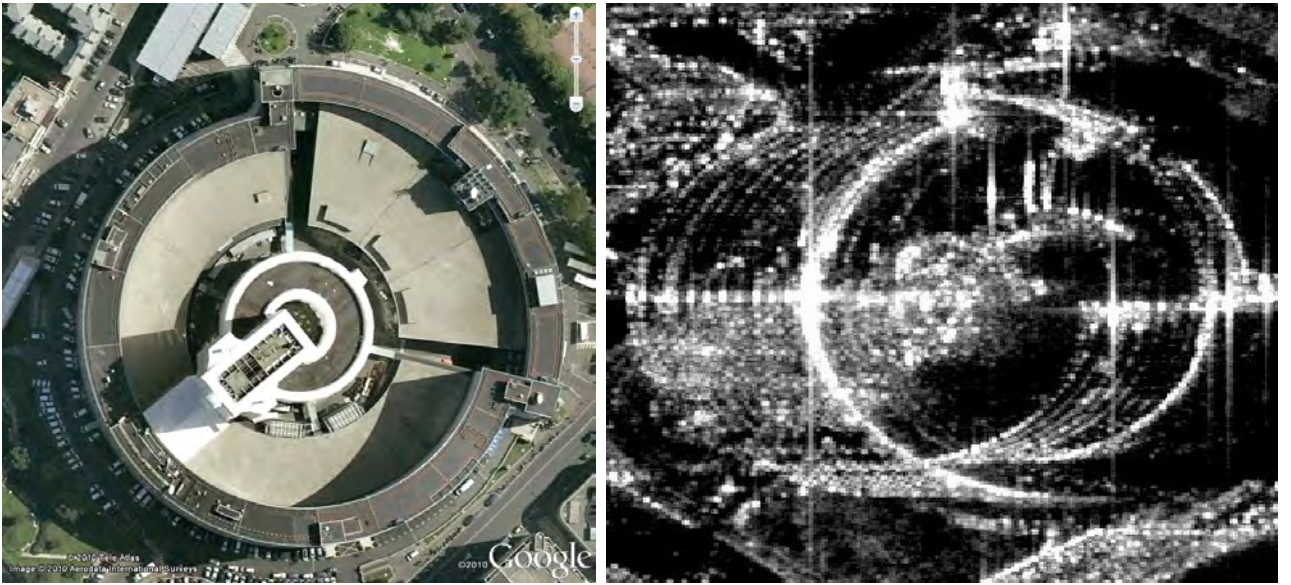


Fig. 3. Comparison of optical image and VHR SAR image for the Maison de la Radio France, Paris. Left: Optical image from bird's eye view (screenshot from Google Earth<sup>TM</sup> viewer; ©Aerodata International Surveys, 2010). Right: SAR temporal average image created by averaging 6 VHR spotlight TerraSAR-X images.

of scatterers in elevation is impossible using one SAR dataset.

Geometrical effects, occurring due to the SAR imaging geometry, complicate the interpretation of SAR data, especially in urban areas. Figure 5 shows three major effects characterizing urban buildings. The direction of the emitted signal is indicated by arrows pointing in range. On the left image, distance  $B - C$  at the building roof is mapped into a much smaller range interval  $B' - C'$ , what is called *foreshortening*. This effect occurs as long as the slope of the roof is smaller than the local angle of incidence. Signal responses from the building wall defined by corners  $A$  and  $B$  are mapped into the range interval  $B' - A'$ . This effect is called *layover* and is difficult to be visually interpreted on SAR images. Layover at the roof would occur if the slope of the roof was equal or bigger than the local angle of incidence of the incoming radar signal. Then, roof corner  $C$  would be hit first by the emitted radar signal and the range coordinate



of  $C'$  would be lower than that of  $B'$ . On the right of figure 5, an example is given for the distribution of SAR image signatures in case of a gable roof building. First, the signal response from the ground in front of the building, the building front wall and the roof is imposed within a layover area indicated by a box in bright gray pointing in range (range interval between dashed lines #1 and #2). Double reflections of signals, commonly referred to as *double bounce*, occur at the rectangular corner formed by the building front wall and the ground in front of the building (intersected by dashed line #2). The path of the double reflected radar signal is equal to the spatial distance between the SAR sensor and the corner tip marked by a bright circle situated on line #2. Due to the summary of double bounce responses within one resolution cell, a highlight occurs in range indicated by a bright box. Parts of the area behind the building are invisible to the SAR sensor and cause *shadow*. The shadow zone ends at the dashed line #3 when first reflections backscattered from the ground in the back of the building are detected.

Changing the local angle of incidence of the radar signal or the aspect angle with respect to the building may completely change the geometrical appearance and radiometry of buildings in SAR data. Especially, ambiguities with regard to building parameters or misinterpretation may occur in the layover area where the distribution of scatterers in elevation is not provided. Case studies simulating basic shapes confirm the interpretation problem, e.g. using a box model (see figure 6a). Both the angle of incidence of the radar signal, which is  $45^\circ$ , and the aspect angle with respect to the box model are indicated by an arrow. The simulated reflectivity map, located in the azimuth-range plane, is displayed in figure 6b. Interpreting the map top-down in range, a zone of layover is followed by a bright double bounce line and a shadow zone of limited extent. Figure 6d shows simulation results for the same imaging geometry in case of a step model (see figure 6c) including two corners oriented in direction to the sensor. The only significant difference between the two reflectivity maps is found in the extent of the shadow area. Since shadow zones of urban buildings are frequently imposed by the signal response from adjacent buildings, the extraction of object geometry is difficult. A closer look reveals differences in the intensity of double bounce. However, building extraction based on radiometrical information is challenging as well, as the backscattered power simultaneously depends on the dimension of objects and on object materials.

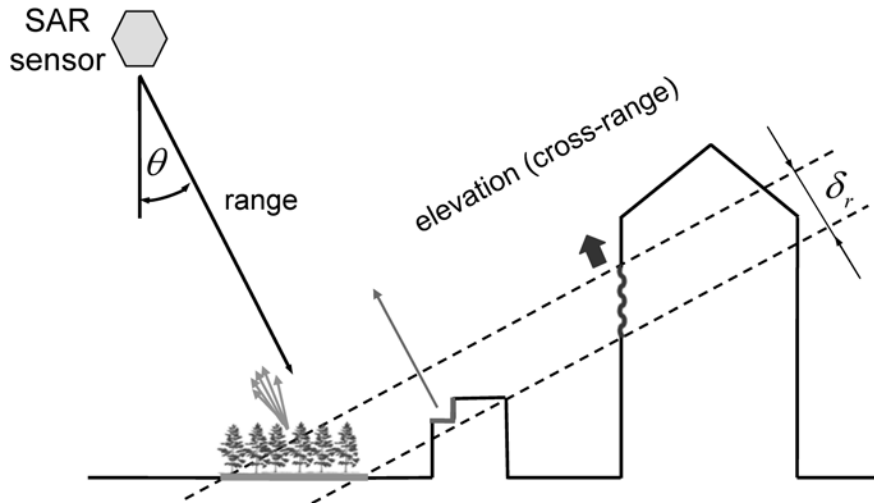


Fig. 4. Imaging geometry within the range-elevation plane. The arc of equal range is locally approximated by a straight line. Signals backscattered from objects distributed in elevation are integrated into the same resolution cell.

#### 2.1.4 SAR image signatures representing buildings

The work presented in this thesis is focused on man-made structures such as buildings, bridges, etc. imaged by a VHR SAR sensor operating in X-Band (wavelength: 3.1 cm). Metallic surfaces

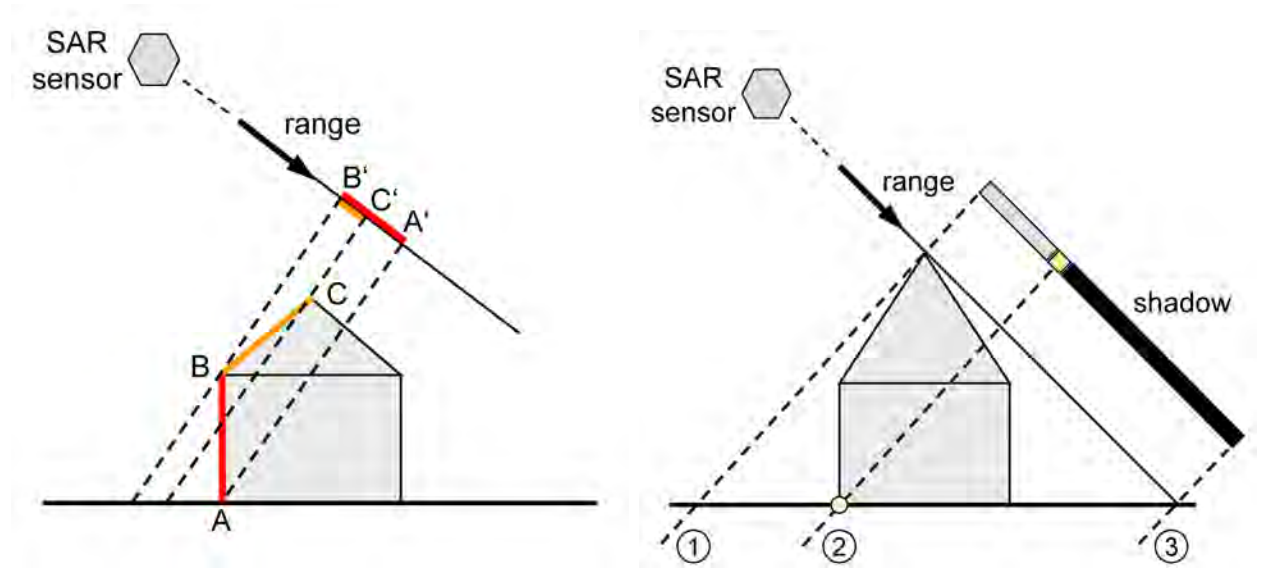


Fig. 5. Geometrical effects in SAR data. Left: Foreshortening and Layover. Right: Distribution of the signal response in range direction for a gable roof building. Shadow occurs for areas invisible to the SAR sensor.

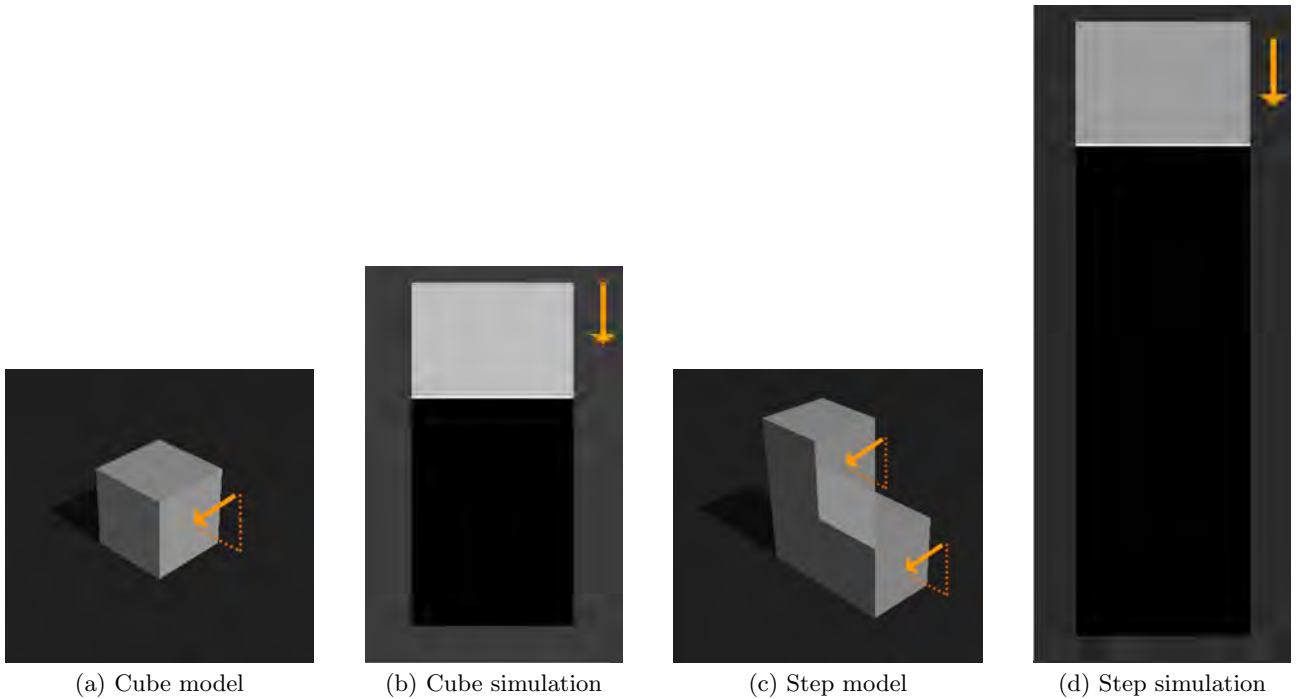


Fig. 6. Simulated reflectivity maps for a box model and a step model. Arrows indicate the imaging geometry with respect to the models. The angle of incidence of the radar signal is  $45^\circ$ . Range: top-down.

or surfaces made of concrete are expected to reflect radar signal in X-Band while surfaces made of glass are penetrated. In contrast, materials in the interior of building walls would have to be accounted for when simulating in L-Band since building walls may be partly penetrated.

When interpreting signatures representing buildings, distinguishing between deterministic reflection effects and random reflection effects is of major importance. Figure 7 shows an aerial image and a SAR temporal average image of the Alexanderplatz located in the center of Berlin, Germany. Overall, the area is dominated by large buildings surrounded by broad roads and little vegetation. Only few residential buildings are visible in the lower right part of the image.

Selected buildings are marked by capital letters A – D in both the optical image and the SAR temporal average image, which has been created by averaging 21 VHR spotlight TerraSAR-X images (see right part of figure 7). Since random signals are suppressed by the averaging process, deterministic signatures are visually more prominent in the SAR image. In the following, SAR image signatures representing buildings are introduced. Moreover, examples are given with regard to the application of those signatures for the extraction of building information from airborne or spaceborne SAR data.



Fig. 7. Optical image and TerraSAR-X temporal average image of the Alexanderplatz in Berlin, Germany. Left: Bird's eye view (screenshot from Google Earth™ viewer; ©AeroWest, 2010). Large buildings marked by letters A – D. Right: SAR temporal average image derived by averaging 21 spotlight VHR TerraSAR-X images captured in VV-polarization. Angle of incidence:  $47^\circ$ . Letters E, F, G, and H mark examples for shadow, foreshortening at gable roofs, double bounce at building walls, and point patterns corresponding to building facades, respectively. Azimuth: bottom-up; Range: from left to right.

### Direct backscattering and shadow

Direct backscattering of radar signals from objects is commonly referred to as *single bounce*. The intensity of salient SAR image signatures corresponding to single bounce depends on the imaging geometry with respect to imaged objects. For instance, the gable roof of a building may be represented by a bright line. However, this effect may only occur if the roof is hit orthogonally by the emitted signal. In case of specular reflections, the direction of the reflected signal is reverse to the direction of the incoming signal and, due to foreshortening, the signal response is integrated into the same range resolution cell. In the lower right part of the SAR image shown in figure 7, linear features corresponding to gable roofs are distinguishable at residential buildings (marked by letter *F*).

In combination with double bounce lines located at the bottom of building facades (see chapter 2.1.3), linear features enable to estimate the height of buildings. In (Simonetto et al., 2005), the height of buildings is determined by analyzing the extent of the building layover, which is limited by a double reflection line and a foreshortening line. First results for object height extraction from TerraSAR-X data are shown in Guida et al. (2010). To this end, height estimates are derived from analyzing the extent of the layover area of cylindrical tanks.

When distinguishable, single bounce contributions represent the extent and shape of objects in the azimuth-range plane. Knowledge about the geometrical shape of urban objects may support the monitoring of single objects, e.g. by means of Persistent Scatterer Interferometry (Gernhardt and Hinz, 2008). For instance, diffuse single bounce may occur at old buildings or facades characterized by washed-out concrete. However, the majority of diffuse signal com-

ponents backscattered from buildings may be hardly visible in SAR data since most building walls show little roughness compared to the signal wavelength. Moreover, diffuse signals from building walls may be overlayed by diffuse backscatter from the ground in front of the building.

The exploitation of shadow provides information about the height of buildings. In figure 7, letter *E* in the SAR image marks an example for shadow at buildings. For instance, the height of building walls invisible to the SAR sensor can be estimated by analyzing the length of building shadows (Bolter and Leberl, 2000). Hill et al. (2006) vary parameters of a 2.5D building model and map it into the azimuth-range plane for comparison with airborne SAR data. Afterwards, the building parameters are optimized by cross-checking the extent of the building shadow by an active-contour library.

## Double reflections

Linear double bounce signatures occur, for instance, in case of signal interaction with facades and the surrounding ground. Ideal corners provoking double bounce are commonly referred to as *dihedrals* and consist of two surfaces oriented orthogonally to each other. A double bounce line shows strong intensity if the dihedral faces the line-of-sight of the SAR sensor. Hence, buildings facades oriented in line-of-flight of the SAR sensor are likely to cause dominant signatures. In the SAR temporal average image shown in figure 7, a double bounce line is marked by letter *G*. In Brunner et al. (2009), the power of double bounce response from building walls is analyzed depending on the aspect angle. Complementary, the geometry of linear signatures corresponding to signals interacting with building walls and the surrounding ground is extracted and discussed in Wegner et al. (2010).

As reported in the literature, double bounce lines occurring in SAR data of urban areas are used for extracting the outline of buildings. In Quartulli and Datcu (2004), the shape of buildings is extracted in the azimuth-range plane from single airborne SAR data, what is performed based on Monte Carlo simulation. Besides other image features, double reflection lines are analyzed for finding the best fit for building parameters. By fusing salient double bounce lines extracted from SAR data captured from orthogonal aspect angles, the detection rate of buildings and the correctness of the extraction of rectangular building outlines can be increased (Thiele et al., 2007b; Xu and Jin, 2007).

Besides geometrical information about the shape of buildings, dominant double bounce lines enable the detection of building heights based on SAR image radiometry. Franceschetti et al. (2007) present a functional model for estimating the height of buildings, characterized by flat roofs, from airborne SAR data based on the intensity of double bounce lines. In order to focus on the influence of object geometry, knowledge about surface materials is necessary. Guida et al. (2010) show first results of object height extraction based on the radiometry of TerraSAR-X data captured in stripmap or spotlight mode.

## Triple reflections

The majority of modern buildings within urban areas show regular shapes including corners. Ideal corner reflectors, commonly referred to as *trihedrals*, are composed by three orthogonal planes. In case of an ideal corner roughly oriented in line-of-sight of the SAR sensor, a salient *point signature* is likely to appear on the SAR image, whose intensity is characterized by a  $2D - \text{sinc}$ -function. In Groot and Otten (1993), it is shown that the signal peak of a corner reflector is always located within one resolution cell even if the size of a corner reflector is larger than the resolution of the SAR system. The effective surface contributing to the radar signal response of a corner reflector, oriented in line-of-sight of the SAR sensor, forms a pentagonal shape (Sarabandi and Chiu, 1996). In figure 7, facades in the SAR temporal average image are dominated by point signatures organized in patterns. As an example, letter *H* marks a point pattern which is likely to be linked to trihedral reflections of radar signals.



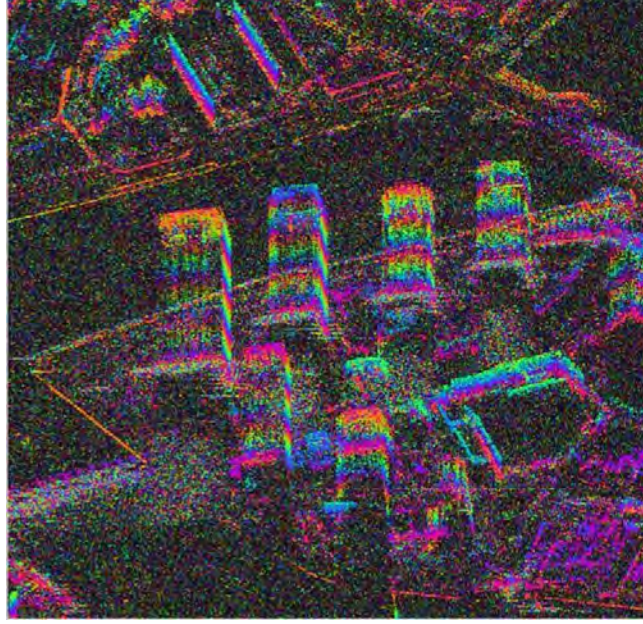


Fig. 8. Interferogram of an urban scene in Tokyo, Japan. Fringes are distinguishable at facades of skyscrapers due to high phase stability. Counting the number of fringes – each corresponding to approx. 44 m of height difference – enables to estimate building heights (Eineder et al., 2008).

Michaelsen et al. (2002) apply a spot detector for finding point signatures in airborne SAR data of urban scenes and use patterns of point signatures as building hints. Focusing on long-time coherent scatterers detected in a stack of SAR data, surface deformation can be monitored from space (Ferretti et al., 2001). Using a stack of VHR resolution SAR data enables the deformation analysis for single urban objects (Gernhardt et al., 2010).

### 2.1.5 Methods for the localization of scatterers using SAR data

In single SAR datasets, the geometrical distribution of scatterers in cross-range direction is not provided. Signal responses from scatterers having the same spatial distance with respect to the sensor are integrated into the same resolution cell even if the scatterers are spatially distributed in elevation. At least two SAR datasets or a stack of SAR data are needed in order to provide angular information in the range-elevation plane. In this context, different approaches for 3D localization of scatterers are reported in the literature and are recapitulated in the following.

#### Synthetic aperture radar interferometry (InSAR)

If only the signal response of one dominant scatterer is integrated into a resolution cell, the scatterer can be localized using two SAR data sets of the same scene captured from a different point of view in across-track, i.e. orthogonally to the line-of-flight. To this end, interferometric information, i.e. phase differences between the corresponding SAR image pixels, is exploited by synthetic aperture radar interferometry (InSAR) (Bamler and Hartl, 1998; Hanssen, 2001) in order to provide digital elevation models (DEMs). The *interferogram* of two SAR images is obtained by

$$v(r, x) = u_1(r, x) \cdot u_2^*(r, x) = |u_1(r, x)| |u_2(r, x)| \exp \{j\Phi(r, x)\} \quad (6)$$

where  $u_1(r, x)$  and  $u_2(r, x)$  are radar signals corresponding to related pixels of two SAR images

imaging the same area of interest. The interferometric phase is defined by

$$\Phi(r, x) = \frac{4\pi}{\lambda} \Delta R \quad (7)$$

and is ambiguous with respect to integer multiples of  $2\pi$ . The sensibility of the phase depends on the signal wavelength  $\lambda$  as well as on the range difference  $\Delta R = R_2 - R_1$  where  $R_1$  and  $R_2$  are the spatial distances between the two sensor positions and the target, respectively.

In figure 8, the interferometric phase is shown for an urban scene in Tokyo, Japan. The SAR data have been captured by TerraSAR-X in spotlight mode. Detailed information can be found in Eineder et al. (2008) and Eineder et al. (2009). The interferometric phase has been obtained from two subsequent passes of the SAR sensor and is represented by a color wheel continuously changing between red, green and blue. Turning the color wheel from red to red corresponds to a phase difference of  $2\pi$  which is referred to as a *fringe*. For the example at hand, fringes are clearly distinguishable at the facades of skyscrapers in the interferogram due to high phase stability.

The height of the building can be estimated by unwrapping the interferometric phase in order to get the absolute phase with respect to a reference point selected within the urban scene. For instance, Bolter and Leberl (2000) extract 2.5D building models from multi-aspect airborne InSAR data. The height of building facades visible to the SAR sensor is estimated based on interferometric information. Gamba et al. (2000) fit horizontal planes to 3D surface information provided by airborne InSAR data in order to estimate the height of buildings. To this end, scan lines are defined in range direction and are used as seeds in an iterative region growing process for the detection of flat regions.

## SAR tomography

In Reigber and Moreira (2000), the first concept for 3D imaging of volume scatterers using SAR tomography (TomoSAR) is presented. The basic principle is shown in figure 9. SAR data sets, spatially and temporally distributed, are captured during different passes of the SAR sensor. Marked by red spots, the corresponding orbit positions of the SAR sensor form a synthetic aperture in elevation direction  $s$ . The spatial baseline between the orbit positions is required for providing angular information in the range-elevation plane. Thereby, the elevation coordinates of two scatterers, marked by yellow points, can be estimated with respect to a *master* (enlarged red spot), i.e. a reference orbit defining elevation 0 m. Thus, the layover problem presented in figure 4 can be resolved for each SAR image pixel.

For one image pixel, each SAR acquisition provides a spectrum sample of the reflectivity function in elevation. The functional model for 3D SAR tomography is defined as

$$g_n = \int_{\Delta s} \gamma(s) \exp(-j2\pi\xi_n s) ds, \quad n = 1, \dots, N \quad (8)$$

where  $g_n$  is the signal measured for an image pixel during pass  $n$ ,  $\Delta s$  is the extent of the imaged object in elevation,  $\gamma(s)$  is the reflectivity function representing the distribution of backscattered intensities in elevation  $s$ , and  $\xi_n$  is the spatial frequency in elevation depending on the sensor position with respect to the master.

The basic aim of SAR tomography is to invert equation 8 in order to derive the intensity and position of signal responses in elevation. Different inversion methods are reported in the literature and may be grouped in *parametric* models and *non-parametric* models. Basic information about these models can be found, for instance, in Stoica and Moses (2005). In theory, parametric models, e.g. non-linear least square adjustment (NLS), provide the best solution.

However, the definition of functional models requires a-priori knowledge about the number of scatterer responses integrated into each resolution cell. Non-parametric methods, e.g. singular value decomposition (SVD) (Fornaro et al., 2003) or adaptive beamforming (Lombardini and Reigber, 2003), aim at reconstructing the reflectivity function  $\gamma(s)$ . Afterward, the maxima of  $\gamma(s)$  have to be found, for instance, by using penalized likelihood criteria (Zhu et al., 2008).

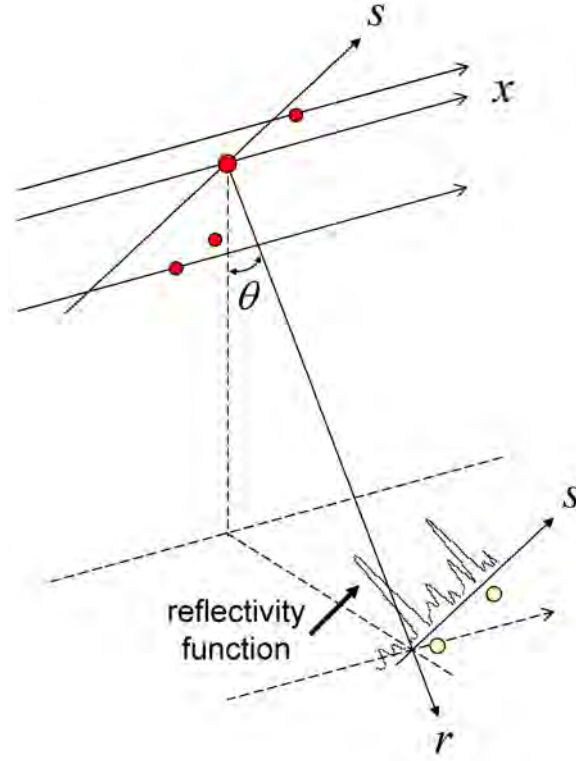


Fig. 9. Synthetic aperture in elevation direction. A stack of SAR datasets is exploited in order to recover the reflectivity function in elevation direction. Red spots: orbits forming the synthetic aperture in elevation direction  $s$ . The enlarged red spot marks the master orbit. Yellow spots: scatterers to be detected. Azimuth direction:  $x$ . Range direction:  $r$ .

Figure 10 shows an example for 3D SAR tomography using VHR spotlight TerraSAR-X data. After the selection of pixel  $P_{SCAT}$  and pixel  $P_{REF}$  defining the reference height 0 m at the ground, the normalized reflectivity function is reconstructed by processing of the SAR data stack (see figure 10b). Two main intensity peaks are distinguishable which correspond to signal responses from the ground and from the building facade. Strong sidelobes occur due to irregular sampling in elevation.

In case of non-parametric models, limitations in tomographic processing occur due to the short length of the synthetic aperture in elevation as well as due to the low number and irregular distribution of samples. Compressive sensing has proven to be reasonable for overcoming these limits (Budillon et al., 2009; Zhu and Bamler, 2010). Moreover, tomographic methods have been extended to 4D-space including the velocity of scatterers (Lombardini, 2005; Zhu and Bamler, 2009). Hence, the topography of urban areas can be provided in case of moving objects and object deformation can be monitored. The application of 4D SAR tomography to medium resolution SAR data and VHR resolution SAR data are presented in Fornaro et al. (2009) and in Zhu and Bamler (2009), respectively.

## Radargrammetry

Radargrammetric methods exploit radiometric information about dominant signatures in SAR datasets captured from different look angles or different aspect angles with respect to the area of interest (LaPrade, 1963; Leberl, 1990). In figure 11, the range shift of building features is

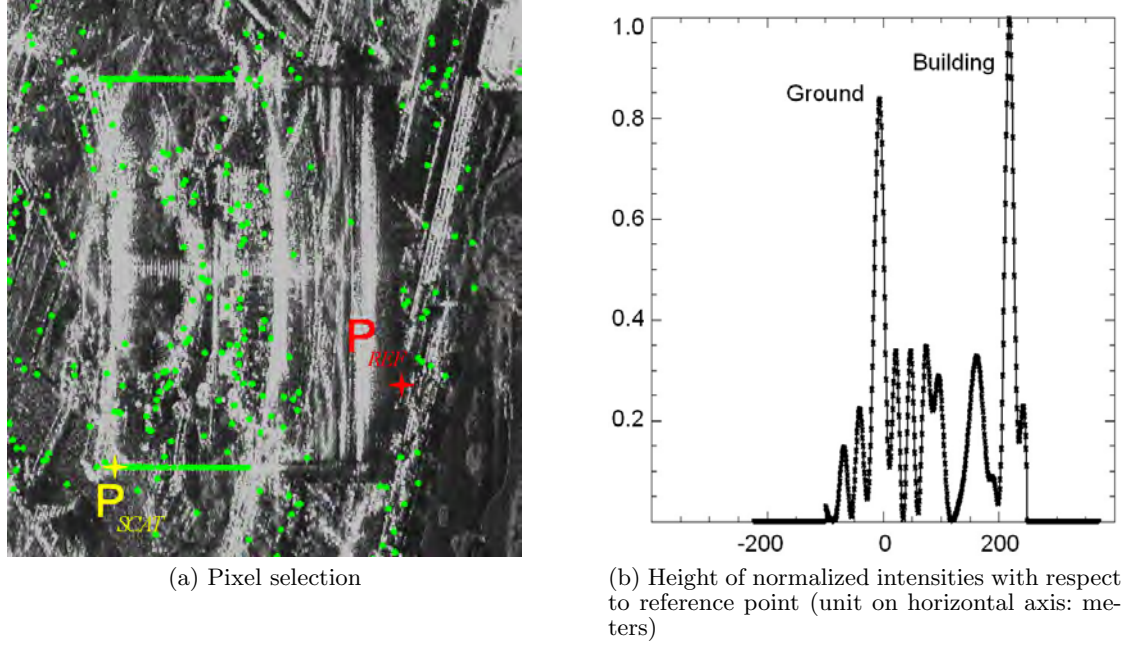


Fig. 10. Tomographic analysis for the Wynn Hotel, Las Vegas, USA (Zhu et al., 2008). A stack of VHR TerraSAR-X data is processed for reconstructing the reflectivity function corresponding to pixel  $P_{SCAT}$ . Height 0 m is defined at reference point  $P_{REF}$  located at the ground. Pixels marked in green are characterized by a high signal-to-noise ratio. For pixel  $P_{SCAT}$ , two intensity peaks are obtained which correspond to signal responses from the ground and the building facade.

shown for two TerraSAR-X images derived from different look angles. The regular structure of building windows and floors (see left image of figure 11) is represented by curved rows of point signatures. In case of a small look angle, the rows of signatures are more distributed in range since the size of the building's layover is large. When increasing the look angle of the SAR sensor, the rows of signatures are concentrated in range. In Adam et al. (2009), the relative shift in slant range occurring in SAR images, called *slave images*, is estimated with respect to a defined master image and is

$$\Delta r = \left( \frac{\sin(\theta_M - \theta_S)}{\sin(\theta_S)} \right) \cdot h \quad (9)$$

where  $\theta_M$  and  $\theta_S$  are the sensor look angles for master and slave image, respectively, and  $h$  is the scatterer height with respect to ground level.

VHR spaceborne SAR sensors enable the extraction of information about single objects. However, the application of radargrammetric methods to VHR spaceborne SAR data is still a task of future research. Adam et al. (2009) present an radargrammetry approach for retrieving the 3D position of scatterers at buildings under the assumption of horizontal and vertical surfaces. Based on the relative shift in range  $\Delta r$  and a-priori knowledge about the look angles  $\theta_M$  and  $\theta_S$  with respect to each target (see equation 9), the height  $h$  of scatterers is derived by means of a Bayesian estimation.

For airborne VHR SAR data, several algorithms for extracting 3D information for urban objects are reported in the literature. For instance, Simonetto et al. (2005) exploit stereoscopic SAR data for distinguishing double bounce lines at building walls from linear features corresponding to foreshortening at building roofs. This is possible since signals interacting with a building wall and the surrounding ground are focused on ground level. In case of flat earth, the range coordinate of such signatures is independent on the look angle. Oriot and Cantalloube (2008) use radargrammetric methods for DEM generation of urban scenes based on circular airborne SAR data. To this end, knowledge about the range shift of SAR image signatures is used for





Fig. 11. Spotlight TerraSAR-X data showing the range shift corresponding to elevated scatterers for different look angles of the SAR. The facade of the imaged building is characterized by metal structures and glass. Left: Building shape in SAR image for look angle of approx.  $27^\circ$ . Right: Building shape in SAR image for look angle of approx.  $38^\circ$ . The range coordinate corresponding to elevated scatterers changes with the look angle of the SAR (Goel and Adam, 2010).

testing height hypotheses for salient image pixels.

### Persistent Scatterer Interferometry

*Persistent Scatterer Interferometry (PSI)* aims at the detection of deformations at the earth surface based on long-time coherent scatterers, which are referred to as *persistent scatterer (PS)*. Phase differences are analyzed for single pixels characterized by high amplitude stability over time where low phase noise is expected. The first approach analyzing the deformation of long-time coherent scatterers was presented by Ferretti et al. (2001) and is referred to as *Permanent Scatterer Interferometry*. Since then, alternative approaches have been reported, e.g. in Kampes (2006). PSI is an opportunistic approach since it relies on the number of available PSs in the scene of interest, regardless where and why they appear. Basically, the number of PSs is much higher in urban areas than in rural areas due to the regularity of urban structures, what favors the occurrence of deterministic signatures.

For PSI processing, a stack of spatially and temporally distributed SAR data is required. After co-registration of the SAR data, a master image is selected defining the reference phase for each PS. Afterward, pixels are selected as PS candidates, e.g. based on amplitude stability over time or based on the signal to noise ratio. A reference DEM, which may be of moderate spatial resolution, is used for suppressing phase contributions from the earth topography. Thereafter, the functional model for estimating the deformation signal for a selected PS may be defined as

$$\Psi_{MS} = \text{Wrap} \left( B_{MS} \cdot \Delta h_{err} + \frac{4\pi}{\lambda} \cdot t_{MS} \cdot \Delta v + \frac{4\pi}{\lambda} \cdot o_{MS} \right) \quad (10)$$

where

- ◇  $\Psi_{MS}$  is the phase difference between master  $M$  and slave  $S$  [unit: radians].
- ◇  $B_{MS}$  is a factor considering the geometrical relation between master and slave image [unit:  $1/m$ ].
- ◇  $t_{MS}$  is the time difference between the acquisition of master and slave.
- ◇  $\text{Wrap}(\cdot)$  is the wrapping operator which is removed by phase unwrapping for obtaining the absolute phase with respect to the reference point.
- ◇  $o_{MS}$  includes atmospheric effects and orbit errors when present [unit:  $m$ ].

For suppressing atmospheric effects of low frequency, adjacent PS candidates are linked by arcs within a network including one reference point for phase unwrapping. Afterward, the differential velocity  $\Delta v$  for each arc and the height correction  $\Delta h_{err}$  to be added to the reference DEM

can be estimated based on statistical assumptions. However, there are two major limitations. First, a deformation model has to be defined in order to separate the deformation signal from atmospheric residuals and noise. Second, the separation of scatterers within the same resolution cell is not possible. A theoretical concept for overcoming the second limitation is reported in Ferretti et al. (2005).

In figure 12, results from VHR PSI are presented for an urban scene in Berlin, Germany, containing four buildings. For estimating the deformation signal, a stack of 26 VHR TerraSAR-X datasets has been processed. Patterns of point signatures are visible on the corresponding SAR temporal average image where random scattering effects are suppressed (see figure 12a). In figure 12b, the deformation signal is estimated for each PS selected in the scene. Knowledge about the spatial correlation of PSs at single urban objects can be introduced to the deformation model in order to increase the reliability of deformation estimation (Gernhardt and Hinz, 2008).

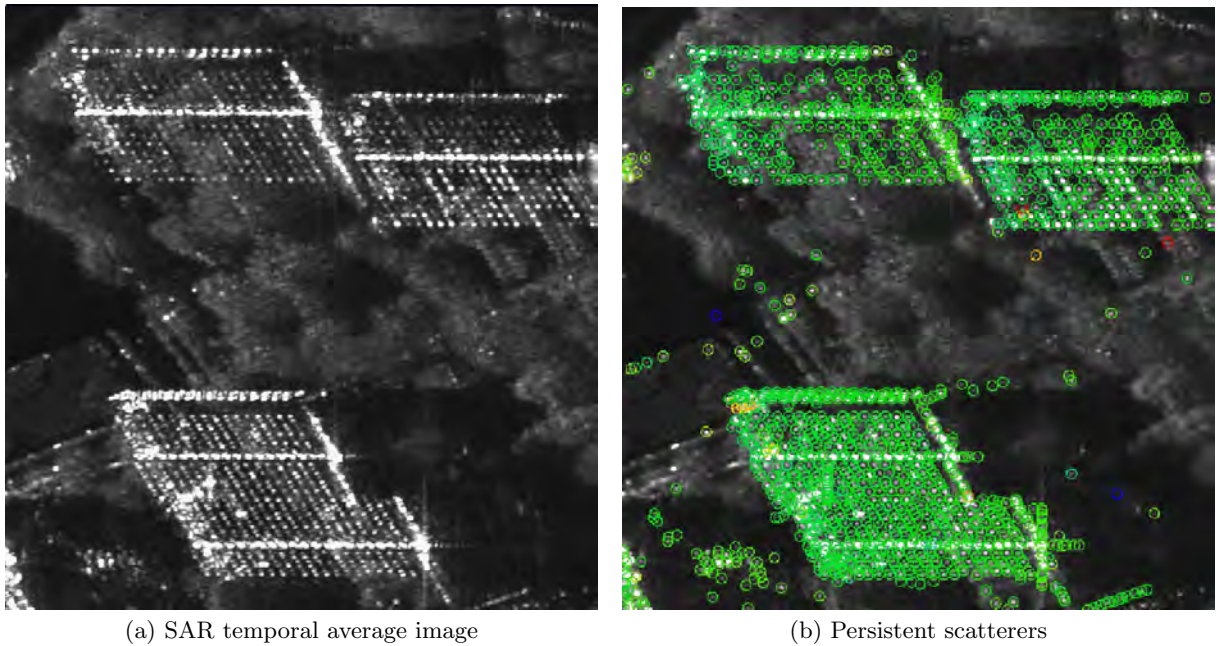


Fig. 12. Results from Persistent Scatterer Interferometry for an urban scene including four buildings in Berlin, Germany (Auer et al., 2010a). Persistent scatterers (PSs) are marked by circles. A color wheel from red to blue indicates the deformation signal and corresponds to a displacement interval between -10 mm/year and 10 mm/year. The SAR data stack has been processed using the PSI-GENESIS software, German Aerospace Center (DLR).

## 2.2 Introduction to render techniques

Rendering aims at providing artificial, photo-realistic images of modeled 3D scenes. To this end, the interaction between optical light and objects has to be approximated. From a physical point of view, helpful tools may be given by the Maxwell equations (see e.g. Tsang and Kong (2001)), the theory of relativity of Albert Einstein and the theory of quantum mechanics. However, the formulation of a functional model based on these theories is complicated and the resulting rendering techniques may be very time consuming. Therefore, render techniques have been developed based on simplifying assumptions and neglect the majority of physical effects. The wavefront of an electromagnetic signal is represented by discrete rays. Hence, simulation is performed numerically and is focused on object geometry which enables the simulation of scenes of high detail.

In the following, basic foundations on render techniques are given. Starting at the render equa-

tion, which theoretically provides an optimum solution, different algorithms for rendering images are briefly introduced. Finally, the relevance of render algorithms for SAR simulation is discussed.

### 2.2.1 The render equation

The major precondition for any functional model approximating *global illumination* within an illuminated scene is the conservation of energy. In other words, the sum of the reflected, transmitted and absorbed signal has to be constant at each surface illuminated by a light source. In sum, the outgoing radiance from a point  $\vec{x}$ , located on a surface, in direction  $\vec{\omega}$  may be described as

$$I_o(\vec{x}, \vec{\omega}) = I_e(\vec{x}, \vec{\omega}) + I_r(\vec{x}, \vec{\omega}) + I_t(\vec{x}, \vec{\omega}) \quad (11)$$

where

- ◇  $I_e(\vec{x}, \vec{\omega})$  is radiance emitted by the surface itself [unit:  $\frac{W}{sr \cdot m^2}$ ;  $sr$ : steradians],
- ◇  $I_r(\vec{x}, \vec{\omega})$  is radiance specular or diffuse reflected at the surface, and
- ◇  $I_t(\vec{x}, \vec{\omega})$  is radiance transmitted through the surface.

In Nicodemus (1965), the basic equation for describing the signal reflection at surfaces is introduced which is commonly referred to as the *bi-directional reflectance distribution function (BRDF)*. In figure 13, a reflection process occurring at a surface is shown. The direction of the incoming intensity is defined by two aspect angles  $\phi_i$  and angle  $\theta_i$  with respect to the surface normal. Likewise, the direction of the reflected signal is defined by two angles  $\phi_r$  and  $\theta_r$ . Based on the given geometry, Nicodemus defines the corresponding BRDF as

$$\varsigma(\theta_i, \phi_i, \theta_r, \phi_r) = \frac{dI_r(\theta_r, \phi_r)}{I_i(\theta_i, \phi_i) \cos(\theta_i) d\Omega_i} \quad (12)$$

The reflectance factor  $\varsigma(\cdot)$ , whose unit is  $\left[\frac{1}{sr}\right]$ , describes the proportion between the signal intensity reflected in direction  $dI_r(\theta_r, \phi_r)$  and the intensity of the signal illuminating the surface within solid angle  $d\Omega_i$ . The numerator and denominator of the BRDF are referred to as *radiance* and *irradiance*, respectively.

Based on the BRDF, Kajiya (1986) introduces the *rendering equation* for solving the problem of global illumination from a theoretical point of view. The rendering equation considers three points on object surfaces whose relative orientation is given:

- ◇ point  $\vec{x}_1$  on surface 1, where a signal is emitted
- ◇ point  $\vec{x}_2$  on surface 2, where a signal is reflected
- ◇ point  $\vec{x}_3$  on surface 3, where the incoming signal intensity is evaluated.

A simplified description of the rendering equation, which provides the sum over all intensities reflected from  $\vec{x}_2$  in direction to  $\vec{x}_3$ , is

$$I(\vec{x}_3, \vec{x}_2) = g(\vec{x}_3, \vec{x}_2) \cdot \left( I_e(\vec{x}_3, \vec{x}_2) + \int_H \varsigma(\vec{x}_3, \vec{x}_2, \vec{x}_1) \cdot I(\vec{x}_2, \vec{x}_1) d\vec{x}_1 \right) \quad (13)$$

where

- ◇  $g(\vec{x}_3, \vec{x}_2)$  is a geometry term and is 0 or  $\frac{1}{r^2}$ , depending on whether the connection between  $\vec{x}_3$  and  $\vec{x}_2$  is interrupted or not. The parameter  $r$  is the spatial distance between  $\vec{x}_2$  and  $\vec{x}_3$ .

- ◇  $I_e(\vec{x}_3, \vec{x}_2)$  is the intensity emitted at point  $\vec{x}_2$  in direction to point  $\vec{x}_3$ , i.e. if surface 2 is a light source.
- ◇  $\varsigma(\vec{x}_3, \vec{x}_2, \vec{x}_1)$  is the bidirectional reflectance distribution function describing the reflection process starting at  $\vec{x}_1$ , including  $\vec{x}_2$ , and ending at  $\vec{x}_3$ .
- ◇  $I(\vec{x}_2, \vec{x}_1)$  is the intensity emitted at point  $\vec{x}_1$  in direction to surface  $\vec{x}_2$ .
- ◇  $H$  is the hemisphere covering the surface marked by point  $\vec{x}_2$ .

While  $g(\vec{x}_3, \vec{x}_2)$ ,  $I_e(\vec{x}_3, \vec{x}_2)$  and  $\varsigma(\vec{x}_3, \vec{x}_2, \vec{x}_1)$  are assumed to be given by scene geometry and object materials,  $I(\vec{x}_2, \vec{x}_1)$  is unknown. Thus, the main task of render algorithms is to approximate the entity of all intensities impinging on point  $\vec{x}_2$  at surface 2 from hemisphere  $H$ . In its basic form, the rendering equation neglects signal diffraction, atmospheric effects, wavelength dependence, and signal polarization.

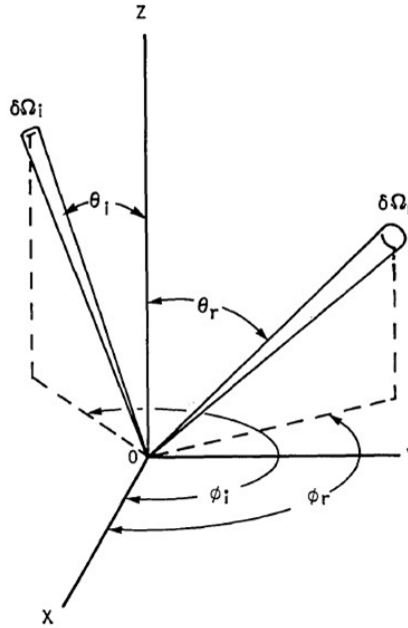


Fig. 13. Geometry of bi-directional reflection process (Nicodemus, 1965).

### 2.2.2 Rendering algorithms

Different algorithms for rendering are reported in the literature which can be considered as approximations of the rendering equation. The components of a scene to be rendered are identical for all rendering methods: besides the geometry and material of objects, at least one light source and a camera is needed. Main differences occur when representating reality, i.e. when approximating the render equation. The focus is either on providing photo-realistic images at a high computational cost, e.g. for animated movies, or on providing near-realistic images in real-time, e.g. for video games. A short history of relevant render algorithms is given in the following.

(Appel, 1968) simulate optical images of objects which are toned by a digital plotter. Using *point by point shading*, rays are followed in inverse direction starting at the projection center of the camera. The main motivation is the simulation of shadow which gives information about the relative position of two or more objects within a simulated scene. Moreover, the visibility of objects to the camera can be checked efficiently. However, the detection of intensities is limited to direct backscattering of type 'diffuse'. Bouknight (1970) present the *scanline algorithm* where the boundaries of 3D objects are transformed into the 2D image plane of the camera. Afterwards, intersections between object boundaries and horizontal scanlines are detected within the image

plane in order to identify the interior and exterior of projected objects. Eventually, interior areas visible to the camera are analyzed for intensity contributions. For simplification, the position of the light source is equal to the camera position. Multiple reflection of signals is neglected. Catmull (1974) adopts the concept of mapping polygons of 3D objects into the 2D image plane. However, depth information for checking the visibility of objects, called *z-buffer*, is provided and stored for a raster imposed on the image plane, what is called *rasterization*. Phong (1975) aims at the simulation of curved objects at a sufficient degree and in real-time. In this context, reflection models for specular and diffuse reflection are introduced in order to increase the radiometrical quality of simulated images. Still, multiple reflection of signals is not considered. Moreover, the diffuse signal interaction within the scene is not modelled and only approximated by means of a constant value (*ambient light*).

In Whitted (1980), the *ray tracing* approach is introduced. While keeping the diffuse reflection model from Phong (1975), the specular reflection model is enhanced in order to include multiple reflections of type 'specular'. Rays are followed in inverse direction starting at the camera. The diffuse signal interaction between objects is not simulated, i.e. object shadow is represented in black color or assigned with a intensity constant. Moreover, the sharpness at intensity edges is exaggerated compared to reality. Further information about ray tracing can be found in Glassner (2002). As an enhancement of standard ray tracing, Cook et al. (1984) introduce *distributed ray tracing*. Rays are spatially distributed near the direction of specular reflection for modeling gloss and depth of field. Moreover, distributing rays in time enables to simulate motion blur. Heckbert and Hanrahan (1984) aim at solving the discrete sampling problem adherent to ray tracing, which is time-consuming and is affected by aliasing. After transforming 3D object polygons to the image plane of the camera, beams are used instead of discrete samples in order to detect intensities within the modeled scene (*beam tracing*). Thereby, intersection polygons are detected at objects visible to the camera. Specular multiple reflection of signals is approximated by using the detected intersection polygons for defining new beams. However, the rendering concept is limited to planar surfaces.

A concept for approximating the transfer of diffuse signals between objects is introduced by Goral et al. (1984) and referred to as *Radiosity*. Based on a scene representation by means of flat polygons, the signal impinging on a polygon face is the sum over the diffuse intensities scattered from all other polygons. Specular reflections are neglected. *Path tracing*, a rendering concept introduced by Kajiya (1986), aims at approximating both specular and diffuse reflections of any kind and, hence, to approximate global illumination. In contrast to the standard ray tracing approach, a ray hitting an object is not followed in specular direction. Instead, the direction of the reflected ray is chosen randomly. By emitting a high number of rays for each image pixel and adding the detected intensities, the render equation is approximated. However, the computational cost is immense, as a low number of rays per pixel yields noisy images. Veach and Guibas (1997) propose a new sampling method, called *Metropolis sampling*, for path tracing. Rays are distributed along initial paths giving a-priori information about the expected distribution of intensities within the rendered image. Hence, computation time can be saved due to a reduced number of rays. Jensen (1996) present an alternative approach for the approximation of global illumination, which is called *photon mapping* and is reasonable for simulating caustics.

The effect of global illumination is distinguishable in figure 14. An image rendered by ray tracing is compared to an image rendered by the combination of ray tracing and radiosity. On the one hand, the potential of ray tracing for simulating specular reflections is obvious. However, global illumination can only be approximated when considering the diffuse signal interaction between objects by means of radiosity.



Fig. 14. Global illumination effect for a multi-body scene. Left: ray tracing neglecting diffuse signal interaction between objects. Ambient light is deactivated. Right: combination of ray tracing and radiosity for the approximation of global illumination. The model scene is available in the POV-Ray hall of fame (POV-Ray, 2011).

### 2.2.3 Relevance of render techniques for SAR simulation

As was already indicated above, rendering algorithms are mainly applied for simulations in the visible spectrum. In optical images, color information depends on the chemical property of objects and, hence, differences in backscattering for different signal wavelengths. Moreover, with little exception, the signal wavelength (approx. 380 nm - 750 nm) can be considered as being small compared to the roughness of object surfaces. Hence, the simulation of diffuse signal interaction at objects is important while specular effects only have to be added in case of specific materials, e.g. metallic surfaces or surfaces made of glass. To conclude, standard ray tracing is not sufficient for the simulation of optical data since global illumination is required for photo-realistic representation (see example in figure 14).

However, tools given by rendering methods are also applied for simulating signal-object interaction in case of larger wavelengths. For instance, Ikegami et al. (1991) use ray tracing for calculating the mean field strength of radio systems along pre-defined profiles within an urban scene. In Schmitz et al. (2009), beam tracing is applied for simulating the propagation of radio signals within an urban scene in near real time. In Lehnert (1993), the detection problem of ray tracing is identified when simulating room acoustics. Artificial signal differences occur if the size of the detection element is not adapted to the density of rays during ray tracing.

The strength of radar responses from objects is influenced by the roughness and permittivity of surfaces. Signals of constant frequency are emitted and detected. The signal wavelength, e.g. 3.1 cm for X-Band, is comparable to the height deviation of objects or even large, e.g. in case of smooth surfaces at man-made objects. Therefore, specular reflections are expected to dominate diffuse reflections at urban objects. The importance of diffuse signal interaction between objects is of less importance than for simulations in the optical spectrum. However, when using rendering methods for SAR simulation, new reflection models have to be defined or given reflection models have to be adapted for describing the interaction of radar signals and objects.

At present, the application of two rendering methods for SAR simulation is reported in the literature: rasterization and ray tracing. Rasterization aims at SAR simulation in real-time, e.g.

- ◇ for simulating direct backscattering of radar signals, e.g. (Rius et al., 1993) (Balz, 2006),
- ◇ for approximating double reflections (Balz and Stilla, 2009), or
- ◇ for checking the visibility of objects (Margarit et al., 2007).



Ray tracing enables the simulation of multiple reflections, e.g. for providing test data for feature extraction algorithms. A detailed literature survey on the simulation of detailed objects based on ray tracing is given in chapter 2.3.3. The approach presented in this thesis is based on ray tracing as well. To this end, the open-source ray tracer POV-Ray is adapted and enhanced in order to provide output data in SAR geometry. An introduction to POV-Ray and its modeling tools is given in Appendix B.

## 2.3 SAR simulation - state of the art

### 2.3.1 Concepts for SAR simulation

In Franceschetti et al. (1995), SAR simulators are categorized in *image simulators* and *raw data simulators*. Simulators of the former kind aim at directly simulating SAR images, i.e. without intermediate raw data used as input for a SAR processor. SAR raw data simulators are developed in order to provide test data for processing algorithms or for the radiometric analysis of SAR data.

Early concepts for SAR image simulators concentrate on the simulation of direct backscattering from open areas. Muhleman (1964) presents a reflection model based on ray optics in order to estimate the mean surface slope and the rotation rate of the Venus. Boyell (1969) simulates direct backscattering from lunar surfaces in real-time on a television screen. Terrain occlusions and shadow are detected along ground range profiles. In Holtzman et al. (1978), SAR images of rural, homogeneous areas are simulated and are recorded on photographic film in order to support information extraction from SAR data. The amount of silver grains on the photographic film is calculated based on the radar equation. The spatial correlation of speckle on resolution cell level is approximated in Raney and Wessels (1988), showing that imposing random speckle noise to a simulated SAR image pixel is not sufficient. Simulation results for airborne SAR images are presented for a rural scene. Gelautz et al. (1998) introduce an approach for simulating SAR amplitude data for alpine regions. To this end, points of a digital elevation model (DEM) are mapped into the azimuth-range plane and post-processed in order to obtain a regular raster. Eventually, simulated SAR data are used for supporting the projection of real SAR data on a DEM of moderate resolution.

Besides the simulation of rural areas, image simulators are applied for the purpose of providing a-priori knowledge about man-made objects. For instance, ray tracing methods are applied in Wohlers et al. (1980) for simulating SAR image signatures of airplanes. The main motivation is to provide test data for automated object identification. However, the simulation of targets is limited to direct backscattering. Nasr and Vidal-Madjar (1991) use ray tracing methods for detecting specular reflectors, dihedral, and trihedral geometries, labeled as 'Elementary Geometric Reflectors (EGRs)', for each target. Afterwards, the target response is derived by summing up the signal of EGRs for each resolution cell and is embedded into SEASAT data. Analyzing the shape of objects in real SAR data is not pursued due to the limited resolution of the SEASAT satellite. Rius et al. (1993) use rendering tools provided by a graphics workstation for simulating the radar cross section of 3D objects. Simulation of radiometric information is performed using physical optics, edge diffraction and signal absorption. Multiple reflections of radar signals are neglected. Bolter (2001) simulate the direct backscattering of radar signals for refining 2.5D building models extracted from multi-aspect airborne InSAR data. Knowledge provided by SAR simulation is used for discarding building layover and occluded shadow areas as data source for building reconstruction. Xu and Jin (2006) simulate polarimetric SAR data based on a mapping and projection algorithm in order to provide test data for building reconstruction methods. Multiple reflections are accounted for but only simulated within the

incident field of the radar signal. Rasterization methods are used in Balz (2006) for simulating SAR images or urban areas in real-time. Depth information of objects visible to the virtual SAR sensor is gathered by a z-buffer. In Balz and Stilla (2009), the approximation of double reflections of radar signals is included into the simulation approach. Melody (2009) analyze the path of multiple reflected radar signals for finding the real position of objects. Thus, hinted objects without direct response but multi-bounce response can be detected within an imaged scene. Brunner (2009) presents a ray tracing approach for simulating the appearance of basic building shapes in VHR SAR data. Simulated SAR data for different incidence angles of the radar signal enable to estimate the height of buildings based on correlation methods. The simulation of double reflections of radar signals is limited to one azimuth resolution cell.

Simulators for providing SAR raw data are based on physical models describing reflection phenomena, e.g. (Tsang and Kong, 2001; Franceschetti et al., 2001). In this context, the geometrical description of single objects is simplified or even neglected. Camporeale and Galati (1991) discuss two SAR simulator concepts for the simulation of raw data. End-to-end simulators enable the analysis of changes to the SAR system response of targets, e.g. the saturation of intensities. In contrast, assuming a constant SAR system response for targets enables to simulate areas of large-scale with reduced calculating time. Franceschetti et al. (1992) define SAR reflection models in order to provide SAR raw data for open terrain. Shadow areas are detected using ray tracing methods. In Franceschetti et al. (2002), the SAR simulation approach is enhanced by reflection models for double and triple bounce at buildings. Simulation results for the approximation of multiple reflections are presented in Franceschetti et al. (2003). Since the focus is on radiometric correctness and on the definition of reflection models in closed form, the SAR simulation approach is limited to basic shapes, e.g. buildings are represented by box models. Bickert et al. (2002) simulate SAR raw data for the purpose of supporting the development of a ground moving target indication (GMTI) algorithm. To this end, radar signals of moving targets are added to a clutter map derived from given SAR data. Speck et al. (2002) present a raw data simulator based on separate modules for 3D objects, such as buildings or vehicles, and the background. Information about the radar cross section of targets is kept in a data base while electromagnetic properties of surfaces are used for approximating backscattering from the ground.

Including angular information in cross-range direction, different InSAR simulators are reported in the literature. For instance, Franceschetti et al. (1998) include signal decorrelation into the definition of electromagnetic models for the simulation of SAR reflectivity maps. Hence, the disturbance of the interferometric signal is not included artificially to the simulated data. Simulation scenarios for layover situations are not presented. Petit and Adragna (2000) apply simulation techniques for evaluating the loss of coherence in case of direct backscattering of the radar signal from sloped surfaces. InSAR simulation methods, using a DEM as input, are presented by Eineder (2003) in order to enable the prediction of shadow and layover areas for mountainous areas of large scale. A grid of points representing the DEM surface is derived by intersecting the DEM with radar signal wavefronts regularly distributed in range. Mori and De Vita (2004) present a InSAR raw data simulator operating in time domain and considering the curvature of the sensor orbit and the earth surface. The approach aims at the simulation of direct backscattering of radar signals for areas of large scale. Focused on urban areas, Thiele et al. (2007a) simulate phase profiles of basic building shapes in case of single bounce of radar signals and compare it to phase profiled extracted from airborne SAR data. The radiometrical correctness of the simulation results is limited since surface backscattering is assumed to only depend on the local angle of incidence of the radar signal. In Thiele et al. (2010), the interference of the signal phase is simulated for adjacent buildings represented by boxes whose heights vary.



### 2.3.2 VHR SAR simulation for urban areas

The strength of radar signals backscattered to the SAR sensor depends on surface parameters (roughness, correlation length, permittivity) but also on the geometry of objects, which may be characterized by regular shapes such as dihedrals or trihedrals. In SAR data of low or medium resolution, most objects are smaller than the resolution of the SAR system. Hence, with regard to SAR simulation, an object representation by means of backscatter coefficients may be appropriate, as shown e.g. by Holtzman et al. (1978) or Speck et al. (2002). When using this method, acceptable results are expected for homogeneous areas of large scale. In contrast, SAR simulation approaches for supporting the interpretation of VHR SAR data have to consider the geometry of a scene of interest as the signal response of single objects may be distributed over a high number of pixels.

In case of multiple reflections of radar signals at single objects, the *description of object geometry* is expected to be fundamental. A compromise has to be found between the radiometric and geometric correctness of simulation results. A reliable representation of the radiometry of multiple reflections is enabled by equations in closed form based on the Maxwell equations. For instance, both the position and the signal power of double bounce signatures corresponding to signal interaction with building walls and the surrounding ground can be simulated. Moreover, the inversion of reflection models in closed form enables the extraction of object heights based on the intensity of SAR image signatures (Franceschetti et al., 2007). For this purpose, surface parameters of objects have to be known a-priori, what may be challenging for man-made objects Brunner et al. (2009). Moreover, the simulation of objects has to rely on basic object shapes, e.g. box models (Franceschetti et al., 2002).

However, non-metallic building corners having a sidelength of 10 cm are anticipated to be visible in VHR SAR data, even if their extent is much smaller than the size of a resolution cell. Examples for building parts forming small corners may be windows, balconies, facade protrusions or roof structures. Hence, a high level of detail of building models may be required in order to enable the simulation of SAR image signatures corresponding to multiple reflections of the radar signal. Rendering methods such as rasterization or ray tracing have been developed for simulating object models of that detailedness at the cost of limited radiometric correctness of rendered images. The propagation of signal wave fronts is approximated by discrete samples – rays – which are not appropriate for substituting radar reflection models in closed form. However, since the work presented in this thesis aims at the geometrical analysis of salient signatures in VHR SAR data, the focus has to be put on the *geometrical correctness* of simulation results. Ray tracing methods are applied for sampling modeled scenes containing man-made objects and for providing output data in SAR geometry. Due to the duality of geometry and radiometry in case of multiple reflections of radar signals, limitations with regard to the correctness of the simulated signal strength have to be accepted.

### 2.3.3 Discussion of most related work

At this point, work related to the simulation approach presented in this thesis is introduced. Three relevant simulators – SPECRAY-EM/FERMAT, GRECOSAR, and PIRDIS – are discussed as they show similarities to the simulation approach presented in this thesis:

- ◇ ray tracing methods are applied for simulating radar signals,
- ◇ multiple reflections of radar signals are accounted for,
- ◇ simulation of VHR SAR data is enabled and pursued, and
- ◇ detailed object models may be simulated.

SPECRAY-EM/FERMAT has been developed in a joint project of ONERA (Office National d'Etudes et de Recherches Aérospatiales) and OKTAL-SE, France, combining knowledge about electromagnetics, render techniques and the handling of data bases. The main objectives are the

calculation of the radar cross section of objects, the prediction of sensor capabilities, and the simulation of objects within environments for testing target detection algorithms. In advance to the simulation procedure, modeled object scenes have to be represented by means of triangles. Sampling of scenes is performed by means of tubes defined by a perspective view in line-of-sight of the sensor (Mametsa et al., 2001). The synthetic aperture is simulated and azimuth processing effects are accounted for. Simulation results are reported for single objects (Hammer et al., 2008) and open terrain including objects (Latger et al., 2005). Models for the reflection of radar signals are defined for metallic, diffuse and specular surfaces. The strength of the signal response is approximated using high-frequency RCS prediction techniques (Knott et al., 2004), namely geometrical optics (GO) for specular reflection and physical optics (PO) for diffuse reflection. Speckle, atmospheric effects, and signal diffraction may be simulated (Berges et al., 2004). Multiple reflections of radar signals are considered. Simulation results are provided in the azimuth-range or azimuth-ground-range plane. A cross-comparison to other SAR simulators based on render techniques can be found in Hammer et al. (2008).

GRECOSAR aims at the simulation of polarimetric SAR data of single objects. The development of the simulator is based on the assumption that object classification is improved by including polarimetric information. Thus, polarimetric SAR data are simulated for testing classification algorithms. Simulation results are presented for vessel models (Margarit et al., 2006) and building models of high detail (Margarit et al., 2007). The approach is based on GRECO (Graphical Electromagnetic Computing), a tool for simulating the radar cross section of objects on a graphics workstation (Rius et al., 1993). Margarit et al. (2006) adapt GRECO to the imaging geometry of a SAR and combine it with a processor for SAR raw data. Curved objects are approximated by triangles in order to enable a intersection test for rays emitted by the virtual SAR antenna. The backscattering from perfectly conducting surfaces is evaluated using physical optics (PO) while multiple reflections are approximated by a combination of geometrical and physical optics (GO + PO). After simulation of the synthetic aperture, the SAR raw data are post-processed. Scattering maps are created by polarimetric decomposition of the simulated SAR data and image features are identified, e.g. the distribution of dihedrals and trihedrals characterizing vessels for different aspect angles (Margarit et al., 2009).

PIRDIS (Platform-Independent Range/Doppler Image Simulation) is a simulator for SAR amplitude data introduced by Meyer-Hilberg (2006). The main objective of the simulation approach is to provide test data for SAR ground moving target indication (GMTI). Moreover, data can be simulated for certain SAR imaging geometries in order to evaluate the performance of future SAR systems. Multiple reflection and polarization of the radar signal is considered as well as atmospheric effects. Physical optics (PO) is used for simulating the backscattering from terrain. Eventually, the simulated SAR image is composed by signal response from the background and signal response from moving or non-moving objects (Meyer-Hilberg et al., 2008).

As mentioned above, all related simulation approaches are focused on object geometry and, hence, consider multiple reflections at objects. The main motivation of the simulation approaches is to provide a reliable approximation of real SAR data in the azimuth-range plane given a certain amount of a-priori knowledge about the scene to be simulated, e.g. object geometry, object movements, surface characteristics or disturbing factors such as certain weather conditions or noise. To this end, radar reflection models are integrated in the ray tracing environment and SAR image characteristics like speckle or the sinc-function as the response of point scatterers are considered. With regard to the application of simulated data, simulations are conducted for different purposes:

- (1) Tools for information extraction from SAR data can be tested, for instance, algorithms for object detection (major objective of SPECRAY-EM/FERMAT and PIRDIS) or for object classification (GRECOSAR).
- (2) Simulated SAR data can be visually compared to SAR data in order to interpret imaged

scenes (major objective of SPECRAY-EM/FERMAT).

- (3) Future SAR system performances can be tested (major objective of SPECRAY-EM/FERMAT and PIRDIS).

In any case, the ideal simulation result would be a copy of real SAR data minimizing systematic errors in provided test data. The interpretation of SAR image signatures is performed on the image level, i.e. the expression 'scatterer' is linked to a salient image pixel. Investigating the origin of SAR image signatures on the object level is not enabled.

However, the interpretation of salient SAR image features corresponding to multiple reflections of the radar signal requires additional support beyond the simulation of data in the azimuth-range plane. The expression 'scatterer' has to be linked to the geometry of structures within simulated scenes. For this purpose, methods are required for analyzing the correspondance of dominant SAR image signatures to regular and non-regular object geometries. More specifically, the inversion of the SAR imaging process has to be simulated. Still, the nature of dominant signatures on SAR images is not known in detail what is crucial when evaluating the reliability and meaning of SAR products, e.g. deformation signals for single objects detected by PSI. As introduced in Section 2.3.1, ray tracing methods are applied in Nasr and Vidal-Madjar (1991) for seeking dihedrals, trihedrals, and specular backscattering surfaces characterizing the signal response of objects. To this end, a-priori knowledge about the geometrical shape of structures provoking dominant SAR image signatures is introduced. However, salient SAR image signatures may also occur at non-ideal scatterers such as trihedrals without tips, non-orthogonal corners, or corners partly occluded with respect to the line-of-sight of the SAR sensor.

For all related SAR simulation approaches, SAR products are interpreted in 2D image space. SPECRAY-EM/FERMAT and PIRDIS simulate the distribution of signals in azimuth and range. Accordingly, scatterers within the same resolution cell are not spatially separated during the simulation process. Layover situations can not be resolved, for instance, in order to find the number of dominant scatterers corresponding to a SAR image pixel. Besides map in the azimuth-range plane, GRECOSAR enables to include the third dimension by simulating interferometric SAR data. However, the spatial distribution of signals in height is visualized on 2D images indicating the SAR sensor's line-of-sight.

The SAR simulation approach presented in this thesis has been developed in order to meet the limitations discussed above. New methods have to be developed for investigating the nature of dominant scatterers in urban areas based on simulated SAR data. To this end, the 3D position of phase centers, i.e. including the elevation domain, is directly simulated. Basic ideas and case studies with regard to the SAR simulation concept are presented in Auer et al. (2008), Auer et al. (2009b), Auer et al. (2009a), Auer et al. (2010b), and Auer et al. (2010a). A detailed introduction and discussion of the developed SAR simulation methods is given in chapters 5 and 6.

## 3 Introduction to RaySAR

### 3.1 3D SAR simulation approach - new aspects

The SAR simulation approach presented in this thesis is focused on developing new methods for supporting the interpretation of salient signatures on VHR SAR images corresponding to man-made objects. In this regard, the SAR simulator, named RaySAR, aims at solving the limitations of related simulators discussed in Chapter 2.3.3 where the interpretation of signal distributions is conducted on 2D image planes. In sum, the simulation approach addresses three new aspects:

- (1) 3D SAR simulation in azimuth, range, and elevation.
- (2) Methods for the geometrical analysis of scatterers are provided.
- (3) The inversion of the SAR imaging system is simulated.

to (1)

A new 3D SAR simulator based on ray tracing methods, named *RaySAR*, is proposed enabling the analysis of signatures in azimuth, range, and elevation. To this end, the open-source ray tracer POV-Ray (Persistence of Vision Ray Tracer) is adapted and enhanced for providing output data in SAR imaging geometry. The SAR system is represented by a camera characterized by orthographic projection in azimuth and elevation as well as by a signal source emitting parallel light. Simulation applications are focused on the simulation of urban environments with limited extent. Focusing of multiple reflections is performed directly without data gathering along a virtual synthetic aperture. RaySAR simulates an ideal SAR system having infinite resolution in azimuth, range, and elevation, i.e. a corner reflector is focused to a point in 3D space. Hence, several scatterers contributing signals to the same SAR image pixel can be separated in elevation. It is not the purpose of RaySAR to simulate the entire imaging chain considering the pulse repetition frequency (PRF) of the SAR system and speckle. In contrast, emphasizing SAR image signatures may be welcome for understanding the geometrical shape of objects in SAR data.

to (2)

Simulated SAR data only form a basis product where SAR image signatures of interest are selected for further analysis. Different reflection levels can be assigned to separate image layers in order to focus on a bounce level of interest, e.g. double or triple bounce. Image pixels containing specular reflections can be distinguished from pixels only characterized by diffuse signal response. The elevation of scatterers can be displayed along profiles pointing in azimuth and range. Moreover, the distribution of intensities in elevation can be simulated for selected pixels, which enables to find the number of scatterer responses integrated into the same resolution cell. Finally, phase centers simulated in SAR imaging geometry can be mapped into detailed 3D object models for analyzing the physical correspondance to object features.

to (3)

RaySAR includes methods for identifying object surfaces contributing to salient image signatures. Hence, object surfaces hit by the virtual radar signal are geometrically linked to signatures within the simulated image, i.e. the SAR imaging system can be inverted. Starting in the real SAR image, signatures can be cross-compared to signatures in the simulated SAR image. Afterwards, surfaces contributing to the signature can be identified within the simulated 3D object model. Thereby, the discussion of the nature of scatterers is shifted from signatures in

the SAR image plane, e.g. points or lines, to the geometry of structures in the object space, e.g. dihedrals, trihedrals or non-regular reflectors.

## 3.2 Motivation for using POV-Ray

In order to meet the requirements summarized at the end of Chapter 1.2, the decision was made to use render methods for SAR simulation. In this context, the minor objective 'integration and enhancement of available software' (Chapter 1.2) was chosen by purpose. When using and adapting tools of available software, the focus can be set on the the main component of this work: the analysis of the nature of scatterers which is mainly covered by research beyond the simulation of SAR data in the azimuth-range plane. Finally, the open-source ray tracer POV-Ray was chosen as appropriate platform for developing a SAR simulator. An brief introduction to POV-Ray can be found in Chapter B.1. In summary, the ray tracing package fitted well into the defined requirement profile due to the following properties:

- ◊ POV-Ray comprises a variety of fast simulation tools.
- ◊ The POV-Ray source code has been continuously developed and improved by a huge community since 1991. Basic modules are thoroughly tested and free from programming errors.
- ◊ The inclusion of own developments is possible due to free access to its source code.
- ◊ POV-Ray uses an efficient concept for tracing rays, more specifically, ray tracing in reverse direction, which starts at the center of each image pixel and follows rays backward on their way to the signal source.
- ◊ POV-Ray offers appropriate interfaces for importing object models of high detail. Moreover, the representation of the radar signal by means of rays enables the simulation of analytical shapes such as curves or spheres.

Basic shapes and the imaging geometry of the SAR sensor within a virtual scene can be defined in the POV-Ray editor. Moreover, basic algorithms such as the ray tracing procedure, intersection tests between rays and objects or the detection of intensities or shadows can be used as provided by the basic POV-Ray software. However, own developments have been added to POV-Ray's source code in order to provide output data in SAR geometry.

## 3.3 SAR simulation concept - modeling, sampling, 3D analysis

An overview of the SAR simulation concept is given in figure 15. Basically, the processing chain contains three main components: modeling, sampling by the ray tracer and scatterer analysis. *Modeling* has to be performed in order to provide necessary input information about objects to be simulated. To this end, the geometry of objects has to be described, e.g. by means of analytical shapes or polygons (see Chapter 4.1 for detailed information). Moreover, surface characteristics have to be assigned to all objects for steering the reflection behavior (see Chapter 4.3). Finally, the position and parameters of the virtual SAR have to be added to the modeled scene (see Chapter 4.2). After the definition of rendering settings, *sampling* of the object scene is conducted based on ray tracing methods provided by POV-Ray (see Chapter 5). For each signal detected in the scene the following information is derived:

- ◊ the 3D-position and signal amplitude corresponding to detected signal contributions,
- ◊ bounce level information for each detected signal,
- ◊ flags for marking specular directions, and

◇ intersection points for the identification of reflecting surfaces.

Based on output data provided by the ray tracer, the *scatterer analysis* is conducted for providing simulation products in two and three dimensions. Detailed information is given in Chapter 6).

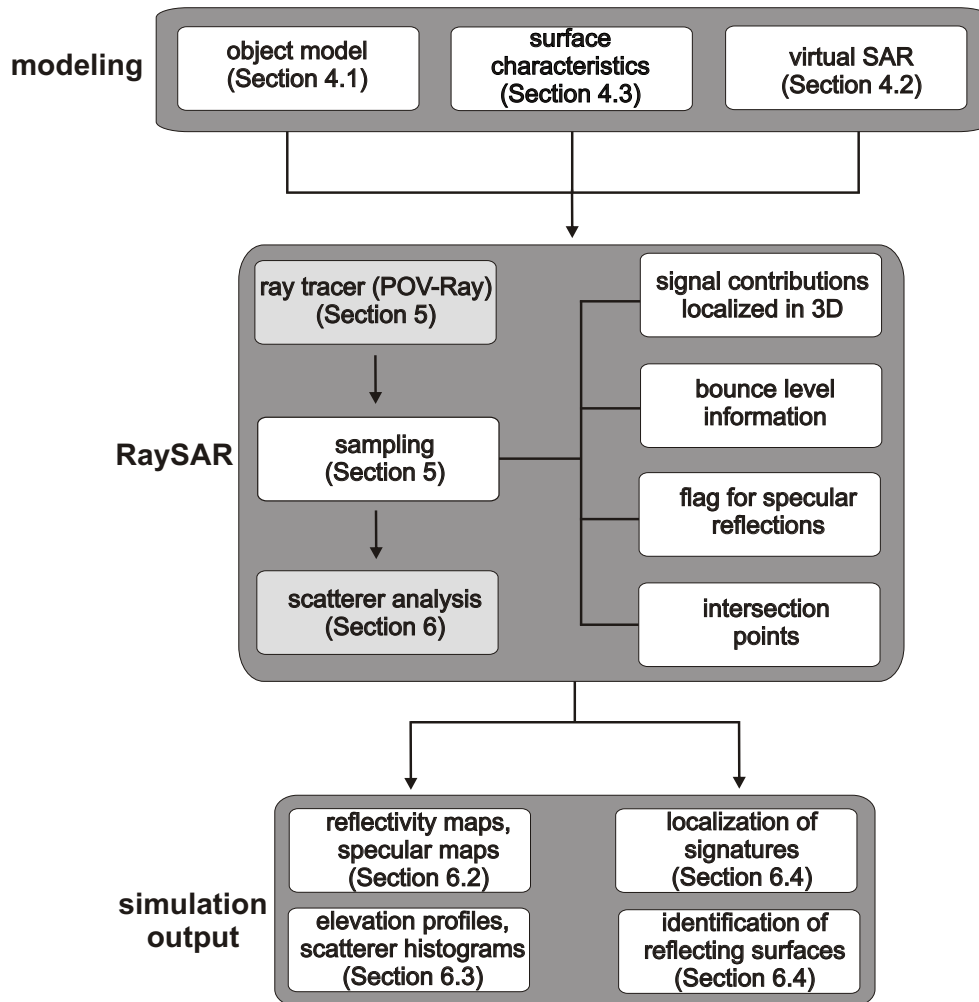


Fig. 15. Simulation concept of RaySAR: modeling - ray tracing - scatterer analysis.

## 4 Modeling - definition of 3D scenes

In advance to the ray tracing procedure, the object scene to be simulated has to be defined. To this end, the geometry of objects has to be represented by means of 2.5D or 3D models. Backscattering characteristics have to be assigned to all object surfaces for modeling the reflection of radar signals. Finally, the imaging geometry of the SAR system has to be defined in the coordinate system of the object scene. Details with respect to the different modeling steps are given in this chapter.

### 4.1 Data sources for 3D building models

Geometrical information about buildings can be provided on several ways, e.g. by own modeling or by importing available building models into the simulation environment. A brief introduction and discussion of different sources for building models is given in the following.

#### Modeling in POV-Ray editor

Modeling in the POV-Ray editor is reasonable for the simulation of basic shapes such as cubes, curved surfaces, or corners. Constructive solid geometry (CSG) may be appropriate in order to create objects characterized by specific geometrical shapes (Hoffmann, 1989). As main advantage of direct modeling in POV-Ray, simultaneous access to object coordinates, transformation parameters, camera parameters and render settings is provided. Hence, case studies for basic shapes can be conducted in a reasonable amount of time. In contrast, the major disadvantage is that modeling is performed in a text editor where objects are not visually displayed. Accordingly, the correctness of the object geometry can not be controlled in a CAD-environment and has to be checked by rendering images. Moreover, the time needed for modeling increases significantly when increasing the level of detail of objects.

From practical experience, the modeling capability of the POV-Ray text editor was helpful for controlling the correctness of the SAR simulation approach, e.g. the radar signal response corresponding to a corner reflector represented by three polygons. Moreover, fine tuning of the SAR imaging geometry and editing of surface parameters has to be conducted in the POV-Ray editor (see chapter B.2).

#### Modeling in CAD software

Compared to modeling in the POV-Ray editor, CAD software offers instant display of objects for visual controlling. Specific modeling tools for directly providing POV-Ray render files are available, e.g. Moray (Moray, 2011) or Wings3D (Wings3D, 2011). Generally, any object model to be simulated by RaySAR has to be integrated in the POV-Ray environment. Thus, object models created by using CAD software such as 3ds Max, Maya, or AutoCAD have to be transformed in the POV-Ray format.

With regard to the simulation approach, the creation of own building models of high detail by using CAD-software was not conducted. Basic shapes were modeled in the POV-Ray editor while buildings models of high detail were provided by partners. Even if the modeling of objects in CAD-software is much faster than in the POV-Ray editor, it is still very time consuming. Furthermore, detailed information about the geometry of objects has to be given a-priori, e.g. by architectural plans.

### Import of 3D models with free access

Building models of many popular buildings are available on the internet, either on homepages corresponding to building sights, e.g. the Eiffel tower (Eiffel, 2011) or on building data bases, e.g. Google<sup>TM</sup> 3D Warehouse (Google, 2011). When using these models as input for the SAR simulator, the modeling effort is reduced to the definition of the SAR imaging geometry and the adaptation of surface reflection characteristics in the POV-Ray editor.

However, significant drawbacks have to be mentioned at this point. The majority of downloadable 3D building models lack in reliability measures as no information is given about the creation of models and the accuracy of data sources. In most of the cases, building details are roughly approximated by a basic geometrical description, e.g. facades represented by flat polygons, imposed with 2D textures suggesting the 3D geometry of building features. Hence, from the radar point of view, the level of detail of most building models is low. Moreover, the access to specific model components is often limited and constant backscattering characteristics have to be selected for all surfaces. The transformation of common CAD model formats into the POV-Ray format may introduce changes to the model scene which can be avoided when directly modeling in the POV-Ray editor. Finally, the application of SAR simulation methods becomes opportunistic since the selection of test sites is driven by the availability and accessibility of 3D models.

To conclude, the application of free accessible 3D models with unknown correctness for SAR simulation is only reasonable for case studies. In this context, basic reflection phenomena can be investigated at objects having a moderate level of detail. In any case, reliable SAR simulation such as the analysis of reflection phenomena for selected SAR image pixels is not enabled.

### City models

The creation of city models is mostly initiated by city governments. Hence, these models are of special interest for SAR simulation since the reliability of data used for providing the building models is known. The level of detail ranges from 2.5D models characterized by flat walls to 3D models including facades details. Models of the latter case may especially serve simulation methods focused on the inversion of the SAR imaging process. Besides, the accessibility to model features may be enabled due to the given contact to the model provider, e.g. for assigning specific backscattering characteristics to different building parts. Hence, systematic radiometric errors can be reduced in combination with a high geometrical correctness of simulation results. While city models of moderate level of detail are developed for areas of large scale, building models of high detail are only available for selected and popular buildings. In this thesis, the analysis of reflection phenomena for selected SAR image pixels is based on detailed building models taken from city models.

### Creating models based on measured data

The data basis for the creation of building models can be provided by airborne and terrestrial laserscanning (LiDAR) or photogrammetry. Point clouds of high density are required for representing edges or curved surfaces characterizing building features. From practical experience, the extraction of facade information from data captured by airborne sensors is challenging due to data gaps, e.g. due to occlusion by vegetation or undersampling of small building features such as window structures or balconies. For testing the RaySAR simulation approach, building models have been created based on multi-aspect airborne LiDAR data captured by the RIEGL LMS-Q560 airborne laserscanner. While the creation of 2.5D building models was enabled without any complications, the full representation of facade details relevant for SAR simulation was impossible. In further studies, the fusion of airborne and terrestrial laserscanning data may be reasonable for solving this problem.



## 4.2 Design of the virtual SAR system

A real SAR system employs central perspective in elevation in combination with orthogonal scanning in azimuth. For spatially limited areas, e.g. individual buildings, and spaceborne geometry, the central perspective in elevation can be well approximated by orthographic projection. In other words, for a local scene located in the far field with respect to the SAR sensor, the wavefront can be assumed to be flat.

Using an orthographic projection offers several advantages: first, a 2-D orthographic camera type is readily available in POV-Ray. Second, the simulation results become independent of the spatial distance between the virtual SAR and the simulated object. Hence, zooming into the object to be simulated is enabled. Finally, an ideal SAR system can be simulated for detecting the positions of signal responses in azimuth, range, and elevation (see chapter 5.1). As main disadvantage, the simulation approach is bound to local scenes where the angle of incidence is assumed to be constant. Mapping errors in range depend on the difference between the assumed incidence angle and the true incidence angle and will increase when the simulated area is enlarged. For reducing the problem, urban areas of large scale may be split up into tiles whose simulated data are connected afterwards. In any case, mapping errors will occur and will be maximum at the seam lines between adjacent tiles.

Figure 16 summarizes the design of the virtual SAR system by means of a basic example where the object scene to be simulated is represented by two spheres. Instead of modeling the synthetic aperture by moving a virtual SAR, a static system is used for directly simulating SAR data. The imaging geometry and extent of the simulated area is defined using the parameters of the orthographic camera (see Appendix B.2). In case of a monostatic system, both the orthographic camera and the signal source are located at the same position in space. The POV-Ray sensor coordinate system and the coordinate system of the virtual SAR are linked as follows:

- ◊ the azimuth axis corresponds to the horizontal axis of the sensor plane.
- ◊ the elevation axis corresponds to the vertical axis of the sensor plane.
- ◊ the range axis is oriented perpendicularly to the sensor plane. Along this axis, depth information is provided by tracing rays.

The local incidence angle and the aspect angle with respect to the imaged object have to be known for adapting the SAR imaging geometry. The detection of shadow along all scan positions in azimuth is enabled by including a cylindrical light source emitting parallel light (see Appendix B.2). Constant signal illumination is guaranteed for all objects within the light cylinder.

## 4.3 SAR simulation radiometry

### 4.3.1 Reflection models for SAR simulation

The RaySAR models for the reflection of radar signals are based on reflection models given by POV-Ray (see Appendix B.2). To this end, the parameters of the POV-Ray models are adapted to approximate the reflection of radar signals. First, the radar signal emitted at a SAR system is represented by a vector containing normalized intensity values, i.e.  $color\ rgb < 1, 1, 1 >$ . Since SAR systems emit a single frequency signal, e.g. in X-Band, only one POV-Ray 'color' channel is required for SAR simulation. Instead of simulating continuous wavefronts, the radar signal is approximated by means of rays. The effect of surface colors on reflected signals is disabled by normalization, i.e.  $color\ rgb < 1, 1, 1 >$ . Moreover, textures of 3D object models are removed. Hence, signals detected by the ray tracer only depend on

- ◊ the imaging geometry with respect to the simulated object

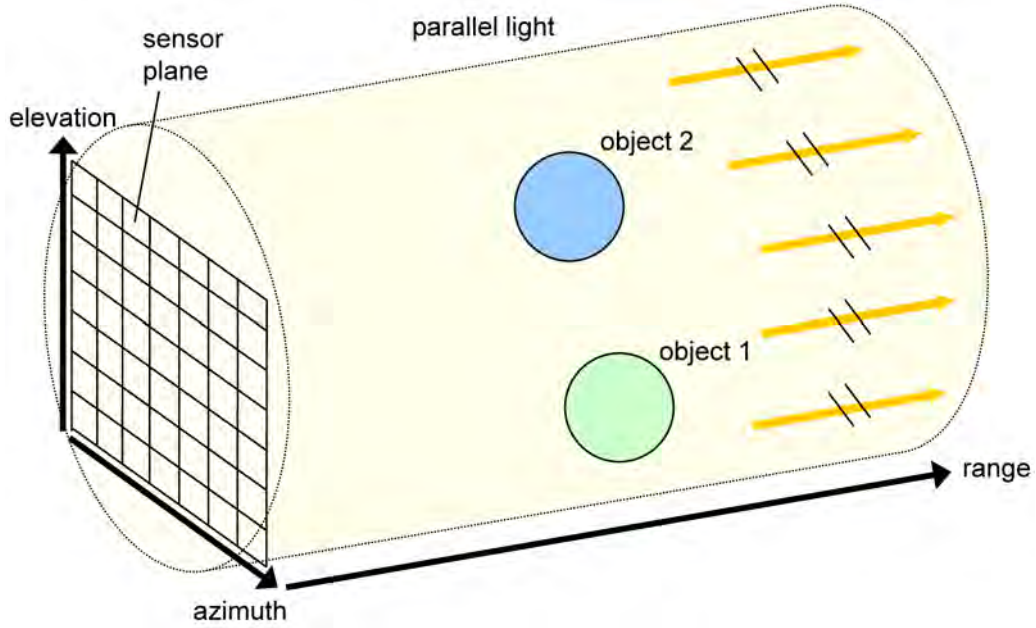


Fig. 16. Design of virtual SAR sensor: orthographic projection in azimuth and elevation for local scenes; parallel light for representing the radar signal.

- ◇ the combination of diffuse and specular reflectivity coefficients
- ◇ weight factors scaling the intensity of multiple reflections

In case of direct backscattering, the diffuse signal is derived by

$$I_d = F_d \cdot I_{sig} \cdot (\vec{N} \cdot \vec{L})^{F_b} \quad (14)$$

where

- ◇  $F_d$  is the diffuse reflection coefficient  $[0 \dots 1]$ ,
- ◇  $I_{sig}$  is the intensity of the incoming signal,
- ◇  $\vec{N}$  is the surface normal vector,
- ◇  $\vec{L}$  is the normalized signal vector pointing from the surface point to the SAR, and
- ◇  $F_b$  is a surface brilliance factor [default value: 1].

Complementary, the specular backscattered signal is derived by a reflection model for specular highlights which is

$$I_s = F_s \cdot (\vec{N} \cdot \vec{H})^{\frac{1}{F_r}} \quad (15)$$

where  $F_s$  is a specular reflection coefficient  $[0 \dots 1]$  and  $F_r$  is a roughness factor defining the sharpness of the specular highlight.  $\vec{H}$  is a bisection vector which is defined by  $\vec{N}$  and signal vector  $\vec{L}$  pointing in direction to the SAR (see Appendix B.2).

Signal polarimetry, signal diffraction at edges as well as media interaction are not accounted for. Moreover, the transmission of radar signals at surfaces, e.g. made of glass, is not considered so far. In this case, direct backscattering and multiple reflection of signals is disabled by setting the reflection coefficients and the weight factor for multiple reflection to zero. Overall, the radiometric correctness of equations 14 and 15 is expected to be only moderate since the original POV-Ray reflection models have been defined for simulating the reflection of electromagnetic signals in the visible spectrum. However, as mentioned before, this limitation was accepted

from the start for being able to simulate detailed object models with limited computing time. Simulation results, as shown in chapters 7 and 7.3, are provided in some minutes of computing time on a standard PC. A detailed discussion of the reflection models and a comparison to common radar reflection models is given in the following.

### 4.3.2 Comparison to radar reflection models

#### Specular reflection

The Fresnel reflection model, e.g. reported in Tsang and Kong (2001), is common for approximating the specular reflection of radar signals. In Appendix A, the corresponding formulas are given. Signal polarization and surface permittivity is considered. The geometrical component of the reflection model is described by

- ◇ the direction of the incoming signal and
- ◇ the normal of the surface being hit by the signal.

One reflection coefficient is calculated for a given reflection geometry with respect to an illuminated surface. The physical component of the reflection model is described by the surface permittivity and the signal polarization. For low permittivity, the strength of the reflection coefficient shows strong dependance on the incidence angle. As an example, figure 17 shows the distribution of the Fresnel reflection coefficient for a range of incidence angles from  $0^\circ$  to  $90^\circ$ . The illuminated surface consists of bare soil having a permittivity of  $5.7 + j \cdot 1.3$  in X-Band. For HH and VV polarization, the maximum coefficient is obtained for an incidence angle of  $90^\circ$ . The distribution of coefficients for VV polarization is characterized by a local minimum at approximately  $65^\circ$  which is called the *Brewster angle*. When simulating a surface of high permittivity (e.g. a real part of 80 for water having a temperature of  $20^\circ$  celsius), the dependance on the incidence angle is decreased.

In contrast to the Fresnel reflection model, the RaySAR model for specular reflection (equation 15) not only provides signal contributions in specular direction. Instead, each signal is represented by a specular highlight (see Appendix B.2) which may be interpreted as a combination of a peak in specular direction surrounded by diffuse components of high intensity. An example for a specular highlight is given on the right of figure 18. The geometrical component of the reflection model requires

- ◇ the direction vector of the incoming signal,
- ◇ the direction vector of the ray followed by the raytracer, and
- ◇ the normal vector at the surface being hit by the signal.

The physical component is limited to the specular reflection coefficient, a value between 0 and 1, for considering signal absorption at surfaces. In contrast to the Fresnel reflection model, the angular dependance of the reflection coefficient on the surface permittivity and signal polarization is not considered. In Table 2, the main differences between the RaySAR model for specular reflection and the Fresnel model are summarized. To conclude, the best simulation results are expected for SAR data captured in HH polarization, where no Brewster angle effect occurs, and for object surfaces characterized by high permittivity.

#### Diffuse reflection

In case of diffuse reflection of radar signals, the Small Perturbation Method (SPM) (Tsang and Kong, 2001) is applicable for surfaces whose roughness is small compared to the signal wavelength. Hence, the SPM is assumed to be appropriate for cross-comparison to the RaySAR model for diffuse reflection, as most surfaces on urban buildings are characterized by low roughness. Basics on the SPM are given in Appendix A. The geometrical component of the SPM is characterized by

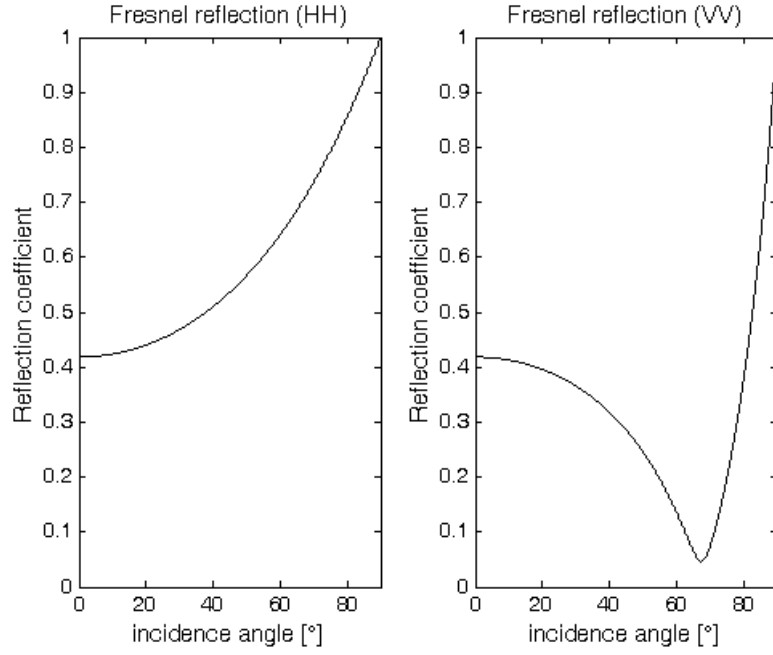


Fig. 17. Simulation example showing the specular reflection of a radar signal at bare soil (Fresnel reflection model). Left: result for HH polarization. Right: result for VV polarization.

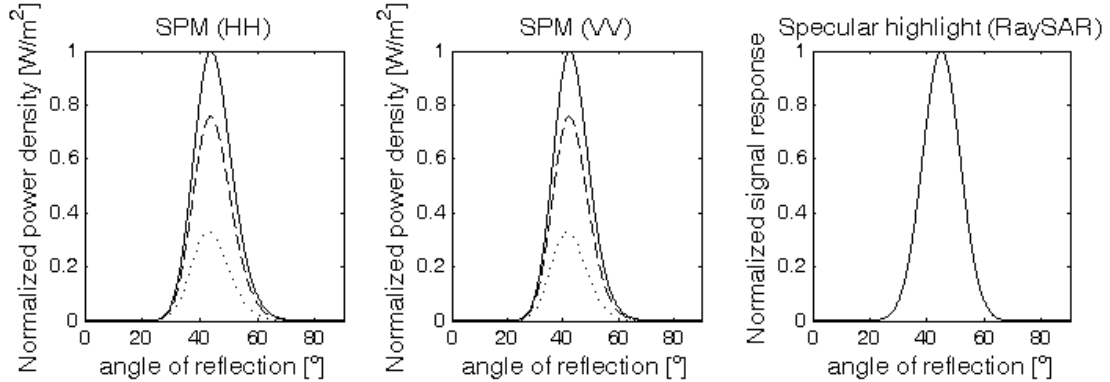


Fig. 18. Comparison of the SPM and the RaySAR model for specular reflection. Incidence angle of the incoming signal:  $45^\circ$ . Left: distribution of power density for bare soil in HH polarization. Continuous line: reflection direction within the incident plane. Dashed line: reflection direction rotated by  $5^\circ$ . Dotted line: reflection direction rotated by  $10^\circ$ . Center: distribution of power density for bare soil in VV polarization. Right: signal simulated by RaySAR reflection model for specular reflection.

- ◇ the direction vector for the incoming signal,
- ◇ the normal vector of the surface being hit by the signal, and
- ◇ the vector describing the direction where the diffuse reflection has to be evaluated.

In addition, the surface roughness is parameterized by the surface standard deviation and the surface correlation length. The physical component of the SPM is equal to that of the Fresnel reflection model. When evaluating diffuse components, the area of illuminated surfaces is considered as well as the fading of signals over distance.

In figure 18, the simulated power density is shown for a radar signal which is diffuse reflected at bare soil. The simulations are provided in HH and VV polarization. The surface being hit by the radar signal is characterized by a standard deviation of 0.4 cm, a correlation length of 8.4 cm, and a permittivity of  $5.7 + j \cdot 1.3$ . The local angle of incidence is  $45^\circ$ . In HH and VV

	<b>Fresnel reflection model</b>	<b>RaySAR model for specular reflection</b>
Model output:	reflection coefficient corresponding to specular direction	highlight surrounding specular direction
Geometrical component represented by:	direction of incoming signal, surface normal	direction of incoming signal, surface normal, ray followed by raytracer
Physical component represented by:	surface permittivity, signal polarization	constant reflection coefficient

Table 2. Comparison of Fresnel reflection model and RaySAR model for specular reflection.

polarization, the maximum of diffuse reflection is derived in near-specular direction (continuous line) which is located within the incident field. When rotating the reflection direction out of the incident field, the power density of the diffuse signal decreases significantly (dashed line:  $5^\circ$ , dotted line:  $10^\circ$ ).

The basic POV-Ray model for diffuse reflection was developed under the assumption that most scatterers can be considered as being of Lambertian type. Hence, the geometrical component is only described by the angle of incidence of the incoming signal with respect to the surface normal. Accordingly, the power of diffuse components is independent from the direction to be analyzed. The physical component is limited to a diffuse reflection coefficient which only enables to consider the absorption of radar signals, i.e. a factor for scaling the diffuse signal response. In contrast to the SPM, signal polarization is not considered. Moreover, the extent of the illuminated area is not required since discrete sampling is applied. In Table 3, the main differences between the RaySAR model for diffuse reflection and the SPM are summarized.

Unfortunately, most surfaces in urban areas do not show Lambertian reflection characteristics. For most man-made objects, the strength of diffuse reflected radar signals depends on the direction of reflection. For direct backscattering of radar signals, the RaySAR model for diffuse reflection enables to consider the dependance on the reflection direction. The reason is that only one discrete position of the SPM has to be represented. However, strong overestimation of the diffuse signal response is expected in case of multiple reflections, i.e. when a radar signal coming from the SAR antenna is diffusely scattered into the modeled scene and thereafter specular reflected in direction to the SAR sensor.

An alternative solution for approximating the diffuse reflection of radar signals is given by the model for specular highlights. More specifically, the RaySAR model for specular reflection can be used for simultaneously approximating the specular and diffuse component of a radar signal. Strong specular reflection can be represented by choosing a high specular reflection coefficient. The distribution of diffuse components can be represented by choosing an appropriate value for the roughness factor in equation 15. On the right side of figure 18, the RaySAR reflection model for specular reflection is used for approximating specular and diffuse components. While the power of the diffuse signal response is much overestimated compared to results from the SPM,

the dependance of the diffuse reflection of radar signals on the direction of reflection is well represented.

	<b>SPM</b>	<b>RaySAR model for diffuse reflection</b>
Model output:	diffuse scattering surrounding specular direction	angular independent scattering
Geometrical component represented by:	direction of incoming signal, surface model, direction of reflection	surface normal, ray followed by raytracer
Physical component represented by:	surface permittivity, signal polarization	constant diffuse reflection coefficient

Table 3. Comparison of Small Perturbation Method (SPM) and the RaySAR model for diffuse reflection.

### 4.3.3 Evaluation of POV Ray reflection models

Overall, the reliability of the radiometric information provided by the RaySAR reflection models is assumed to be moderate due to the limitations discussed above. However, this is not a major problem since the SAR simulation concept does not aim at providing realistic copies of SAR data. From the radiometrical point of view, a rough approximation of common radar models by means of the RaySAR models is enabled. The angular dependance of reflection is covered by the RaySAR model for specular reflection.

Generally, the overestimation of diffuse signal responses is preferred to underestimation. If the geometry of a building feature is represented by the 3D model of the scene, the SAR simulator will tend to emphasize SAR image signatures corresponding to diffuse reflections. Including enhanced reflection models may improve the radiometry of simulation results. However, these models are expected to be very sensible to the choice of surface parameters. Signatures, visible in the real SAR data, may be underestimated or even missing in the simulated SAR image, which is considered as the worst case scenario.

Choosing the appropriate specular reflection coefficient for the simulation of urban objects is challenging. Based on simulation results using the Fresnel reflection model (see figure 17), a value of 0.7 is chosen for standard simulation while a coefficient close to 1 is used when specular multiple reflections shall be simulated without loss of amplitude. For any surface, the sum of specular and diffuse reflection coefficients should be at most 1. Otherwise, the strength of the radar signal would be increased when impinging on the surface.

When simulating diffuse reflections of radar signals at objects, the level of detail of the object model is crucial. In other words, the parameters of the RaySAR reflection models have to be adapted to the 3D object model at hand. The RaySAR reflection model for diffuse reflection should be only applied if the object model lacks of details or if only the simulation of single

bounce is of interest. Thereby, the shape of objects represented by flat surfaces can be made visible in the the azimuth-range plane. Moreover, shadow maps can be provided.

In case of detailed 3D object models, the RaySAR model for specular reflection should be used for the reliable representation of multiple reflections. For VHR SAR systems in X-Band, the expression 'detailed' is linked to the following precondition: when simulating an object, all trihedrals having a sidelength of larger than 10 cm have to be represented in the 3D object model. If object surfaces show little roughness compared to the signal wavelength (3.1 cm in X-Band), a rough approximation of the SPM model is enabled. To this end, the roughness parameter of the specular highlight model has to be chosen appropriately for each surface in order to model the angular dependance of signal reflection. For instance, the diffuse backscattering displayed in figure 18, simulated for bare soil having a surface standard deviation of 0.4 cm and a surface correlation length of 8.4 cm, can be approximated by using a roughness factor of  $3.3 \cdot 10^{-3}$ . When using the SPM, the power densities larger than  $0.05 \frac{W}{m^2}$  cover an angle interval of approximately  $32.8^\circ$  and  $31.6^\circ$  in HH and VV, respectively. The RaySAR model for specular reflection yields signal responses covering an angle interval of  $32.2^\circ$ . When reducing the surface standard deviation to 0.1 cm and doubling the surface correlation length of 16.4 cm, the roughness factor may be chosen as  $8.5 \cdot 10^{-4}$ . Then, the SPM power densities larger than 0.05 cover an angle interval of  $16.5^\circ$  and  $16.3^\circ$  for HH and VV, respectively. The main lobe of the radar signal simulated by the RaySAR model for specular reflection is located within an angle interval of  $16.4^\circ$ . Table 4 gives a short summary for the setting of surface parameters in RaySAR. For man-made objects, a constant permittivity of  $5.7 + j \cdot 1.3$  is chosen for ground surfaces and buildings.

The simulation of signal interactions with objects and the surrounding ground is not straightforward. In most cases, the ground has to be represented by a flat plane where no diffuse signal would be detected when using the parameters given by Table 4. When using the RaySAR model for diffuse reflection, the assumption of Lambertian backscattering will cause strong overestimation of multiple reflections where ground is involved. A good compromise may be using a high roughness value for the reflection model for specular highlights, e.g. 0.3, in combination with a decreased specular reflection coefficient, e.g. 0.3, in order to enable direct backscattering of radar signals from the ground in combination with angle dependent multiple reflections. In any case, geometrical information is needed for reliable simulation of ground surfaces.

To conclude, any definition of reflection parameters can only provide a rough approximation of real signal reflections. Especially, appropriate setting of the reflection coefficients and, hence, the absorption of radar signals is hard to be realized. Hence, limitations in the representation of SAR image radiometry have to be accepted. However, the geometrical component of specular and diffuse reflection of radar signals can be considered. This is of major importance since the development of RaySAR is focused on simulating the geometrical distribution of signal responses.

## 4.4 Modeling step - summary

In this chapter, the modeling of 3D object scenes has been addressed from three aspects: the definition of 3D object models, the definition of the virtual SAR system, and the definition of radar reflection models.

The modeling of geometrical shapes can be performed in the POV-Ray editor. In contrast, modeling of detailed objects is very time consuming and requires knowledge about the origin of data. Hence, when applying RaySAR to real SAR data, the simulation of objects is focused on available object models of known origin.

The virtual SAR system is represented by an orthographic camera in azimuth and elevation.

	Low roughness	Medium roughness
Surface geometry:	Surface standard deviation: 0.1 cm, Surface correlation length: 16.8 cm	Surface standard deviation: 0.4 cm, Surface correlation length: 8.4 cm
Specular coefficient (RaySAR):	0.7	0.5
Weight for specular reflection (RaySAR):	0.7	0.5
Roughness parameter (RaySAR):	$8.5 \cdot 10^{-4}$	$3.3 \cdot 10^{-3}$

Table 4. Definition of surface parameters for angular-dependent diffuse signal reflection from bare soil (permittivity:  $5.7 + j \cdot 1.3$ ).

Zooming into the SAR scene is possible in order to simulate object parts of interest. However, the extent of the simulated scene is limited due to the assumption of a flat wavefront in the far field.

POV-Ray reflection models, originally developed for rendering optical images, have been adapted for simulating the specular and diffuse reflection of radar signals. The dependance of the specular reflection of radar signals on surface materials, as shown by simulations using the Fresnel reflection model, is not supported. Hence, considering the absorption of specular reflections is not straightforward. Lambertian backscattering is assumed for the RaySAR model for diffuse reflection. Hence, the model is appropriate for simulating direct backscattering and for representing the extent of layover and shadow. The simultaneous application of the specular and diffuse reflection model will cause strong overestimation of diffuse multiple reflections. The reason is that the angular dependance of diffuse signal response is not considered. In contrast, the RaySAR reflection model for specular reflection enables to simulate diffuse signal responses as well. The model can be adapted to the Small Perturbation Method (SPM) if the surface roughness is small compared to the signal wavelength.

For surfaces of little roughness, parameters have been defined for adapting the RaySAR model for specular reflection to the results from the SPM. To this end, the permittivity of dry ground has been assumed for surfaces in urban areas. The angular-dependance of the diffuse reflection of radar signals can be considered at the cost of an overestimation of the corresponding signal strength. Using specific radar models instead of simplified models may be reasonable. However, the definition of the surface parameters is expected to be sensible to the underestimation of diffuse signal responses, which is considered as the worst case for the geometrical analysis of SAR image signatures.



## 5 Sampling - extraction of data in SAR geometry

In the preceding chapter, the necessary modeling steps for providing a scene for SAR simulation have been introduced. Next, ray tracing methods are applied for providing output data in SAR geometry. In this chapter, the application of the ray tracing algorithm to SAR simulation is introduced followed by a discussion of potentials and limitations of the simulation concept. When evaluating the approach, the main focus is on the simulation of multiple reflected signals.

### 5.1 Extraction of geometrical information

#### 5.1.1 Detection of reflection contributions

At this point, the 3D object to be simulated has been integrated into the POV-Ray environment where reflection parameters have been defined for all surfaces. Ray tracing means sampling the 3D object scene based on pixel centers located in the sensor (image) plane, which form a regular raster in azimuth and elevation. Before starting the rendering process, the number of samples within the SAR sensor plane has to be defined. The positions of signatures in range depend on the imaging geometry with respect to simulated objects and, hence, are expected to be irregular distributed.

Ray tracing is performed in an iterative manner for each pixel within the sensor plane. Moreover, ray tracing is conducted in reverse direction, i.e. starting at the sensor and ending at the signal source. Tracing a single ray is continued as long as

- ◇ the maximum reflection level has not been reached. For the RaySAR simulator, the chosen threshold is 5.
- ◇ the ray's weight, representing the brightness of multiple reflected signals, does not fall below a chosen threshold.
- ◇ scene objects are intersected. Otherwise, the ray leaves the scene without yielding any further signal contributions.

The search of signal contributions is conducted for each pixel in the sensor plane. Figure 19 shows the ray tracing procedure for the double reflection of a radar signal within an object scene containing two spheres. At a pixel center, located at azimuth position  $x_p$  and elevation position  $s_p$ , a *primary ray* is created perpendicularly to the image plane of the orthographic sensor. The ray is followed along its way to the object scene where an intersection point #1 is detected at object 1. If the number of detected intersection points is larger than 1, the shortest distance to the SAR sensor marks the object visible to the SAR. At the corresponding intersection point, three rays are created:

- ◇ one ray pointing in direction to the signal source. If that ray is interrupted by another scene object, intersection point #1 is not directly illuminated by the signal source and, hence, is situated in the shadow.
- ◇ one ray transmitting the object surface. Originally, this ray has been introduced for simulating liquids or glass in optical images. In case of SAR simulation, this ray is neglected since the majority of urban surfaces is not expected to be penetrated by radar signals in X-Band.
- ◇ one *secondary ray* pointing in specular direction. This ray is constructed based on the incoming ray and the surface normal at the intersected surface. The basic assumption is that dominant signal contributions will come from this direction. Ray tracing is continued in that direction.

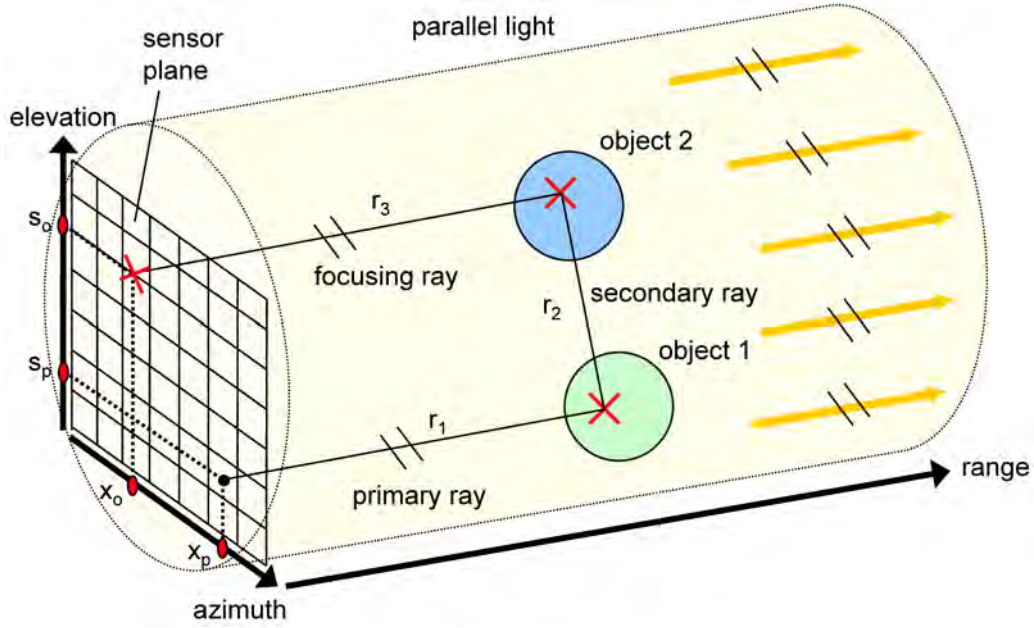


Fig. 19. Localization of signal contributions by means of RaySAR for the double reflection of a radar signal. Rays are followed in reverse direction ( $r_1 \rightarrow r_2 \rightarrow r_3$ ), i.e. starting at the SAR sensor and ending at the SAR antenna.

If intersection point #1 is situated in the shadow, no signal is detected. Otherwise, the signal amplitude is calculated using the RaySAR reflection models described in chapter 4.3. Furthermore, a decision is made whether the current reflection process at the intersection point #1 is of type 'specular' or not. To this end, the reflection geometry at intersection point 1 is analyzed (see chapter 5.1.4). Eventually, the 3D coordinates of a radar signal backscattered from object #1 are:

$$\begin{aligned} x_s &= x_p \\ r_s &= r_1 \\ s_s &= s_p \end{aligned} \tag{16}$$

The search for a double reflected signal is started by following the secondary ray which intersects object 2 (intersection point #2). Again, a shadow test is conducted. Given the SAR antenna as signal source, the amplitude of the signal reflected in direction of the secondary ray is calculated and weighted using the reflection coefficient assigned to object 1. The analysis for specular/non-specular reflection is performed locally at intersection point #2 since the secondary ray has been already defined in specular direction. For providing the coordinates of the double bounce process, a ray parallel to the primary ray has to be created at intersection point #2. In the following, this ray is referred to as *focusing ray*. The intersection point between the focusing ray and the planar signal source determines the origin of the radar signal at the virtual SAR and is found in the world coordinate system of the simulated object model. This point is not related to the antenna of a real SAR system (see chapter 4.2). Instead, the signal origin is a mean for simulating the 3D position of multiple reflected radar signals. To this end, the coordinates of the signal origin are transformed into the image coordinate system of the virtual sensor (see cross at  $x_0$  and  $s_0$  in figure 19), what is possible due to the known sensor position and line-of-sight. Thereafter, the azimuth, range, and elevation coordinate of the double reflected radar signal is derived by

$$x_s = \frac{x_0 + x_p}{2} \tag{17}$$

$$r_s = \frac{r_1 + r_2 + r_3}{2} \quad (18)$$

$$s_s = \frac{s_0 + s_p}{2} \quad (19)$$

A detailed discussion of these equations is provided in chapter 5.1.2 and 5.1.3. The search for triple reflections is continued after the definition of a new secondary ray at intersection point #2, which is not displayed in figure 19. In case of an intersected object, another focusing ray is needed for finding the coordinates of the triple bounce signal. Eventually, output information is gathered for each detected radar signal and stored in a *signal vector*, which is

$$S_s = \begin{bmatrix} x_s & r_s & s_s & A_s & b_s & f_s & X_i & Y_i & Z_i \end{bmatrix} \quad (20)$$

where

- ◇  $x_s$ ,  $r_s$ , and  $s_s$  describe the position of the signal phase center.
- ◇  $A_s$  is the amplitude of the detected signal [normalized value between 0 and 1].
- ◇  $b_s$  is the bounce level corresponding to the detected signal, e.g. 1 in case of single bounce.
- ◇  $f_s$  is a flag for marking specular reflections [0 for non-specular, 1 for specular] (see chapter 5.1.4).
- ◇  $X_i$ ,  $Y_i$ , and  $Z_i$  are the coordinates of the detected intersection point. The position of the point is captured optionally in order to identify the reflecting surfaces contributing to a salient SAR image signature (see chapter 6.4.2).

In case of  $n$  signal contributions,  $S_s$  is extended to a *signal matrix* of size  $n \times 6$  where different signal contributions are organized in rows.

RaySAR simulates a non-squinted SAR. For direct backscattering from objects, the signal response is found at the zero doppler position along the synthetic aperture. Instead of simulating the spatial resolution of signatures, only the position of the amplitude peak is simulated in the azimuth-range plane. Hence, the *geometrical resolution* of the virtual SAR system is infinite, i.e. a trihedral is focused at one point in space. By purpose, the dependance of SAR products on the number and distribution of samples or the length of the synthetic aperture in azimuth and elevation is not considered. In contrast, phase centers are directly simulated assuming a static SAR system. Discrete sampling by means of the ray tracer enables the simulation of analytical shapes, e.g. a sphere defined by one point and a radius, but also causes disadvantages. Signal contributions are represented by vector data which have to be rasterized in order to provide SAR images. Since the ray tracer can be considered as a kind of scanner, the spatial resolution of the SAR simulator has to be chosen appropriately. In this context, the expression 'spatial resolution' refers to the level of object detail represented by the resulting point cloud (Lichti, 2004). While surface information is well represented by means of point patterns, the simulation of edges is moderate due to discrete sampling of a continuous structure.

The simulation of detailed 3D models is enabled by neglecting physical effects affecting the signal interaction with objects, such as signal diffraction at edges or creeping waves on metallic surfaces. However, for signals in X-Band, these effects are expected to be much weaker than specular reflections, which are of main interest in this thesis. Moreover, the majority of signal reflections are expected to occur in the optics region (object size  $> 10$  times the signal wavelength) where physical surface effects are minimal (Knott et al., 2004).

### 5.1.2 Focusing in azimuth

Real SAR data are derived by processing raw data captured along the synthetic aperture in azimuth. The corresponding processing effects have to be accounted for when simulating the

geometrical distribution of signatures. In this chapter, the potentials and limitations of RaySAR with regard to the approximation of azimuth focusing are discussed.

When simulating direct specular or diffuse backscattering from objects, the azimuth coordinate of the radar signal is equal to the azimuth coordinate of the primary ray. In case of specular reflected signal of higher bounce levels, the simulation is based on experimental results for corner reflectors (see chapter 2.1.4). A SAR system images a trihedral corner reflector as a single point target even if the physical size of the trihedral is larger than the spatial resolution of the SAR. Hence, the signal peak corresponding to a trihedral reflector is always located within one resolution cell. In RaySAR, the concept of the focusing ray has been introduced for considering this processing effect. In other words, the azimuth coordinate of the primary ray has to be adapted by an *azimuth correction* (see equation 17). Eventually, RaySAR focuses the signal response of a trihedral at one single point. In chapter 6, simulation results are presented in order to confirm the geometrical correctness of the simulation approach for a corner reflector. For dihedral reflectors facing the sensors line-of-sight, the calculation of azimuth coordinates can be performed the same way than for trihedrals. However, no azimuth correction is required since the secondary ray is located within the incident field of the primary ray. In contrast, equation 18 has to be used for calculating the range coordinate of all kinds of double bounce signals.

As explained in chapter 5.1.1, ray tracing is focused on specular reflections. Nonetheless, the diffuse reflection of a signal is analyzed at each intersection point detected within the modeled scene. The SAR simulator allows for the localization of diffuse signal contributions occurring due to the combination of one diffuse and several specular reflections. Comparable to specular contributions, equations 17 and 18 are also applied for focusing diffuse signal contributions in azimuth and range. To the knowledge of the author, experiments on the focusing of diffuse signal responses are not reported in the literature. Therefore, a case study is presented in order to discuss the applicability of equation 17 for the localization of diffuse signal responses.

### Case study on azimuth focusing

Consider a wedge, having a width and height of 100 m and being composed by two surfaces orthogonal to each other, which faces the line-of-sight of a virtual SAR. The squint angle of the virtual SAR is  $0^\circ$ . Both surfaces of the wedge are specular reflectors and are represented by a grid of points (see red and blue spheres in figure 20a). The ground surrounding the wedge, indicated by a gray surface, is assumed to be flat and of Lambertian type, i.e. diffuse signal responses are expected all over the synthetic aperture of the virtual SAR. The look angle of the SAR with respect to the wedge is  $40^\circ$ . A pulse repetition frequency of 4000 Hz is assumed in combination with TerraSAR-X parameters given in Table 1. For this case study, the earth curvature and rotation are neglected. According to the given imaging geometry, the length of the synthetic aperture in azimuth is 2.8 km providing approximately 1500 samples for each scatterer. Due to the large spatial distance between the edge and the radar antenna in space, the incoming signal is assumed to have a flat wavefront in azimuth and range direction when hitting the wedge on the earth surface.

Along the virtual SAR, signal contributions are detected due to the interaction of the emitted signal with the points on the wedge surface and the surrounding ground. At this point, the focus is on a reflection process where the incoming signal is specular reflected at a wedge point (marked by letter *A* in figure 20a) and diffusely reflected from a ground point or vice versa. Two reflection processes of that kind are visualized in figure 20a, marked by green and black color. The area of reflection on the ground will slightly change along the synthetic aperture what is indicated by the spatial distance between the ground points *B* and *B'*. In the following, all reflecting ground points along the synthetic aperture are referred to as point *B*.

For each reflection process, signals may follow both directions of a two-way system, i.e. *ground*

$\rightarrow \text{wedge} \rightarrow \text{sensor}$  or  $\text{wedge} \rightarrow \text{ground} \rightarrow \text{sensor}$ . The main signal contribution to the range history of the double reflection process will be detected as long as both scatterers  $A$  and  $B$  are simultaneously illuminated by the SAR antenna beam, i.e. as long as the two-way system is enabled. For the case study at hand, the majority of reflection processes is not located in the incident field of the signal and, hence, the illumination periods for points  $A$  and  $B$  are different. Only at the edge of the wedge, the double reflection of signal appears within the incident field. In theory, after the processing of SAR raw data, the azimuth coordinate of the corresponding double bounce signal is found at the center of the range history captured during the shared illumination period  $t_{AB}$  of points  $A$  and  $B$ . At this position, the range history pertinent to the double reflection process reaches its minimum. Figure 20b shows the distribution of the diffuse signal response when simulating the virtual synthetic aperture in azimuth. Two lines are visible which represent the orientation of the wedge surfaces. The length of the lines is larger than the length of the corresponding wedge surfaces due to the difference in illumination time for points  $A$  and  $B$  and due to the Lambertian backscattering behavior of the ground. Direct backscattering of the wedge surface is neglected. Hence, no layover area can be distinguished.

If the reflection behavior of wedge and ground was changed to 'diffuse' and 'specular', respectively, the length of lines would represent the length of the corresponding wedge surfaces. Any signal contribution would require specular reflection from the ground in front of the wedge and diffuse reflection from the wedge surfaces, i.e. for any signal response, points  $A$  and  $B$  would be located in the incident field of incoming radar signal. Accordingly, no difference in illumination time would occur for points  $A$  and  $B$ .

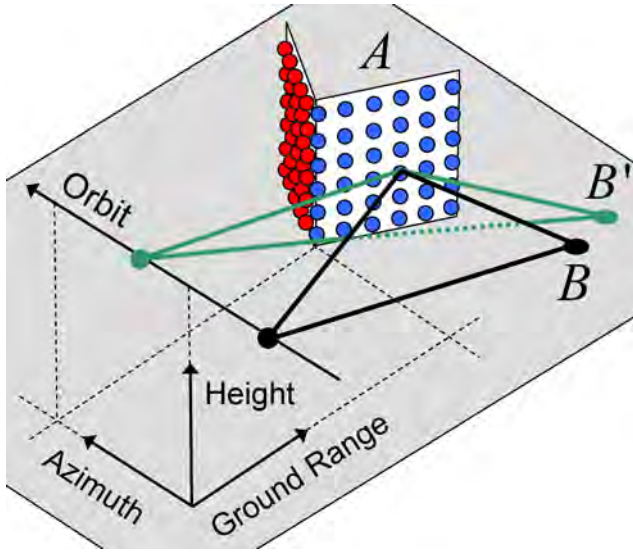
RaySAR performs a direct simulation of signal responses in the azimuth-range plane. The principle for locating double reflected signals at the wedge is shown in figure 21a. The line-of-sight of the orthographic SAR system is perpendicular to the sensor plane. Primary rays are emitted at each pixel, defined along the axes  $u$  and  $v$ , orthogonally to the sensor plane. For the case study, the position of pixels is chosen equal to the position of surface points on the wedge. Following the ray along its path reveals an intersection point on the ground whose position in azimuth is detected with sub-pixel accuracy. Afterward, the azimuth coordinate of the double bounce signal is calculated by taking the mean distance between the azimuth coordinate of the pixel and the azimuth coordinate of the intersection point on the ground. The geometrical distribution of the simulated signal response from the wedge is presented in figure 21b.

When comparing the simulation result based on the virtual SAR to the result from direct simulation – as provided by RaySAR – the difference in the simulation of range coordinates is negligible. In contrast, the differences in azimuth range from 0 m to  $\pm 0.8$  m (see figure 22a). Increasing the pulse repetition frequency (PRF) of the virtual SAR, e.g. to 8000 Hz, the differences are reduced significantly (see figure 22a). RaySAR simulates an SAR system which is not affected by effects occurring due to discrete sampling along the synthetic aperture.

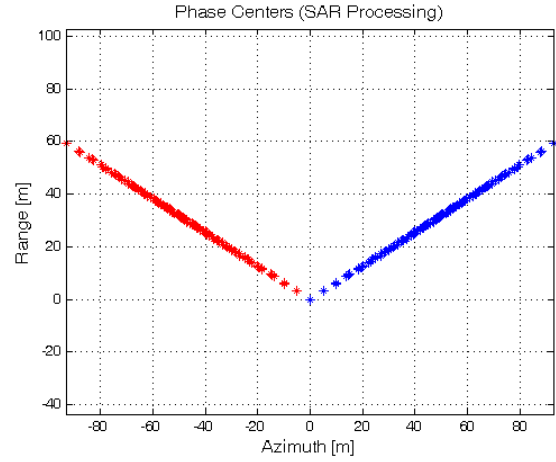
## Discussion of azimuth focusing

Azimuth focusing effects have to be accounted for when simulating VHR SAR data. In this context, the *area of reflection*, i.e. the area covered by a multiple reflection process at the earth surface, is of main importance. For the case study shown before, the area of reflection is described by the interaction of the radar signal with two wedge surfaces and the adjacent ground. After sampling of the scene, the simulated vector data have to be rasterized in order to derive a SAR image in the azimuth-range plane. When neglecting the azimuth focusing effects discussed in chapter 5.1.2, no errors occur if the area of reflection is assigned to one resolution cell. In contrast, simulated images are erroneous if the area of reflection covers more than one SAR image pixel.

With regard to the RaySAR simulation concept, no azimuth correction is required if the first and last signal reflection occur within the incident field, e.g. in case of double reflection at a

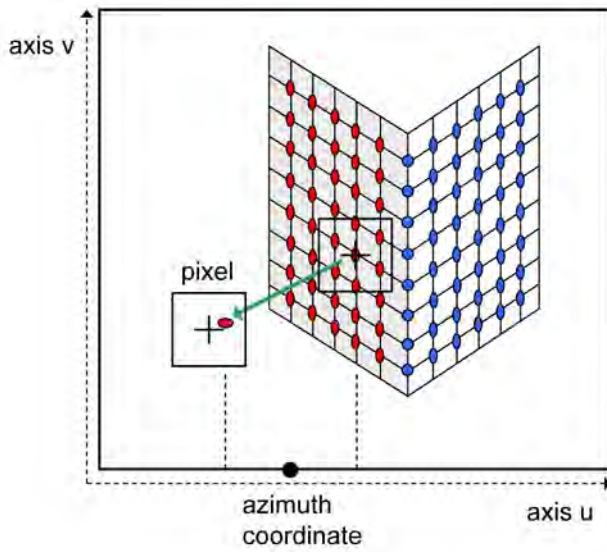


(a) Simulation of the synthetic aperture

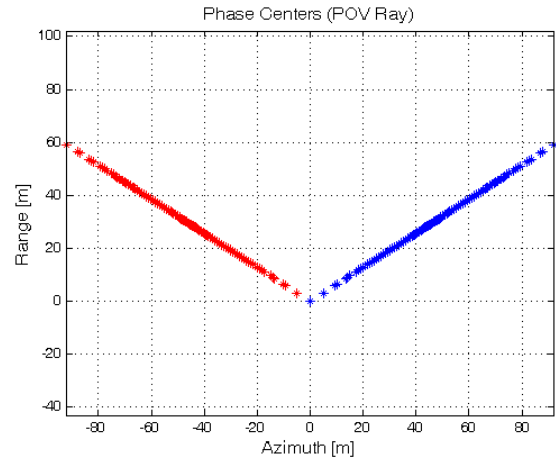


(b) Distribution of target response (synthetic aperture); Double bounce contribution with smallest distance to the SAR defines range coordinate 0 m.

Fig. 20. Simulation of diffuse double bounce for a virtual SAR. The wedge is composed by two specular surfaces which are represented by point patterns (red and blue spheres). Lambertian reflection is assumed for ground points  $B$  and  $B'$ .



(a) Simulation using RaySAR concept; secondary ray indicated by green arrow



(b) Distribution of the target response (RaySAR); The double bounce contribution with the smallest distance to the SAR defines range coordinate 0 m.

Fig. 21. Simulation of diffuse double bounce using the RaySAR concept. Primary rays are defined orthogonally to the image plane. For the scattering process at hand, the azimuth coordinates are located at half the distance between the origin of the primary ray and the azimuth position of the intersection point detected at the ground.

wall oriented in line-of-flight of the SAR sensor. For a detected signal, the amount of azimuth correction increases with the distance between

- ◇ the azimuth coordinate of the pixel where the primary ray was started, and
- ◇ the current intersection point detected on an object by following the ray.

For the wedge example, the main factors influencing this distance are the orientation and height of the wedge. With regard to man-made objects, the wedge may be well taken for characterizing the basic shape of building walls. Linear signatures are likely to appear when imaging building walls in VHR SAR data. If the linear features are longer than the footprint of

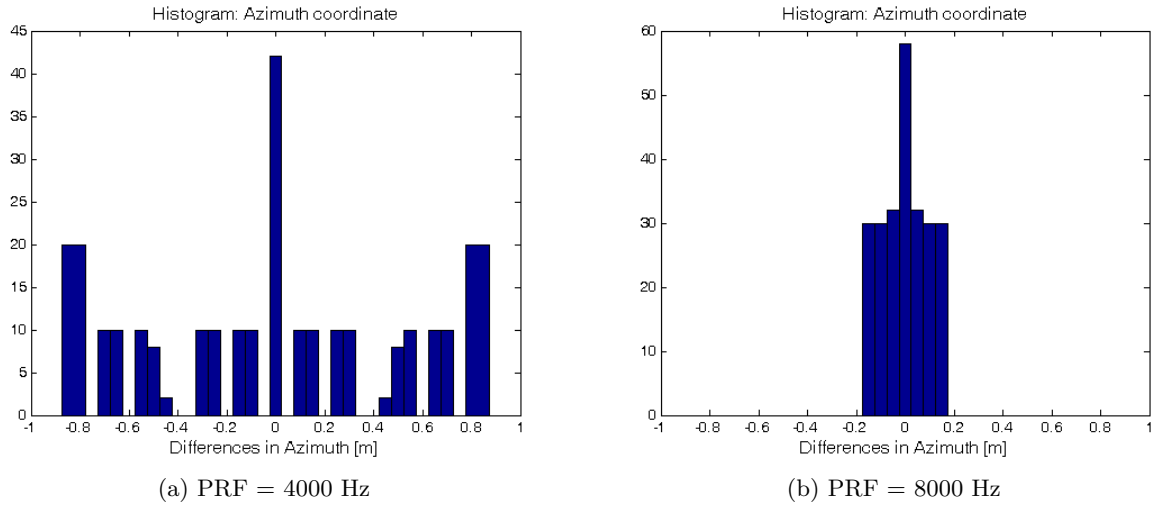


Fig. 22. Azimuth differences between direct simulation (RaySAR concept) and the simulation of the synthetic aperture for different PRFs.

the building wall, the ground surrounding the building will be of Lambertian type. In contrast, the linear signatures will correspond to the footprint of building walls if the ground surface is a angular dependent diffuse reflector or a specular reflector of the radar signal. Then, diffuse backscattering characteristics are required for the building walls in order to derive a visible line in the SAR image.

As shown in chapter 5.1.1, RaySAR locates specular and diffuse multiple reflected radar signals with infinite resolution. Differences in the curvature and length of the range history corresponding to a scatterer are not considered. Thus, defocusing effects affecting diffuse signal responses are not be accounted for. The blurring of diffuse signal contributions may be roughly approximated by convolving simulated data with an adapted *sinc*<sup>2</sup>-function. However, this would only be an artificial effect without any link to the geometry of the imaging process. Overall, the azimuth position of simulated diffuse signal responses is expected to be of lower correctness than for specular signal responses. Nonetheless, as confirmed by the case study, RaySAR enables to provide an approximate solution.

### 5.1.3 Focusing in elevation

A complex SAR image can be considered as a spectrum sample of the reflectivity function in elevation describing the signal response of an imaged object. When having a stack of SAR data, frequency samples are distributed in elevation and, due to different angles of view, provide information about the amplitude and position of signals in elevation. In non-parametric TomoSAR approaches (see chapter 2.1.5), a continuous reflectivity function is reconstructed by inverse Fourier transform of pixel measurements provided by a stack of SAR data.

In theory, the best result for the processing of SAR data is expected for specular reflections, e.g. on dihedrals or trihedrals. Then, the backscattered amplitude is constant along the synthetic aperture in elevation while only the spatial frequency changes. The inverse Fourier transform of the signal spectrum yields a *sinc*-function whose maximum determines the position of the scatterer in elevation direction.

Within the SAR data stack, frequency samples are irregularly distributed in elevation and are low in numbers. Hence, the reconstruction of the reflectivity function in elevation is affected by strong sidelobes and elevation ambiguities. With regard to the processing of a SAR data stack, the result of tomographic reconstruction can be improved on several ways. When extending the



distribution of samples along the synthetic aperture in elevation, the resolution of the main lobe of the *sinc*-function is increased. Furthermore, regular sampling will decrease the height of sidelobes of the reconstructed *sinc*-function. Finally, increasing the number of samples in elevation will avoid ambiguities in elevation direction.

RaySAR simulates tomographic results provided for an infinite size of the synthetic aperture in elevation and an infinite number of samples. In case of direct specular or diffuse backscattering from a surface, the position of the corresponding signature will be found where the line of sight of the orthographic sensor hits the surface perpendicularly (see figure 23b). Then, the elevation coordinate is equal to the elevation coordinate of the pixel where the primary ray was defined (see equation 16). Distributed scatterers are represented by discrete samples. The density of samples depends on both the number of pixels on the sensor plane and the geometrical shape of simulated objects.

When simulating multiple reflections, an *elevation correction* is required if the reflection process is not bound to a constant elevation coordinate, e.g. a dihedral located in the range-elevation plane. The position of the signal corresponding to the dihedral is found where the sensor's line of sight hits the corner tip perpendicularly (see figure 23a). At this elevation position, the spatial distance between the corner tip and the synthetic aperture in elevation is minimum. For assigning the elevation correction, the position of the signal origin at the virtual SAR antenna is required for calculating the elevation coordinate of the detected signal (see equation 19).

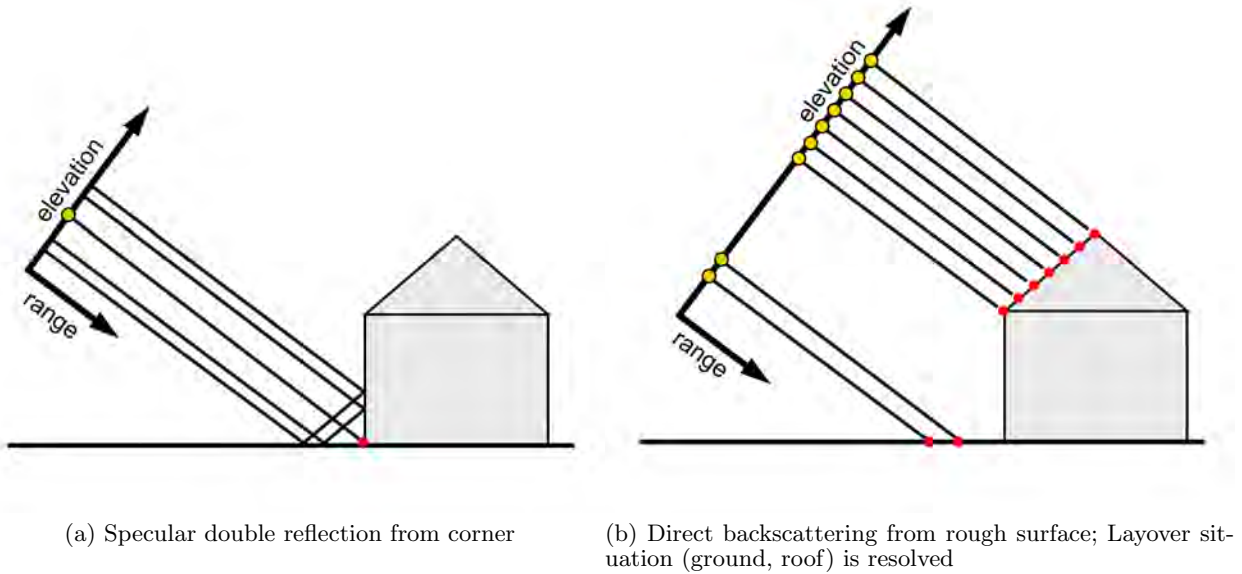


Fig. 23. Concept for simulating elevation coordinates in case of direct backscattering and specular double reflection. Specular corner reflectors are located at one single position in elevation. Height information about surfaces is provided by samples distributed in elevation. The location of scatterers is indicated in red. The simulated elevation positions are indicated in yellow.

### Discussion of sampling in elevation direction

In RaySAR, the spatial distribution of radar signals in elevation is represented by discrete samples. Hence, ray tracing enables to find the elevation position of signal peaks. The aim is not to provide a copy of profiles reconstructed by SAR tomography. Based on the simulated distribution of scatterers, the resolution of the simulated profile may be reduced. To this end, a constant spatial resolution would have to be assumed for specular or diffuse scatterers in elevation direction. However, adding this artificial effect neglects the geometry of the simulated object. Thus, no gain of information is expected for the investigation of the nature of scatterers.



Signal responses directly backscattered from objects are regularly distributed in the azimuth-elevation plane. In contrast, multiple reflections may be irregularly distributed due to the need for an elevation correction. For obtaining a reflectivity profile in elevation, a rasterization step is needed (see chapter 6.3). The localization of directly backscattered signals in elevation is helpful for resolving layover situations at man-made objects (see figure 23b). Furthermore, the interpretation of scatterers is supported since the spatial distribution of single bounce contributions provides information about the geometrical shape of objects. Specular multiple reflections at dihedrals or trihedrals are located at one single point in elevation. Thus, point scatterers spatially distributed in elevation can be separated for each resolution cell.

Comparable to the azimuth direction, the correctness of the localization of diffuse reflected signals is lower than for specular reflected signals. However, the resulting elevation position of diffuse signal responses is expected to be close to reality. In chapter 6.3, basic shapes are simulated by RaySAR. To this end, the output data provided by the ray tracer are exploited in order to analyze signal responses in elevation direction. In this context, the functionality of the simulation in elevation direction is verified by simulation results for a corner reflector.

#### 5.1.4 Detection of specular reflections

In RaySAR, the simulation of SAR image radiometry is limited due to simplified reflection models. Additional information may be helpful for interpreting salient signatures in real SAR data which are not appropriately represented by the simulated map. To this end, a geometrical analysis of signal reflections, applied during the sampling of the modeled scene, enables to detect specular reflections at dihedrals, trihedrals or other structures. Rays only following specular directions on their way from the signal source to the sensor are marked by a flag value. In figure 24, the basic concept for the geometrical analysis is visualized. Tracing a ray starts at the center of an image pixel within the sensor plane. The primary ray  $\vec{R}$ , intersecting the sensor plane orthogonally, is followed and an intersection point  $P$  is detected on an object surface. At this position, a virtual ray  $\vec{S}$  is defined in specular direction based on the surface normal  $\vec{N}$  and the incoming ray  $\vec{R}$  by

$$\vec{S} = \vec{R} - 2\vec{N} \cdot (\vec{N} \cdot \vec{R}) \quad (21)$$

Vector  $\vec{L}$ , pointing in direction to the signal source, and vector  $\vec{S}$  define a scalar angle which is

$$\cos(\alpha) = |\vec{S} \cdot \vec{L}| \quad (22)$$

If  $\alpha$  is smaller than a defined threshold  $\Delta\alpha$ , which is  $1^\circ$ , the signal reflection is classified as 'specular'. Then, the default flag value is changed from 0 to 1. Since the geometrical analysis is conducted for all primary and secondary rays, one flag value is defined for each signal response detected in the simulated scene. In figure 24, an example for diffuse reflection is given since vector  $\vec{L}$  is not situated in the cone defined by vector  $\vec{S}$  and angle  $\Delta\alpha$ .

## 5.2 Evaluation of the simulation of multiple reflections

In this chapter, the potentials and limitations of ray tracing with regard to the simulation of multiple reflections are discussed. The need for the discussion is based on the fact that, to the knowledge of the author, a thorough evaluation of the applicability of ray tracing for the simulation of multiple reflections of radar signals is not reported in the literature. Generally, the

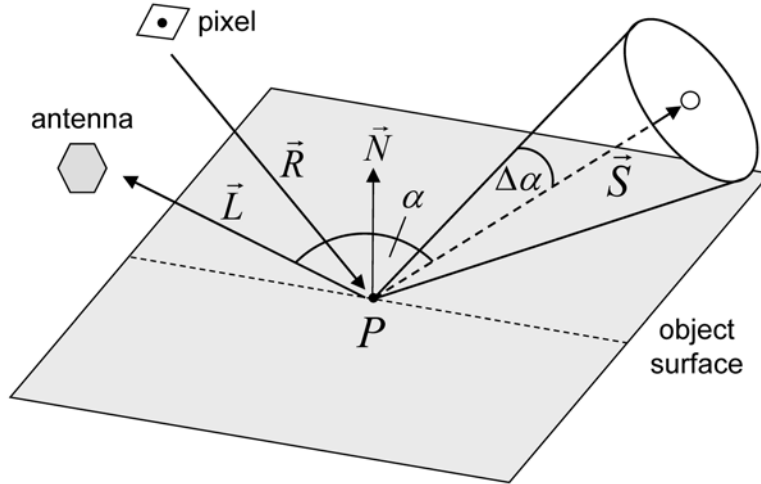


Fig. 24. Detection of specular reflections based on the geometry of reflection. For the example at hand, the signal reflection is of kind 'diffuse' and is marked by flag value 0.

method for localization of signal responses may vary for different SAR simulation approaches based on ray tracing. For instance, signal responses may be directly simulated, as for the approach presented in this thesis, or by post-processing of signal responses captured along a virtual synthetic aperture. However, the basic limitations of the ray tracing algorithm will affect the simulation products of both simulation concepts.

### 5.2.1 Strength of multiple reflected signals

The focus of the RaySAR concept is on deterministic reflection effects. In this context, the simulation of specular multiple reflections at dihedrals and trihedrals is of special interest. For both kinds of object geometries, the power of the signal response depends on the corner size (see e.g. Knott et al. (2004)). In case of a dihedral facing the line-of-sight of the SAR, the radar cross section is given by

$$\sigma = \frac{8\pi \cdot a^2}{\lambda^2} \quad [m^2] \quad (23)$$

where  $a$  is the area of one surface of the reflector and  $\lambda$  is the signal wavelength. The radar cross section of a trihedral is given by

$$\sigma = \frac{4\pi \cdot e^4}{3\lambda^2} \quad [m^2] \quad (24)$$

where  $e$  is the length of the corner edge. The components  $a^2$  and  $e^4$  within the equations are linked to the representation of signal intensity instead of signal amplitude.

RaySAR applies discrete sampling of dihedrals and trihedrals. Hence, both the number of samples and the strength of the simulated signal responses increase linearly with the size of dihedrals or trihedrals. The quadratic components of equations 23 and 24 are not accounted for, i.e. ray tracing provides the amplitude of multiple reflected signals. However, the dependence of a signal response on the corner size is considered. For calculating the amplitude for a pixel in the azimuth-range plane, the simulated signal contributions have to be summed up coherently (see chapter 6.2). For deriving the signal intensity corresponding to a multiple reflected signal, the amplitude would have to be squared. However, using the amplitude information for the

visualization of simulated data is reasonable as the difference in signal strength is mapped easier into a 8-bit grayscale image.

Thus, the decision between signal representation by means of amplitude or intensity is not crucial. The main challenge is the simulation of the proportion between the specular and diffuse signal amplitude. More specifically, strong overestimation of diffuse reflections may disturb the appearance of specular reflections on the simulated SAR image. That is why the application of the RaySAR model for diffuse reflection (see equation 14) is only reasonable for the simulation of Lambertian scatterers. Besides, dihedrals and trihedrals have to be sampled sufficiently. To this end, the number of pixels on the sensor plane has to be chosen high enough. Then, small object features are hit by an appropriate number of rays.

A further peculiarity of ray tracing to be discussed is the separate treatment of bounces. For each pixel in the sensor plane, direct backscattering of a signal is analyzed by following a primary ray. After the first signal bounce, the ray tracing procedure is continued by means of secondary rays. Eventually, further detected signal contributions are added to the signal detected by the primary ray. The only parameter for linking the reflections of an emitted signal is given by a weight factor for defining the absorption of a signal reflected at a surface (see *reflection* command in Appendix B.2).

In reality, the radar signal is emitted at the SAR sensor and is reflected at objects in the far field where the signal wavefront can be assumed to be flat. Thereafter, the signal is located in the near field with respect to the last bounce. When hitting the next surface, the wavefront can not be considered as being flat any more and a different kind of signal reflection occurs. In RaySAR, each signal reflection is evaluated the same way. The assumption of the same reflection phenomenon for each signal bounce leads to a systematic error affecting the correctness of the signal amplitude.

### 5.2.2 Proportion between multiple reflections and direct backscattering

In data provided by VHR SAR sensors, the signal-to-clutter ratio increases significantly compared to SAR sensors of medium resolution. In this context, the expression *signal* refers to pixels containing stable amplitude and phase information which are, for instance, exploited by PSI (see chapter 2.1.5). The diffuse signal response from other objects surrounding the signature in the azimuth-range plane is referred to as *clutter*. In case of an increase of the signal-to-clutter ratio, salient SAR image signatures corresponding to regular structures, such as dihedrals or trihedrals, can be better distinguished from the diffuse signal response from nearby surfaces.

RaySAR enables to consider this effect. In order to confirm this assumption, the simulation procedure shall be recapitulated for a basic shape. Figure 25 shows the generalized shape of a simulated building model in the range-elevation plane. The building wall and the nearby ground form a dihedral which faces the line-of-sight of the virtual SAR sensor. Signal contributions are detected by ray tracing and are represented by discrete samples. Displayed in orange color, signal components of the background occur due to the diffuse backscattering of signals from the ground and the building wall. Signal components displayed in red color refer to the specular reflection of radar signals at the building wall and are focused at the bottom of the wall.

For providing a SAR image in the azimuth-range plane, the discrete samples have to be rasterized (see chapter 6.2). To this end, the size of the resolution cell in azimuth and range has to be defined. Thereafter, the signal amplitude is derived by summing up all signal contributions within the resolution cell. In figure 25a, all signal contributions within the range interval of width  $\Delta r$  are integrated. Hence, the double bounce signal is disturbed by a high number of diffuse signal contributions. The strength of the double bounce signal is independent of the resolution cell size  $\Delta r$  as the signal response is focused at one position. In contrast, diffuse

signal contributions are spatially distributed depending on the chosen size of the resolution cell. Figure 25b visualizes this effect for the building model when decreasing the resolution cell size by factor 2. Then, the number of diffuse signal components disturbing the double bounce signal is reduced.

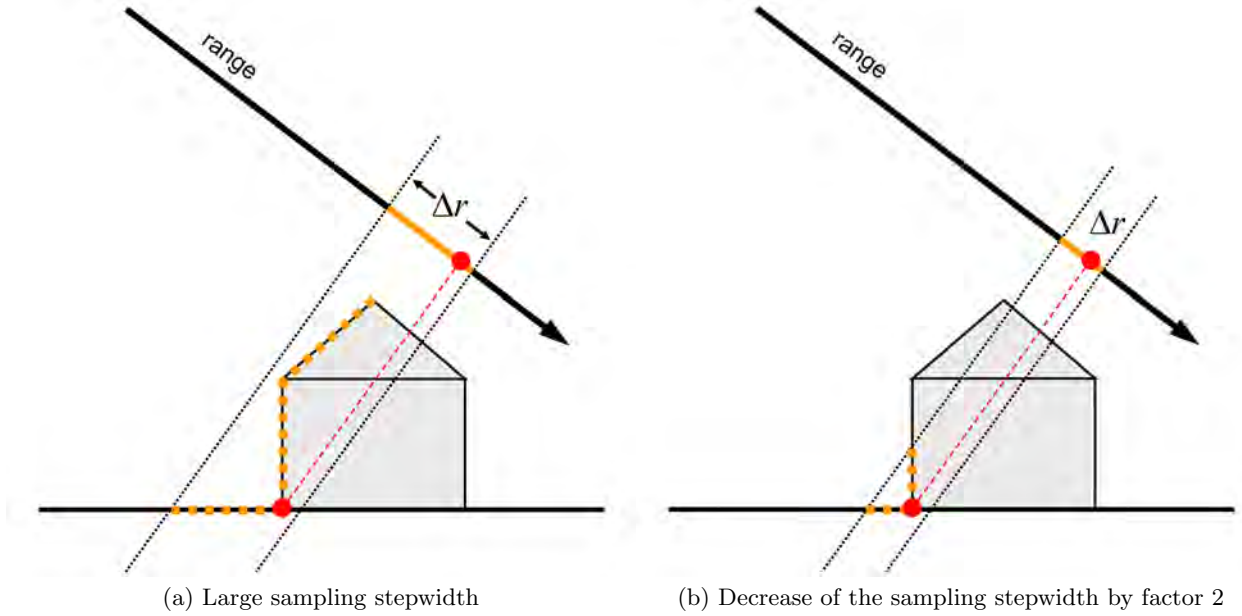


Fig. 25. Proportion between a specular double bounce signal and direct backscattered signals in RaySAR. When decreasing the resolution cell size in range, the number of diffuse signal components (marked in orange color) per pixel decreases. In contrast, the signal power corresponding to specular double bounce is located at the corner (red ball) and is independent from the sampling stepwidth in range.

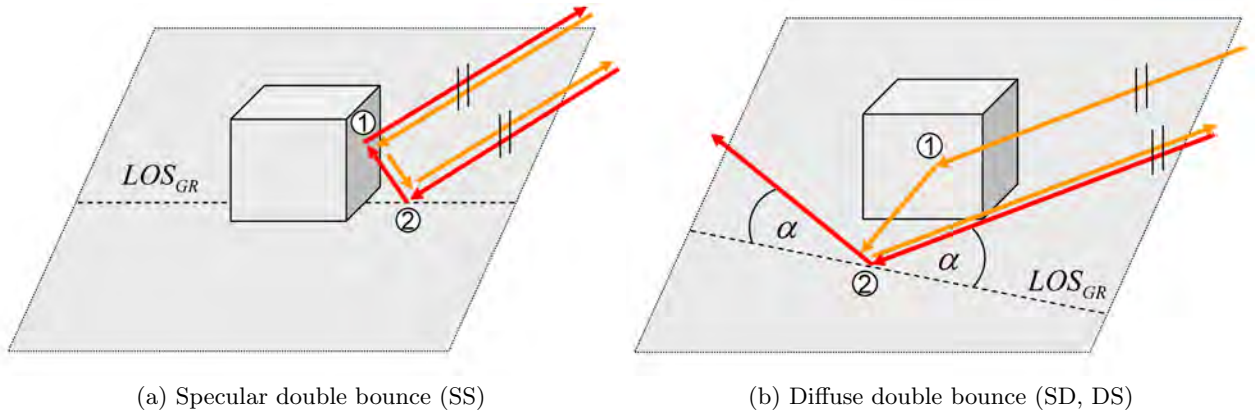


Fig. 26. Representation of the specular and diffuse signal response in case of double bounce. Using an orthographic system, specular double bounce is followed in both directions (orange and red). Diffuse double bounce is only followed in one direction (orange) since ray tracing follows secondary rays in specular direction.  $LOS_{GR}$  indicates the ground range component of the line-of-sight of the SAR sensor.

### 5.2.3 Geometrical and radiometrical completeness

Specular reflections of radar signals within a simulated scene have to be fully covered by the SAR simulation concept since they are expected to be linked to dominant SAR image signatures. In addition, diffuse reflections of radar signals from surfaces may be visible depending on the roughness of surfaces. In this context, a reflection process containing several diffuse signal bounces is assumed to be negligible.

The majority of rough surfaces is not characterized by Lambertian backscattering. Thus, the strength of diffuse reflected signals depends on the angle of reflection and is maximum near the specular direction (see chapter 4.3). Moreover, the loss of signal amplitude on rough surfaces is expected to be much stronger than on specular surfaces. Based on these assumptions, a SAR simulator has to account for multiple reflections including at most one diffuse reflection. In the following, a reflection process including one diffuse reflection is referred to as *diffuse single, double, triple, or multiple bounce*. A reflection process corresponding to a specular reflected signal is referred to as *specular single, double, triple, or multiple bounce*.

As shown in chapter 2.2.2, ray tracing is focused on the simulation of specular reflections. Figure 26a shows an example for specular double bounce occurring at a cube, i.e. *signal source*  $\rightarrow$  *ground/cube surface*  $\rightarrow$  *cube surface/ground*  $\rightarrow$  *sensor* (twice specular; type *SS*). The dashed line  $LOS_{GR}$  indicates the ground range component of the line-of-sight of the SAR sensor. During ray tracing, both directions of the two-way system are analyzed. Hence, the position and the amplitude of the signal response is provided.

In case of the diffuse reflection of radar signals, ray tracing by POV-Ray does not account for diffuse signal reflections between scene objects (see figure 14). After the emission of a signal at the virtual antenna only the first signal bounce may be of diffuse type. In figure 26b, an example for a reflection process of the combination 'diffuse + specular' (type *DS*) is marked in orange color. First, the radar signal is diffusely scattered at point 2 in direction to point 1 located at the cube surface. Afterward, the radar signal is specularly reflected in direction to the SAR sensor. Ray tracing follows the ray in inverse direction, which is indicated by the direction of the orange rays. Diffuse signal components are analyzed at point 2 *after* following the secondary ray in specular direction at point 1. Analyzing the signal path the other way around, i.e. in direction from point 2 to point 1, is not possible since the secondary ray at point 2 is defined in specular direction. In sum, the geometrical description of the diffuse double bounce is given by the path *sensor*  $\rightarrow$  *point 1*  $\rightarrow$  *point 2*  $\rightarrow$  *antenna* while only half of the signal strength is derived.

At this point, measures shall be introduced for evaluating the completeness of the simulation of diffuse and specular reflections. To this end, the limitations of ray tracing are analyzed with respect to the geometrical and radiometrical completeness. In this context, the term *completeness* means the capability to handle a reflection process of certain type by the ray tracer. Specular signal reflections of any reflection level are geometrically and radiometrically covered by 100% as the ray tracer follows the signal in both directions. Likewise, diffuse single bounce is geometrically and radiometrically covered by 100%. The geometry of signal responses corresponding to diffuse double bounce is fully covered from the geometrical point of view (see figure 26b). Both reflection processes SD as well as DS are represented by the raytracer, respectively, due to the orthographic imaging geometry of the virtual SAR sensor. However, only half of the radiometrical component is simulated. As only one diffuse reflection is expected to be relevant for each reflection process, the reflection processes SSD, SDS, and DSS are of interest for bounce level 3. Ray tracing enables to cover the geometry of SSD and DSS in one direction, respectively, while SDS is not considered. Thus, 33% of relevant diffuse triple bounce is not covered by the ray tracer. Moreover, the loss of radiometrical information increases from 50% in diffuse double bounce to 66% in diffuse triple bounce. Geometrical information of fourfold and fivefold bounce, which may be of interest for certain object geometries, is covered by 50% and 40%, respectively, in combination with further loss of radiometrical information (25% and 20%). In Table 5, the geometrical and radiometrical completeness is summarized for different bounce levels.

From the geometrical point of view, the simulation of diffuse signals by means of ray tracing is reasonable for bounce levels 1 to 3. For diffuse signals of higher bounce level, only a small insight can be given into the real signal response. However, the majority of diffuse multiple reflections is expected to be negligible. The diffuse signal reflection between objects could be included by using advanced render methods, such as Radiosity or Path Tracing. Thereby, the

Type	Relevant reflection processes	Geometrical completeness	Radiometrical completeness
Diffuse single bounce	D	100%	100%
Diffuse double bounce	DS, SD	100%	50% (can be compensated by factor 2 for the signal amplitude)
Diffuse triple bounce	DSS, SDS, SSD	66% (DSS, SSD)	33%
Diffuse fourfold bounce	SSSD, SSDS, SDSS, DSSS	50% (SSSD, DSSS)	25%
Diffuse fivefold bounce	SSSSD, SSSDS, SSDSS, SDSSS, DSSSS	40% (SSSSD, DSSSS)	20%

Table 5. Evaluation of the geometrical and radiometrical completeness of diffuse signal response detected by RaySAR. Relevant signal responses are composed by one diffuse reflection (D) and other bounces of specular type (S). Reflection processes containing more than one diffuse reflection are assumed to be negligible.

simulation of signal reflections of kind SDS should be enabled in combination with 100% of radiometrical completeness at the cost of a significant increase of calculating time. However, the improvement of the simulation of diffuse signal reflections is a future research topic.

### 5.3 Sampling step - summary

In RaySAR, ray tracing methods are applied for the sampling of modeled scenes. The continuous wave front of the radar signal is approximated by means of rays which are followed in inverse direction, i.e. from the sensor to the signal source. The signal response from objects is located directly without the formation of a virtual SAR. To this end, focusing rays have to be defined at intersection points detected within the simulated scene. Thereby, azimuth and elevation corrections can be applied. RaySAR simulates an ideal SAR system having infinite resolution in azimuth, range, and elevation. Hence, the signal response is localized by finding the position of the amplitude peak in 3D. In case of multiple reflections of radar signals, the simulation of specular signal contributions is expected to be of higher correctness than for diffuse signal contributions. Performing a geometrical analysis of reflection phenomena enables to identify pixels containing specular reflections, which are likely to be part of salient SAR image

signatures.

The dependance of the backscattered signal on the size of dihedrals and trihedrals is considered. However, the separate treatment of bounces leads to systematic errors when simulating multiple reflections. The proportion between signal, i.e. signal characterized by stable phase information, and clutter can be approximated. In this context, the parameters describing the diffuse reflection on surfaces have to be defined appropriately. By trend, RaySAR overestimates the amplitude of diffuse signal contributions (see chapter 4.3) what leads to an underestimation of the proportion between signal and clutter.

With regard to the completeness of the simulation of signal responses, specular reflections of radar signals are covered by 100%. However, multiple reflections are followed in specular direction which leads to a partial loss of diffuse signal. While radiometric information is already lost starting for bounce level 2, geometrical information about diffuse signals is lost for bounce levels higher than 2. To conclude, the application of ray tracing methods is reasonable for the simulation of diffuse reflections having a bounce level up to 3. For higher bounce levels, only an insight into the real SAR data can be provided. Advanced rendering methods may be included in the future for a better approximation of global illumination.

## 6 Methods for SAR simulation in 3D

### 6.1 3D models for simulation examples

Simulation results presented in this chapter show the basic functionality of the simulation approach. In order to ease the visual control of the simulated products, two basic objects have been modeled in the POV-Ray editor:

- ◇ a *corner reflector*, facing the line-of-sight of the virtual SAR, whose edges have a length of 1.5 m, respectively. The local angle of incidence of the radar signal is  $45^\circ$ . With regard to the signal response, the corner surfaces are characterized by strong specular reflection and weak diffuse reflection of the radar signal. For rendering, the dimension of the azimuth-elevation plane is 5 m x 5 m containing 800 x 800 pixels. On the one hand, the corner reflector model enables a visual interpretation of the signal response simulated in 2D and 3D. It is shown, that the simulation results correspond to experiments with regard to the focusing of specular reflections. On the other hand, a demonstrative example is provided for the identification of surfaces contributing to a SAR image signature.
- ◇ a *step model*, displayed in figure 6c, which is oriented in line-of-flight of the virtual SAR. The width, length and height of the model is 20 m, 40 m, and 40 m, respectively. The local incidence angle of the radar signal is  $45^\circ$ . The azimuth-elevation plane, having a size of 100 m x 120 m, is covered by 1000 x 1200 pixels. The ground is characterized by weak diffuse backscattering while the step surfaces show both specular and diffuse reflection of the radar signal. When imaging the step model by the virtual SAR, a layover situation occurs. Hence, the potential of RaySAR with regard to resolving layover situations can be tested and explained. Besides, visual interpretation is enabled due to the simple structure of the simulated body.

As far as the radiometric correctness of simulation results is concerned, the reflection behavior of surfaces is not adapted to parameters described in chapter 4.3. At this point, the geometrical component of simulated results is of main interest. To this end, the diffuse backscattering from object models is emphasized in order to visualize the geometrical shape of signatures in the azimuth-range plane.

### 6.2 Simulation in azimuth and range

After the sampling of the modeled scene, the simulation of SAR products in the azimuth-range plane forms the basis for further analysis. As shown in chapter 5, the ray tracer included into the RaySAR simulation package provides radar signal contributions in discrete form. For instance, the spatial distribution of the simulated signal response for the corner reflector model is shown in figure 27a. Diffuse single bounce (blue color) indicates the dimension of the corner while diffuse double bounce (green color) occurs at the intersection lines between the corner surfaces. The signal corresponding to specular triple bounce is focused at the corner tip (red point).

For providing a reflectivity map in the azimuth-range plane, the discrete samples are rasterized based on the following input information for each detected signal:

- ◇ azimuth and range coordinates
- ◇ bounce level information
- ◇ amplitude information



First, the size of the reflectivity map in azimuth and range has to be predefined in order to select signal contributions of interest. Moreover, the size of resolution cells in azimuth and range has to be defined. The maximum bounce level is limited by a threshold. The simulation of products in ground-range is enabled by including knowledge about the angle of incidence of the radar signal. Finally, the image radiometry can be adapted by displaying the simulated amplitude information with a chosen dB scale or by clipping amplitude peaks at a threshold. When simulating a reflectivity map, a histogram is provided which shows the the dynamic range of pixel amplitudes. Based on this information, the image radiometry can be adapted by repeating the simulation step. Thereby, the visualization of signatures by means of 8bit gray values can be improved.

After imposing a virtual grid onto the azimuth-range plane, the signal contributions are summed up within each resolution cell of the reflectivity map (see figure 28). The summation of signal responses is performed either coherently, i.e. using amplitude and phase information in the imaginary plane or by only summing amplitude values, i.e. zero phase is assumed.

For coherent summation of the radar signal, the amplitude  $A$  and range  $r$  of the simulated signal response is exploited. The signal phase is derived by

$$\Phi = \frac{-4\pi}{\lambda} \cdot r - n \cdot \pi \quad (25)$$

where  $\lambda$  is the signal wavelength and  $n$  is an integer for keeping the phase within the interval between 0 and  $2\pi$ . Thereafter, the complex radar signal corresponding to a ray tracing sample is

$$u = A \cdot \cos(\Phi) + j \cdot A \cdot \sin(\Phi) \quad (26)$$

Compared to the assumption of zero phase, the coherent summation of radar signals provides results of higher correctness, as the loss of amplitude is considered in case of distributed scatterers. However, non-coherent summation avoids the extinction of signal responses within layover areas. Hence, geometrical information about weak SAR image signatures is preserved. From practical experience, the non-coherent summation of signals is applied for the simulation of basic shapes while coherent summation is used when analyzing signatures in real SAR data.

In figure 27b, the simulated reflectivity map of the corner reflector is displayed. The pixel spacing in azimuth and range has been defined as 0.2 m and 0.2 m, respectively. As expected, the signal is focused at one pixel in azimuth and range. The dynamic range of the image has been adapted to the specular signal response. Hence, the diffuse signal response from the corner surfaces is not visible since it is too weak compared to the triple bounce signal.

As introduced in chapter 5.1.4, specular reflections and diffuse reflections can be distinguished. To this end, a flag value is available for each detected signal contribution. Based on this information, a binary map can be created which classifies the image into pixels containing specular reflections and pixels which only contain diffuse signal contributions. Both the size and the sampling stepwidth of the binary map are adapted to the reflectivity map. In case of the corner reflector example, specular reflections are only found for the bright image pixel on the reflectivity map. Hence, the binary map looks equal to the map shown in figure 27b.

Due to discrete sampling of scenes, ray tracing suffers from a detection problem (see chapter 2.2.3). In homogeneous areas, the number of ray tracing samples may vary for adjacent resolution cells. Thus, a homogeneous surface may be characterized by pixels of slightly different gray values in the simulated reflectivity map. Figure 28 visualizes this effect for signal contributions distributed in the azimuth-range plane. The visual impression of the detection problem will be strong if

- ◇ the number of single bounce samples is comparable to the number of pixels on the reflectivity map
- ◇ the dynamic range of pixel amplitudes in the reflectivity map is small

However, the detection problem mainly affects resolution cells including the signal response from distributed scatterers. For instance, no disturbing effect can be distinguished on the simulated maps displayed in figure 6. In order to suppress artificial SAR image signatures occurring due to the detection problem, bilinear filtering by means of a 3x3 matrix can be applied at the cost of spatial resolution.

Besides a reflectivity map containing all SAR image signatures, signal responses corresponding to different bounce levels can be assigned to different image layers. Necessary knowledge is given by the bounce level information provided during the sampling step. For instance, single bounce contributions for the step model are shown in figure 29a. Following the reflectivity map top-down in range direction, signal responses from the front wall of the step and the ground are integrated in a layover area colored in bright gray. Afterward, the extent of the shadow area is visualized in black color. In figure 29b, the amplitude of the double reflected radar signal is displayed. A bright linear feature, pointing in azimuth direction, occurs since the step model faces the line-of-sight of the virtual SAR sensor.

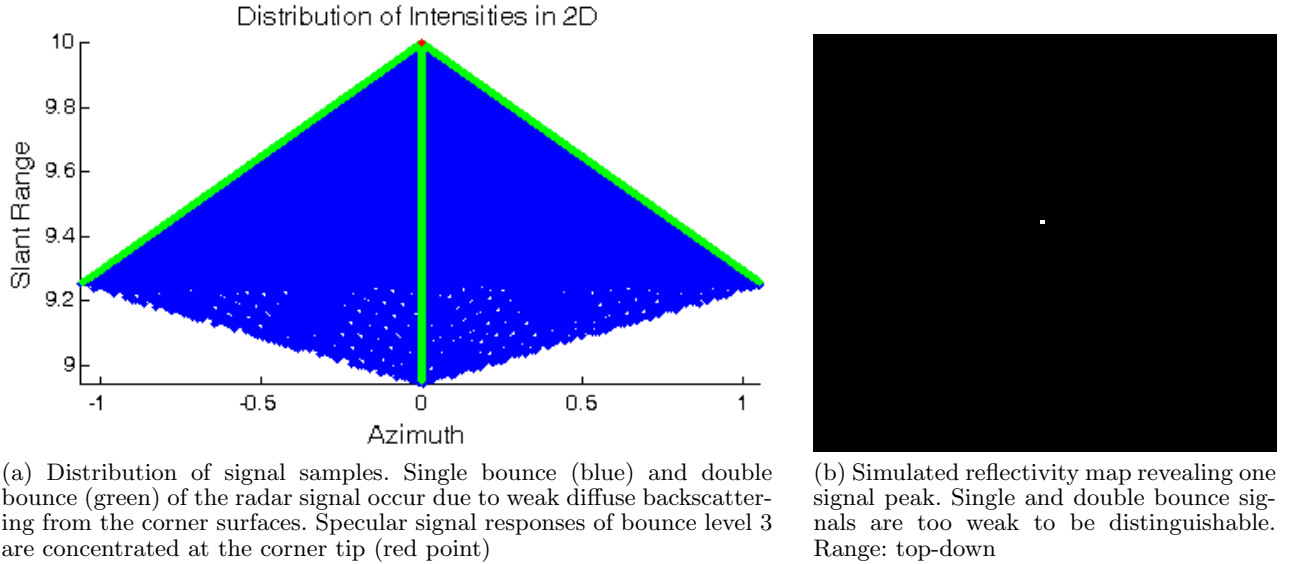


Fig. 27. Simulation results for the corner reflector model provided by RaySAR.

## 6.3 Analysis in elevation

The analysis of the elevation position of detected signal contributions is based on the simulated reflectivity map. Different simulation products which exploit elevation information are introduced in the following.

### 6.3.1 Height profiles

Elevation information provided by ray tracing enables to analyze layover situations since scatterers within one resolution cell can be separated. Hence, the interpretation of SAR image signatures corresponding to layover, as shown in the example in figure 6, can be supported. In this context, simulation products may be provided in two reference systems:

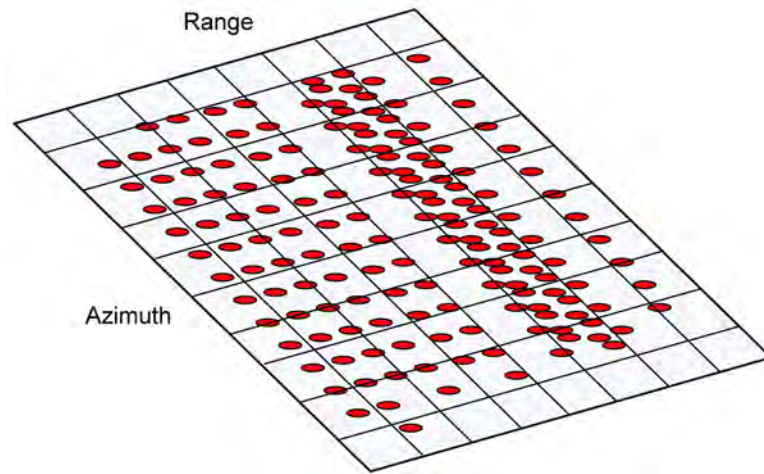


Fig. 28. Rasterization of ray tracing samples: signal contributions are summed up within each resolution cell in the azimuth-range plane. The summation is performed either coherently, i.e. using amplitude and phase information, or only using amplitude information.

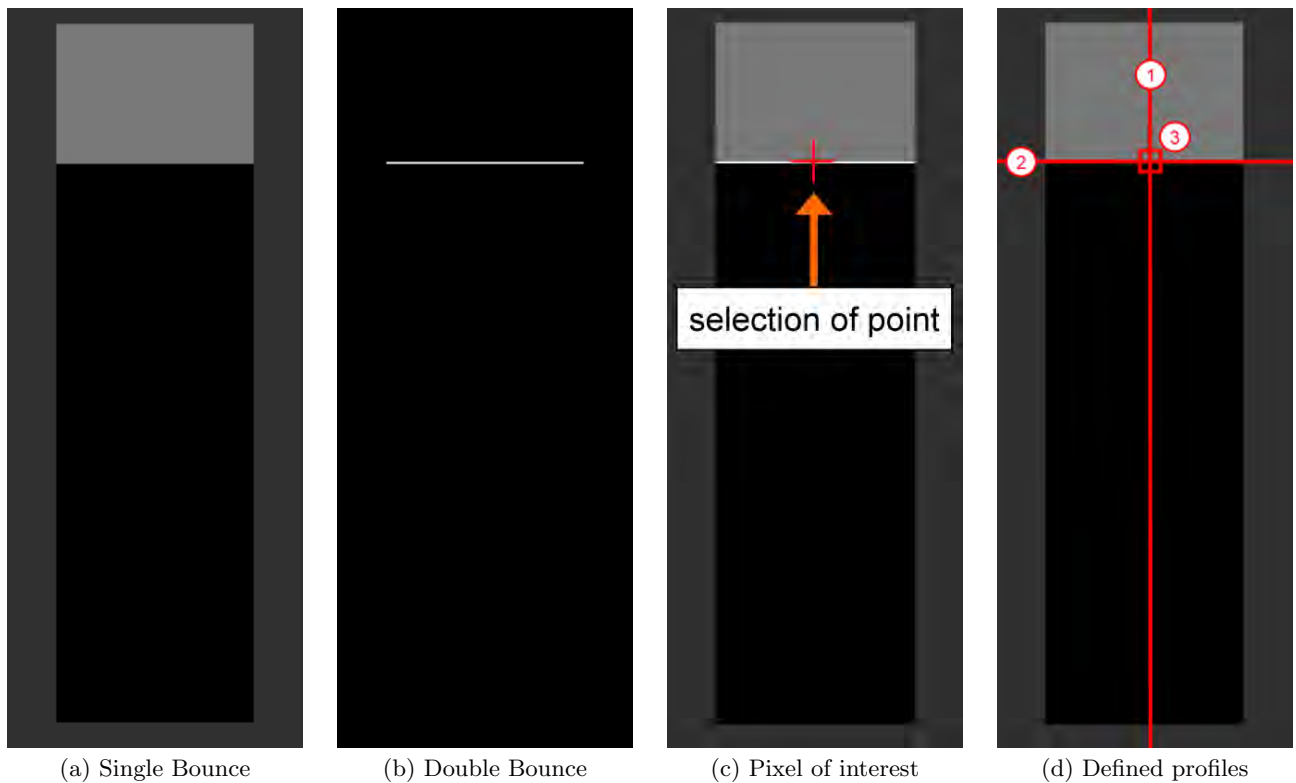


Fig. 29. Step model: separation of bounces and definition of elevation profiles for a pixel of interest. Profiles #1 and #2 are defined for displaying elevation information in range and azimuth. Profile #3 is defined perpendicularly to the image plane and enables to display the distribution of signal responses in cross-range direction. Azimuth: left-right. Range: top-down.

- (1) *elevation*: coordinates in cross-range direction which are directly provided by the sampling step. The elevation coordinate of 0 m corresponds to the center of the sensor plane defined for the rendering process.
- (2) *height over ground*: height with respect to a reference point on the ground surrounding the simulated object. The transformation of the elevation coordinates to the height-over-ground system is enabled by the known angle of incidence of the radar signal and the assumption of a flat ground surrounding the building.

The height profiles are provided as follows. First, a pixel is selected on the reflectivity map for defining the crossing of profiles. For instance, in figure 29c, a pixel within a double bounce line is marked on the reflectivity map of the step model. Thereafter, height profiles are defined at the selected pixel which point in range (profile 1) and azimuth (profile 2), respectively (see figure 29d). For each height profile, the appropriate intensity contributions are gathered. The search is limited by the width of the selected pixel. The corresponding height profiles provide information about the 3D position of the focused signal while amplitude information is not included. Bounce level information is used for distinguishing different types of signal response.

Figure 30 shows the range and azimuth profile for the step model where height information is represented by elevation coordinates. On the left, the range axis is displayed versus the elevation axis. Following the range axis from left to right, layover situations can be analyzed as signal responses from different parts of the step show the same spatial distance with respect to the SAR sensor. Likewise, the double reflected signal, displayed in green color, is found at the same range coordinate but spatially separated in elevation. The extent of the shadow area is indicated by a lack of signal response in the range interval between approximately 77.5 m and 134.5 m. On the right part of figure 30, the height profile in azimuth is displayed. Again, the signals corresponding to different bounce levels overlap but are spatially separated in elevation. Moreover, the extent of the step model in azimuth is represented.

For comparing simulated data to results from the tomographic analysis of real SAR data, signal contributions can be transformed into the 'height over ground'-system. To this end, a rotation in the range-elevation plane has to be conducted using the equations

$$r_{\text{rot}} = \cos(\theta_{\text{rot}}) \cdot r - \sin(\theta_{\text{rot}}) \cdot s \quad (27)$$

$$s_{\text{rot}} = \sin(\theta_{\text{rot}}) \cdot r + \cos(\theta_{\text{rot}}) \cdot s \quad (28)$$

with

$$\theta_{\text{rot}} = \theta - \frac{\pi}{2} \quad (29)$$

where  $r$  and  $s$  are the range and elevation coordinates of signal samples and  $\theta$  is the angle of incidence of the radar signal. The reference height of 0 m for the ground level is introduced by shifting the rotated elevation coordinates by equation

$$s_{\text{hog}} = s_{\text{rot}} - s_{\text{rot\_gr}} \quad (30)$$

The parameter  $s_{\text{rot\_gr}}$  is the minimum of the elevation coordinates rotated by equation 28 and is assumed to represent the ground level.

In figure 31, the profiles #1 and #2 for the step model are shown in the height-over-ground system. In this context, the position of multiple reflected radar signals is of main interest as the correspondance to object geometry may be lost for objects of high detail. In case of the basic step model, double reflections are focused at the intersection lines between step surfaces. Hence, the link to the geometrical structure of the step model is preserved. The 3D position of the direct backscattered signal is strictly linked to the geometry of the step model.

### 6.3.2 Amplitude distribution in elevation

Profile #3 defined in figure 29c is oriented perpendicularly to the reflectivity map. While profiles #1 and #2 only represent the position of signal responses, profile #3 enables to visualize the strength of signal responses in cross-range direction for the selected pixel. To this end,

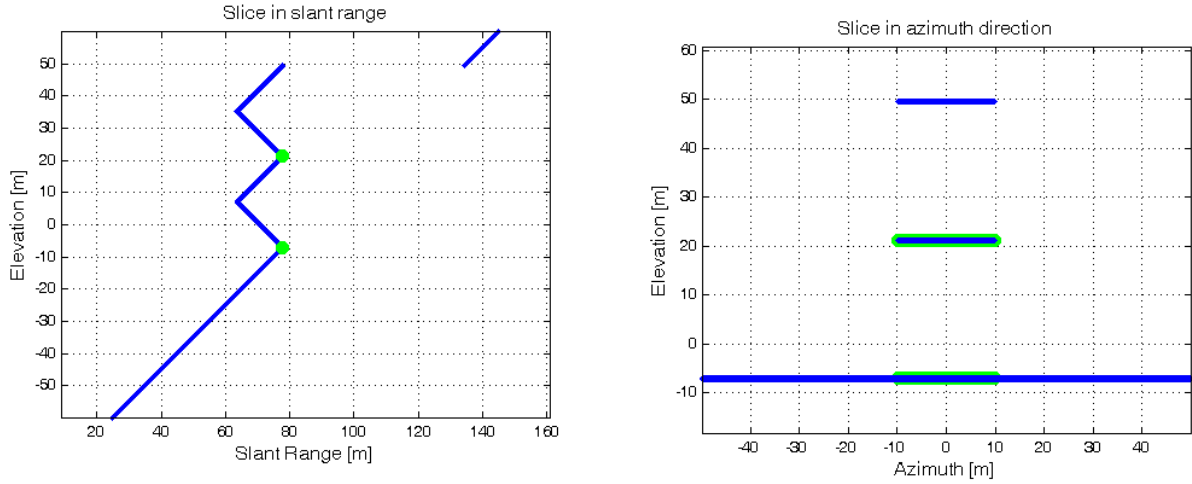


Fig. 30. Step model: elevation coordinates of detected signal contributions for defined profiles. Left: Profile pointing in range. Object layover (between 63.5 m and 77.5 m) and shadow (between 77.5 m and 134.5 m) can be identified. Right: Profile showing the extent of the layover area in azimuth. Blue: single bounce. Green: double bounce.

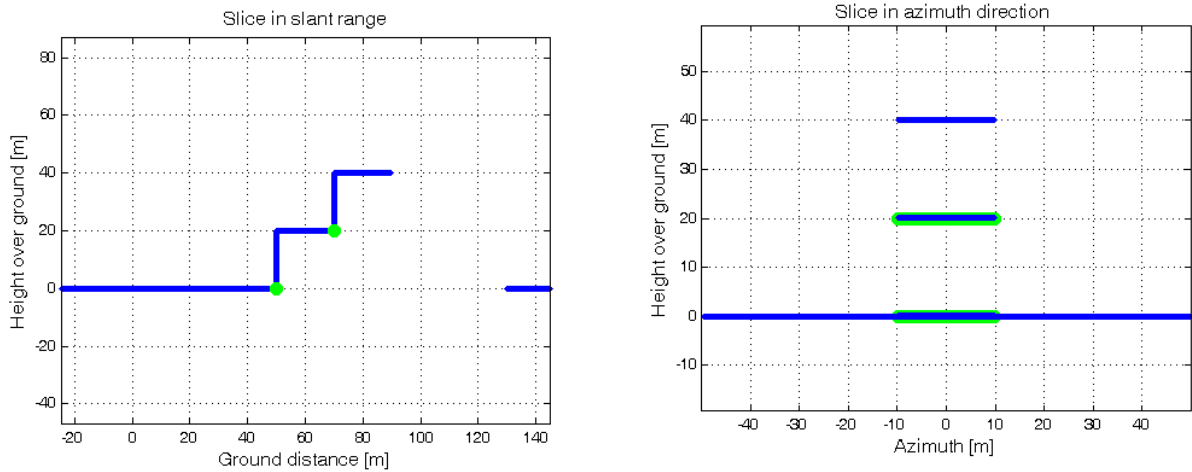


Fig. 31. Step model: height over ground of detected signal contributions for defined profiles. The height coordinate of the double reflected signal can be directly extracted. Blue: single bounce. Green: double bounce.

both the amplitude and the 3D position of signal contributions is needed. The relevant signal contributions are gathered according to the dimension of the selected pixel in azimuth and range. As for the reflectivity map, the irregular distributed signal samples have to be rasterized by deviding the elevation axis into bins of constant stepwidth. Thereafter, the signal components are summed within each bin and the resulting signal is color-coded due to the given bounce level information. At the present state of RaySAR, the summation of signal contributions is not performed coherently due to two reasons:

- ◇ *Phase stability*: The specular reflection of radar signals at corners is expected to provide stable phase information, i.e. the result of coherent summation is equal to the summation of amplitudes with zero phase. Diffuse signal components are sparse in elevation in VHR SAR data and can be imagined as  $\delta$ -impulses. Only little change of the signal phase is expected for signal contributions corresponding to a diffuse scatterer. When decreasing the stepwidth

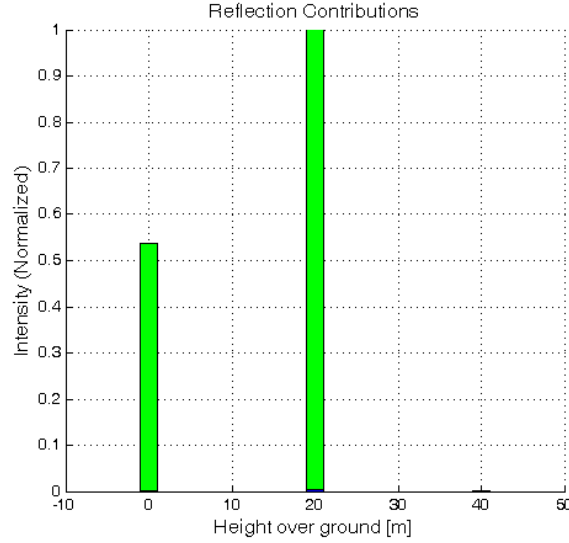


Fig. 32. Step model: distribution of signal responses in height over ground (profile 3). Single and double bounce are located at the same position in elevation. Compared to double bounce scattering from the steps (green), the strength of single bounce (blue) is almost negligible and close to zero.

in elevation, the local variation of the signal phase will be further reduced. Hence, the error occurring due to the assumption of a constant phase for each bin is expected to be small.

- ◇ *Limited radiometric correctness*: Generally, the simulation of the amplitude of diffuse signal components in RaySAR is limited (see chapter 4.3). Thus, the gain of radiometric correctness by coherent summing of diffuse signals is expected to be limited as well.

As for the height profiles, transforming the profile in the 'height over ground' system is possible. In figure 32, the normalized distribution of reflectivity is displayed for the pixel selected on the reflectivity map of the step model. For providing the profile, the sampling stepwidth in elevation has been set to 2 m. Double bounce, displayed in green color, is focused at 0 m and 20 m, which corresponds to the height of the corners in the step model. The double bounce signal at 0 m is less dominant since weak specular reflection has been chosen for the ground. Single bounce contributions, displayed in blue color, occur at 0 m, 20 m and 40 m, respectively, and are almost negligible compared to double reflected signals.

### 6.3.3 Scatterer histograms

In the profile shown in figure 32, the strength of signal responses within a SAR image pixel is distributed over resolution cells in elevation. Thereby, a combined display of elevation information and amplitude information is possible. However, due to the definition of a sampling stepwidth in elevation, the profile does not enable to simulate the elevation resolution of tomographic SAR system. Therefore, a further method for distinguishing scatterers within a resolution cell has been developed: *scatterer histograms*.

For providing a scatterer histogram, the reflectivity map of the simulated scene has to be given and the resolution of the virtual tomographic system  $\delta_s$  has to be defined. First, an empty histogram is generated having the same extent and pixel spacing as the reflectivity map. Thereafter, the signal contributions, provided by the ray tracing procedure, are assigned to the resolution cells of the histogram based on their given azimuth and range coordinates. The elevation coordinate  $s_1$  of the first signal component allocated to a resolution cell is kept. For any further incoming signal component, the spatial distance in elevation with respect to the

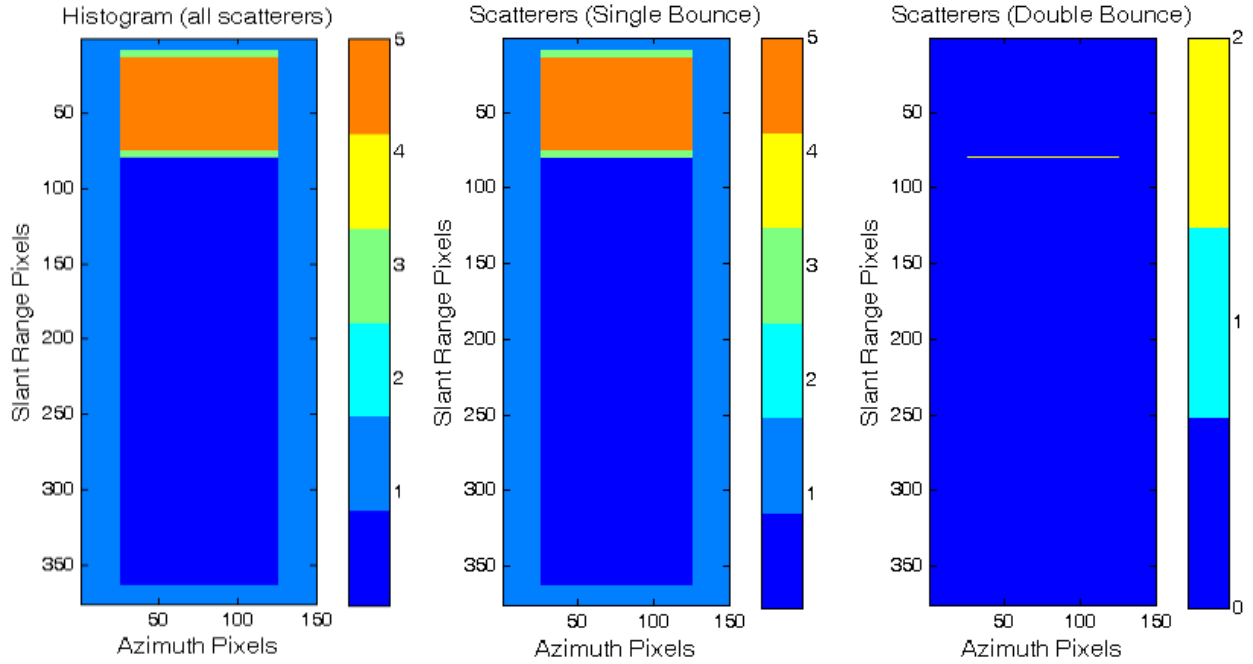


Fig. 33. Step model: histograms showing the number of scatterers for each resolution cell. Left: Histogram containing all bounce levels. Center: Single bounce separated for each resolution cell. Right: Double bounce separated for each resolution cell. Spatially overlapping signals corresponding to different reflection levels are considered as one signal component.

already existing signal response is checked. A new elevation entry  $s_2$  is kept if

$$|s_1 - s_2| > \delta_s \quad (31)$$

Afterward, further signal components have to be tested with respect to elevation heights  $s_1$  and  $s_2$ . Eventually, the number of scatterers is color-coded for each resolution cell of the histogram. Due to given bounce level information, histograms can be provided for different reflection levels. The resulting histograms for the step model are shown in figure 33. For separating scatterers within one pixel, the resolution of the virtual tomographic SAR system has been set to 2 m. On the left, the scatterer histogram including all bounce levels is displayed. In case of the backscattering of a diffuse signal from the step surfaces, up to five scatterers are included into one resolution cell. Double bounce contributions are located at the corners of the step model and, hence, overlap with diffuse single bounce contributions. This is also visible when having a closer look to the height profile pointing in range (figure 34), which is a zoom into the range profile in figure 30. Starting at near range, only signal components backscattered from the ground are detected. Three scatterers occur when the signal simultaneously hits the ground and the tips of the step model. Afterwards, distinguishing the signal response from the different step surfaces and the ground is enabled. Finally, single and double bounce contributions are merged to three scatterers followed by shadow without any signal response.

Since single and double bounce contributions overlap in elevation, the histogram for single bounce (center of figure 33) is equal to the histogram including all reflection levels. A separate layer for double bounce is required to identify the layover of two double bounce lines (right part of figure 33).

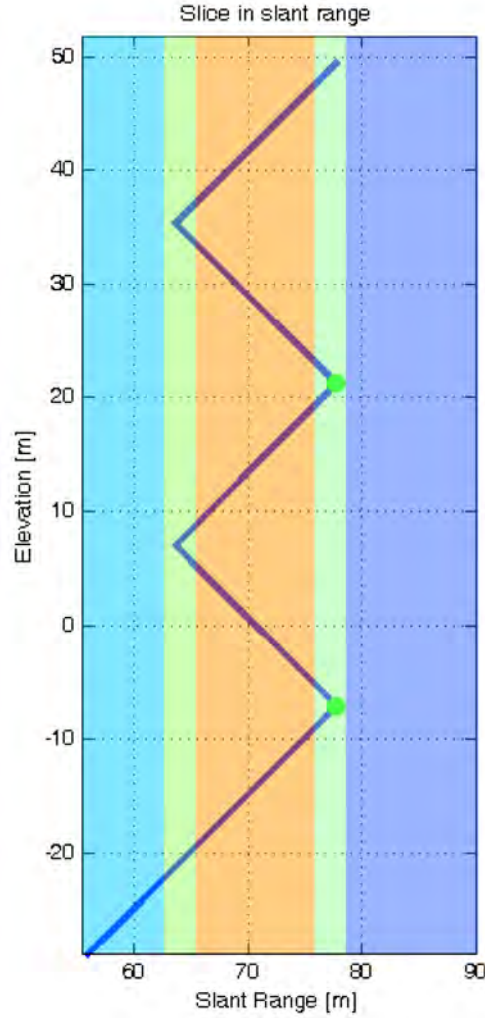


Fig. 34. Interpretation of a scatterer histogram (zoom into the range profile in figure 30). Lines in dark blue: distribution of single bounce contributions. Green spots: location of double bounce contributions. Along the profile, which is located in the range-elevation plane, the number of scatterers varies due to layover situations. Areas colored in light blue, light green, orange, and dark blue represent range intervals which contain one scatterer, three scatterers, five scatterers and shadow, respectively. The width of the green bands in slant range depends on the spatial resolution in elevation.

## 6.4 3D analysis of multiple reflections

SAR simulation in the azimuth-range plane supports the visual interpretation and selection of deterministic signatures. Height profiles, defined in the azimuth-elevation plane or the range-elevation plane, provide an insight into the 3D data provided by sampling the modeled scene. These profiles can be used for interpreting profiles derived by tomographic processing of real SAR data. However, knowledge about the nature of scatterers, which is a major objective of this work, is only provided by linking the detected radar signals to the geometry of the simulated object. Two methods for solving different aspects of this task are introduced in the following.

### 6.4.1 3D localization of signatures

The main motivation for localizing radar signals in 3D is to investigate the correspondance to building features. Hence, it can be analyzed whether a signal represents the geometry of an imaged object. In case of the step model, double reflections are located at the step surface and, thus, may be used for extracting geometric information. However, the link between signature and object geometry is expected to be partly lost when radar signals are multiple reflected



at detailed objects. At buildings, radar signals are expected to interact locally with facade or roof structures. Moreover, the signal will regionally interact with adjacent buildings and the surrounding ground.

With regard to simulation methods, mapping the simulated signal contributions onto the object model is the obvious method. Thereby, the correspondence of signal responses to the object geometry can be visualized. For defining the mapping process, the following input information is required:

- ◇ 3D coordinates of the simulated signal response,
- ◇ bounce level information for each signal response,
- ◇ a 3D model of the simulated object, and
- ◇ knowledge about the imaging geometry of the virtual SAR system in the world coordinate system, i.e. the sensor position and a vector defining the sensor's line-of-sight.

For basic case studies, the simulated object may be of basic shape. However, when analyzing signatures in real VHR SAR data, the level of detail of the corresponding object model is expected to be crucial. Simulation examples given in chapter 7.1 confirm this assumption. For merging the geometrical information of signal and object, the simulated signal contributions are transformed from the image coordinate system of the SAR sensor to the world coordinate system of the object model. Thereafter, the discrete signal contributions are exported into 3D model files, where they are represented by cubes. In detail, the mapping procedure is conducted as follows.

First, a bounce level of interest has to be chosen. Moreover, the transformation can be limited to specular signals using the available flag value for specular reflection (see chapter 5.1.4). Thereafter, the corresponding data are selected based on the given constraints. Redundant geometrical information is removed for reducing the computational load. For instance, multiple-reflected signal contributions located at the same position in space are reduced to one signal sample, whose position is

$$\vec{x}_s = \begin{pmatrix} x_s \\ r_s \\ s_s \end{pmatrix} \quad (32)$$

Being defined in imaging geometry of the virtual SAR, the components of signal sample  $\vec{x}_s$  point in azimuth, range, and elevation direction, respectively. This sample is transformed into the world coordinate system by means of two rotations and one shift. First, the sensor coordinate system, which is a left system, is changed into a right system by multiplying the elevation coordinates with factor -1. is Thereafter, a rotation is performed around the azimuth axis in order to account for the look angle of the SAR system. To this end, the line-of-sight of the sensor

$$\vec{r} = \begin{pmatrix} x_r \\ r_r \\ s_r \end{pmatrix} \quad (33)$$

and the nadir direction  $\vec{v}_n$ , pointing in direction to the ground, are required in normalized form.

Then, the vector including the rotation angles in azimuth, range, and elevation is

$$\rho_1 = \begin{bmatrix} \arccos(\vec{r} \cdot \vec{v}_n) - \frac{\pi}{2} \\ 0 \\ 0 \end{bmatrix} \quad (34)$$

Second, a rotation around the z-axis has to be conducted in order to account for the aspect angle with respect to the north direction. For that purpose, the following rotation vector is used:

$$\rho_2 = \begin{bmatrix} 0 \\ 0 \\ -\arctan\left(\frac{x_r}{r_r}\right) \end{bmatrix} \quad (35)$$

Finally, the resulting signal sample  $\vec{x}_{s'}$  is shifted to the sensor position for obtaining the signal position  $\vec{x}_{s''}$  in the world coordinate system. Likewise, all other selected signal samples are transformed.

For visualization purposes, the signal contributions are exported into a 3D model file where they are represented by cubes. Color-coding of the cubes may be applied in order to represent the bounce level of the corresponding signals. The size of the cube has to be pre-defined by the operator. Eventually, the model files of both the selected signal and the simulated object can be merged in CAD software. In figure 35a, the result of the mapping procedure is presented for the basic shape of a corner reflector. The phase center is located at the corner tip and is marked in white color.

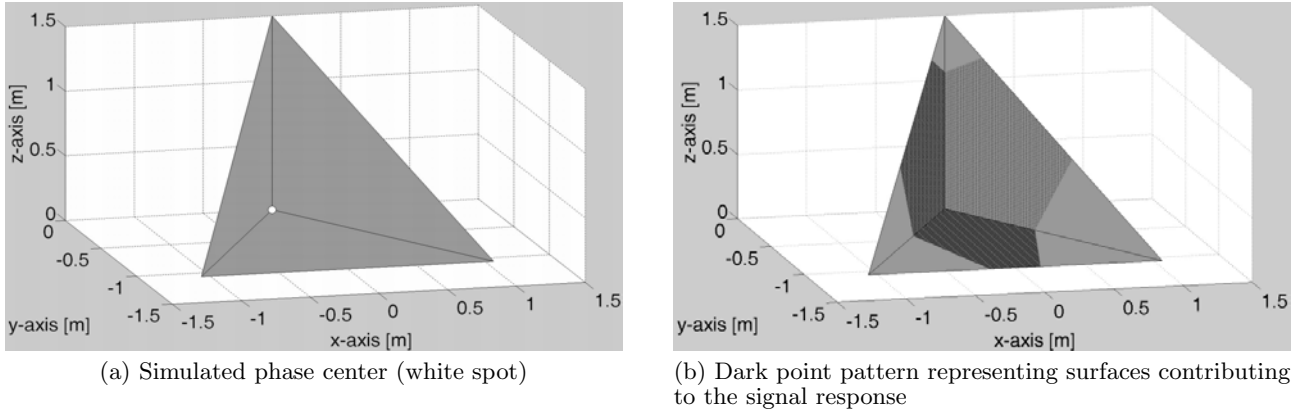


Fig. 35. 3D analysis of signal reflection at corner reflector (length of corner edges: 1.5 m). The simulation results correspond to investigations published by Sarabandi and Chiu (1996).

### 6.4.2 Identification of reflecting surfaces

Besides the localization of signal responses in 3D, the SAR simulation concept aims at the inversion of the SAR imaging process. In other words, surfaces contributing to a salient SAR image pixel have to be identified on the object model. When solving this task, the basic precondition to be met is a sufficient level of detail for the 3D object model. Hence, the object structure contributing to a signature of interest in the real SAR data has to be appropriately described by the corresponding 3D model. Normally, the object geometry will be too complex

and, hence, will not be perfectly met by the 3D model. However, the level of generalization should be low enough. Then, RaySAR enables to approximate the inversion of the imaging process of a SAR system.

As ray tracing is performed by means of samples, no surfaces are detected on reflecting objects. Instead, the distribution of intersection points can be mapped onto the object model. Thereby, the interaction of signals with scene objects is indicated. The proceeding of the mapping procedure is introduced in the following.

As explained in chapter 5.1.1, the coordinates  $X_i$ ,  $Y_i$ , and  $Z_i$  of each intersection point can be stored optionally during the sampling step. The position of the intersection points is defined in the world coordinate system of the object model. Thus, each detected signal is assigned to an intersection point. The necessary link between the azimuth-range plane and the 3D object geometry is provided by selecting a pixel of interest on the simulated reflectivity map (see chapter 6.2). The size of the selected pixel limits the search for signal contributions and, hence, also limits the search for intersection points. Redundant geometrical information is locally removed, i.e. nearby intersection points corresponding to the same bounce level are reduced to one sample. When being exported to a 3D model file, the intersection points are represented by cubes whose size has to be predefined. The area of redundancy for intersection points is equal to the cube size. Hence, no cubes of the same bounce level will overlap in the 3D model file.

In case of single bounce of a radar signal, the coordinate of the corresponding intersection point can be directly extracted from the signal vector (see equation 20). In case of higher reflection levels, intersection points of lower reflection levels have to be considered as well. For instance, a triple bounce component may be given in the signal matrix by

$$S_s = \begin{bmatrix} \cdot & \cdot & \cdot & \cdot & \cdot & \cdot & \cdot & \cdot & \cdot \\ x_{s1} & r_{s1} & s_{s1} & A_{s1} & 1 & f_{s1} & X_{i1} & Y_{i1} & Z_{i1} \\ x_{s2} & r_{s2} & s_{s2} & A_{s2} & 2 & f_{s2} & X_{i2} & Y_{i2} & Z_{i2} \\ x_{s3} & r_{s3} & s_{s3} & A_{s3} & 3 & f_{s3} & X_{i3} & Y_{i3} & Z_{i3} \\ \cdot & \cdot & \cdot & \cdot & \cdot & \cdot & \cdot & \cdot & \cdot \end{bmatrix} \quad (36)$$

where the fifth column contains the bounce level information, i.e. numbers from 1 to 3. When analyzing the triple bounce effect, the selection of a SAR image pixel will lead to the azimuth and range coordinates  $x_{s3}$  and  $r_{s3}$ . These coordinates are directly linked to the intersection point located at  $X_{i3}$ ,  $Y_{i3}$ , and  $Z_{i3}$ . At this point, the radar signal was reflected for the first time in the scene, i.e. the intersection point for the first bounce is found. Since ray tracing follows one ray after another one, the corresponding signal response is ordered with increasing bounce level (see signal matrix in equation 36). Hence, starting at the current row in signal matrix  $S_s$ , the intersection points describing the second and third bounce can be found in the two rows above. In order to enable the identification of scatterers, intersection points corresponding to a signal reflection have to be stored even if no signal is detected. For the example at hand, the first and second row of matrix  $S_s$  always have to exist to fully describe the path of the reflected signal. For SAR simulation without the identification of scatterers, these rows are not stored if the amplitude values  $A_{s1}$  and  $A_{s2}$  are zero.

In figure 35b, the surfaces contributing to the triple bounce signal of the corner reflector model are marked by a dark pattern of points. As expected, the effective reflecting surface, contributing to the specular highlight in figure 27b, is smaller than the corner surface and forms a pentagonal shape. In reality, the illuminated surface of the corner reflector will slightly change along the synthetic aperture and, thus, will be slightly different to the simulated result. However, the difference will be small due to the small angular range of the spaceborne SAR system.

The density of intersection points on the reflecting surfaces enables to visually control the sampling of the corner reflector. Eventually, color-coding may be applied for displaying different bounce levels. In the corner reflector example, color-coding is disabled since only triple reflection of the radar signal occurs.

## 6.5 Discussion

Simulated reflectivity maps only enable the visual comparison to real SAR data. Visual interpretation is hardly supported as signatures corresponding to different bounce levels may be confused. Hence, reflectivity maps can only be considered as a basic product to be used for triggering further analysis of SAR image signatures.

When assigning different bounce levels to separate layers, however, the focus can be put on signatures of interest. For instance, linear features corresponding to foreshortening can then be visually distinguished from double bounce lines. With regard to the application to real SAR data, layers containing different bounce levels can provide specific geometrical information about objects, e.g.:

- ◇ *Layer for single bounce*: provides the geometrical shape of objects in the azimuth-range plane and enables to identify layover situations. To this end, the emphasis of a signal response from the object of interest is reasonable. Moreover, the extent of shadow can be visualized.
- ◇ *Layer for double bounce*: provides geometrical information about the location of diffuse or specular double reflections. Double reflections of signals can occur at one single object, e.g. at protrusions on a building facades, or due to signal interaction with adjacent objects, e.g. a building wall and the surrounding ground.
- ◇ *Layer for triple bounce*: provides the position of signal responses corresponding to diffuse or specular triple reflections. Triple bounce of specular kind is expected to cause dominant point signatures in SAR data. Moreover, point signatures may be helpful for coregistering simulated and real SAR data as the power peak of a trihedral is always located within one resolution cell.

When creating the image layers, the signal contributions are separated based on bounce level information. Accordingly, diffuse and specular reflections of the same bounce level are integrated into one image layer. However, distinguishing between specular and non-specular signal responses should be enabled for two purposes. First, specular reflections may be underestimated by RaySAR due to inappropriate settings for the reflection models or due to local undersampling of object features. The identification of specular reflections may help to compensate for these limitations as specular signal responses are marked. Moreover, the focus should be on specular signals when exploiting the simulated data for analyzing real SAR data. The reason is that for specular reflections the geometrical correctness of azimuth focusing is higher than for diffuse reflections (see chapter 5.1.2). For distinguishing specular reflections, binary maps are created for each bounce level where specular reflections are marked. Hence, pixels containing specular signal responses from e.g. direct backscattering, dihedrals or trihedrals can be identified in the simulated data.

Height profiles can be extracted for each pixel on the reflectivity map. By analyzing the distribution of radar signals in the elevation-range plane, layover situations can be resolved. Moreover, the elevation of the simulated radar signal can be displayed with respect to a reference point on the ground. Then, the height of multiple reflected signals can be analyzed on simulated objects. The simulated profiles can be compared to height profiles from SAR tomography, which are commonly visualized in height with respect to a reference point.

For each pixel of the reflectivity map, the amplitude distribution can be simulated. To this end, the sampling stepwidth in elevation has to be defined. The radiometric correctness of

simulated amplitudes is moderate due to the simplified reflection models of RaySAR. However, the position of the simulated amplitudes can be compared to signal peaks extracted from reflectivity functions provided by SAR tomography. Comparable to the azimuth domain, the best result is expected for specular reflected signals whose signal peak is located within one resolution cell in elevation. Nonetheless, the spatial resolution of the tomographic SAR system can not be considered when simulating the amplitude distribution in elevation. Hence, as a complementary tool, scatterer histograms enable to count the number of scatterers within each resolution cell on the reflectivity map, given a spatial resolution in elevation. In this regard, the selection of relevant radar signals can be limited to a bounce level of interest. For instance, a histogram containing all bounce levels provides a general overview of layover effects in the simulated scene. Separate histograms for multiple reflections enable to recover the layover of dominant scatterers. Finally, simulated scatterer histograms may support SAR tomography based on parametric models where the number of scatterers within a resolution cell has to be known a-priori.

Height profiles in azimuth and range only provide an insight in the simulated 3D data. The nature of scatterers has to be investigated in the world coordinate system of the object. To this end, the simulated signals can be mapped into the model scene in order to merge the radar signal and the object geometry in CAD software. Thereby, the detected signal can be located on the simulated object. The 3D distribution of simulated radar signals can be compared to results provided by methods for localizing scatterers in real SAR data (see chapter 2.1.5). For identifying scatterers at objects, the surfaces contributing to an image signature can be marked in the model scene. More specifically, salient signatures can be analyzed with regard to their origin. Thus, methods focused on the exploitation of salient SAR image features can be supported, e.g. methods for object extraction/monitoring or Persistent Scatterer Interferometry (see chapters 2.1.4 and 2.1.5).

## 7 Case studies

This chapter presents results of different case studies which have been provided using the RaySAR simulator. In this context, case studies using RaySAR can be categorized either in examples for forward simulation or in examples for the inversion of the SAR imaging process (see figure 36). Forward simulation is focused on the simulation of SAR images in order to provide a rough approximation of real SAR data. Thereby, the interpretation of SAR image signatures can be supported. The potentials of RaySAR can be tested whereas the application to real SAR data is limited. Three simulation examples of that kind are given in this chapter. First, a basic 3D model of the University of Stuttgart is simulated in order to evaluate the necessary level of detail for building models (chapter 7.1.1). Thereafter, simulation results are presented for a detailed 3D model of the Eiffel Tower (chapter 7.1.2). Finally, a case study is conducted for a multi-body scene where the visual interpretation is hampered by the overlay of signatures (chapter 7.2).

The inversion of the SAR imaging process requires a geometrical link between simulated and real signatures. In this regard, the modeling step is crucial for the correctness of simulation results. Based on output data provided by the ray tracer, the origin of signal contributions can be analyzed on the 3D object model. In chapter 7.3, the capability of RaySAR for analyzing the nature of scatterers is shown for an urban scene containing the main railway station of Berlin. Salient persistent scatterers are selected on a SAR image and are linked to simulated signatures. Simulated height profiles are compared to results from SAR tomography. Moreover, the 3D positions of simulated signatures, which correspond to persistent scatterers, are found in the model of the urban scene. Finally, the reflecting surfaces contributing to signatures of interest are identified.

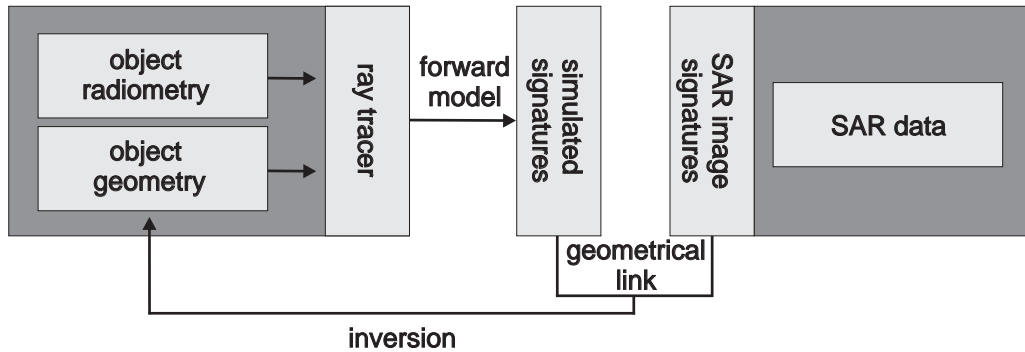


Fig. 36. Case studies: forward simulation and inversion of SAR imaging process.

### 7.1 Differences in the level of detail

#### 7.1.1 University of Stuttgart

The first case study is conducted for the building complex of the University of Stuttgart, Germany, which has been imaged by TerraSAR-X. In figure 37a and figure 37b, a top view and a perspective view onto the building complex are shown. The urban scene contains two almost similar buildings surrounded by ground which is covered by grass, concrete or asphalt. Figure 37b approximately visualizes the line-of-sight of TerraSAR-X with respect to the buildings. For both buildings, one facade characterized by rows and columns of windows and one facade containing two columns of windows are imaged by the SAR sensor. The roofs are partly covered by building parts of cuboid form and by metallic structures.

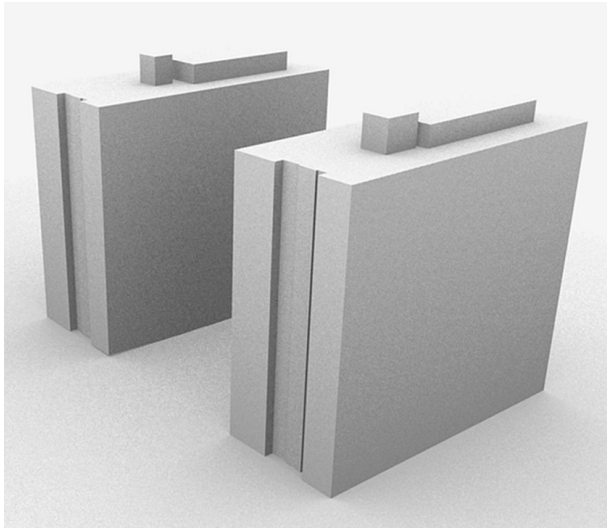
A refined 3D building model is used for simulating SAR images of the university. Figures 37c and 37d depict the coarse 3D model, taken from the 3D city model of Stuttgart and the refined 3D model of the university, respectively. Increasing the level of detail of the 3D model has been conducted based on facade grammar (Becker, 2009). For the model at hand, the grammar has been defined by introducing a-priori knowledge derived by analyzing photos of the facade. Still, the correctness of the resulting building model is limited since facade structures have been synthesized purely based on grammar rules. For instance, the size and location of windows will be slightly different compared to reality. However, the 3D model enables a case study on multiple reflections occurring at windows.



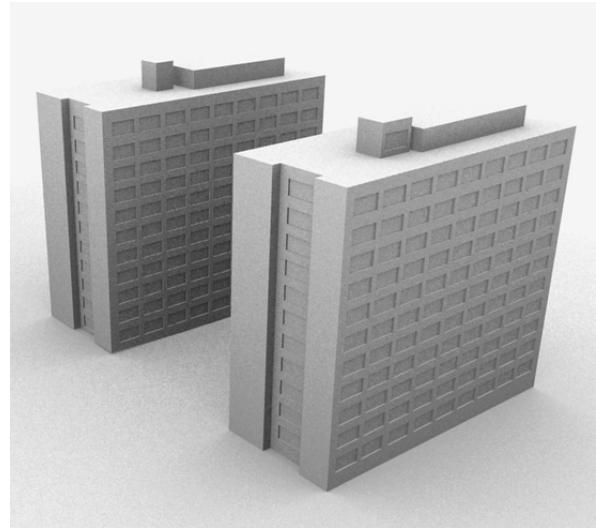
(a) Top view (screenshot from Google Earth™ viewer; ©AeroWest, 2010)



(b) Perspective view ©Bing Maps™



(c) Basic city model



(d) Refined city model based on facade grammar (Becker, 2009)

Fig. 37. University of Stuttgart: urban scene and modeling.

The surfaces of the model parts are characterized as follows. Building surfaces show strong specular reflection and low diffuse reflection what is based on the assumption that concrete is smooth compared to the 3 cm wavelength of the radar signal. The ground is covered by different kinds of materials such as grass or concrete which are represented by one single plane in the 3D model. In order to visualize shadow and diffuse double bounce lines, moderate diffuse reflection and weak specular reflection is assumed for the ground. The imaging geometry of the virtual SAR is adapted to the real data. For sampling the 3D model, the density of rays in azimuth



and elevation is set to 0.1 m and 0.1 m, respectively.

In figure 38, real data and different simulation products provided by RaySAR can be compared. The TerraSAR-X spotlight image of the building complex was acquired on May 12, 2008, from an ascending orbit in VV polarization with a local angle of incidence of  $37.1^\circ$  (see figure 38a). The pixel spacing of the SAR image is 0.75 m times 0.75 m in azimuth and ground range, the spatial resolution of the SAR image is 1.69 m times 2 m, respectively. For visualizing weak and strong signatures on the same image, the SAR image has been clipped at 17% of its intensity maximum. The direct backscattering from building walls seems to be weak as building outlines are hardly visible. Overall, the appearance of the university buildings is mainly characterized by point signatures. For facades facing the SAR sensor, intensity peaks are less in numbers and smaller than for facades not oriented to the SAR sensor, where intensity peaks form a bunch of point signatures.

The pixel spacing of simulated maps is adapted to the TerraSAR-X image. As the level of detail of the building model is moderate, the reflectivity map is restricted to bounce levels 1-3 (see figure 38b). As expected, the radiometric correctness of the reflectivity map is limited due to the overestimation of diffuse signal contributions, e.g. from the ground. However, the geometrical distribution of linear and point-like signatures is confirmed. The linear signatures are linked to diffuse double bounce occurring due to Lambertian backscattering from the ground. Facades are represented by point patterns which are caused by triple reflections at windows. The spatial distribution of triple bounce signals is shown in figure 38c and enables to visually interpret a high number of salient signatures in the real SAR data. Facades not oriented in direction to the sensor are characterized by a high density of point signatures in azimuth what is clearly visible on the SAR image as well. For the building on the right, several columns of simulated point signatures can not be distinguished on the SAR image. The reason may be that ground objects located within the layover area of the building disturb the signal response from the facade. As the ground is represented by a flat plane, ground objects are not considered in the 3D model. Moreover, polarimetric effects, not accounted for in the simulation, may cause the prevention of signal peaks. As the SAR data are captured in VV polarization, specular reflections near the Brewster angle may extinguish (see figure 17). Finally, irregularities at windows may prevent the occurrence of point signatures.

For the urban scene at hand, triple reflections of radar signals provide the most prominent signatures. One major reason may be that most signatures are linked to specular reflections. This assumption is supported by the simulated specular map which reveals that the simulator mainly detected triple reflections of specular type (see figure 38d).

Convolving the reflectivity map with the 2D SAR system response reveals that point signatures form lines which can be distinguished at the left building on the TerraSAR-X image as well (see figure 38e). Diffuse backscattering from the ground is suppressed. The spatial resolution on the simulated map has been chosen as being half of the resolution of the real SAR sensor, i.e. 0.85 m x 1 m in azimuth and ground range.

As shown in figure 12b, dominant point signatures representing building facades are selected as candidates for PSI. If the deformation signal has to be monitored for single buildings, relevant PS candidates have to be distinguished from irrelevant ones. To this end, RaySAR may provide a-priori knowledge for PS selection by characterizing the object layover in the azimuth-range plane. In figure 38f, the simulated layover area is shown for the University of Stuttgart. The diffuse backscattering from the ground has been removed. In contrast, building surfaces are assigned with strong diffuse backscattering. Eventually, the binary image describing the layover area is derived by simulating a reflectivity map which is restricted to reflection level 1 and clipped at a low amplitude level.

To conclude, the first case study reveals that basic facade details may be sufficient for representing a high number of prominent signatures representing buildings in SAR data. This is



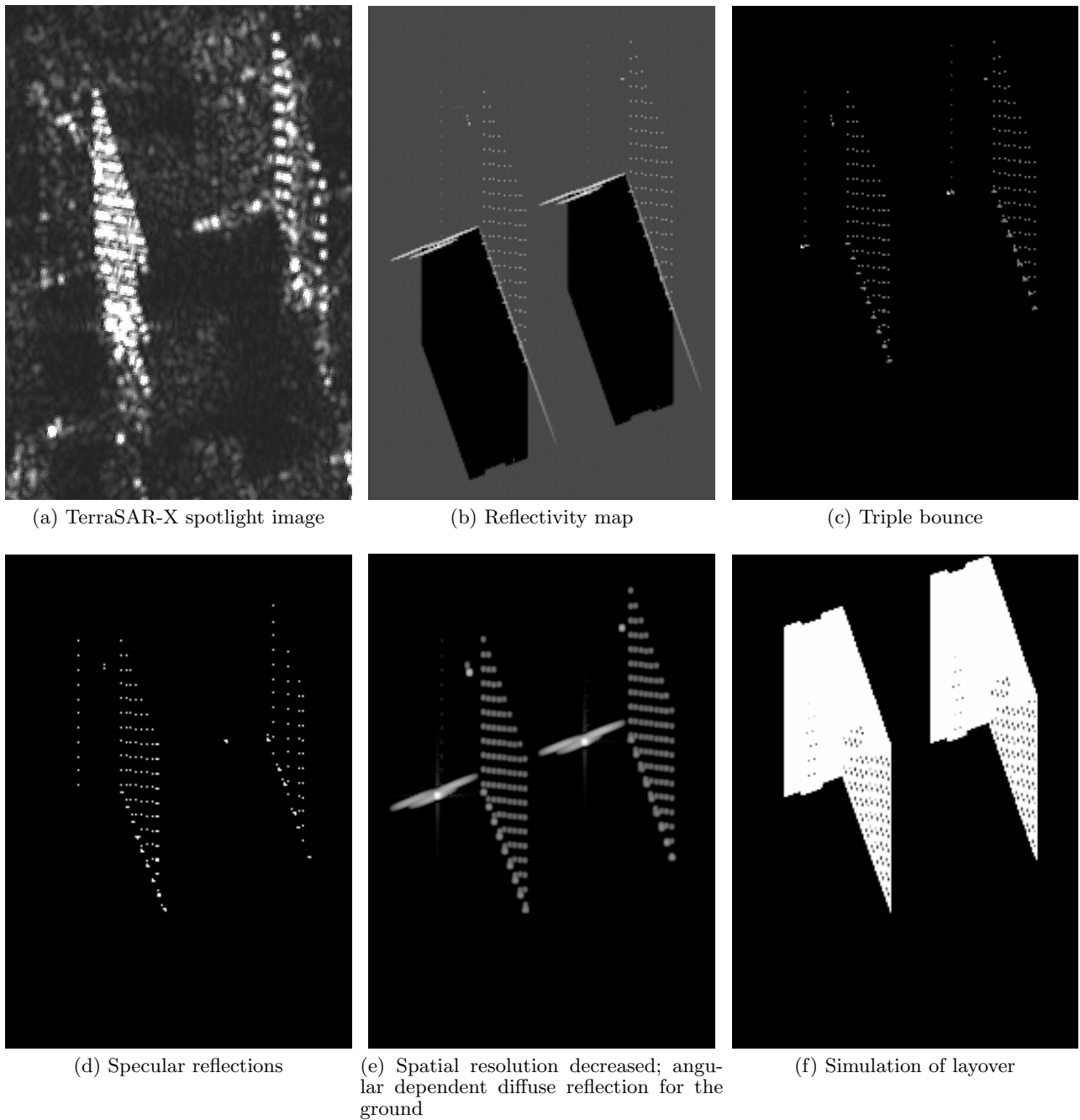


Fig. 38. TerraSAR-X vs. different simulated maps for the University of Stuttgart, Germany. Ground-range: top-down.

promising in the context of urban applications as for the majority of urban objects only basic 3D models are available. The simulation of 2.5D building models is reasonable for providing layover masks or for simulating the extent of shadow areas. If multiple reflections have to be confirmed, these models have to be refined with basic facade details such as windows or balconies.

### 7.1.2 Eiffel Tower, Paris

The geometrical reliability of the simulated reflectivity map depends on the level of detail of the 3D model scene. A highly interesting example for visually comparing simulated SAR images with real VHR SAR data is the Eiffel Tower, Paris. A top-view onto the urban scene is given in

figure 39a. The tower, distinguishable in the center of the image, is surrounded by vegetation (trees, bushes, meadows) and asphalt, which is mainly found beneath the tower.



(a) Top view on Eiffel Tower (screenshot from Google Earth™ viewer; ©Aerodata International Surveys, 2010); north direction: bottom-up.



(b) 3D model (Eiffel, 2011)

Fig. 39. Eiffel Tower: urban scene and 3D model.



(a) Crossbars



(b) Rows of lambs distributed all over the tower surface



(c) Rivets on tower surface

Fig. 40. Details of Eiffel tower, Paris. Crossbars and vertical bars are partly covered with lambs and rivets.

In figure 39b, the 3D model of the Eiffel Tower is seen which is available on the Eiffel Tower homepage for non-commercial purposes (Eiffel, 2011). It shows a high level of detail as it is composed by 9.488 facets. However, even if basic structures such as vertical bars or cross-bars (see figure 40a) are represented, the 3D model still lacks in details. For instance, the cross-bars are approximated by flat patches what is close to reality. However, a closer look reveals that the cross-bars are characterized, for instance, by rows of lambs or round rivets (see figure 40b and figure 40c). Thus, direct backscattering or multiple reflections of radar signals at those details

can not be confirmed by the simulator. Comparable to the university example in chapter 7.1.1, a compromise is necessary when defining the surface parameters of the tower.

Strong specular reflection and a high reflectivity factor are assigned to all tower surfaces. In addition, weak diffuse backscattering is added for roughly approximating local multiple reflections at the crossbar details explained above. Since double bounce contributions caused by the interaction between tower and ground are of interest, a flat plane is defined beneath the tower model. It is characterized by low diffuse reflection in combination with strong reflectivity.

The imaging geometry of the virtual SAR, i.e. the angle of incidence and the heading angle, is adapted to the TerraSAR-X orbit. To this end, the tower is rotated and the local incidence angle is set to  $34.6^\circ$ . The number of rays in the azimuth-elevation plane is set to 1.000 in azimuth times 4.000, resulting in a sampling density of 0.1 m times 0.1 m. Sampling the 3D model yields 4.13 million signal contributions.

For providing the reflectivity map, the pixel sampling is adapted to the sampling of the real SAR data, i.e. 0.43 m x 0.4 m in azimuth and ground range. The maximum number of reflections is set to 5 (figure 42a). In sum, the sampling of the 3D model and the creation of the reflectivity map take 5 minutes and 14 seconds on a standard PC (2 GHz Dual Core, 4 GB RAM).

For comparison, a temporal average image has been created based on 6 TerraSAR-X spotlight datasets. Hence, the appearance of the Eiffel Tower on the SAR image is characterized by deterministic reflection effects as speckle is reduced (see figure 41a). Signal responses from the tower as well as from distributed scatterers on the ground are distinguishable. Due to a multi-looking factor of 2 in azimuth and range, the pixel spacing in the SAR image is 0.86 m x 0.8 m in azimuth and ground range.

Figure 41 contains two simulated reflectivity maps. On the first one, signal contributions have been added non-coherently. For creating the second reflectivity map, the coherent summation of signal components has been considered (see figure 41c). On this map, the appearance of the tower components is more difficult to be distinguished as the layover of radar signal may cause the extinction of signal amplitudes. The coherently summed reflectivity map is more realistic than the non-coherently summed one. However, the appearance of the Eiffel Tower can be better visually interpreted in figure 41b.

Compared to the real SAR image, many signatures are clearly visible on the reflectivity map as well. The shortest distance with respect to the SAR sensor is obtained for the pinnacle (marked by letter *A*), followed by cross beam structures (*B*) in higher regions of the tower, two main platforms (*C*, *D*), three visible feet of the tower (*E*, *F*, *G*) and the shadow zone (*H*). During the sampling step, a low amount of signal power penetrated the cross beam structures and caused single bounce backscattering from the background of the tower. By contrast, this region is almost completely shadowed in the SAR image. This might appear due to signal diffraction at tower crossbeams which is not considered in the simulation process. Moreover, the 3D model does not contain any structures in the interior of the tower what is different to the real tower (see figure 39b and figure 40a).

In the 3D model used for SAR simulation, objects in the neighborhood of the tower are neglected since the ground is represented by a flat plane. Hence, the overlay of radar signals from tower and ground objects can not be confirmed by RaySAR but is clearly visible on the real SAR image. For instance, signatures *C* – *G* are overlaid with diffuse signals from vegetation or man-made structures in the neighborhood of the tower.

Double bounce signatures caused by signal interaction with the tower and the surrounding ground show up at the bottom (*I*) and at both sides of the tower (*J*, *K*). While signature (*I*) is also apparent on the real SAR image, signatures (*J*) and (*K*) are not distinguishable. On the one hand, these signatures may disappear because of objects covering the ground which avoid signal backscattering to the sensor. Moreover, the diffuse reflection from the ground is defined



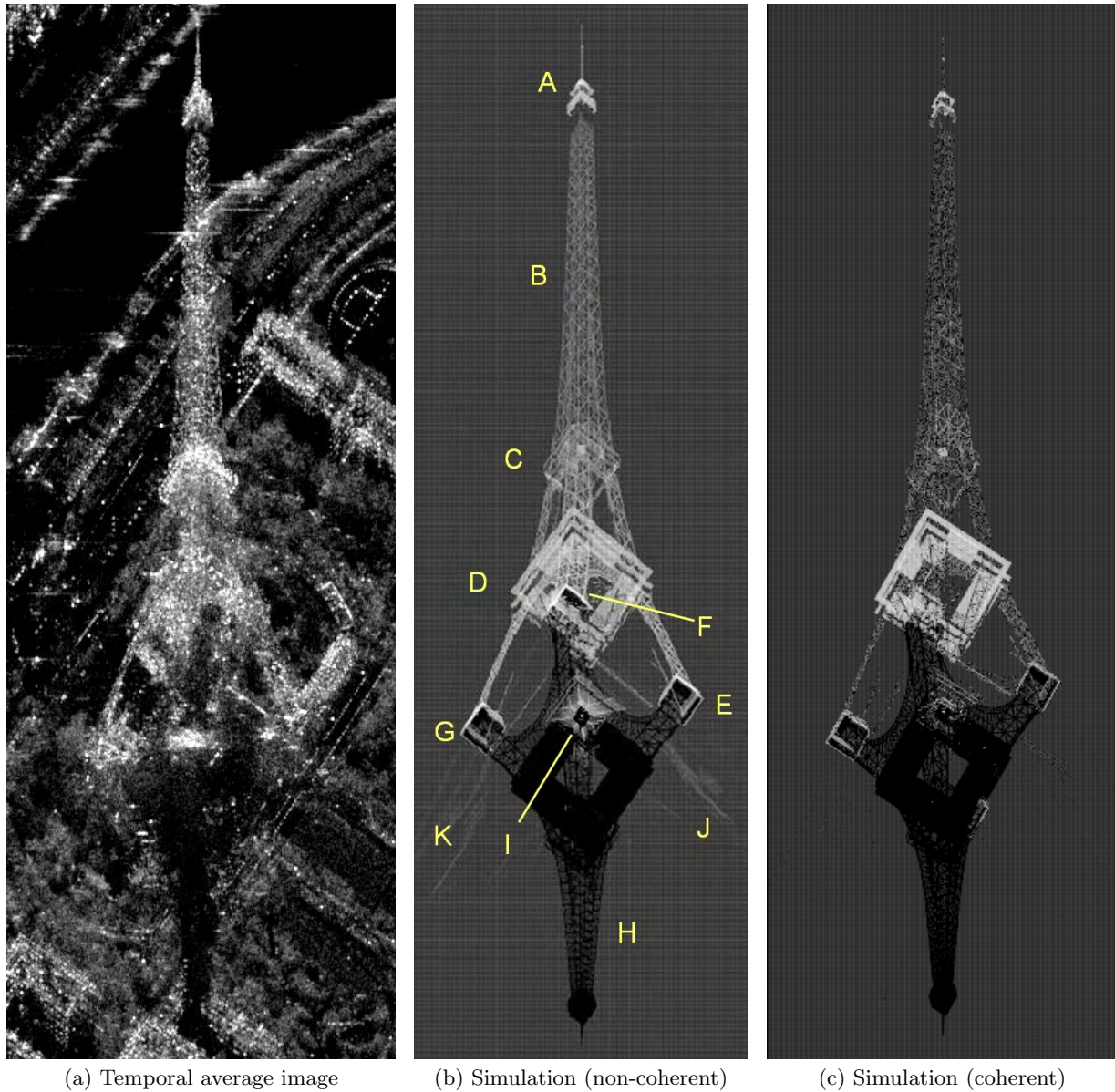


Fig. 41. TerraSAR-X vs. simulation for the Eiffel Tower. Visible tower components A: pinnacle; B: cross beam structures; C,D: platforms; E,F,G: feet; H: shadow zone; I,J,K: double bounce contributions between tower and surrounding ground; Ground range: top-down.

as being of Lambertian type, i.e. almost independent on the angle of reflection. In reality, diffuse signal components commonly dependent on the reflection angle. Therefore, the diffuse signal components in the Eiffel Tower scene are overestimated by RaySAR.

Assigning the signatures  $A - K$  to single and double bounce is enabled due to separate image layers for different reflection levels (see single bounce in figure 42b and double bounce in figure 42c). The distribution of the simulated signal samples is visualized in figure 42a. However, signal contributions having a bounce level higher than two are too weak to be distinguishable on the reflectivity map.

The second case study reveals that the potential of RaySAR depends significantly on the level of detail of simulated object models. However, even for object models characterized by a high level of detail, a compromise may be reasonable when defining surface properties. For instance, the assumption of pure specular reflection for the Eiffel Tower model would have only enabled to confirm double reflections occurring due to signal interaction with the ground and the tower.

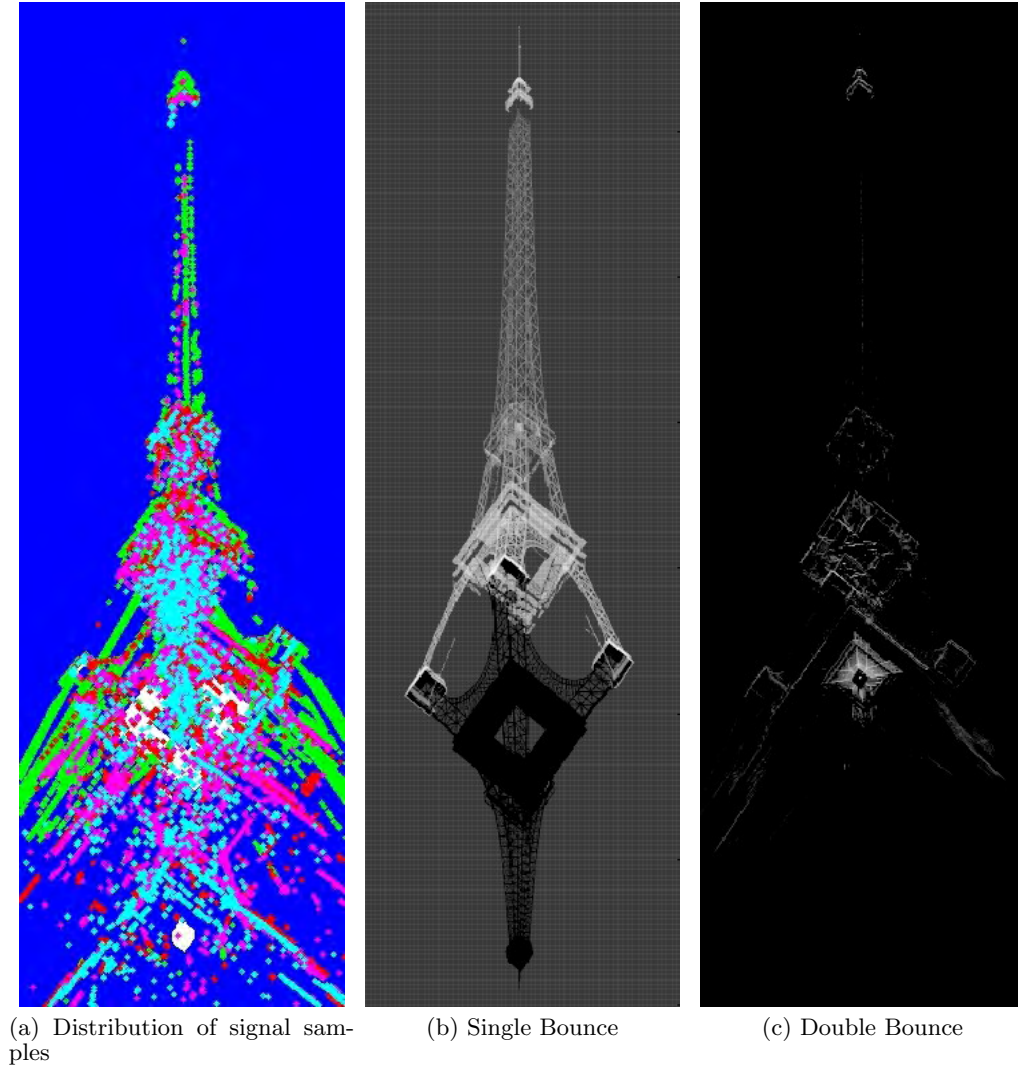


Fig. 42. Separation of bounce levels for the Eiffel Tower; Distribution of reflection levels: single bounce (blue), double bounce (green), triple bounce (red), fourfold bounce (magenta), fivefold bounce (cyan); Ground range direction: top-down.

Thus, the appearance of the cross-bars would have missed on the reflectivity map. For visualizing the shape of the Eiffel Tower in the simulated data, details of very small size such as lambs or rivets are generalized to a certain kind of surface roughness. Compared to the real SAR data, RaySAR enables a detailed simulation of the appearance of objects in the azimuth-range plane, even if physical effects are neglected. Moreover, the Eiffel Tower case study confirms that developing simulation methods based on given software is reasonable as simulation products can be provided within a short amount of processing time.

## 7.2 Multi-body scenes: Wynn Hotel, Las Vegas

### 7.2.1 Simulation of 2D maps

Multi-body scenes enable to test the capability of RaySAR to resolve layover situations. To this end, the area surrounding an object has to be represented in the simulated 3D model. For a case study on SAR simulation in 3D, the Wynn hotel in Las Vegas, USA, has been chosen. By coincidence, the concave surface of the hotel is oriented perpendicularly to the flight path of TerraSAR-X. The urban scene, shown in figure 43, also includes adjacent man-made structures

surrounding the building complex. The 3D model has been taken from the Google Earth<sup>TM</sup> warehouse (Google, 2011). Compared to reality, the 3D model is strongly generalized. For instance, the hotel facade is approximated by flat surfaces. In reality, horizontal protrusions are present on each floor of the building (indicated by white stripes on the left part of figure 43). Building components surrounding the hotel partly differ from their real appearance, as is seen on the right of figure 43. However, the level of detail of the 3D model is sufficient to enable a case study on SAR simulation in elevation direction. The ground beneath the hotel complex is represented by a flat plane.

For the processing of real SAR data, a stack containing 16 TerraSAR-X VHR spotlight datasets is available for tomographic analysis. The angle of incidence of the master scene is  $32.7^\circ$ . In elevation direction, the sensor positions are distributed within an orbital tube of 270 m. A TerraSAR-X image of the urban scene is shown in figure 44a with range direction pointing top down. It has been created by averaging all SAR datasets within the stack. Straight and curved linear signatures as well as dominant point signatures can be clearly distinguished. Signal components directly backscattered from the hotel are overlaid with signal components from adjacent buildings and vegetation located in front of the hotel.

Starting at near range, the first eye-catching signature has the shape of a curved rectangle whose transparent area seems to be framed by a bright border (signature *A*). The corresponding reflections are assumed to appear at the roof of the hotel. Afterward, several lines are distinguishable on the right part of the image showing strong contrast to the background (signature *B*). Surprisingly, the hotel facade is almost invisible on the SAR image apart from three rows of point signatures aligned in range direction – signatures  $F_1$ ,  $F_2$ , and  $F_3$  – likely caused by dihedrals or trihedrals on each floor of the building. Moving on in range direction, the transparent part ends at a bright arc which is assumed to contain double bounce contributions derived by signal interaction with the hotel wall and the surrounding ground (signature *C*). Finally, after a region characterized by smeared appearance (signature *D*) and another smeared line orientated in azimuth direction (signature *E*), a short shadow region appears.

For simulating images in the azimuth-range plane, both the geometric and the radiometric parameters of the 3D model have to be defined. The imaging geometry of the virtual SAR, i.e. aspect angle and angle of incidence, is adapted to the real SAR. While the angle of incidence is given by the orbit parameters of TerraSAR-X, the aspect angle with respect to the building is roughly approximated.

The radiometric parameters are chosen as follows. For all components of the scene, high specular reflection is used for representing direct reflections from flat and partly metallic surfaces. As the level of detail is low, low diffuse reflection is added as well in order to visualize the geometrical extent of objects. The reflectivity is assumed as being of a high level. Thus, the simulation is concentrated on the visualization of multiple reflections.

After sampling the scene by means of the ray tracer, a reflectivity map is created (see figure 44b). The pixel size of the map is adapted to the real SAR image. Analyzing the image from near range to far range, the layover effect mentioned above is confirmed.

Signature *A* is also represented on the simulated image and is linked to the roof. In contrast to the real SAR image, the curved rectangle is not transparent since diffuse reflection has been assigned to all parts of the roof. As visible in the layer dedicated to double bounce, the assumption of signature *C* to be caused by double bounce between the hotel and the surrounding ground is confirmed by the simulator (see figure 44c).

While the outline of the shadow zone is similar in both images, the linear signature *E* is only partly confirmed by the simulator and marked with bounce level 4 (see figure 44d). Two out of three vertical dashed lines, labeled by letters  $F_1$  and  $F_3$ , are linked to double bounce occurring at the hotel wall (see figure 44c). The linear appearance does not correspond to reality, as the



signatures in the real SAR image are composed by rows of points. The reason for the difference is the absence of wall protrusions on the 3D model of the hotel which are present on each floor of the building. For instance, the number of floors can be derived by counting the number of points corresponding to signature  $F_1$ . Likely, adding the protrusions to the 3D model would lead to the dashed appearance of the signatures in the simulated map.

The lack of protrusions also leads to the fact that signature  $F_2$  misses in the simulated map. In reality, the protrusions enable specular double bounce on each floor of the building, what leads to a group of linear signatures. The 3D model used for SAR simulation lacks of those details and, hence, no double bounce signal is obtained.

Signatures  $B$  and  $D$  do not appear on the reflectivity map. Possible reasons may be limitations of RaySAR with regard to the simulation of diffuse signal contributions, the moderate level of detail of the building model, and inappropriate modeling of the reflection behavior of surfaces.

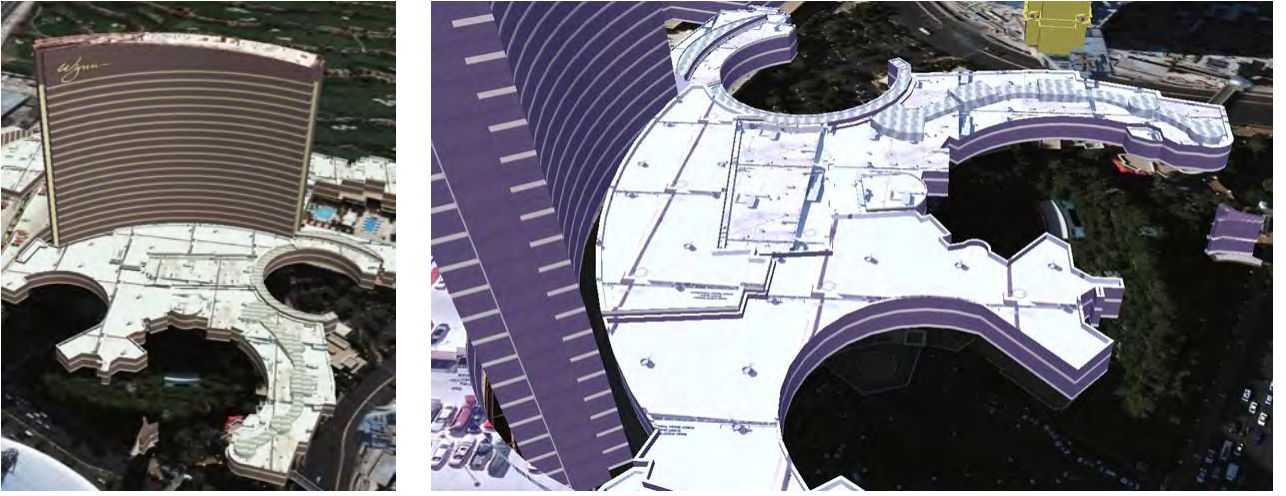


Fig. 43. 3D Model of Wynn Hotel, Las Vegas (USA); ©Google Earth™.

### 7.2.2 Scatterer histograms

Based on the simulated reflectivity map, scatterer histograms can be derived (see chapter 6.3.3). As elevation coordinates of detected signals are provided by the ray tracer, scatterers within the same resolution cell can be separated. The histogram for the Wynn Hotel model is shown in figure 45a and indicates the number of scatterers for each image pixel. Both the sampling of the histogram as well as the image margins are equal to the reflectivity map shown in figure 44b. The resolution of the virtual SAR system is set to 20.25 m. Layover areas are marked by green, yellow and orange color for two, three and four scatterers per pixel, respectively.

Compared to the SAR image in figure 44a, it is interesting to see that areas containing several scatterers do not necessarily show bright appearance. This is due to the fact that most of the overlaid signals are single bounce contributions of diffuse type, which show lower intensity than, for instance, focused double bounce lines. The assumption of a dominance of diffuse single bounce within the scene is confirmed by the histogram in figure 45b), which only separates signal contributions of bounce level 1 for each pixel. Double bounce signals appearing at building walls are focused at the same height than single bounce signals and, hence, are mostly not distinguishable on the histogram in figure 45a.

Scatterer histograms may support the interpretation of results derived from 3D SAR tomography. Moreover, a-priori knowledge could be introduced into the tomographic analysis based on parametric models.

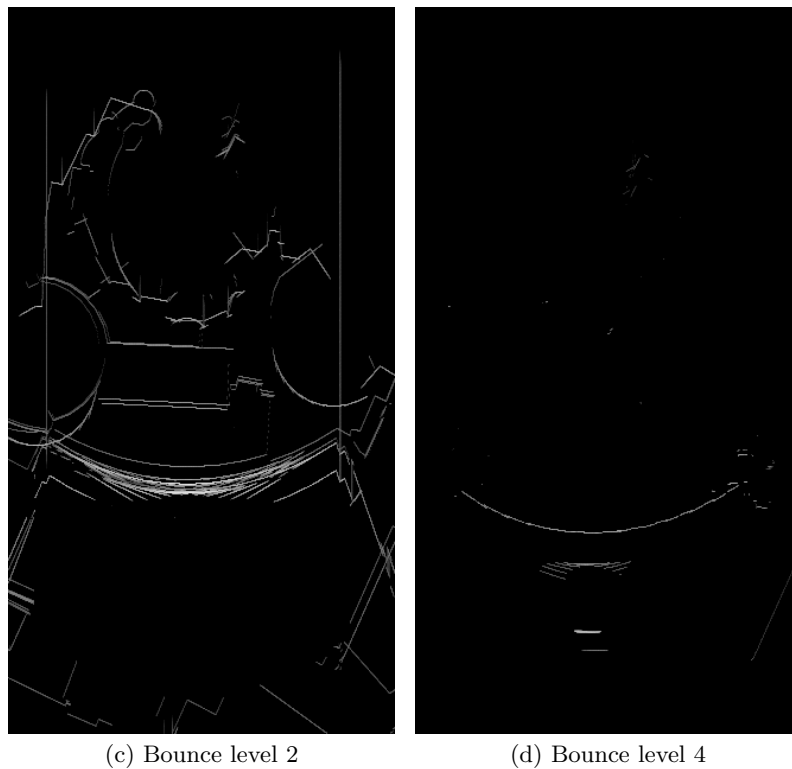
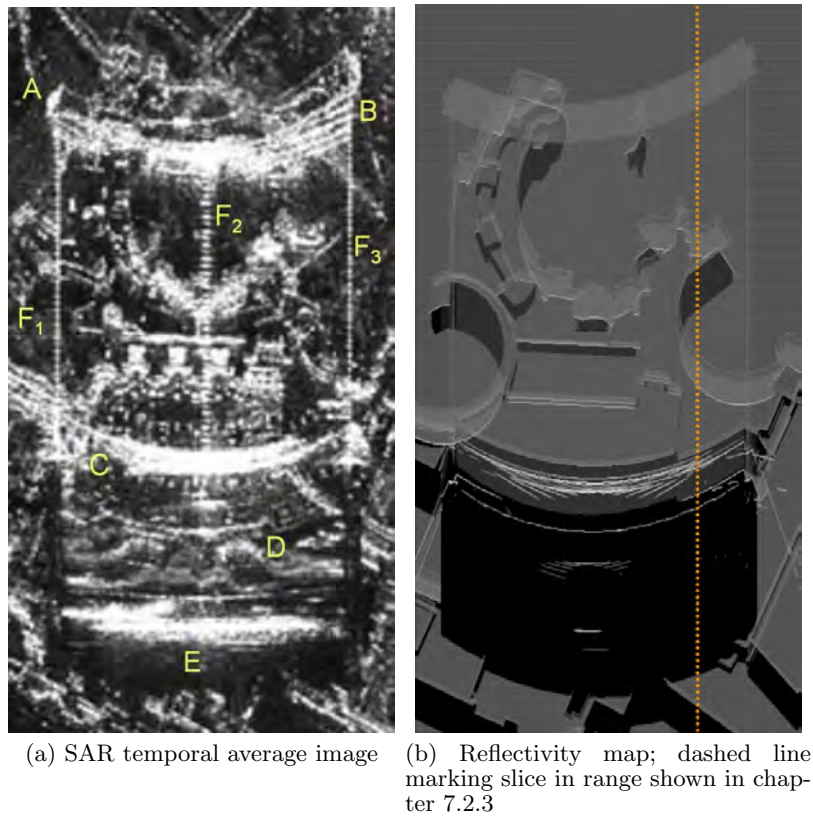


Fig. 44. Wynn Hotel: SAR image vs. simulation; left: VHR spotlight TerraSAR-X image; right: simulated reflectivity map; range: top-down.

### 7.2.3 Height profiles for visualizing elevation information

Besides scatterer histograms, RaySAR provides further tools for analyzing the position of signal samples in elevation. As shown in chapter 6.3.1, single pixels can be selected on the reflectivity



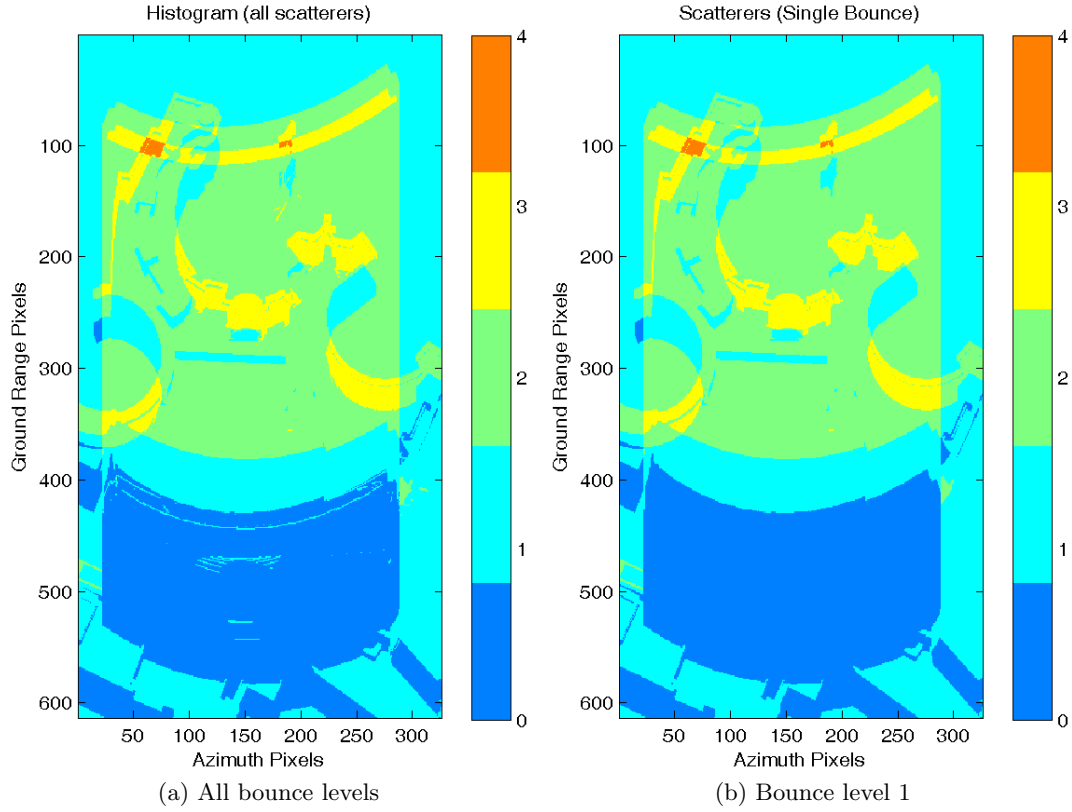


Fig. 45. Scatterer histograms indicating the number of scatterers for each resolution cell; range: top-down.

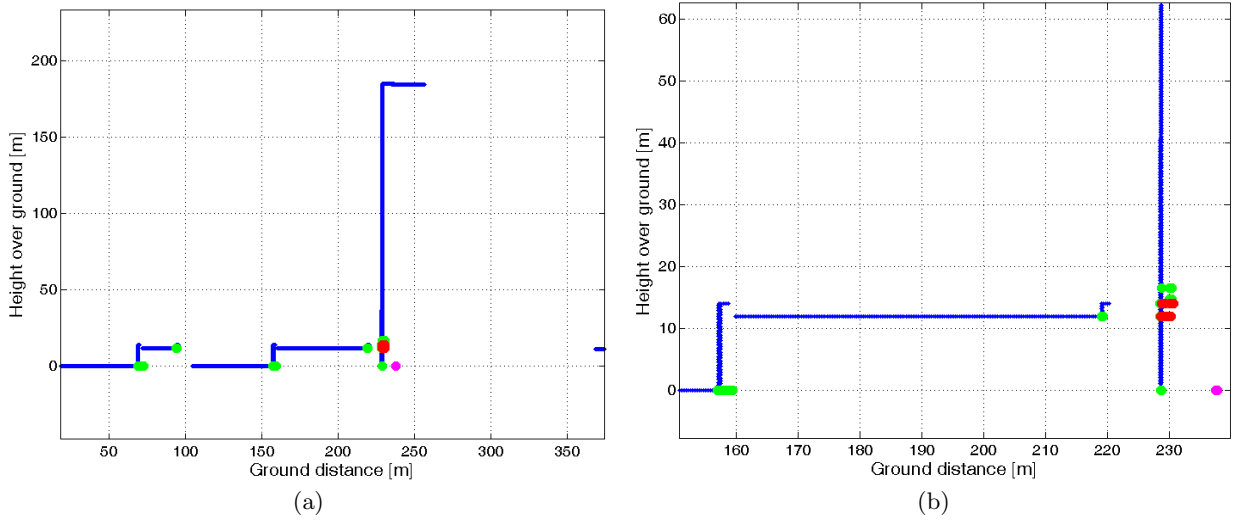


Fig. 46. Wynn Hotel: slice in range; blue: single bounce, green: double bounce, red: triple bounce, magenta: fourfold bounce. Artificial corners appear at the front wall of the hotel; Some multiple reflected signals are located within the hotel.

map for defining slices oriented in azimuth, range and elevation. Afterward, the relevant signal contributions are gathered for each slice according to the dimensions of the pixel on the image and the elevation interval to be displayed. In case of the Wynn hotel example, a pixel has been marked within the frame representing the building roof. The corresponding range profile is indicated by a dotted line in figure 44b.

In figure 46, the corresponding height profile is shown. Height values are defined with respect

to the height level of the surrounding ground. Single bounce contributions, marked in blue, are distributed all over the building surfaces and the ground. This is related to the fact that low diffuse backscattering has been assigned to all surfaces of the 3D model. Double bounce contributions appear at building walls and are focused to points marked in green. Besides, signal components of bounce levels 3 and 4 are found and are marked in red and magenta. These contributions are located near the bottom of the hotel facade. Due to shadowing, the full shape of the building is not represented.

A zoom into the height profile is shown on the right part of figure 46, visualizing the ground distance interval between 160 m and 240 m. The majority of the double reflections are found at the intersection between horizontal and vertical surfaces. However, some signal contributions of bounce level 2 and 3 are localized on the facade or even on the inside of the building. These signal components do not correspond to real building corners of the hotel. For instance, the elevated double bounce contributions occur due to signal interaction with roof structures in front of the building (ground distances: approx. 160 m - 215 m, 217 - 220 m) and the hotel facade. The fourfold bounce signal within the hotel occurs since the spatial distance followed by the corresponding radar signals is longer than for double or triple reflections.

As shown by the Wynn hotel example, multi-body scenes considering the surrounding of simulated objects are required for representing layover scenarios. Multiple reflections are not always bound to one single building but may occur due to signal interactions with different buildings. Scatterer histograms support the visual interpretation of layover effects on SAR images and may be used for providing a-priori knowledge about the number of scatterers for each resolution cell. Height profiles help to resolve layover situations and to analyze the correspondence of signal contributions to building details. However, height profiles do not enable to visualize the distribution of signal responses in 3D but only give a small insight to the elevation domain. A case study on 3D applications of RaySAR is presented in the following.

## 7.3 Analysis of scatterers: main railway station, Berlin

### 7.3.1 Characteristics of urban scene

For the application of RaySAR to real SAR data, a local urban scene is chosen which includes the main railway station of Berlin, Germany. Figure 47 shows a perspective view onto the building complex. In the center part of the building, two building components of cuboid form cross the rail tracks. In the following, these building components are referred to as *building part 1* and *building part 2*, respectively. The building parts are linked by a roof made of glass and metallic bows. A tower of triangular cross-section is situated next to building part 2. It is characterized by vertical and horizontal stripes which form little corners at the intersection points. The railway is covered by a roof which is curved along and across the rail track. The glassy surface of the roof is stabilized by metallic bows.

Both building parts 1 and 2 show regular structures as, for instance, five floors are stabilized by vertical and horizontal bars made of metallic material. A closer look onto the building facade is shown in figure 48. The facade is characterized by glassy surfaces which are connected by metallic stripes. Parts made of concrete can be seen through the glass patches between the horizontal iron bars (see center of figure 48). Both the vertical and horizontal bars show linear protrusions in vertical and horizontal direction, respectively, which intersect at each floor of the building (see right of figure 48).

The motivation for simulating the building complex of the main railway station in Berlin is the simultaneous availability of persistent scatterers (PSs) and a geometrical description of facades. For PSI processing, 20 TerraSAR-X spotlight images have been captured on a descending orbit



Fig. 47. Perspective view onto the central part of the main railway station, Berlin. Two building components of cuboid form: building part 2 (left), building part 1 (right). Tower of triangular cross-section located on the left.

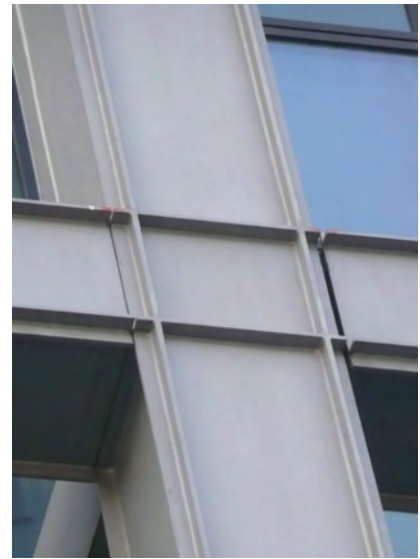


Fig. 48. Structure of the main railway station, Berlin. Left: Horizontal and vertical bars surrounding the building. Center: The facade is made of glass and partly covers concrete separating different floors of the building. Glassy surfaces are connected by metallic structures. Right: Corners occurring at the intersection area between horizontal and vertical bars. For all floors of the building, these corners can be found on the front and back side of the vertical bars. Corner sidelength: approx. 5 cm.

with a heading angle of  $190.670^\circ$  with respect to the north direction and a local angle of incidence of  $36.063^\circ$ , both angles corresponding to the center of the railway station in azimuth and range. During PSI processing, a temporal average image is generated in ground range geometry which is shown in figure 50. It has been created by averaging the SAR datasets of the stack in order to reduce random scattering. The spatial resolution of the SAR image is 1.10 m in azimuth and 0.6 m in slant range, the pixel spacing is 0.433 m and 0.383 m, respectively.

Different clipping levels can be chosen in order to emphasize SAR image signatures of interest. In figure 50a, the intensity of the image has been clipped at 3.4% of its maximum intensity. Patterns of point signatures are visible as well as the diffuse signal response from surfaces. The width of point signatures is large as the signal mainlobe is cut at a low level. For improving the





Fig. 49. 3D model of the main railway station, Berlin, shown in the Google Earth™ viewer. The model has been provided by the Berlin Business Location Center (Virtual-Berlin, 2011), State of Berlin. Image: ©AeroWest, 2010.

localization of the point signatures in the azimuth - ground range plane, the intensity peaks have to be clipped at a higher level, e.g. as shown in figure 50b. In this case, the intensity threshold was set to 34.7%.

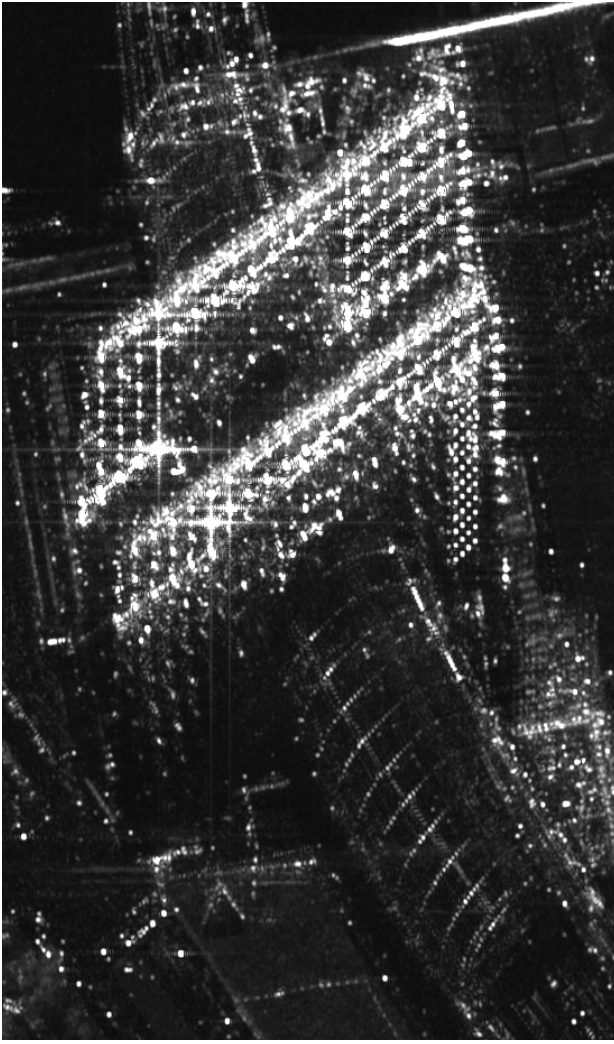
For SAR simulation, a 3D building model is used which has been created based on architectural plans (see figure 49). It has been provided by the Berlin Business Location Center (Virtual-Berlin, 2011), State of Berlin. The model is part of a city model of Berlin which can be imported into Google Earth by means of a .kmz-file. Realizing the city model of Berlin was financially assisted by the European regional development fund (ERDF).

When comparing the 3D model to the real building, the building parts 1 and 2 are strongly generalized. Facade details such as the horizontal and vertical stripes connecting the glass patches are not considered. Likewise, the small corners on the tower are only represented by texture information. Hence, corner reflections occurring at the tower will miss in the simulation result. Although generalized, the basic facade features, i.e. the vertical and horizontal iron bars, are geometrically represented. The main difference compared to reality is the representation of horizontal bars by means of balconies. In reality, the bars are isolated from the facade (see figure 48).

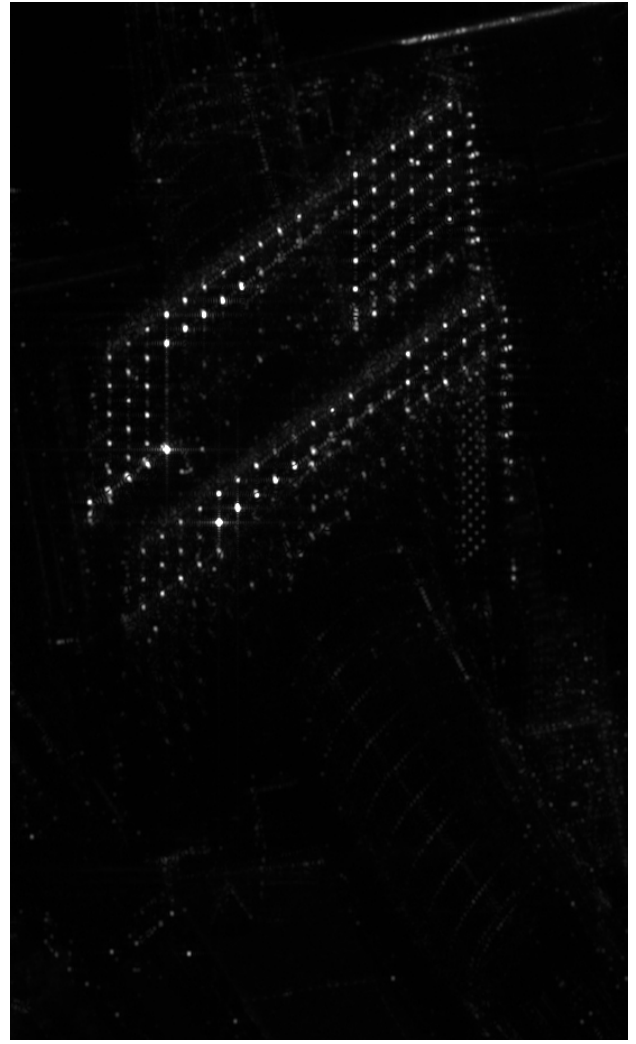
First, texture information for model surfaces is removed as only the geometrical description of the model is used. A flat surface is defined beneath the above-ground parts of the railway station in order to represent the ground level. Since the basic geometry of the building is given by the 3D model, the diffuse RaySAR reflection model is deactivated while the reflection model for specular reflection also represents the angular dependence of diffuse reflections. The simulation is focused on building parts 1 and 2 as the regularity of structures is expected to be responsible for the occurrence of PSs.

For describing reflection characteristics of surfaces, the visible components of the scene are grouped into 6 categories (using the parameters discussed in chapter 4.3):

- ◇ *building parts 1 and 2*: Strong specular reflections are expected at metallic surfaces. In contrast, the glassy facade is expected to be penetrated by the radar signal. However, some parts of the penetrating signal will hit parts of concrete behind the glass and enable multiple reflections. As a compromise, the specular component is conserved by choosing the following parameters for the reflection model for specular reflection: reflection 0.7, specular 0.7,



(a) Temporal average image clipped at 3.4%



(b) Temporal average image clipped at 34.7%

Fig. 50. SAR temporal average images of the main railway station of Berlin, Germany: different clipping thresholds for the intensity are chosen for distinguishing salient point signatures. Ground range: top-down.

roughness 0.00085.

- ◇ *glassy roof parts*: The major part of the radar signal is expected to penetrate the glassy surfaces. Hence, the reflection of signal is assumed to be weak. Parameters: reflection 0.1, specular 0.1, roughness 0.00085.
- ◇ *tower*: In the 3D model, the geometrical structure of the tower is only indicated by texture information. In order to enable the backscattering of signal from the tower, the width of the specular highlight is increased. Parameters: reflection 0.3, specular 0.3, roughness 0.3.
- ◇ *metallic bows*: Due to the metallic surface of the bows, the reflection capability is activated. Parameters: reflection 0.7, specular 0.7, roughness 0.00085.
- ◇ *building ground parts*: The ground beneath the building is made of concrete whose reflection characteristics are similar to dry ground. Moreover, specular reflections are expected to be weaker than for metallic structures. Parameters: reflection 0.5, specular 0.5, roughness 0.0033.
- ◇ *ground*: The ground surrounding the building complex is covered by concrete and sand. As a compromise, the backscattering characteristics are assumed as being similar to those of dry ground. Parameters: reflection 0.5, specular 0.5, roughness 0.0033.

When defining the virtual SAR sensor, the aspect angle with respect to north direction and the local angle of incidence are adapted to the master scene within the stack of TerraSAR-X data. To this end, the local angle of incidence at the railway station is interpolated based on the

given imaging geometry of the master orbit. The size of the sensor plane is 225 m x 300 m and is covered with 1.650 x 2.200 pixels. Thereby, the sampling density in azimuth and elevation is 0.136 m x 0.136 m. Due to the high number of rays and model polygons, the sampling step lasts 20 minutes on a standard PC (2.01 GHz, 4 GB RAM) and yields 4.68 million signal samples.

### 7.3.2 Simulation of maps in azimuth and range

The spatial distribution of signal responses provided by the sampling step is shown in figure 51. On the left image, signal contributions of bounce levels 1-3 are marked by blue, green, and red color, respectively. Signal contributions are detected all over the scene, with the exception of some shadow areas whose extent is displayed in white color. Single and double bounce contributions form laminar or linear signatures. In contrast, triple bounce contributions are partly organized in point patterns. When adding bounce levels 4 and 5, marked in magenta and cyan in the right part of figure 51, further signal contributions occur on the facades of the building center and in the shadow area. These contributions are distinguishable as linear features or focused as spots. However, the majority of the single to fivefold bounce samples are characterized by low amplitude and, hence, will not be distinguishable on the simulated reflectivity map.

Based on the given distribution of signal samples, reflectivity maps are simulated in the azimuth - ground range plane. To this end, the sampling is adapted to the real SAR image shown in figure 50. The simulated reflectivity map for bounce levels 1-3 is shown in figure 52a. Within each resolution cell, the signal contributions have been added coherently. The simulated map has been clipped at 8.1% of its maximum amplitude and is displayed using 8-bit grayscale.

Despite the low clipping level, almost no signatures are distinguishable. The signal response of the railway station is characterized by a pattern of point signatures corresponding to the facades of building parts 1 and 2. Following the ground range axis top-down, the first point pattern represents building part 1. As building parts 1 and 2 are connected by a roof, the effective height of the facade of building part 2, i.e. the facade area visible to the SAR sensor, is smaller than for building part 1. Hence, the corresponding pattern of point signatures is of smaller size. On the real SAR image, the tower is represented by a pattern of bright points. As expected, these signatures are not confirmed by the simulation as the tower model is composed by flat surfaces. Hence, only diffuse signal components are detected which are weak compared to the point signatures. As the corresponding pixels obtain gray value 0, the diffuse backscattering from the tower is not distinguishable on the reflectivity map. No multiple reflected signal is derived from the ground and the building roof, as no corresponding geometrical information is provided by the 3D model scene. The direct backscattering from the ground is negligible compared to the signal response of the point signatures. To conclude, the visible part of the railway station is reduced to a low number of point signatures. As the reflection behavior of surfaces is adapted to the SPM model, the increase of the number of signatures heavily depends on the increase of the level of detail of the 3D model scene, i.e. the representation of facade/roof details or objects on the ground.

In figure 52b, pixels containing specular reflections are marked. The majority of the salient signatures on the corresponding reflectivity map are caused by specular multiple reflections. Hence, given strong specular reflections in the scene, signatures corresponding to the diffuse reflection of radar signals are almost negligible. Obviously, the pixels marked on the specular map are located in the center part of the map where the signal responses of building parts 1 and 2 are expected. In addition to the point signatures, two linear features occur where the roof is intersected by metallic bows. At these positions, two dihedrals are formed for a specific roof orientation with respect to the SAR sensor. Nonetheless, the linear features are hardly distinguishable on the reflectivity map due to the chosen clipping level.

When adding signal contributions of bounce level 4 and 5 to the reflectivity map, the number



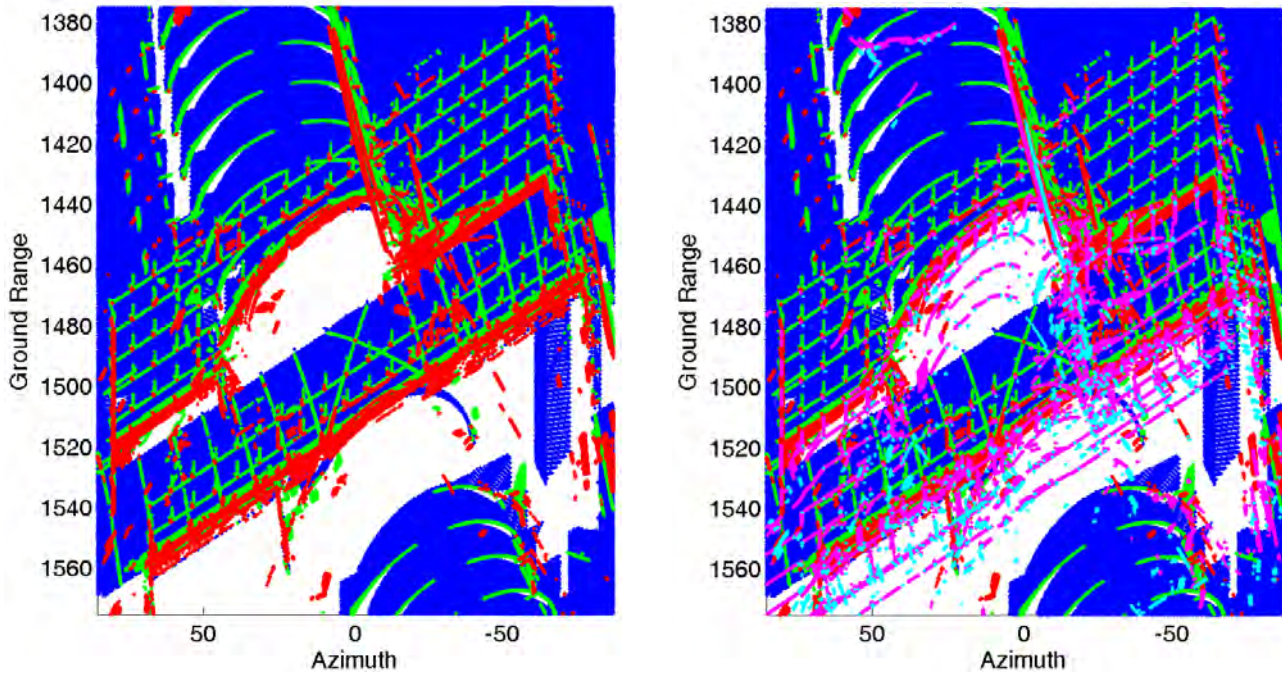


Fig. 51. Main railway station, Berlin: spatial distribution of radar signal responses. Left: reflection levels 1-3. Right: reflection levels 1-5. Blue: single bounce; green: double bounce; red: triple bounce; magenta: fourfold bounce; cyan: fivefold bounce.

of point signatures increases significantly (see figure 53a). Basically, as discussed in chapter 5.2.3, signal contributions of bounce levels higher than 3 are expected to be weak or even negligible. This is not the case for the simulated reflectivity map. Due to the loss of amplitude for each signal reflection, the strength of the fivefold bounce signatures is much weaker than those corresponding to triple bounce. However, a large number of simulated fivefold bounce contributions are of specular kind what is confirmed by figure 53b. Therefore, it is reasonable to consider all bounce levels when analyzing salient signatures on the real SAR image.

### 7.3.3 Correspondence of simulated signatures to persistent scatterers

In the following, simulated maps and output data provided by RaySAR are exploited for a directed analysis of PSs. The position of the PSs in the azimuth-range plane is given by PSI processing using the PSI-GENESIS software of the German Aerospace Center (DLR). Thus, the geometrical link between the SAR temporal average map shown in figure 50 and the PSs is given. The analysis of PSs is concentrated on two areas marked by frames in figure 54, displaying the signal response from building parts 1 and 2.

The first area, marked by a red frame (area *red*), is characterized by a regular pattern of salient points oriented in slant direction. In between the pattern, diagonal rows of point signatures are distinguishable, which show less intensity. In contrast, the area bounded by a green frame (area *green*), mainly contains non-regular distributed signatures. Only in the center part, a diagonal row of point signatures shows regularity. However, the visible point signatures seem to be blurred compared to those in area *red*.

For comparing the simulated and real signatures, the reflectivity map has to be geometrically linked to the SAR image. As the 3D model of the railway station is not georeferenced, the simulated maps can not be directly imposed on the real SAR image. However, a significant number of point signatures is confirmed by the SAR simulator which can be used for distinguishing the railway station on the real SAR image. For simplicity, the search for the railway station is

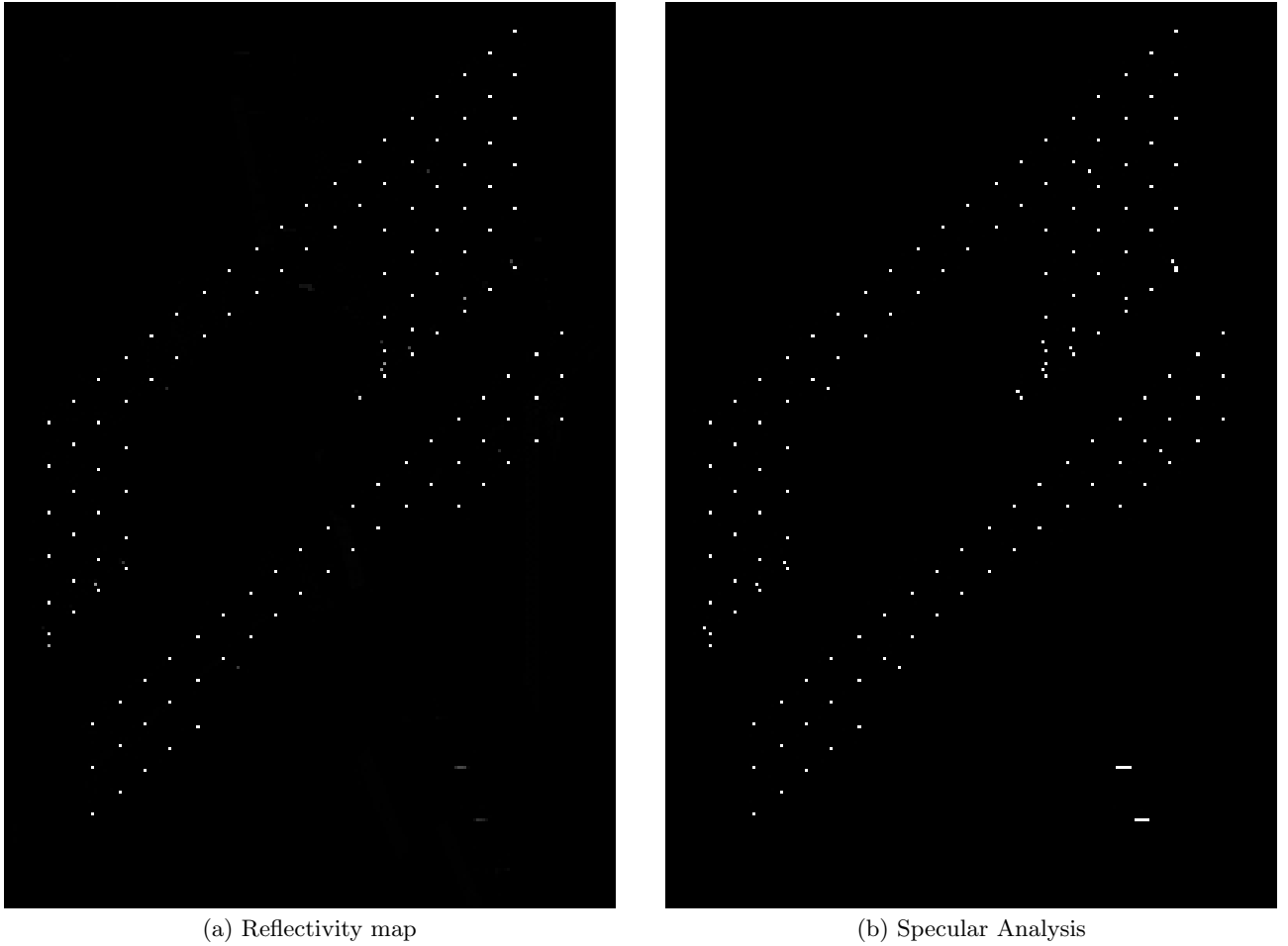


Fig. 52. Main railway station, Berlin: simulation results for bounce levels 1-3 (compare to figure 50b). Dynamic range: the reflectivity map is clipped at 8.1% of its maximum amplitude. Ground range: top-down.

reduced to a section of image B, having a size of 1219 times 2503 pixels in azimuth and ground range. Thereafter, the specular map containing bounce levels 1 to 3 is cross-correlated with the SAR image in frequency domain. The reason for taking the specular map is that RaySAR is assumed to provide the best geometrical correctness for specular reflections. Hence, knowing the position of signal peaks is considered as being sufficient for distinguishing the building. For representing the real SAR data, figure 50b is taken where the width of the mainlobe of point signatures is smaller than for figure 50a. Thereby, the reliability of the localization of intensity peaks in azimuth and ground range should be increased.

However, practical tests for the railway station example have shown that the reflectivity map can be used as well without any difference in the resulting relative shift. Besides, the cross-correlation is robust for different clipping levels of the real SAR data as shown in figure 50. As a result, point signatures occurring due to specular triple reflections of radar signals are confirmed as being prominent hints for an urban object characterized by a regular facade.

Based on the determined relative shift, the simulated maps can be imposed on the SAR image. In this context, only non-zero grayvalues are accepted in order to keep the background information of the real SAR image. For area *red*, the results are shown in figure 55. In figure 55a, the simulated signatures are color-coded on the SAR image shown in figure 50a. No single and double bounce contributions are distinguishable as they are of type diffuse and correspond to gray value 0 for the chosen clipping level. In contrast, pixels containing triple, fourfold and fivefold bounce contributions are not negligible and are marked in red, orange, and green color, respectively. A pattern of point signatures is composed by pixels containing triple bounce



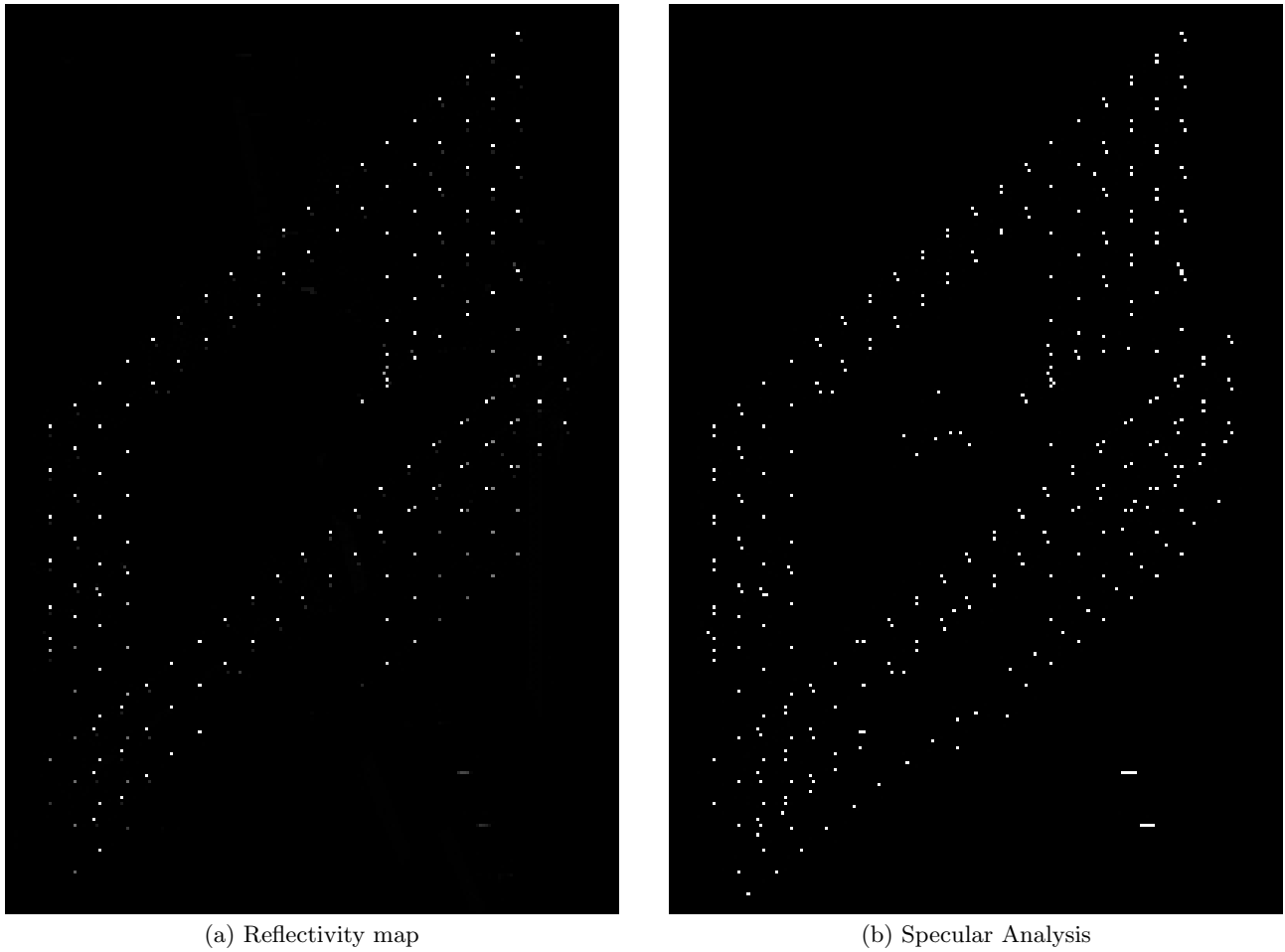


Fig. 53. Main railway station, Berlin: simulation results for bounce levels 1-5 (compare to figure 50b). Dynamic range: the amplitude of the reflectivity map is clipped at 8% of its maximum. Ground range: top-down.

contributions. Near to these pixels, fivefold bounce contributions are found which are located on the inside of intensity peaks.

While the majority of strong point signatures is represented, a large number of point signatures of smaller size is not confirmed by the simulated maps, for instance, bright spots on the diagonals. These features are likely to be caused by metal strings connecting the patches of glass on each building floor. However, these details are not represented by the 3D building model and, hence, can not be reproduced.

Next, the simulated signatures are compared to PSs localized in the scene. In figure 55b, pixels containing the peak position of PSs are marked in red color on the SAR image clipped at low intensity. Only those PSs are accepted which fit to the assumed deformation model assuming a linear and a seasonal component. Compared to figure 55a, almost all bright spots simulated by RaySAR are situated very close to PSs.

In figure 55c, the simulated signatures of the clipped reflectivity map are imposed on figure 50b, which has been clipped at high intensity. Thereby, the location of the intensity peaks can be better compared. The majority of the simulated triple bounce peaks fit well to the point pattern visible on the SAR image. Fivefold bounce contributions are now located outside of bright spots. Hence, based on the information from the simulated data, the combination of strong triple reflection with moderate fivefold bounce is likely. When clipping the image at low intensity, both peaks are merged to one peak (see figure 55a). The result of the specular analysis during the ray tracing step is shown in figure 55d. Here, all pixels containing specular

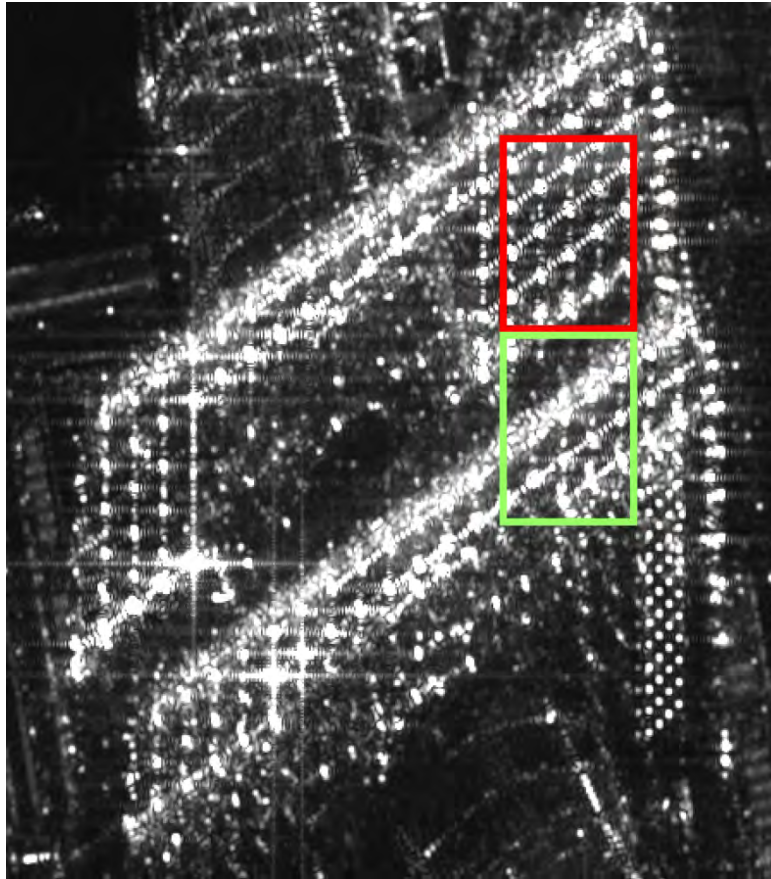
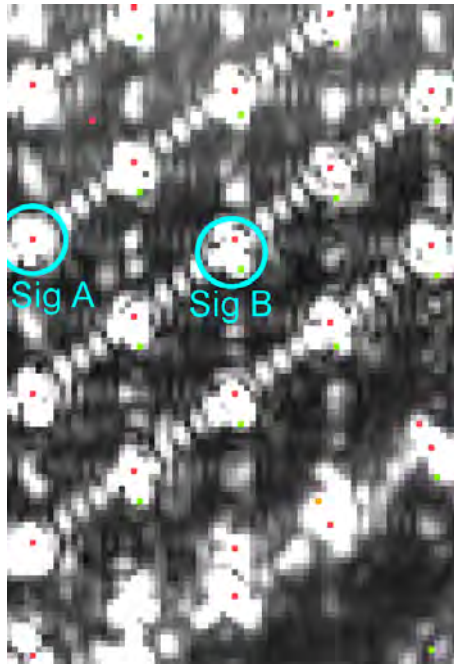


Fig. 54. Main railway station, Berlin: area of interest. Red frame: area *red* characterized by a regular pattern of point signatures. Green frame: area *green* which mainly contains non-regular distributed point signatures. Ground range: top-down.

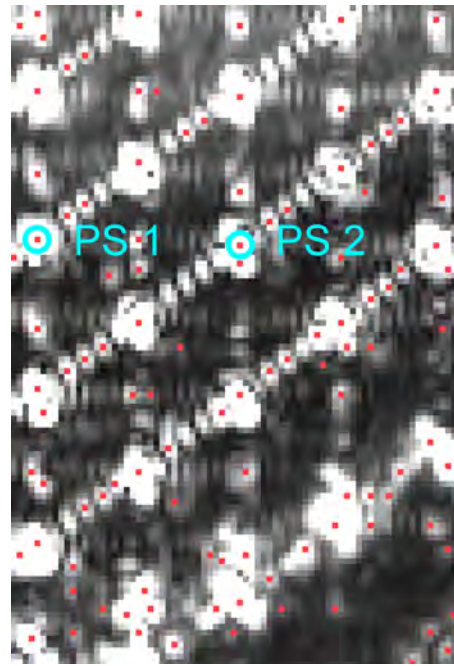
reflections are marked independently of the corresponding amplitude value. Thereby, specular reflections can be recovered which may be lost in the reflectivity map due to the chosen clipping level. For the example at hand, all signatures on the reflectivity map correspond to specular reflections with the exception of one pixel containing fourfold bounce signals.

As area *red* is mainly characterized by a regular pattern, it is reasonable to observe the simulation results for a second image section, area *green*, mainly characterized by a non-regular distribution of signatures (see figure 56). Therein, a high number of salient point signatures are identified as being linked to triple bounce or to a combination of triple and fivefold bounce (figure 56a). Irregular distributed signatures on a broad diagonal band are not confirmed. These image features are likely to be linked to roof structures which are not geometrically described by the 3D model. Comparable to area *green*, signal contributions of bounce levels 2 and 4 are too weak with regard to the chosen clipping level and, hence, are negligible. In figure 56b, the corresponding distribution of PSs is seen which show less regularity than in area *red*.

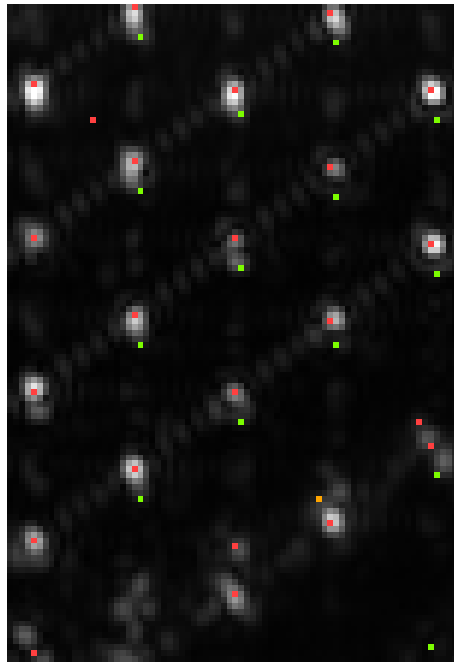
The position of triple bounce contributions is anticipated to be reliable as the relative shift with respect to the corresponding point signatures is small. This is confirmed by figure 56c, where the simulated signatures are imposed on the SAR image clipped at high intensity. In contrast, pixels marked as fivefold bounce do not definitely fit to intensity peaks but are now located outside of salient point signatures. The specular map, shown in figure 56d, reveals that all simulated signatures are of specular type. In addition, some further pixels are marked which miss on the reflectivity map due to low amplitude values. However, these pixels do not directly correspond to intensity peaks on the real SAR image.



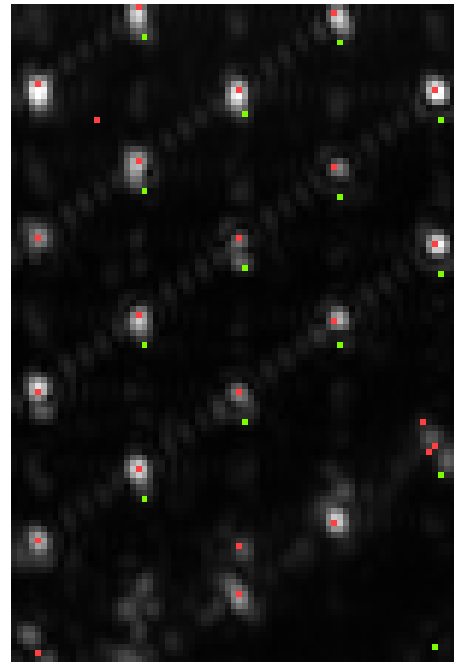
(a) Simulated signatures imposed on area *red* in figure 50a; red: triple bounce; orange: fourfold bounce; green: fivefold bounce



(b) PSs imposed on area *red* in figure 50a. Processing results provided by Stefan Gernhardt, Remote Sensing Technology, Technische Universität München. PSs 1 and 2: persistent scatterers for comparing height profiles in chapter 7.3.4.



(c) Simulated signatures imposed on area *red* in figure 50b; red: triple bounce; orange: fourfold bounce; green: fivefold bounce

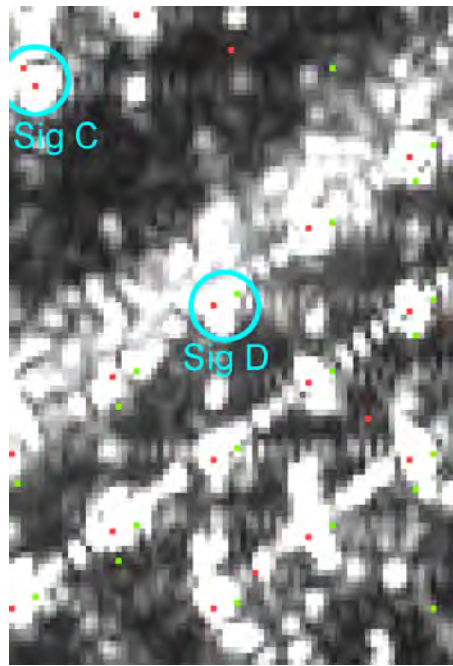


(d) Specular reflections imposed on area *red* in figure 50b; red: triple bounce; orange: fourfold bounce; green: fivefold bounce

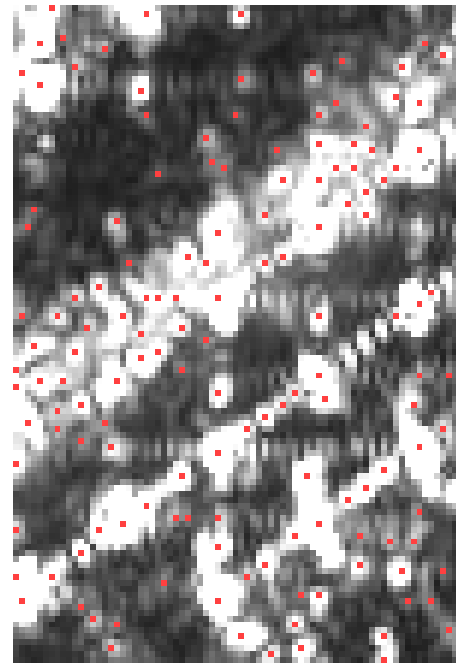
Fig. 55. Main railway station of Berlin: simulation vs. SAR image for area *red*. Signatures and PSs imposed on figures 50a and 50b clipped at 3.4% and 34.7%, respectively. Ground range: top-down.

### 7.3.4 Comparison of simulated height profiles to results from SAR tomography

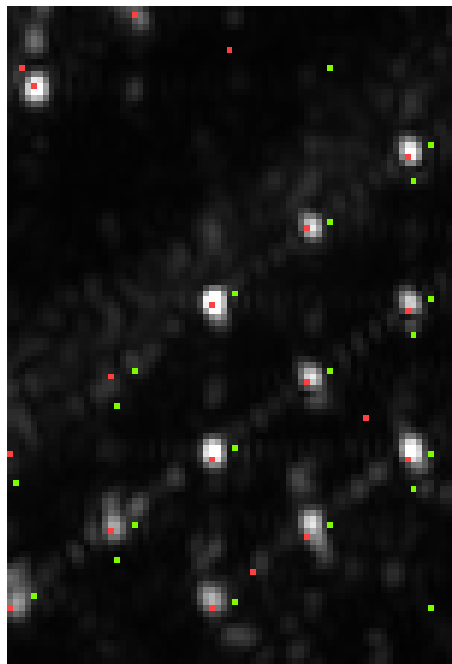
As the simulated image is linked to the real SAR image, a directed analysis of signatures by means of RaySAR is enabled. In figures 55 and 56, it is seen that salient point signatures



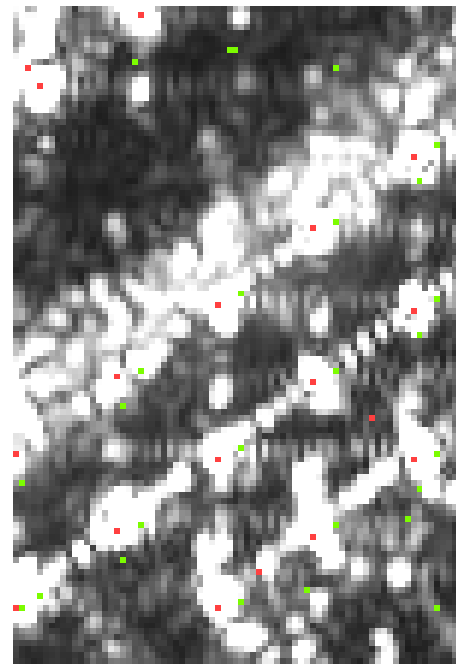
(a) Simulated signatures imposed on area *green* in figure 50a; red: triple bounce; green: fivefold bounce



(b) PSs imposed on area *green* in figure 50a. Processing results provided by Stefan Gernhardt, Remote Sensing Technology, Technische Universität München.



(c) Simulated signatures imposed on area *green* in figure 50b; red: triple bounce; green: fivefold bounce



(d) Specular reflections imposed on area *green* in figure 50a; red: triple bounce; green: fivefold bounce

Fig. 56. Main railway station of Berlin: simulation vs. SAR image for area *green*. Signatures and PSs imposed on figures 50a and 50b clipped at 3.4% and 34.7%, respectively. Ground range: top-down.

representing building parts 1 and 2 are exploited as PSs. Pixels selected as PSs only contain the signal response from one dominant scatterer. PSI provides the height of the scatterer with respect to a reference point in the network of PSs. Likewise, the stack of VHR SAR data can be processed by means of tomographic methods. Thereby, the height of the scatterer can be derived with respect to a reference point which is located, for instance, on the ground surrounding the monitored object. In case of the main railway station of Berlin, a comparison of simulation

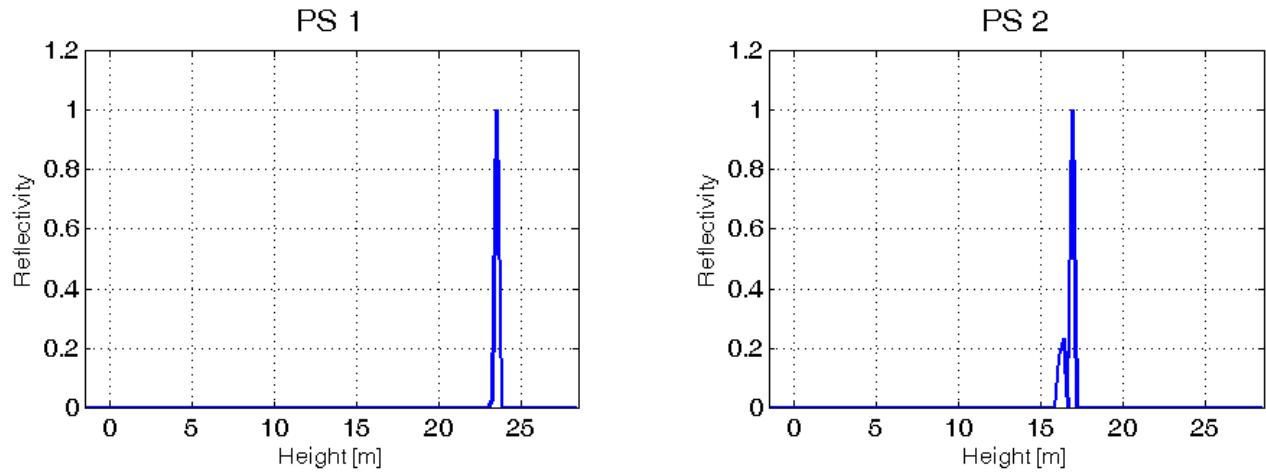


Fig. 57. Height profiles for two PSs from tomographic processing of the data stack (method: compressive sensing). The reference point has been selected on the ground surrounding the railway station. The processing results are provided by Xiaoxiang Zhu, Remote Sensing Technology, Technische Universität München.

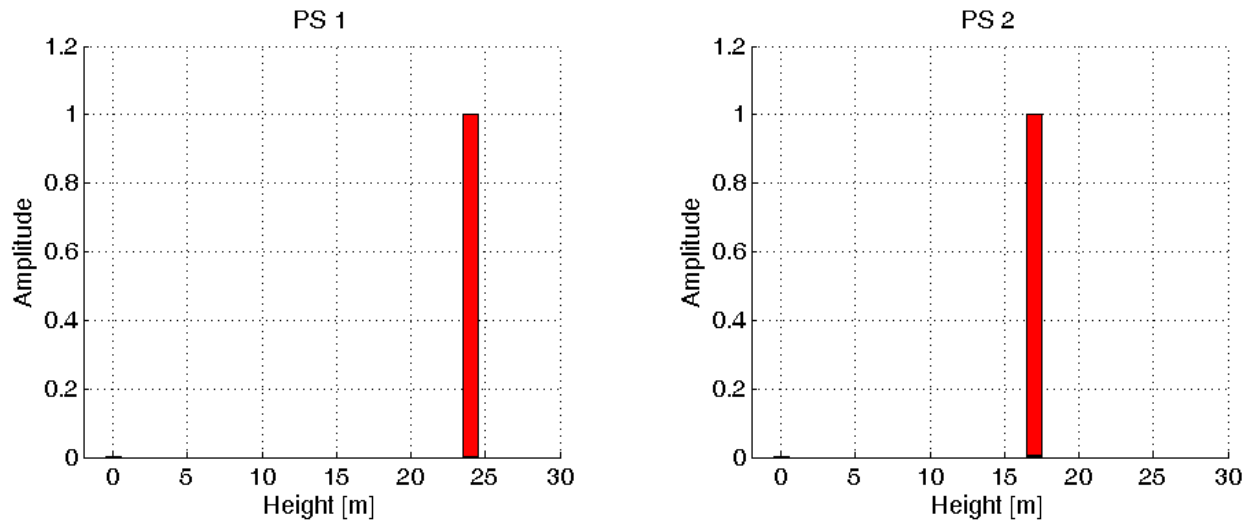


Fig. 58. Simulated height profiles for two signatures representing the PSs from figure 55b. Stepwidth in height: 1 m. Red color marks signal contributions of bounce level 3. Reference height: horizontal plane beneath the 3D model of the railway station.

results with results of SAR tomography is made in the following.

First, two PSs are selected which correspond to signatures on the simulated reflectivity map (labeled as PS 1 and PS 2 in figure 55b). In this regard, a relative shift of one pixel is accepted. Tomographic processing is conducted by means of compressive sensing in order to derive the reflectivity function in elevation for the selected pixels (Zhu and Bamler, 2010). In figure 57, the result is visualized in height with respect to the ground level. As expected, one dominant scatterer is detected for pixels PS 1 and PS 2, respectively, at heights of approximately 23 m and 17 m. Compared to the maxima of the profiles, the diffuse signal response from the ground in front of the railway station is negligible.

The simulated profiles are provided as detailed in chapter 6.3.2. After the selection of each image pixel, relevant signal contributions are separated from irrelevant ones. Afterward, the elevation coordinates are transformed into the height-over-ground system what is possible due to the known angle of incidence and the known height reference, defined by the plane beneath the building model. The stepwidth in height is set to 1 m. For each step along the height axis,

signal contributions of different bounce levels are separated and summed. For the simulated signatures corresponding to pixels PS 1 and PS 2, the resulting height profiles are shown in figure 58. Similar to the tomographic profiles, one dominant scatterer is found for each height profile, respectively, located at height steps 24 m and 17 m. In addition to information about the position of scatterers, the reflection level is classified as triple bounce and is marked in red color. Signal contributions of other reflection levels, e.g. single bounce from the ground, are too weak to be distinguishable. According to the simulation result, the signal peaks in the tomographic profiles are linked to triple reflections of radar signals.

Height differences between the real and simulated peak positions are likely. The reason is that the ground is only roughly approximated by means of a flat plane in the 3D model of the scene. In reality, the ground surrounding the railway station is not perfectly flat and, thus, the reference heights of simulation and tomographic processing may be different. However, the simulation example reveals that RaySAR enables to simulate the distribution of scatterers in height or elevation direction. With regard to the application of simulated height profiles, the classification of bounce levels may be helpful for complex layover situations where several dominant scatterers are separated within a resolution cell.

### 7.3.5 Identification of scatterers

The simulation output provided by the ray tracer is exploited for analyzing the nature of PSs. To this end, signatures exploited as PSs are selected and the corresponding scatterers are identified within the 3D model scene of the test site. The chosen signatures are marked by circles in figures 55a and figures 56a.

Signature A, named Sig A in figure 55a, is characterized by high intensity and is linked to one PS visible in figure 55b. The simulated reflectivity map and the specular map indicate that the signature is likely to occur due to specular triple bounce. This basic information may be helpful for classifying signatures on the real SAR image. However, no information about the origin of signatures is provided. Therefore, the geometrical link between signatures and scatterers, i.e. between image pixels and object geometry, has to be found.

After selecting the pixel on the reflectivity map, the corresponding intersection points are extracted which have been captured when sampling the 3D building model during ray tracing (see chapter 5.1.1). Thereafter, the intersection points are mapped onto the 3D building model as explained in chapter 6.4.2.

The extent of scatterer A, corresponding to signature A, is shown in figure 59 where signal contributions of bounce levels 1-3 have been detected at building part 1. Intersection points are represented by small cubes whose color indicates the bounce level, i.e. blue for single bounce, green for double bounce, red for triple bounce. However, the simulated single and double reflections are of diffuse type and are negligible due to low amplitude. This is also seen in figure 55a where only triple and fivefold bounce signals are distinguishable. Therefore, the analysis of signature A is concentrated on the signal of bounce level 3 which follows two paths: *vertical bar - facade - horizontal bar (and vice versa)*, and *facade - horizontal bar - vertical bar (and vice versa)*.

The spatial density of cubes confirms the appropriate sampling of the scatterer by means of rays. In comparison to reality, the size of the scatterer is overestimated since the full facade functions as a reflecting surface. As shown in figure 48, only two horizontal layers of concrete are expected to reflect at each floor at the building. Besides information about the sampling of objects, a rough hint is provided with regard to the power of signals. As shown by equations 23 and 24, the amplitude of the signal response depends on the corner size. In figure 59c, the distribution of cubes represents only a portion of a trihedral. The corresponding signal amplitude depends on the trihedral area covered by intersection points. However, it should be



kept in mind that surface materials and the geometry of reflection are major factors as well.

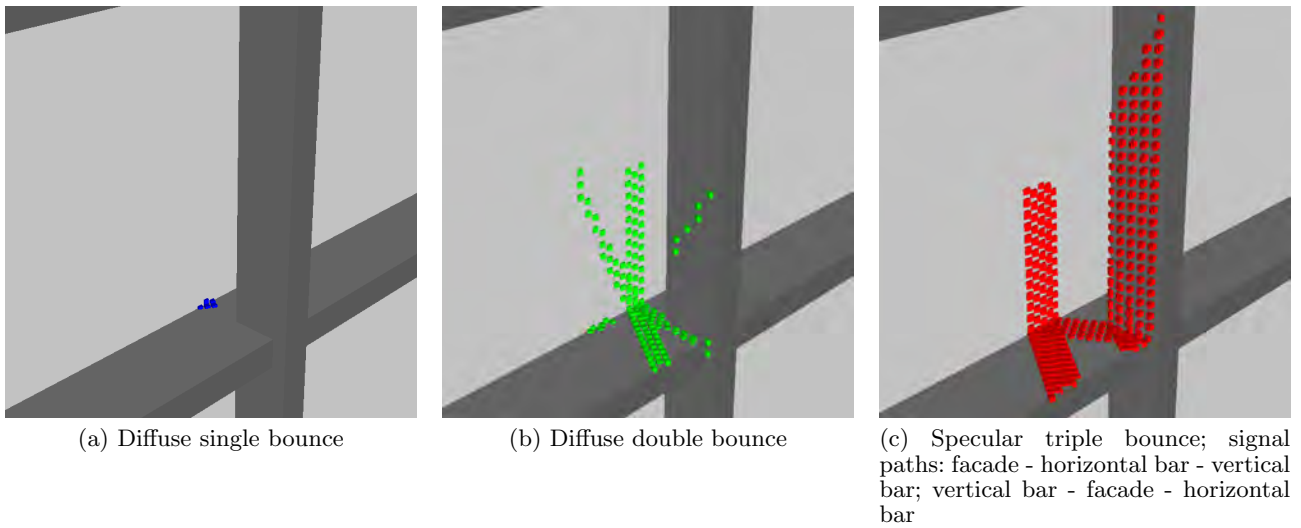


Fig. 59. Identification of scatterer for signature A. Cube size: 5 cm. Blue: single bounce; Green: double bounce; Red: triple bounce.

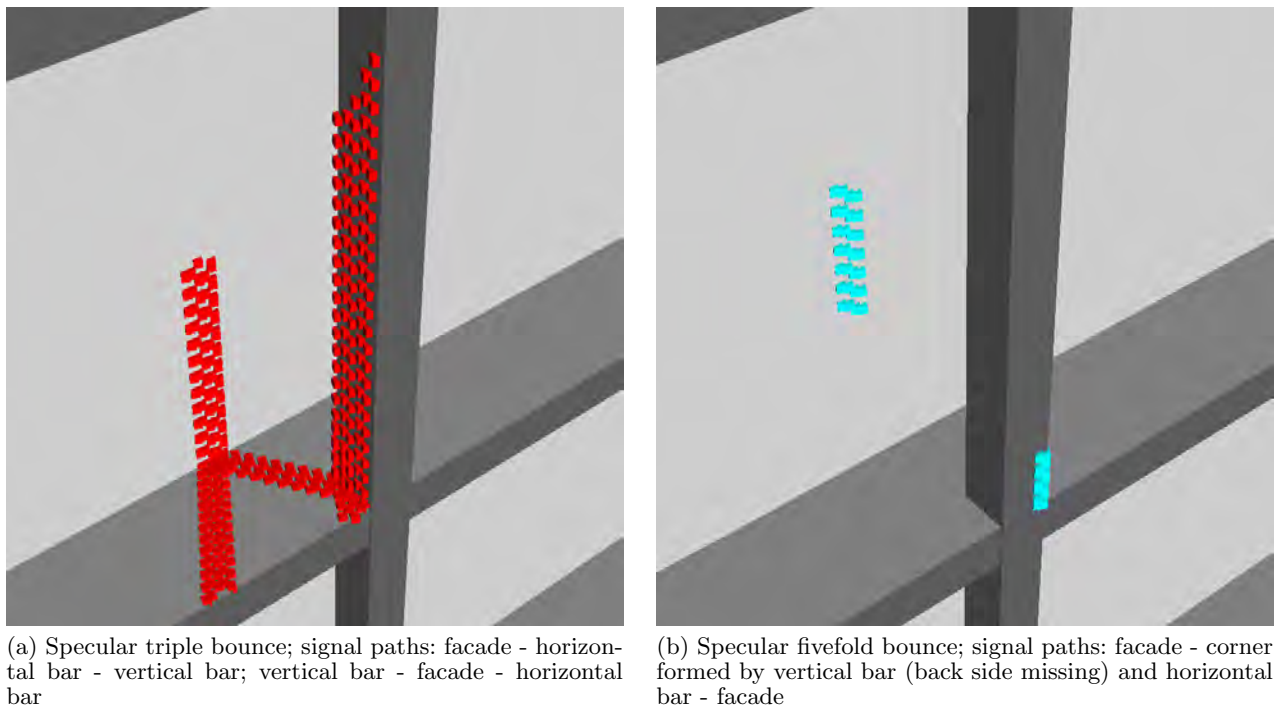


Fig. 60. Identification of scatterers for signature B. Cube size: 5 cm. Red: triple bounce; Cyan: fivefold bounce.

Signature B contains two nearby PSs which both represent strong intensity peaks. Simulating the scene yields one dominant peak of specular triple bounce and one weak peak of specular fivefold bounce. The positions of the signal peaks of signature B mainly differ in range direction. When mapping the corresponding intersection points on the building model, the scatterer causing the triple bounce phenomenon has the same nature than scatterer A.

The specular fivefold bounce is an artificial effect as the signal at building part 1 follows the path *facade - corner defined by horizontal bar and vertical bar (which is not closed at the back side) - facade (and vice versa)*. A simplified visualization of the reflection phenomena corresponding to signature B is shown in figure 61a. Signal paths can be seen for specular triple bounce and

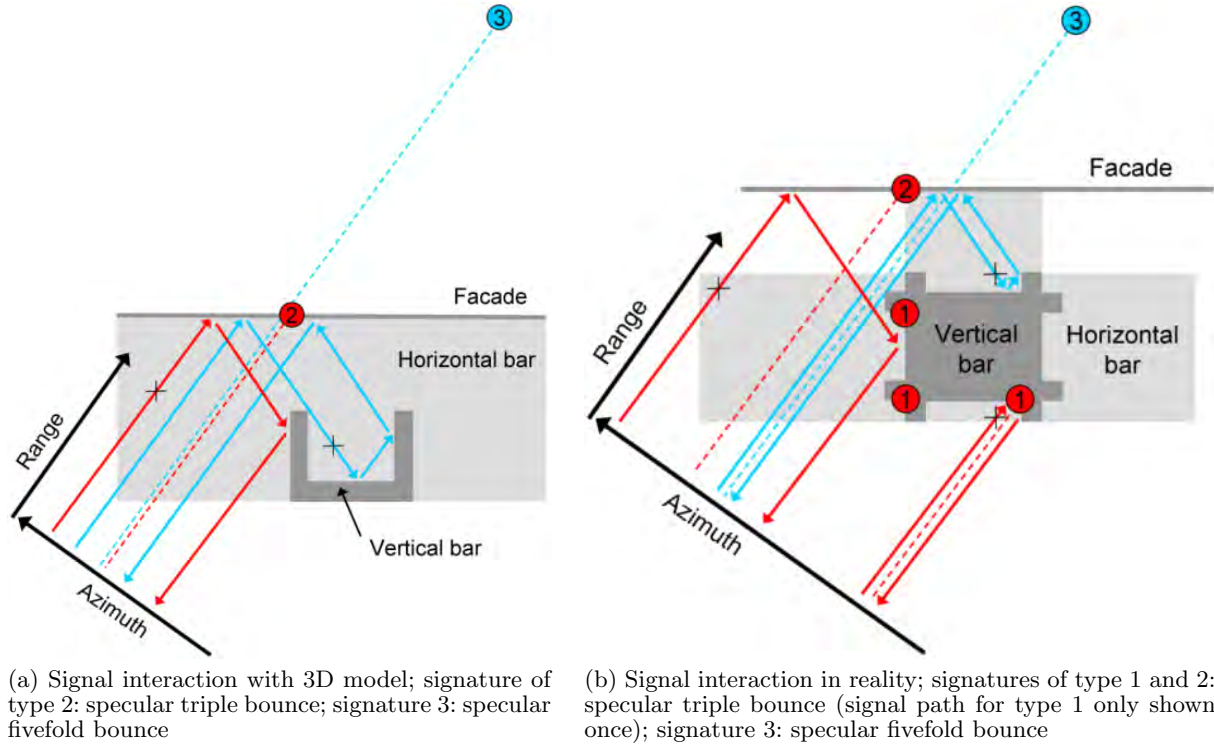


Fig. 61. Signal reflections at bars: expected differences between simulation and reality. For simplification, the visualization of the reflection phenomena is reduced to the azimuth-range plane. Signal reflections on the horizontal bar are indicated by crosses (marked in black). Continuous arrows: signal paths; the dashed lines indicate the azimuth position of the resulting image signatures.

specular fivefold bounce, respectively. In order to simplify the visualization, the reflections are mapped on the azimuth-range plane. Reflections on the horizontal bar are indicated by black crosses. Based on the given geometry, RaySAR detects two dominant signatures labeled by numbers 2 and 3.

In reality, the backside of the vertical bar is not open. All vertical and horizontal bars show linear protrusions pointing in vertical and horizontal direction, respectively. At the intersection points of horizontal and vertical bars, small corners are formed on each floor of the building (see right part of figure 48). The corners have a sidelength of approximately 5 cm and are made of metallic material. As indicated in figure 61b, these corners also occur on the backside of vertical bars and may enable a reflection phenomenon similar to the simulated fivefold bounce.

Signature C contains one dominant PS and a nearby PS of medium strength. Likewise, the simulation yields a strong signal peak (point signature C1) and a weak signal peak (point signature C2) of bounce level 3, which both are of specular type. In figure 56a, signature C2 is located on the top-left of signature C1.

For signature C2, the corresponding scatterer is located at building part 1 and is displayed in figure 62a. The signal path is either *vertical bar - facade - ground (and vice versa)* or *facade - vertical bar - ground (and vice versa)*. For a better visualization of the intersection points at the building, the signal interaction with the ground is not shown in the figure. Both signal paths are likely since the facade part interacting with the signal is located at the center of each floor. In reality, this area is characterized by concrete covered with glass. As glass is penetrated by the radar signal, the concrete is expected to enable the reflection of radar signals. The strength of the corresponding signal is multiplied by the number of floors as all signatures are located at the same position in azimuth and range.

Scatterer C1, corresponding to signature C1, is also found at building part 1. At this position, the radar signal follows the paths *vertical bar - horizontal bar - ground (and vice versa)* and *hor-*



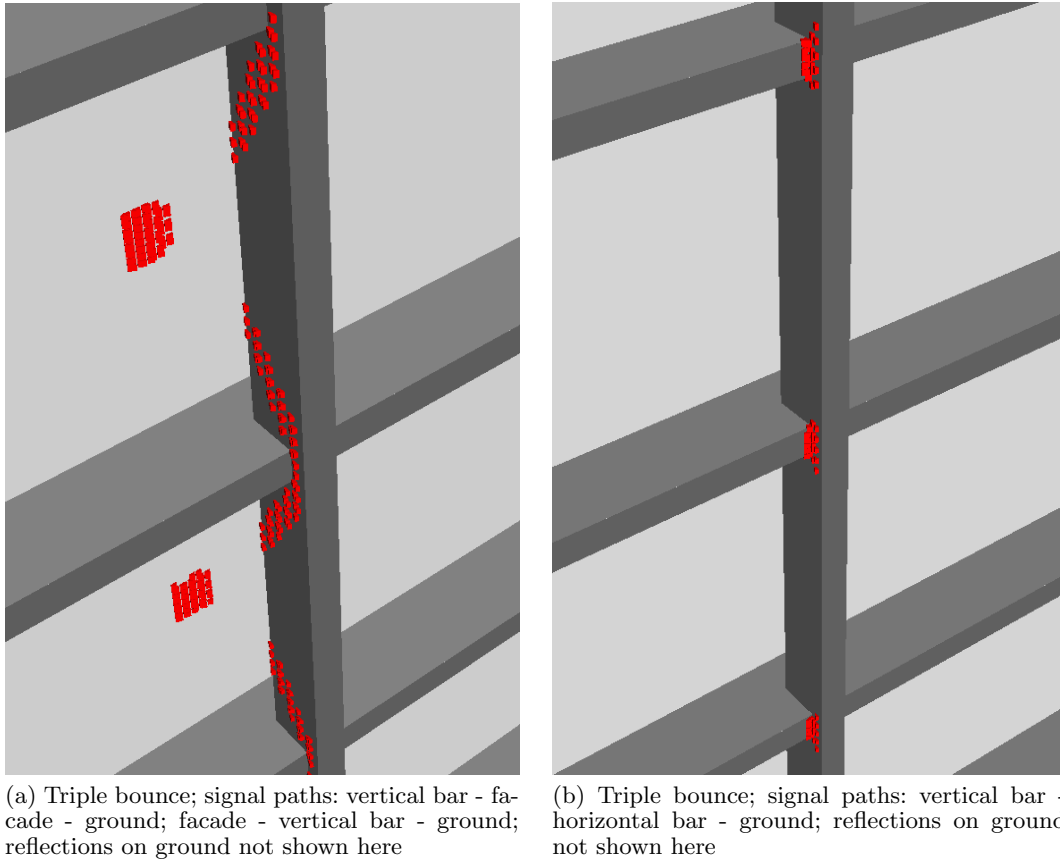


Fig. 62. Identification of scatterers for signature C. Cube size: 5 cm. Red: triple bounce.

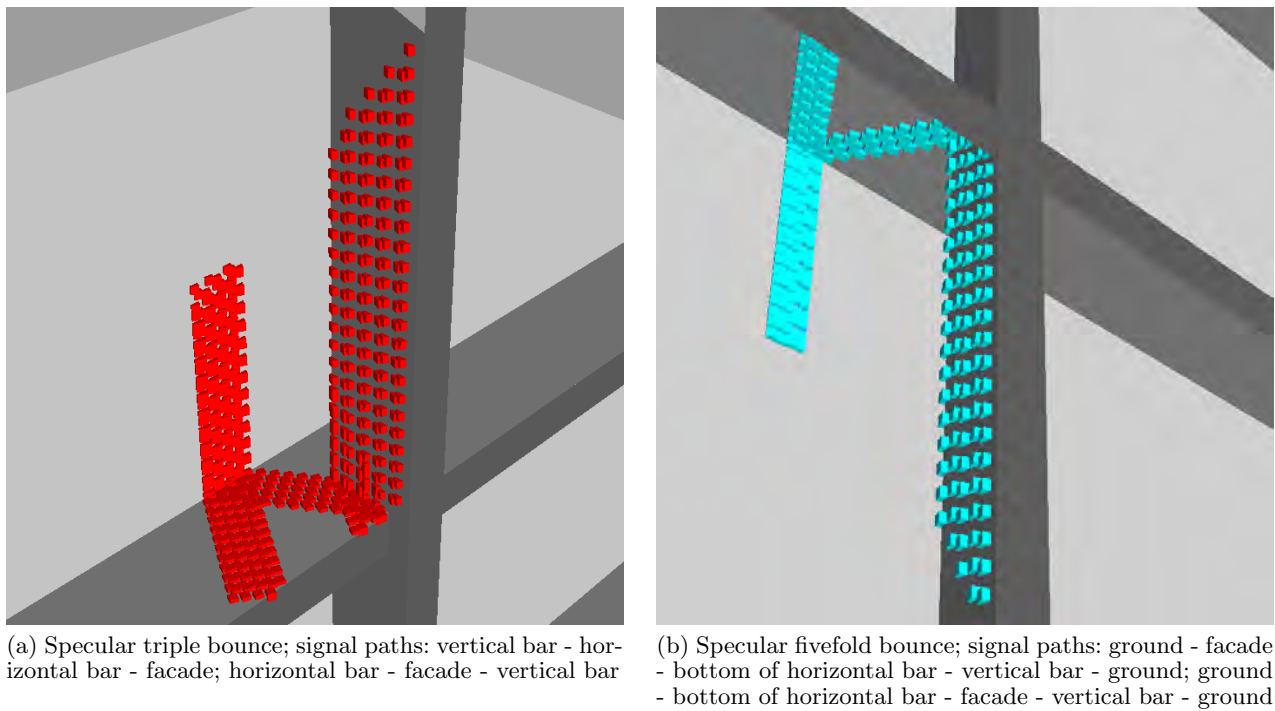


Fig. 63. Identification of scatterers for signature D. Cube size: 5 cm. Red: triple bounce; Cyan: fivefold bounce.

*horizontal bar - vertical bar - ground (and vice versa)* (see figure 62b). This reflection phenomenon is linked to a specific kind of vertical bar whose end reaches beyond the end of horizontal bars. Thus, a dihedral is formed which points in vertical direction. Again, the signal is amplified by

the number of building floors. As the facade of the main railway station is not involved, the azimuth and range coordinates of the resulting signal peak are slightly different to those of signature C2.

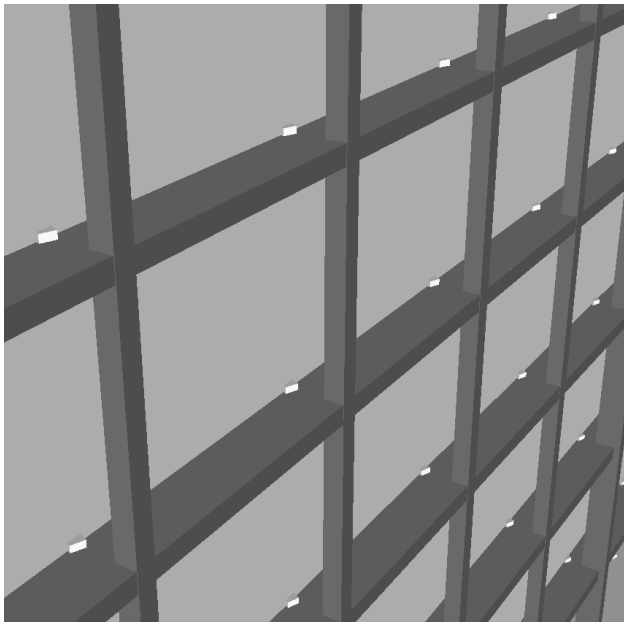
Specular triple reflections of type signature A are spatially separated in azimuth and range for different floors of the building. Thus, a pattern of point signatures – characterized by 5 diagonal rows – represents building part 1 in figure 50. The triple bounce phenomena corresponding to signature C are focused at ground level and are distinguishable in a 6th diagonal row.

For both signatures C1 and C2, the properties of the ground are crucial. Basically, the corresponding scatterers can be considered as a small cutout from a large trihedral corner reflector including the ground. For enabling signal reflections at the ground, the ground parts have to be visible to the SAR sensor, i.e. the building has to be isolated from other buildings. In case of objects covering parts of the ground, some of the triple reflections will be lost and, hence, the multiplication factor depending on the number of floors will be reduced. Finally, specular triple reflections will be disabled if the ground is sloped. Then, the trihedral formed by the facade structures and the ground is disturbed or lost and only diffuse triple reflections may represent signature C. If the signature is still distinguishable on the SAR image, it is expected to be smeared in azimuth and range. For a regular facade, this smearing effect is further supported by the fact that the signal response from different floors is not summed up any more, i.e. triple bounce signatures of type C1 or C2 show different positions for different floors. When having a look at the TerraSAR-X image, the 6th row of point signatures shows a smeared appearance. This may be partly related to the fact that the ground surrounding the main railway station is not a horizontal surface.

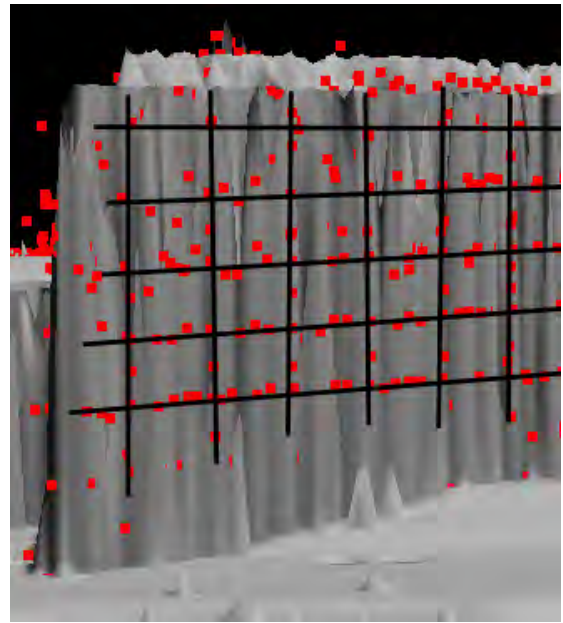
Signature D shows strong intensity and represents one PS. The simulator identifies a strong peak of specular triple bounce (signature D1) and a weak peak of specular fivefold bounce (signature D2). The positions of the signal peaks mainly differ in azimuth (see figure 56a). As there is only one PS detected, the high intensity of signature D1 may be the reason why signature D2 is hinted.

The identification of scatterer D1 reveals the same reflection process than for signature A but occurs at building part 2. In contrast, scatterer D2 is found at building part 1 where the radar signal follows the paths *ground - facade - bottom of horizontal bar - vertical bar - ground (and vice versa)* or *ground - bottom of horizontal bar - facade - vertical bar - ground (and vice versa)*. With regard to this reflection phenomenon, the facade surface and the ground are crucial components. Compared to the simulation example, the effective reflecting surface of the facade is reduced to a small horizontal band of concrete covered by glass. As for the ground, the same conditions have to present than for signature C. However, the influence of objects covering the ground is much stronger. In contrast to triple reflections, the fivefold reflections are not localized at the same position in range. Hence, there is no multiplication factor depending on the number of building floors, i.e. the factor is 1. Thus, the fivefold bounce signal is lost completely in case of objects disturbing the ground as reflecting surface.

The investigation of different types of signatures representing the main railway station reveals interesting consequences for PSI. Signatures A and B occur locally at the facade. Deformation signals corresponding to these signatures only contain relative movements between facade structures. In contrast, signature C is linked to signal interaction with two surfaces on the facade and the the ground. Hence, relative movements between the ground and facade structures may affect measured deformation signals. Finally, signature D occurs due to fivefold bounce signals following the path *ground - facade* and vice versa. Thereby, relative movements between the ground and the facade may be included twice in the radar signal.



(a) Signatures of type 'A' mapped on building part 1 (marked by white cubes having a size of 20 cm)



(b) PSs (red cubes) mapped on a LiDAR DEM form a point pattern (rows and columns indicated by black lines)

Fig. 64. Main railway station: simulated phase centers of bounce level 3. Rows of ghost corners are located on the building facade.

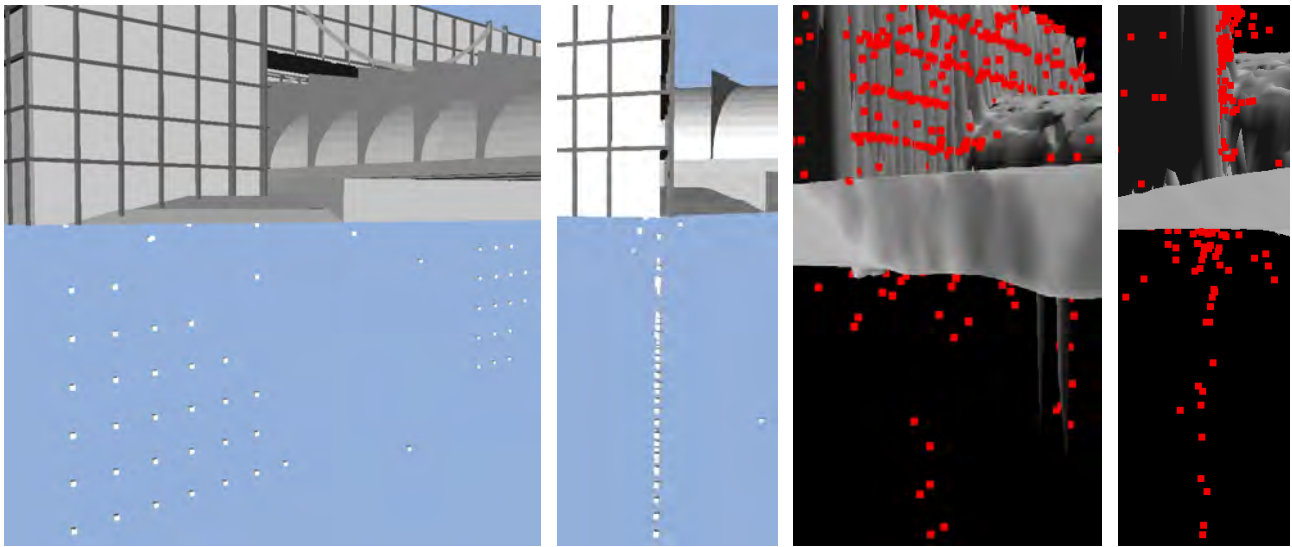


Fig. 65. Main railway station: simulated phase centers of bounce level 5. First and second image (from left to right): simulated pattern of fivefold bounce signatures localized below the ground level at building part 1. Point signatures form a planar pattern (cube size: 40 cm). Third and fourth image: PSs localized at building part 1 imposed on a DEM derived from LiDAR data (all bounce levels). A significant number of PSs are localized beneath the ground level.

### 7.3.6 3D positions of simulated signal responses

As RaySAR provides data in azimuth, range, and elevation, the simulated signatures can be mapped onto the 3D building model. To this end, the known imaging geometry is used for transforming the signatures into the world coordinate system of the 3D model (see chapter 6.4.1). In figure 64a, the phase centers of type 'signature A' are marked by white cubes on building part 1. A pattern of point signatures is found on the facade. Each point signature is located at the tip of a virtual corner which is composed by

- ◇ one plane defined by the surface of a vertical bar,
- ◇ one plane defined by the surface of a horizontal bar,
- ◇ one plane defined by the facade of building part 1.

As the triple bounce signatures are not necessarily caused by physical corners, they represent *ghost corners*. Likewise, a point pattern of the same kind can also be found at building part 2. However, the number of point signatures is less in numbers than for building part 1 as the glassy roof in between building parts 1 and 2 reduces the effective height of the facade of building part 2. In figure 64b, the localized PSs are mapped onto a LiDAR DEM of the main railway station. In contrast to figure 64a showing only triple bounce contributions, PSs of all bounce levels are displayed. As simulated by RaySAR, the point pattern on the facade is confirmed. Overall, the PS show little deviation from the horizontal and vertical lines colored in black which have been introduced artificially. A major factor influencing the deviation from the point pattern is the limited accuracy of the localization in elevation due to the narrow orbital tube of TerraSAR-X.

When mapping the simulated fivefold bounce signatures of type 'D2' into the 3D model, they are found beneath the ground level at building part 1. On the left part of figure 65, two perspective views onto the resulting point pattern are shown. As for the triple reflections, the signatures are organized in a vertical point pattern. Since the signatures are linked to multiple reflections at horizontal and vertical bars, the spatial distribution depends on the regularity of structures on the facade of building part 1.

Mapping the PSs onto the DEM reveals that some of the PSs are localized beneath building part 1 and are approximately grouped on a vertical plane as well (right part of figure 65). The points are less in numbers than in the simulated result and are irregularly distributed. Again, the deviation from the vertical plane is affected by the limited accuracy of the localization in elevation. With regard to limitations of the simulated result, the ground is only roughly approximated as the ground level is represented by a flat plane in the 3D model. As indicated by the LiDAR DEM, the real ground in front of the facade slightly varies in height and is partly covered with objects. Hence, the majority of the simulated fivefold bounce signal is unlikely to occur since specular reflections are disturbed or made impossible. Nonetheless, the appearance of regular patterns of PSs below the ground level is confirmed for other isolated buildings in the center of Berlin. Hence, even if the difference between the simulation result and the distribution of PSs is evident, a strong hint is given that also specular fivefold bounce signatures are exploited as PSs.

## 8 Discussion and outlook

In the introduction part of this thesis, three objectives are summarized which lead to research conducted for the development and application of simulation methods. In the following, the results of the thesis are discussed with reference to these objectives.

The first objective is to enable *3D SAR simulation using object models of high detail*. Using a specific imaging concept, that is an orthographic camera in combination with a source emitting parallel signals, this objective has been realized. The resulting SAR simulator is named RaySAR and has been developed based on ray tracing methods. Signal contributions are simulated in azimuth, range, and elevation. Thereby, data are provided in SAR geometry and are used for providing different simulation products, which can be compared to real SAR data. Reflectivity maps in the azimuth-range plane support the visual interpretation of real data. Moreover, these maps are used for selecting pixels of interest whose correspondence to scatterers can be analyzed. For instance, elevation profiles can be defined in order to separate signal contributions in cross-range direction. By linking the simulated reflectivity maps to real SAR data, the inversion of the SAR imaging system can be simulated. Hence, in case of SAR image signatures confirmed by RaySAR, the interaction of radar signals with surfaces can be visualized in the simulated 3D models.

The 3D position of signal contributions is derived directly without simulating the synthetic aperture. RaySAR represents an ideal SAR system which, for instance, focuses the signal response of a trihedral at one point in space. Only the peak position of signatures is simulated whereas providing a copy of real SAR data is not pursued. By direct simulation of the signal response from objects, calculating time is saved as no processing of raw data is required. Thus, simulation results for different imaging geometries or different object properties can be provided within minutes.

SAR simulation based on ray tracing reveals several limitations. First, the radiometrical correctness of simulated signal responses is moderate. In order to improve the image radiometry, the reflection models of RaySAR may be exchanged with more reliable ones. However, only little improvement is expected, especially in case of multiple reflections. While specular reflections are covered by 100%, the representation of diffuse multiple reflections lacks of completeness concerning both the geometry and the radiometry. For example, the ray tracer enables will not geometrically describe 50 % of diffuse fourfold bounce signals occurring in a scene.

The reliability of the simulation results depends significantly on the level of detail of object models. For VHR SAR data, theoretical assumptions indicate that the geometry of corners having a sidelength larger than 5 cm should be represented in 3D models. However, the availability of those details in 3D models is only realistic for prominent objects. At present, basic city models are available in 2.5D or 3D where only basic facade details are geometrically described. To this end, different case studies have been conducted for discussing the influence of the level of detail of object models:

- ◊ **Moderate level of detail:** 3D models characterized by a low level of detail enable to simulate the appearance of objects in the SAR image plane. Basic support is given for orienting in SAR data or for the visual interpretation of large image signatures. In most cases, diffuse reflection of Lambertian type has to be assigned to surfaces in order to guarantee that objects are distinguishable in the simulated data, e.g. object outlines or shadow areas. The separation of different reflection levels by means of image layers enables to provide a-priori knowledge about objects. Signals of reflection level 1 describe object outlines in the SAR image plane which may be used, for instance, for grouping signatures representing single objects. The bottom lines of objects can be described by means of double bounce signatures. For 3D models of low detail, only large corners are simulated which may be used for linking

simulated data and real SAR data. However, the low level of detail of the object models limits the directed analysis of signatures.

- ◇ **Detailed 3D object models** enable more realistic simulations as the geometry of small object features is described. The major gain of information is observed for reflection levels higher than 2. For instance, point patterns representing building facades in VHR SAR data can be reproduced. In this context, the dependance of diffuse reflection on the direction of reflection can be confirmed. Then, the appearance of objects is likely to be reduced to a low number of signatures on the simulated image. Nonetheless, this will correspond to the object appearance on the real SAR image if the surface parameters have been defined appropriately. Eventually, finding the link between simulated and real data becomes more robust as the geometrical and radiometrical correctness of simulated signatures increases.

The second objective of the thesis is *to enhance the knowledge about the nature of scatterers*. In order to fulfil this task, several case studies have been conducted for single/multi body scenes as well as for object models characterized by different levels of detail. Still, the investigation of reflection phenomena is in the early stages. However, a first insight into the nature of scatterers at buildings is enabled.

- ◇ **Double bounce:** Linear signatures at building walls which are rotated with respect to the line-of-sight of the SAR sensor require Lambertian-like diffuse signal reflection. In other words, the diffuse reflection of the radar signal has to be almost independent from the reflection angle. The diffuse scatterer may be either the facade or the ground surrounding a building. In contrast, the intensity of double bounce lines is expected to be weak if the diffuse reflection depends on the reflection angle.
- ◇ **Triple bounce:** When being localized in 3D, the majority of signal contributions of reflection level 3 are located either on facades or at the bottom of building walls. The first case occurs due to local triple bounce at features on the facade, e.g. windows or balconies. In contrast, the second case requires signal interaction with the ground surrounding the building and two signal reflections on the building facade. At facades characterized by rows of windows, point patterns corresponding to specular triple bounce are the most prominent image signatures. When aiming at the simulation of those signatures, at least basic facade details have to be geometrically described in the 3D model.
- ◇ **Reflection levels larger than 3:** Two case studies – the Wynn hotel and the main railway station – give strong hints that signals of reflection levels higher than 3 are apparent in VHR SAR data. Moreover, signatures of reflection level 5 are likely to be exploited as persistent scatterers. When localizing signal responses at buildings, e.g. by means of PSI, some of them wrongly found beneath the ground level. The simulation results for the main railway station reveal that this phenomenon is likely to be related to multiple reflections. Specular fivefold bounce is expected for isolated buildings surrounded by flat terrain which is covered, for instance, by concrete or asphalt. In this case, the reliability of the position of simulated fivefold bounce signatures also depends on the ground model. Hence, the ground has to be modeled in detail, for instance, by using a high resolution DEM.

A high number of signatures lack of correspondance to features of the imaged object, i.e. they do not represent the geometry of the scatterer. For instance, the majority of the point signatures representing the main railway station of Berlin fit into this category and, hence, may be labeled as *ghost corners*. Therefore, the extraction of object information based on multiple reflected radar signals may lead to errors. This problem should be kept in mind since lines or point signatures are confirmed by the simulator as being prominent hints for urban objects.

The third objective of the thesis is to develop a *SAR simulator based on existing software packages*. Parts of RaySAR are based on POV-Ray, an open-source raytracer. Own developments have been added to the source code in order to provide output data in SAR geometry. Using an existing software has proven to be reasonable as the available methods are fast and reliable. In addition, using existing tools saved development time which could be used for working on the

core of this thesis: the development of a 3D SAR simulator and the investigation of the origin of SAR image signatures.

The current status of RaySAR offers several aspects for future work which mainly concern the enhancement of RaySAR and the analysis of reflection phenomena.

First, potentials for improving the SAR simulator have to be tested. In this regard, the focus may be on increasing the completeness of diffuse multiple reflections. In its current form, RaySAR does not enable to cover all relevant diffuse multiple reflections. Instead, only a small insight into diffuse reflection phenomena is possible. However, concentrating on the simulation of multiple reflections including one diffuse reflection is reasonable. For instance, fourfold bounce signatures representing the Wynn Hotel may be explained in more detail (see chapter 7.2). As the ray tracer is only a component of the RaySAR package, it can be exchanged with more sophisticated rendering methods, which consider the exchange of diffuse signals between objects. Adding the radiosity algorithm (Goral et al., 1984) to basic ray tracing may be a way to solve this task. An alternative solution may be the application of path tracing (Kajiya, 1986) where rays are randomly distributed at intersected surfaces. Nonetheless, both methods will lead to a significant increase of the calculating time which hampers the testing of different imaging geometries or the simulation of SAR image stacks.

Second, the exploitation of VHR SAR data leads to the need of new simulation methods to be added to RaySAR. For instance, 2D simulation methods may be applied or extended for providing a-priori knowledge for object extraction or change detection using real SAR data. PSI processing may make use of grouping patterns of point signatures within the simulated outline of urban objects. As shown in Gernhardt and Hinz (2008), the reliability of deformation estimation can be increased when monitoring groups of scatterers. Simulating the outline of buildings or building shadow may also support algorithms for change detection as image signatures can be assigned to single objects of interest. New concepts for tomographic SAR may be tested by means of data stacks simulated for basic object models. To this end, the SAR imaging geometry and phase noise of real SAR missions can be considered.

Finally, the developed methods for 3D analysis enable further case studies on the nature of scatterers. Especially, a categorization of ghost corners is reasonable. This can be seen for the main railway station of Berlin (see chapter 7.3.6). Ghost corners on the building facade lack of correspondence to metallic bars but describe the main corpus of the building. In contrast, triple bounce signals located on the ground or fivefold bounce signals found beneath the ground level do not represent the geometry of the building. The simulation of highly detailed models may enable to recover new reflection phenomena. Unfortunately, 3D models of high detail are only available for prominent buildings. Hence, in most cases, reflection phenomena will have to be explained by means of 3D models describing the main features of objects. This may be sufficient as, for instance, the simulation of the University of Stuttgart reveals that prominent image signatures representing a building can be confirmed when considering basic facade details.

# A Radar reflection models

Specular reflections of radar signals are commonly described by the Fresnel reflection model. For diffuse reflections, different reflection models such as the Small Perturbation Method (SPM) or the Kirchhoff Approach (KA) have been defined for different levels of surface roughness. In the following, the Fresnel reflection model and the SPM are briefly recapitulated. Detailed information can be found, for instance, in Franceschetti et al. (2001) and Tsang and Kong (2001).

## Fresnel reflection model

The Fresnel reflection coefficients, providing the portion of signal reflected in specular direction, depend on the angle of incidence of the incoming signal  $\theta_i$  as well as on the complex relative dielectric constant defined as

$$\varepsilon_r = \frac{\varepsilon_2}{\varepsilon_1} \quad (\text{A.1})$$

describing the proportion between the permittivity of the upper medium and lower medium in a simulated scene. In the SAR simulation case, the upper and lower medium represent the atmosphere and a reflecting surface at the earth surface, respectively. The Fresnel coefficient in horizontal polarization is calculated by

$$r_h = \left| \frac{\cos \theta_i - \sqrt{\varepsilon_r - \sin^2 \theta_i}}{\cos \theta_i + \sqrt{\varepsilon_r - \sin^2 \theta_i}} \right|^2 \quad (\text{A.2})$$

and the Fresnel coefficient in vertical polarization is defined as

$$r_v = \left| \frac{\varepsilon_r \cos \theta_i - \sqrt{\varepsilon_r - \sin^2 \theta_i}}{\varepsilon_r \cos \theta_i + \sqrt{\varepsilon_r - \sin^2 \theta_i}} \right|^2 \quad (\text{A.3})$$

## Small Perturbation Method (SPM)

The Small Perturbation Method (SPM) approximates the diffuse reflection of radar signals at surfaces whose surface height variation is small compared to the signal wavelength. From the geometrical point of view, the strength of diffuse reflected signals depends on three angles: the angle of incidence  $\theta_i$  of the incoming signal and two angles defining the direction of reflection, i.e.  $\theta_r$  representing the reflection angle with respect to the surface normal and  $\vartheta_r$  defining the rotation with respect to the incident field. The power density of a signal diffusely reflected into a certain direction is derived by

$$|E_{pq}|^2 = \frac{4a |k^2 \cos \theta_r \cos \theta_i \beta_{pq}|^2 W(\eta_{xy})}{(2\pi R)^2} \quad (\text{A.4})$$

where  $a$  is the area of the surface,  $k = \frac{2\pi}{\lambda}$  is the signal wavenumber, and  $R$  is the spatial distance between SAR and object.  $W(\kappa_x, \kappa_y)$  is the surface power spectrum, i.e. the Fourier transform of the surface autocorrelation function. It may be defined by means of standard surface models such as gaussian or exponential shapes or by using fractals (Franceschetti et al., 2001). In this



thesis, an isotropic gaussian surface was used for surface representation, which may be defined as

$$W(\kappa_x, \kappa_y) = \pi \sigma^2 L_c^2 \cdot \exp \left[ - \left( \frac{\sqrt{\kappa_x^2 + \kappa_y^2} \cdot L_c}{2} \right)^2 \right] \quad (\text{A.5})$$

where  $\sigma$  is the surface standard deviation and  $L_c$  is the surface correlation length. Finally, signal polarimetry is considered by parameter  $\beta_{pq}$ . At this point, the examples of  $HH$  and  $VV$  are introduced:

$$\beta_{hh} = \frac{(\varepsilon_r - 1) \cos(\vartheta_r)}{\left( \cos \theta_r + \sqrt{\varepsilon_r - \sin^2 \theta_r} \right) \cdot \left( \cos \theta_i + \sqrt{\varepsilon_r - \sin^2 \theta_i} \right)} \quad (\text{A.6})$$

$$\beta_{vv} = \frac{\left( \sqrt{\varepsilon_r - \sin^2(\theta_r)} \cdot \sqrt{\varepsilon_r - \sin^2(\theta_i)} \cdot \cos \vartheta_r - \varepsilon_r \sin(\theta_i) \sin(\theta_r) \right) \cdot (\varepsilon_r - 1)}{\left( \varepsilon_r \cos \theta_r + \sqrt{\varepsilon_r - \sin^2 \theta_r} \right) \cdot \left( \varepsilon_r \cos \theta_i + \sqrt{\varepsilon_r - \sin^2 \theta_i} \right)} \quad (\text{A.7})$$

The parameters for cross-polarization can be found in Franceschetti et al. (2001).

## B POV-Ray: Introduction and Modeling

### B.1 Introduction to POV-Ray

The idea for POV-Ray (POV-Ray, 2011), where the abbreviation POV stands for *Persistence of Vision*, was born in May 1991 when David Buck offered the development of a new ray tracer to the render community. POV-Ray should be based on DKB-Trace, an existing ray tracer developed by Buck for Amiga graphics which had been adapted to be used on personal computers (Buck, 2011). Since then, POV-Ray has been enhanced and has currently reached version 3.6.2. It is an open-source software programmed in C++ where own developments can be added to its source-code. Ray tracing, radiosity and a simplified version of photon mapping are supported. Modeling is performed in a text editor for defining scene objects and render settings. To this end, POV-Ray owns a programming language which is translated by a parser for being used in the C++ source code. In addition, modeling software is available for providing POV-Ray scenes, e.g. Moray (Moray, 2011) or Wings3D (Wings3D, 2011). Transforming standard model formats in to the POV-Ray format (.pov) is possible, e.g. by using AccuTrans 3D (AccuTrans, 2011). Further information about POV-Ray can be found, for instance, in Wolfe (1999) and in Lama (2004). Basics with regard to modeling in the POV-Ray editor are introduced in the next subsection.

### B.2 Modeling in the POV-Ray editor

Modeling in the POV-Ray editor is introduced from two aspects. First, tools for describing the scene geometry are presented. Afterward, parameters for defining the reflection characteristics of objects are explained. In this context, the focus is on tools and parameters relevant for SAR simulation.

#### Scene geometry

Basically, a scene to be rendered has to contain three kinds of elements: at least one light source, a camera for defining the observer's point of view and the geometry and material of objects. The standard light source is *point light* whose origin is situated at one point in space. The emission of parallel light is obtained using the POV-Ray command *parallel*. For instance, the properties of a light source emitting parallel light can be defined by

$$\text{light\_source}\{\text{color rgb} < I_1, I_2, I_3 > \text{ parallel translate} < x_1, y_1, z_1 > \text{ point\_at} < x_2, y_2, z_2 > \}$$

The command *color rgb*  $< I_1, I_2, I_3 >$  represents the emitted signal by one channel for blue, green, and red light, respectively. Furthermore, the position of the light source and the direction of the emitted signal are defined by vectors *translate*  $< x_1, y_1, z_1 >$  and *point\_at*  $< x_2, y_2, z_2 >$ , respectively.

Various camera types are offered by POV-Ray. A perspective camera, which is the standard camera type, is defined by means of a projection center and an image plane, located in front of the projection center. Rays for detecting intensities in the 3D scene are defined by connecting the projection center and the center of pixels on the image plane. The number of rays depends on the number of pixels on the image plane. The parallelism of rays is obtained by using an orthographic camera. In contrast to a perspective camera, the sampling density at objects is independent from the spatial distance sensor-object and, hence, only depends on the spatial

distance between adjacent pixel centers in the image plane. The definition of an orthographic camera in the POV-Ray editor requires the following command:

*camera{orthographic location  $\langle x_1, y_1, z_1 \rangle$  look\_at  $\langle x_2, y_2, z_2 \rangle$  right  $n_1 \cdot x$  up  $n_2 \cdot y$ }*

Vectors *location*  $\langle x_1, y_1, z_1 \rangle$  and *look\_at*  $\langle x_2, y_2, z_2 \rangle$  are required for defining the sensor position and sensor orientation. The width and height of the image plane is adapted by the products *right*  $n_1 \cdot x$  and *up*  $n_2 \cdot y$ , respectively, where  $n_1$  and  $n_2$  are real numbers. Finally, the number of pixels on the image plane has to be defined.

Basic modeling of objects in the POV-Ray editor is conducted in two ways. First, objects can be composed by standard shapes, e.g. polygons, spheres or planes. Moreover constructive solid geometry (CSG) can be used for creating objects by subtraction, merging, and unifying of objects (commands: *difference*, *merge*, *union*) or by finding the intersection between objects (command: *intersection*). Additional information about CSG can be found, for instance, in Hoffmann (1989). Besides modeling in the POV-Ray editor, 3D models of common formats (e.g. Wavefront, VRML, 3ds Max) can be imported into the POV-Ray environment. In any case, the adaptation of surface properties and the definition of the virtual sensor has to be done in the POV-Ray editor.

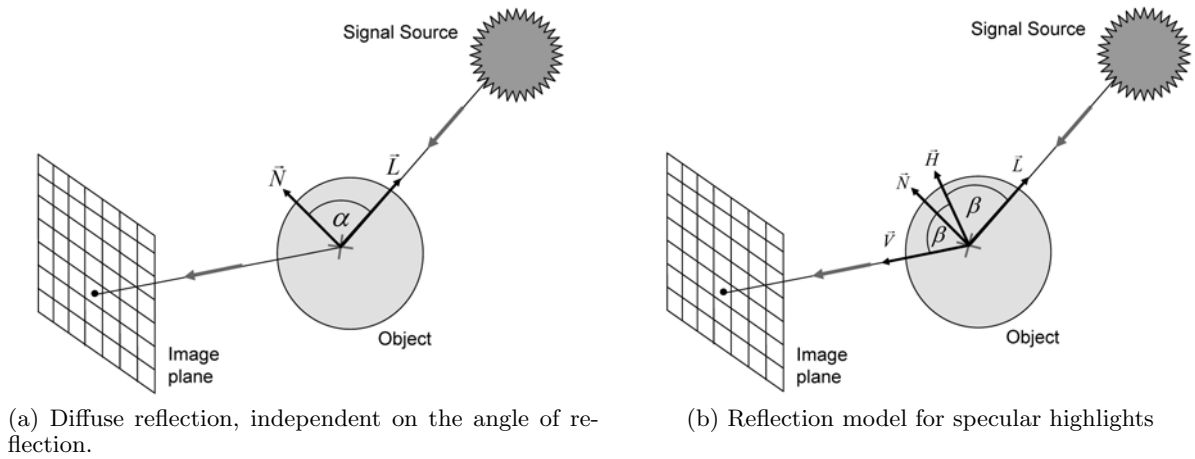


Fig. 66. POV-Ray reflection models.  $\vec{L}$ : vector pointing to light source  $\vec{N}$ : surface normal.  $\vec{V}$  pointing to the pixel center  $\vec{H}$ : bisection vector in between  $\vec{L}$  and  $\vec{V}$

## Scene radiometry

In POV-Ray, the reflection characteristics of objects are described by parameters for diffuse and specular reflection. Generally, diffuse reflections may be categorized into two groups: A.) diffuse reflection of signals emitted by a signal source and B.) diffuse reflection of signals between different scene objects. In case of A.), the diffuse intensity at a surface is derived using the formula

$$I_d = F_a \cdot F_d \cdot I_{sig} \cdot C \cdot (\vec{N} \cdot \vec{L})^{F_b} \quad (\text{B.1})$$

where

- ◇  $F_a$  is a media attenuation factor [value within interval 0 - 1],
- ◇  $F_d$  is the diffuse reflection coefficient [0 - 1],
- ◇  $I_{sig}$  is the intensity of the incoming signal [value between 0 and 1 for channels blue, green, and red],

- ◇  $C$  is the color of the surface hit by the signal [value between 0 and 1 for channels blue, green, and red],
- ◇  $\vec{N}$  is the surface normal vector,
- ◇  $\vec{L}$  is the normalized signal vector pointing from the surface point to the signal source, and
- ◇  $F_b$  is a surface brilliance factor.

According to equation B.1, diffuse reflection at object surfaces is assumed to be of type 'lambertian'. Figure 66a displays a diffuse reflection process. The reflected intensity only depend on the incidence angle  $\alpha$  of the incoming signal hitting the surface. Diffuse signal reflections between objects, which corresponds to case B.), are not considered by the raytracing concept and may only be represented by constant intensity (POV-Ray command *ambient*).

Specular highlights are added artificially in case of a specific geometry defined by the incoming ray and the reflected ray. As shown in figure 66b, surface normal  $\vec{N}$  and signal vector  $\vec{L}$ , both fixed at the intersection point detected by the ray tracer, define bisection vector  $\vec{H}$ . In case of specular reflection, the angle between vectors  $\vec{N}$  and  $\vec{H}$  equals zero. The corresponding equation for specular highlights is defined as

$$I_s = F_s \cdot C \cdot (\vec{N} \cdot \vec{H})^{\frac{1}{F_r}} \quad (\text{B.2})$$

where  $F_s$  is a specular reflection coefficient [0 - 1] and  $F_r$  is a roughness factor defining the sharpness of the specular highlight. In sum, the surface characteristics of an object may be defined by using the command

```
texture {
  pigment { color rgb < I1, I2, I3 > }
  finish { reflection { Fw } diffuse Fd specular Fs roughness Fr }
}
```

The color of the surface is defined by command *pigment {·}*, while surface reflection is modeled by command *finish {·}*. Command *reflection {·}* is required for weighting specular reflected rays by factor  $F_w$  chosen from the interval between 0 and 1. In case of multiple reflections, ray tracing is stopped if the ray's weight falls below a given threshold, if the pre-defined trace level maximum is reached, or if no further intersection point is detected within the modeled scene.

## C List of abbreviations

<b>BRDF</b>	bi-directional reflectance distribution function
<b>CAD</b>	computer-aided design
<b>CSG</b>	constructive solid geometry
<b>DEM</b>	digital elevation model
<b>DLR</b>	German Aerospace Center
<b>ERS</b>	european remote sensing satellite
<b>GENESIS</b>	generic system for interferometric SAR
<b>GMTI</b>	ground moving target indication
<b>GO</b>	geometrical optics
<b>InSAR</b>	interferometric synthetic aperture radar
<b>KA</b>	Kirchhoff approach
<b>LiDAR</b>	light detection and ranging
<b>NLS</b>	non-linear least square adjustment
<b>PO</b>	physical optics
<b>POV</b>	persistence of vision
<b>PRF</b>	pulse repetition frequency
<b>PS</b>	persistent scatterer
<b>PSI</b>	persistent scatterer interferometry
<b>RCS</b>	radar cross section
<b>SAR</b>	synthetic aperture radar
<b>SPM</b>	small perturbation method
<b>SVD</b>	singular value decomposition
<b>TanDEM-X</b>	TerraSAR-X-Add-on for Digital Elevation Measurements
<b>TomoSAR</b>	tomographic synthetic aperture radar
<b>VHR</b>	very high resolution
<b>VRML</b>	virtual reality modeling language

# References

- AccuTrans, 2011. AccuTrans 3D. Micromouse Productions, [www.micromouse.ca](http://www.micromouse.ca) [checked: 24.02.2011].
- Adam, N., Eineder, M., Yague-Martinez, N., Bamler, R., 2008. High resolution interferometric stacking with TerraSAR-X. In: Proceedings of IEEE International Geoscience and Remote Sensing Symposium (IGARSS), Vol. 2, 117–120.
- Adam, N., Zhu, X., Minet, C., Liebhart, W., Eineder, M., Bamler, R., 2009. Techniques and examples for the 3D reconstruction of complex scattering situations using TerraSAR-X. In: Proceedings of IEEE International Geoscience and Remote Sensing Symposium (IGARSS), Vol. 3, 900–903.
- Appel, A., 1968. Some techniques for shading machine renderings of solids. In: Proceedings of the spring joint computer conference AFIPS, ACM, New York, NY, USA, 37–45.
- Attema, E., Duchossois, G., Kohlhammer, G., 1998. ERS-1/2 SAR land applications: overview and main results. In: Proceedings of IEEE International Geoscience and Remote Sensing Symposium (IGARSS), Vol. 4, 1796–1798.
- Auer, S., Balz, T., Becker, S., Bamler, R., 2010a. 3D SAR simulation of urban areas based on detailed building models. *Photogrammetric Engineering & Remote Sensing*, Journal of the American Society for Photogrammetry and Remote Sensing 76 (12): 1373–1384.
- Auer, S., Hinz, S., Bamler, R., 2008. Ray tracing for simulating reflection phenomena in SAR images. In: Proceedings of IEEE International Geoscience and Remote Sensing Symposium (IGARSS), Vol. 5, 518–521.
- Auer, S., Hinz, S., Bamler, R., 2010b. Ray-tracing simulation techniques for understanding high-resolution SAR images. *IEEE Transactions on Geoscience and Remote Sensing* 48 (3): 1445–1456.
- Auer, S., Zhu, X., Hinz, S., Bamler, R., 2009a. 3D analysis of scattering effects based on ray tracing techniques. In: Proceedings of IEEE International Geoscience and Remote Sensing Symposium (IGARSS), Vol. 3, 17–20.
- Auer, S., Zhu, X., Hinz, S., Bamler, R., 2009b. Ray tracing and SAR-tomography for 3D analysis of microwave scattering at man-made objects. In: *International Archives of Photogrammetry, Remote Sensing and Spatial Information Sciences*, Vol. 38-3/W4, 157–162.
- Balz, T., 2006. Real-time SAR simulation of complex scenes using programmable graphics processing units. In: Proceedings of the ISPRS TCVII Mid-term Symposium, Enschede.
- Balz, T., Stilla, U., 2009. Hybrid GPU-based single- and double-bounce SAR simulation. *IEEE Transactions on Geoscience and Remote Sensing* 47: 3519–3529.
- Bamler, R., 1992. A comparison of range-doppler and wavenumber domain SAR focusing algorithms. *IEEE Transactions on Geoscience and Remote Sensing* 30 (4): 706–713.
- Bamler, R., Eineder, M., 2008. The pyramids of gizeh seen by TerraSAR-X - a prime example for unexpected scattering mechanisms in SAR. *IEEE Geoscience and Remote Sensing Letters* 5 (3): 468–470.
- Bamler, R., Hartl, P., 1998. Synthetic aperture radar interferometry. *Inverse Problems* 14: R1–R54.
- Becker, S., 2009. Generation and application of rules for quality dependent facade reconstruction. *ISPRS Journal of Photogrammetry and Remote Sensing* 64 (6): 640–653.
- Berges, A., Latger, J., Mametsa, H., 2004. FERMAT a new radar simulation approach. In: Proceedings of International Conference on Radar Systems (RADAR).
- Bickert, B., Meyer-Hilberg, J., Schmid, J., 2002. A radar raw data generator and modular algorithm simulation system for MTI development. In: Proceedings of the European Conference on Synthetic Aperture Radar (EUSAR).
- Bolter, R., 2001. Buildings from SAR: Detection and reconstruction of buildings from multiple view high resolution SAR data. Ph.D. thesis, Technische Universität Graz, Graz.
- Bolter, R., Leberl, F., 2000. Detection and reconstruction of buildings from multiple view interferometric SAR data. In: Proceedings of IEEE International Geoscience and Remote Sensing Symposium (IGARSS), Vol. 2, 749–751.
- Bouknight, W., 1970. A procedure for generation of three-dimensional half-toned computer graphics presentations. *Commun. ACM* 13 (9): 527–536.

- Boyll, R., 1969. Computer simulation of lunar displays. In: Proceedings of SPIE Conference, Vol. 2, 339–356.
- Breit, H., Fritz, T., Balss, U., Lachaise, M., Niedermeier, A., Vonavka, M., 2010. TerraSAR-X SAR processing and products. *IEEE Transactions on Geoscience and Remote Sensing* 48 (2): 727–740.
- Brunner, D., 2009. Advanced methods for building information extraction from very high resolution SAR data to support emergency response. Ph.D. thesis, University of Trento.
- Brunner, D., Bruzzone, L., Ferro, A., Lemoine, G., 2009. Analysis of the reliability of the double bounce scattering mechanism for detecting buildings in VHR SAR images. In: Proceedings of RadarCon 2009, Pasadena, USA.
- Buck, D., 2011. The early history of POV-Ray. [www.povray.org](http://www.povray.org) [checked: 24.02.2011].
- Budillon, A., Evangelista, A., Schirinzi, G., 2009. SAR tomography from sparse samples. In: Proceedings of IEEE International Geoscience and Remote Sensing Symposium (IGARSS), Vol. 4, IV–865–IV–868.
- Camporeale, C., Galati, G., 1991. Digital computer simulation of synthetic aperture systems and images. *European Transactions on Telecommunications* 2 (NO: 3): 343–352.
- Catmull, E., 1974. A subdivision algorithm for computer display of curved surfaces. Ph.D. thesis, University of Utah.
- Cook, R. L., Porter, T., Carpenter, L., 1984. Distributed ray tracing. *SIGGRAPH Comput. Graph.* 18 (3): 137–145.
- Cumming, I., Wong, F., 2005. *Digital Processing of Synthetic Aperture Radar Data: Algorithms and Implementation*. Artech House Publishers.
- Eiffel, 2011. Le site officiel de la tour eiffel. [www.tour-eiffel.fr](http://www.tour-eiffel.fr) [checked: 24.02.2011].
- Eineder, M., 2003. Efficient simulation of SAR interferograms of large areas and of rugged terrain. *IEEE Transactions on Geoscience and Remote Sensing* 41 (6): 1415–1427.
- Eineder, M., Adam, N., Bamler, R., Yague-Martinez, N., Breit, H., 2009. Spaceborne spotlight SAR interferometry with TerraSAR-X. *IEEE Transactions on Geoscience and Remote Sensing* 47 (5): 1524–1535.
- Eineder, M., Adam, N., Brcic, R., Yague-Martinez, N., Fritz, T., 2008. High bandwidth spotlight SAR interferometry with TerraSAR-X. In: Proceedings of IEEE International Geoscience and Remote Sensing Symposium (IGARSS) 2008, Vol. 2, 113–116.
- Ferretti, A., Bianchi, M., Prati, C., Rocca, F., 2005. Higher-order permanent scatterers analysis. *EURASIP J. Appl. Signal Process.* : 3231–3242.
- Ferretti, A., Prati, C., Rocca, F., 2001. Permanent scatterers in SAR interferometry. *IEEE Transactions on Geoscience and Remote Sensing* 39 (1): 8–20.
- Fornaro, G., Reale, D., Serafino, F., 2009. Four-dimensional SAR imaging for height estimation and monitoring of single and double scatterers. *IEEE Transactions on Geoscience and Remote Sensing* 47 (1): 224–237.
- Fornaro, G., Serafino, F., Soldovieri, F., 2003. Three-dimensional focusing with multipass SAR data. *IEEE Transactions on Geoscience and Remote Sensing* 41 (3): 507–517.
- Franceschetti, G., Guida, R., Iodice, A., Riccio, D., Ruello, G., Stilla, U., 2007. Building feature extraction via a deterministic approach: application to real high resolution SAR images. In: Proceedings of IEEE International Geoscience and Remote Sensing Symposium (IGARSS), 2681–2684.
- Franceschetti, G., Iodice, A., Migliaccio, M., Riccio, D., 1998. A novel across-track SAR interferometry simulator. *IEEE Transactions on Geoscience and Remote Sensing* 36 (3): 950–962.
- Franceschetti, G., Iodice, A., Riccio, D., 2001. *Fractal Models for Scattering from Natural Surfaces*. Academic Press, Ch. 1.6.5, 467–485.
- Franceschetti, G., Iodice, A., Riccio, D., 2002. A canonical problem in electromagnetic backscattering from buildings. *IEEE Transactions on Geoscience and Remote Sensing* 40 (8): 1787–1801.
- Franceschetti, G., Iodice, A., Riccio, D., Ruello, G., 2003. SAR raw signal simulation for urban structures. *IEEE Transactions on Geoscience and Remote Sensing* 41 (9): 1986–1995.
- Franceschetti, G., Lanari, R., 1999. *Synthetic Aperture Radar Processing*. CRC Press LLC.
- Franceschetti, G., Migliaccio, M., Riccio, D., 1995. The SAR simulation: an overview. In: Proceedings



- of IEEE International Geoscience and Remote Sensing Symposium (IGARSS), Vol. 3, 2283–2285.
- Franceschetti, G., Migliaccio, M., Riccio, D., Schirizzi, G., 1992. SARAS: a synthetic aperture radar (SAR) raw signal simulator. *IEEE Transactions on Geoscience and Remote Sensing* 30 (1): 110–123.
- Gamba, P., Houshmand, B., Saccani, M., 2000. Detection and extraction of buildings from interferometric SAR data. *IEEE Transactions on Geoscience and Remote Sensing* 38 (1): 611–617.
- Gelautz, M., Frick, H., Raggam, J., Burgstaller, J., Leberl, F., 1998. SAR image simulation and analysis of alpine terrain. *ISPRS Journal of Photogrammetry and Remote Sensing* 53 (1): 17–38.
- Gernhardt, S., Adam, N., Eineder, M., Bamler, R., 2010. Potential of very high resolution SAR for persistent scatterer interferometry in urban areas. *Annals of GIS* 16 (2): 103–111.
- Gernhardt, S., Hinz, S., 2008. Advanced displacement estimation for PSI using high resolution SAR data. In: *Proceedings of IEEE International Geoscience and Remote Sensing Symposium (IGARSS)*, Vol. 3, 1276–1279.
- Glassner, A. S., 2002. *An Introduction to Ray Tracing*, 9th Edition. Morgan Kaufmann, San Francisco.
- Goel, K., Adam, N., 2010. A bayesian method for very high resolution multi aspect angle radargrammetry. In: *Proceedings of the European Conference on Synthetic Aperture Radar (EUSAR)*.
- Google, 2011. Google 3D warehouse. <http://sketchup.google.com/3dwarehouse> [checked: 24.02.2011].
- Goral, C. M., Torrance, K. E., Greenberg, D. P., Battaile, B., 1984. Modeling the interaction of light between diffuse surfaces. *SIGGRAPH Comput. Graph.* 18 (3): 213–222.
- Groot, J., Otten, M., 1993. Corner reflector imaging by high resolution SAR. In: *Proceedings of SAR Calibration Workshop ESA WPP-048, ESTEC, Noordwijk, The Netherlands*, 43–50.
- Guida, R., Iodice, A., Riccio, D., 2010. Assessment of TerraSAR-X products with a new feature extraction application: Monitoring of cylindrical tanks. *IEEE Transactions on Geoscience and Remote Sensing* 48 (2): 930–938.
- Hammer, H., Balz, T., Cadario, E., Soergel, U., Thoennessen, U., Stilla, U., 2008. Comparison of SAR simulation concepts for the analysis of high resolution SAR data. In: *Proceedings of the European Conference on Synthetic Aperture Radar (EUSAR)*.
- Hanssen, R., 2001. *Radar Interferometry: Data Interpretation and Error Analysis*, 1st Edition. Kluwer Academic Publishers, Dordrecht, The Netherlands.
- Heckbert, P. S., Hanrahan, P., 1984. Beam tracing polygonal objects. In: *SIGGRAPH '84: Proceedings of the 11th annual conference on Computer graphics and interactive techniques*, ACM, New York, NY, USA, 119–127.
- Henderson, F., Lewis, A., 1998. *Principles & Applications of Imaging Radar*. John Wiley & Sons, Inc., New York.
- Hill, R., Moate, C., Blacknell, D., 2006. Urban scene analysis from SAR image sequences. In: *Proceedings of the European Conference on Synthetic Aperture Radar (EUSAR)*.
- Hoffmann, C. M., 1989. *Geometric & Solid Modeling*. Morgan Kaufmann Publishers, San Mateo, California.
- Holtzman, J., Frost, V., Abbott, J., Kaupp, V., 1978. Radar image simulation. *IEEE Transactions on Geoscience Electronics* 16 (4): 296–303.
- Ikegami, F., Takeuchi, T., Yoshida, S., 1991. Theoretical prediction of mean field strength for urban mobile radio. *IEEE Transactions on Antennas and Propagation* 39 (3): 299–302.
- Jensen, H. W., 1996. Global illumination using photon maps. In: *Proceedings of the eurographics workshop on Rendering techniques '96*, Springer-Verlag, London, UK, 21–30.
- Kajiya, J. T., 1986. The rendering equation. *SIGGRAPH Comput. Graph.* 20 (4): 143–150.
- Kampes, B., 2006. *Radar Interferometry - Persistent Scatterer Technique*. Springer, Dordrecht, The Netherlands.
- Knott, E., Shaeffer, J., Tuley, M., 2004. *Radar Cross Section*, 2nd Edition. SciTech Publishing, NC.
- Krieger, G., Moreira, A., Fiedler, H., Hajnsek, I., Werner, M., Younis, M., Zink, M., 2007. TanDEM-X: A satellite formation for high-resolution SAR interferometry. *IEEE Transactions on Geoscience and Remote Sensing* 45 (11): 3317–3341.
- Lama, T., 2004. *3D-Welten*. Hanser, München.
- LaPrade, G. L., 1963. An analytical and experimental study of stereo for radar. *Photogrammetric*

- Engineering 29 (2): 294–300.
- Latger, J., Mametsa, H., Berges, A., 2005. SPECRA Y EM / FERMAT - a new modelling radar approach from numerical models of terrain to SAR images. In: Proceedings of International Conference on Radar Systems (RADAR).
- Leberl, F., 1990. Radargrammetric Image Processing. Artech House, Boston, MA.
- Lehnert, H., 1993. Systematic errors of the ray-tracing algorithm. Applied Acoustics 38 (2-4): 207–221.
- Lichti, D., 2004. A resolution measure for terrestrial laser scanners. International Archives of Photogrammetry, Remote Sensing and Spatial Information Sciences 34 34 (B5): 552–558.
- Lombardini, F., 2005. Differential tomography: a new framework for SAR interferometry. IEEE Transactions on Geoscience and Remote Sensing 43 (1): 37–44.
- Lombardini, F., Reigber, A., 2003. Adaptive spectral estimation for multibaseline SAR tomography with airborne L-band data. In: Proceedings of IEEE International Geoscience and Remote Sensing Symposium (IGARSS), Vol. 3, 2014–2016.
- Lombardo, P., 2004. A multichannel spaceborne radar for the COSMO-SkyMed satellite constellation. In: Proceedings of IEEE Aerospace Conference, Vol. 1, 111–119.
- Louet, J., Bruzzi, S., 1999. ENVISAT mission and system. In: Proceedings of IEEE International Geoscience and Remote Sensing Symposium (IGARSS), Vol. 3, 1680–1682.
- Mametsa, H. J., Rouas, F., Berges, A., Latger, J., 2001. Imaging radar simulation in realistic environment using shooting and bouncing rays technique. In: Proceedings of SPIE Conference, SAR Image Analysis, Modeling and Techniques IV, 34–40.
- Margarit, G., Mallorqui, J., Fortuny-Guasch, J., Lopez-Martinez, C., 2009. Phenomenological vessel scattering study based on simulated inverse SAR imagery. IEEE Transactions on Geoscience and Remote Sensing 47 (4): 1212–1223.
- Margarit, G., Mallorqui, J. J., Lopez-Martinez, C., 2007. GRECOSAR, a SAR simulator for complex targets: Application to urban environments. In: Proceedings of IEEE International Geoscience and Remote Sensing Symposium (IGARSS), 4160–4163.
- Margarit, G., Mallorqui, J. J., Rius, J. M., Sanz-Marcos, J., 2006. On the usage of GRECOSAR, an orbital polarimetric SAR simulator of complex targets, to vessel classification studies. IEEE Transactions on Geoscience and Remote Sensing 44 (12): 3517–3526.
- Melody, J., 2009. Predicted-wavefront backprojection for knowledge-aided SAR image reconstruction. In: Proceedings of RadarCon 2009, Pasadena, USA.
- Meyer-Hilberg, J., 2006. PIRDIS: A new versatile tool for SAR/MTI systems simulation. In: Proceedings of the European Conference on Synthetic Aperture Radar (EUSAR).
- Meyer-Hilberg, J., Neumann, C., Senkowski, H., 2008. GMTI systems simulation using the SAR simulation tool PIRDIS. In: Proceedings of the European Conference on Synthetic Aperture Radar (EUSAR).
- Michaelsen, E., Soergel, U., Stilla, U., 2002. Grouping salient scatterers in InSAR data for recognition of industrial buildings. In: Proceedings of 16th International Conference on Pattern Recognition, Vol. 2, 613–616.
- Moray, 2011. Moray. [www.stmuc.com/moray](http://www.stmuc.com/moray) [checked: 24.02.2011].
- Mori, A., De Vita, F., 2004. A time-domain raw signal simulator for interferometric SAR. IEEE Transactions on Geoscience and Remote Sensing 42 (9): 1811–1817.
- Muhleman, D., 1964. Radar scattering from venus and the moon. Symposium on Radar and Radiometric Observations of Venus during the 1962 Conjunction 69: 34–41.
- Nasr, J., Vidal-Madjar, D., 1991. Image simulation of geometric targets for spaceborne synthetic aperture radar. IEEE Transactions on Geoscience and Remote Sensing 29 (6): 986–996.
- Nicodemus, F., 1965. Directional reflectance and emissivity of an opaque surface. Appl. Opt. 4 (7): 767–773.
- Oriot, H., Cantalloube, H., 2008. Circular SAR imagery for urban remote sensing. In: Proceedings of the European Conference on Synthetic Aperture Radar (EUSAR).
- Perski, Z., Van Leijen, F., Hanssen, R., 2007. Applicability of PSInSAR for building hazard identification. study of the 29 January 2006 Katowice Exhibition Hall collapse and the 24 February 2006

- Moskow Basmanny Market collapse. In: Proceedings of the Envisat Symposium.
- Petit, D., Adragna, F., 2000. A new interferogram simulator: 2SIR. study of coherence losses for tortured reliefs. In: Proceedings of SAR Workshop: CEOS - Working Group on Calibration and Validation, Vol. 450, 591–596.
- Phong, B., 1975. Illumination for computer generated pictures. *Communications of the ACM* 18 (6): 311–317.
- Pitz, W., Miller, D., 2010. The TerraSAR-X satellite. *IEEE Transactions on Geoscience and Remote Sensing* 48 (2): 615–622.
- POV-Ray, 2011. POV-Ray. Persistence of Vision Raytracer Propriety Limited, [www.povray.org](http://www.povray.org) [checked: 24.02.2011].
- Quartulli, M., Datcu, M., 2004. Stochastic geometrical modeling for built-up area understanding from a single SAR intensity image with meter resolution. *IEEE Transactions on Geoscience and Remote Sensing* 42 (9): 1996–2003.
- Raney, R., Wessels, G., 1988. Spatial considerations in SAR speckle consideration. *IEEE Transactions on Geoscience and Remote Sensing* 26 (5): 666–672.
- Reigber, A., Moreira, A., 2000. First demonstration of airborne SAR tomography using multibaseline L-band data. *IEEE Transactions on Geoscience and Remote Sensing* 38 (5): 2142–2152.
- Rius, J., Ferrando, M., Jofre, L., 1993. GRECO: graphical electromagnetic computing for RCS prediction in real time. *IEEE Antennas and Propagation Magazine* 35 (2): 7–17.
- Sarabandi, K., Chiu, T.-C., 1996. Optimum corner reflectors for calibration of imaging radars. *IEEE Transactions on Antennas and Propagation* 44 (10): 1348–1361.
- Schmitz, A., Rick, T., Karolski, T., Kobbelt, L., Kuhlen, T., 2009. Simulation of radio wave propagation by beam tracing. In: Proceedings of Eurographics Symposium on Parallel Graphics and Visualization.
- Simonetto, E., Oriot, H., Garelo, R., 2005. Rectangular building extraction from stereoscopic airborne radar images. *IEEE Transactions on Geoscience and Remote Sensing* 43 (10): 2386–2395.
- Skolnik, M., 1990. Radar Handbook. McGraw-Hill Professional.
- Soergel, U., Thoennessen, U., Brenner, A., Stilla, U., 2006. High-resolution SAR data: new opportunities and challenges for the analysis of urban areas. *IEE Proceedings - Radar, Sonar and Navigation* 153 (3): 294–300.
- Speck, R., Hager, M., Süß, H., 2002. An end-to-end simulator for spaceborne SAR-systems. In: Proceedings of the European Conference on Synthetic Aperture Radar (EUSAR).
- Stoica, P., Moses, R., 2005. Spectral analysis of signals. Prentice Hall, New Jersey.
- Thiele, A., Cadario, E., Schulz, K., Thoennessen, U., Soergel, U., 2007a. InSAR phase profiles at building locations. In: International Archives of Photogrammetry, Remote Sensing and Spatial Information Sciences, Vol. 3/W49A, 203–208.
- Thiele, A., Cadario, E., Schulz, K., Thoennessen, U., Soergel, U., 2007b. Building recognition from multi-aspect high-resolution InSAR data in urban areas. *IEEE Transactions on Geoscience and Remote Sensing* 45 (11): 3583–3593.
- Thiele, A., Hinz, S., Cadario, E., Adam, N., 2010. 3D building reconstruction by exploiting SAR and GIS data. In: Proceedings of the European Conference on Synthetic Aperture Radar (EUSAR).
- Tsang, L., Kong, J., 2001. Scattering of Electromagnetic Waves: Theories and Applications. John Wiley & Sons, Inc., New York.
- Veach, E., Guibas, L. J., 1997. Metropolis light transport. *Computer Graphics* 31 (Annual Conference Series): 65–76.
- Virtual-Berlin, 2011. Virtual-Berlin. [www.virtual-berlin.de](http://www.virtual-berlin.de) [checked: 24.02.2011].
- Wegner, J., Auer, S., Soergel, U., 2010. Geometrical investigation of SAR double-bounce lines. *Photogrammetric Engineering and Remote Sensing, ISPRS Hannover Workshop Issue* 76(9): 1071–1080.
- Werninghaus, R., Buckreuss, S., 2010. The TerraSAR-X mission and system design. *IEEE Transactions on Geoscience and Remote Sensing* 48 (2): 606–614.
- Whitted, T., 1980. An improved illumination model for shaded display. *Commun. ACM* 23 (6): 343–349.

- Wings3D, 2011. Wings3D. [www.wings3d.com](http://www.wings3d.com) [checked: 24.02.2011].
- Wohlers, M., Hsiao, S., Mendelsohn, J., Gardner, G., 1980. Computer simulation of synthetic aperture radar images of three-dimensional objects. *IEEE Transactions on Geoscience and Remote Sensing* 16 (3): 258–271.
- Wolfe, R., 1999. *3D Graphics: A Visual Approach*. Oxford University Press.
- Xu, F., Jin, Y.-Q., 2006. Imaging simulation of polarimetric SAR for a comprehensive terrain scene using the mapping and projection algorithm. *IEEE Transactions on Geoscience and Remote Sensing* 44 (11): 3219–3234.
- Xu, F., Jin, Y.-Q., 2007. Automatic reconstruction of building objects from multiaspect meter-resolution SAR images. *IEEE Transactions on Geoscience and Remote Sensing* 45 (7): 2336–2353.
- Zhu, X., Adam, N., Bamler, R., 2008. First demonstration of space-borne high resolution SAR tomography in urban environment using TerraSAR-X data. In: *Proceedings of CEOS SAR Workshop on Calibration and Validation*.
- Zhu, X., Bamler, R., 2009. Very high resolution SAR tomography via compressive sensing. In: *Proceedings of FRINGE Workshop*.
- Zhu, X., Bamler, R., 2010. Tomographic SAR inversion by  $L_1$  -norm regularization - the compressive sensing approach. *IEEE Transactions on Geoscience and Remote Sensing* 48: 3839–3846.

# List of Figures

1	Imaging geometry of a SAR sensor	10
2	Different resolution levels of SAR data for an urban area in Las Vegas, USA.	14
3	Comparison of optical image and VHR SAR image for the Maison de la Radio France	14
4	Imaging geometry within the range-elevation plane	15
5	Geometrical effects in SAR data	16
6	Simulated reflectivity maps for a box model and a step model	16
7	Optical image and TerraSAR-X temporal average image of the Alexanderplatz in Berlin, Germany	17
8	Interferogram of an urban scene in Tokyo, Japan	19
9	Synthetic aperture in elevation direction	21
10	Tomographic analysis for the Wynn Hotel, Las Vegas, USA	22
11	Range shift of elevated scatterers for different look angles of the SAR	23
12	Results from PSI for an urban scene in Berlin, Germany	24
13	Geometry of bi-directional reflection process	26
14	Global illumination effect for a multi-body scene	28
15	Simulation concept of RaySAR	36
16	Design of virtual SAR sensor	40
17	Simulation example using Fresnel reflection model	42
18	Comparison of the SPM and the RaySAR model for specular reflection.	42
19	Localization of signal contributions by means of RaySAR	48
20	Simulation of diffuse double bounce for virtual SAR	52
21	Simulation of diffuse double bounce using the RaySAR concept	52
22	Azimuth differences between the direct simulation (RaySAR concept) and the simulation of the synthetic aperture.	53
23	Concept for simulating elevation coordinates in case of direct backscattering and specular double reflection	54
24	Detection of specular reflections based on reflection geometry	56
25	Representation of the proportion between signal and clutter in RaySAR	58
26	Representation of the specular and diffuse signal response in case of double bounce	58
27	Simulation results for the corner reflector model provided by RaySAR.	64
28	Rasterization of discrete samples provided by the ray tracer	65
29	Step model: separation of bounces and definition of elevation profiles for pixels of interest	65

30	Step model: elevation coordinates of detected signal contributions for defined profiles	67
31	Step model: height over ground of detected signal contributions for defined profiles	67
32	Step model: distribution of signal response in height over ground	68
33	Step model: histograms showing the number of scatterers for each resolution cell	69
34	Interpretation of scatterer histogram	70
35	3D analysis of signal reflection at corner reflector	72
36	Case studies: forward simulation and inversion of SAR imaging process	76
37	University of Stuttgart: urban scene and modeling	77
38	TerraSAR-X vs. different simulated maps for the University of Stuttgart, Germany	79
39	Eiffel Tower: urban scene and 3D model	80
40	Details of Eiffel Tower, Paris	80
41	Eiffel Tower: SAR image vs. simulated image	82
42	Eiffel Tower: separation of bounce levels	83
43	3D Model of Wynn Hotel, Las Vegas	85
44	Wynn Hotel: SAR image vs. simulation	86
45	Wynn Hotel: scatterer histograms	87
46	Wynn Hotel: slice in range	87
47	Perspective view onto the central part of the main railway station, Berlin	89
48	Geometrical structure of the main railway station, Berlin.	89
49	3D model of the main railway station, Berlin	90
50	SAR temporal average images of the main railway station of Berlin, Germany	91
51	Main railway station, Berlin: spatial distribution of radar signal responses	93
52	Main railway station, Berlin: simulation results for bounce levels 1-3	94
53	Main railway station, Berlin: simulation results for bounce levels 1 to 5	95
54	Main railway station, Berlin: area of interest	96
55	Main railway station Berlin: simulation vs. SAR image for area <i>red</i>	97
56	Main railway station Berlin: simulation vs. SAR image for area <i>green</i>	98
57	Height profiles derived by tomographic processing of the data stack	99
58	Simulated height profiles for two signatures representing PSs	99
59	Identification of scatterer for signature A	101
60	Identification of scatterers for signature B	101
61	Signal reflections at bars: expected differences between simulation and reality	102
62	Identification of scatterers for signature C	103

---

63	Identification of scatterers for signature D	103
64	Main railway station: simulated phase centers of bounce level 3	105
65	Main railway station: simulated phase centers of bounce level 5	105
66	POV-Ray reflection models	113



# List of Tables

1	Parameters of the TerraSAR-X satellite	11
2	Comparison of the Fresnel reflection model and the RaySAR model for specular reflection	43
3	Comparison of the Small Perturbation Method (SPM) and the RaySAR model for diffuse reflection	44
4	Definition of surface parameters for angular-dependent diffuse signal reflection from bare soil	46
5	Evaluation of the geometrical and radiometrical completeness of diffuse signal responses detected by RaySAR	60

# Acknowledgments

After four years filled with lots of excitements and, sometimes, sorrows as well, the work has been done. When looking back in time, it is doubtless that reaching this moment would not have been possible without the support of colleagues, friends and my family.

Firstly, I am very grateful to my supervisor Richard Bamler. Besides being available for theoretical questions, he was a perfect guide with respect to professionalism, scientific work and time management. He showed much interest in my work what was very motivating for me.

Many thanks to Stefan Hinz who encouraged me to start my PhD thesis at the Technische Universität München (TUM). Especially during the first two years of my thesis, he was always available when basic questions of a PhD newcomer had to be answered. Besides, he showed to me how to orient oneself in the field of research.

I am glad that I had the opportunity to work with Antonio Iodice and his colleagues from the university of Naples, namely Raffaella Guida, Pasquale Imperatore, Gerardo di Martino, Antonio Natale, Daniele Riccio, Guiseppe Ruello, and Ivana Zinno. During three stays abroad, they supported me in learning the theory of signal reflection. Limitations and potentials of my work could be discussed from different point of views. Moreover, they gave me insights to the neapolitan way of life, for instance, by having (extended) dinners at Sophia Loren's pizzeria or by watching memorable SSC Napoli football matches in neapolitan bars.

At any time, the working environment for the thesis was optimal. Stefan Gernhardt and Xiaoxiang Zhu (Technische Universität München) as well as Nico Adam and Michael Eineder (German Aerospace Center) supplied processing results and new ideas. Horst Hammer (Fraunhofer IOSB, Karlsruhe) offered to compare simulated images in order to test parts of the RaySAR package. Uwe Sörgel and Jan Wegner (Leibniz Universität Hannover), Timo Balz (Wuhan University), and Susanne Becker (Universität Stuttgart) supported fundamental simulation case studies. Ronny Hänsch (Technische Universität Berlin) provided photos and measures which were very helpful to understand reflection phenomena occurring at the main railway station of Berlin. Eventually, three stays abroad in Naples would not have been possible without the support of the International Graduate School of Science and Engineering (IGSSE) at TUM.

In the end, some sentences are dedicated to the private part of my life. I am very grateful to my parents, Irmgard and Franz Auer, as they always encouraged me to follow my interests and enabled a carefree life. Certainly, I would not have made my way to research without their support. Finally, I want to thank Andrea for her patience, jolliness, and love. Moments with you remind me that life is wonderful.